

**Measurement of Atmospheric Muons  
at IICHEP in Madurai, for better estimation  
of Neutrino Fluxes at INO Site in Theni**

*By*

**Apoorva Dipak Bhatt**

**PHYS01201404007**

**Bhabha Atomic Research Centre, Mumbai**

*A Thesis submitted to the  
Board of Studies in Physical Sciences  
in partial fulfillment of the requirements  
for the Degree of*

**DOCTOR OF PHILOSOPHY**

*of*

**Homi Bhabha National Institute**









**July, 2019**



# Homi Bhabha National Institute

## Recommendations of the Viva Voce Committee

As members of the Viva Voce Committee, we certify that we have read the dissertation prepared by **Apoorva Dipak Bhatt** entitled “**Measurement of atmospheric muons at IICHEP in Madurai, for better estimation of neutrino fluxes at INO site in Theni**” and recommend that it may be accepted as fulfilling the thesis requirement for the award of Degree of Doctor of Philosophy.


Composition	Name	Signature	Date
Chairman	S. Umashankar		15.11.19
Guide/Convener	Gobinda Majumder		15/11/19
Examiner	Prafulla Behera		15/11/19
Member	Nayana Majumdar		15/11/19
Member	L. M. Pant		15/11/19
Member	B. Satyanarayana		15/11/19

Final approval and acceptance of this thesis is contingent upon the candidate's submission of the final copies of the thesis to HBNI.

I hereby certify that I have read this thesis prepared under my direction and recommend that it may be accepted as fulfilling the thesis requirement.

**Date:** 15<sup>th</sup> November, 2019

**Place:** Mumbai

  
Prof. Gobinda Majumder



## STATEMENT BY AUTHOR

This dissertation has been submitted in partial fulfillment of requirements for an advanced degree at Homi Bhabha National Institute (HBNI) and is deposited in the Library to be made available to borrowers under rules of the HBNI.

Brief quotations from this dissertation are allowable without special permission, provided that accurate acknowledgement of source is made. Requests for permission for extended quotation from or reproduction of this manuscript in whole or in part may be granted by the Competent Authority of HBNI when in his or her judgement the proposed use of the material is in the interests of scholarship. In all other instances, however, permission must be obtained from the author.



Apoorva Dipak Bhatt

(Enrolment Number PHYS01201404007)

## STATEMENT BY AUTHOR

The author of this book is indebted to the following persons for their assistance in the preparation of this book: ...

The author is indebted to the following persons for their assistance in the preparation of this book: ...

The author is indebted to the following persons for their assistance in the preparation of this book: ...

The author is indebted to the following persons for their assistance in the preparation of this book: ...

The author is indebted to the following persons for their assistance in the preparation of this book: ...

...  
...  
...

## DECLARATION

I, hereby declare that the investigation presented in the thesis has been carried out by me. The work is original and has not been submitted earlier as a whole or in part for a degree/diploma at this or any other Institution/University.



Apoorva Dipak Bhatt

(Enrolment Number PHYS01201404007)

## CONTENTS

Introduction ..... 1

Chapter 1 ..... 10

Chapter 2 ..... 20

Chapter 3 ..... 30

Chapter 4 ..... 40

Chapter 5 ..... 50

Chapter 6 ..... 60

Chapter 7 ..... 70

Chapter 8 ..... 80

Chapter 9 ..... 90

Chapter 10 ..... 100

Chapter 11 ..... 110

Chapter 12 ..... 120

Chapter 13 ..... 130

Chapter 14 ..... 140

Chapter 15 ..... 150

Chapter 16 ..... 160

Chapter 17 ..... 170

Chapter 18 ..... 180

Chapter 19 ..... 190

Chapter 20 ..... 200

Chapter 21 ..... 210

Chapter 22 ..... 220

Chapter 23 ..... 230

Chapter 24 ..... 240

Chapter 25 ..... 250

Chapter 26 ..... 260

Chapter 27 ..... 270

Chapter 28 ..... 280

Chapter 29 ..... 290

Chapter 30 ..... 300

Chapter 31 ..... 310

Chapter 32 ..... 320

Chapter 33 ..... 330

Chapter 34 ..... 340

Chapter 35 ..... 350

Chapter 36 ..... 360

Chapter 37 ..... 370

Chapter 38 ..... 380

Chapter 39 ..... 390

Chapter 40 ..... 400

Chapter 41 ..... 410

Chapter 42 ..... 420

Chapter 43 ..... 430

Chapter 44 ..... 440

Chapter 45 ..... 450

Chapter 46 ..... 460

Chapter 47 ..... 470

Chapter 48 ..... 480

Chapter 49 ..... 490

Chapter 50 ..... 500



# List of Publications arising from the thesis

## Publications in Refereed Journal

### Published:

1. Improvement of time resolution in large area single gap Resistive Plate Chambers,  
A.D.Bhatt, G.Majumder, N.K.Mondal, Pathaleswar, B.Satyanarayana,  
Nucl. Instrum. Meth. A, **844**, February 2017, 53–61.
2. Update of INO-ICAL reconstruction algorithm,  
S. Seth, A. Bhatt, G. Majumder, A. Mishra,  
JINST, **13**, September 2018, P09015.

## Symposium and conference proceedings

### Published:

1. Improvement of time measurement with the INO-ICAL resistive plate chambers,  
A. D. Bhatt, V. M. Datar, G. Majumder, N. K. Mondal, Pathaleswar, B. Satyanarayana,  
13th Workshop on Resistive Plate Chambers and Related Detectors (RPC2016),  
JINST, **13**, September 2018, P09015.
2. Techniques to Improve Time Resolution of Large Area RPCs,  
A. D. Bhatt, V. M. Datar, G. Majumder, N. K. Mondal, Pathaleswar, B. Satyanarayana,  
XXII DAE High Energy Physics Symposium,  
Springer Proceedings in Physics, **203**, 97–99.

**Communicated:**

1. Update on muon reconstruction for INO-ICAL,  
A. D. Bhatt, G. Majumder,  
Proceedings of XXIII DAE High Energy Physics Symposium.
2. Muon momentum spectra with mini-ICAL,  
A. D. Bhatt, G. Majumder, V. M. Datar, B. Satyanarayana,  
Proceedings of XXIII DAE High Energy Physics Symposium.

*27/2/21*

Apoorva Dipak Bhatt

(Enrolment Number PHYS01201404007)

**Dedicated to,**  
**Prof. Sudhir Pandya**  
**&**  
**Dr. Tushar Pandya**



## ACKNOWLEDGEMENTS

Each generation stands on the shoulders of those who have gone before them, just as I did as inspired by the work of many before me. My research would have been impossible without the aid and support of many people and now, I take this opportunity to acknowledge them.

Firstly, I would like to express my sincere gratitude to my advisor Prof. Gobinda Majunder for the continuous support of my Ph.D study and related research, for his patience, motivation, and immense knowledge. His guidance helped me in all the time of research and writing of this thesis. I could not have imagined having a better advisor and mentor for my Ph.D study.

I express my gratitude to Prof. N.K. Mondal and Prof. V. M. Datar, the past and present project directors of INO, for their motivation and support. Their passion towards research has been an inspiration. I thank my doctoral committee members, Prof. S. Uma Shankar, Prof. Nayana Majumdar and Dr. L. M. Pant for their insightful comments, timely advice and encouragement. I am extremely grateful to Dr. B. Satyanarayana for the invaluable guidance, especially, in electronics instrumentation front, and also, for being the constant pillar of support from my day one as an INO graduate student.

I would like to thank all the members of INO collaboration, and the INO Graduate Training Program, which gave me an excellent learning experience. Also, I sincerely acknowledge the mini-ICAL team for their great effort during the building and commissioning of mini-ICAL detector. I owe my gratitude to the present and past colleagues at TIFR, K. C. Ravindran sir, Kalmani sir, Nagraj sir, Upadhya sir, Shobha madam, Vermaji, Joshiji, Pavanji, Mandarji, Shindeji, Vishalji, Santoshji, Ganeshji, Darshanaji, Vidhyaji, Yuvraaj, Pathaleshwar, Dipankar and Thoithoi with whose support this work has been accomplished. I am thankful to the support staff at TIFR.

I sincerely thankful to fellow students on the mini-ICAL team, Neha, Surya and

Pethuraj for their useful discussions. I am thankful to my friends at INO, Tarak, Vivek, Moonmoon, Varchaswi, Chandan, Kolahal, Deepak T, Amina, Ali, Neha D, Abhijeet, Harisree, Jaydeep, Mamta, Jim, Honey and Hariom. I am fortunate to get the company of Lovy, Sagar, Rahul, Medha, Ram Krishna, Jhansi, Kartik, Bajarang, Siddhesh, Atreyee, Sanjeev, Ninad, Murthy, Shamik and Rakesh for their enthusiastic company and making my stay in TIFR memorable.

Last but not the least, it is my family whose selfless efforts made me what I am. I am extremely grateful to my parents for nurturing me for being confident enough to pursue my dreams. Thank you, Papa and Mummy, for having faith in me. It is your encouragement that keeps me going even at the hardest moments.

.....without them, it would have remained a dream!

Apoorva Bhatt

# Contents

<b>Synopsis</b>	<b>xix</b>
<b>List of Figures</b>	<b>xxxiii</b>
<b>List of Tables</b>	<b>xxxvii</b>
<b>1 Introduction</b>	<b>1</b>
1.1 Neutrino - The Ghost Particle . . . . .	1
1.1.1 Sources of neutrinos . . . . .	3
1.1.2 Neutrinos in the Standard Model . . . . .	6
1.1.3 Neutrino oscillations and experiments . . . . .	7
1.2 The India-based Neutrino Observatory . . . . .	12
1.2.1 The ICAL Detector . . . . .	13
1.2.2 Resistive plate chambers . . . . .	15
1.3 Neutrinos @ ICAL . . . . .	16
1.4 Prototype Detectors . . . . .	23
1.5 miniICAL . . . . .	24
1.6 Chapter summary . . . . .	25
<b>2 Time resolution of RPC</b>	<b>27</b>
2.1 Experimental setup . . . . .	28
2.2 Study of muon trajectory . . . . .	33
2.3 Study of timing measurements . . . . .	34
2.4 Position dependent efficiency versus time delay . . . . .	38

2.5	Position dependent pixel-wise time offset correction . . . . .	43
2.6	Improvement of time resolution and reduction of up/down ambiguity	44
2.7	Effect of lateral hit position on strip for time measurement . . . . .	46
2.8	Spurious noise near spacer buttons . . . . .	52
2.9	Summary . . . . .	55
<b>3</b>	<b>The ICAL detector simulation and muon reconstruction</b>	<b>57</b>
3.1	ICAL detector simulation framework . . . . .	58
3.2	Database for ICAL simulation framework . . . . .	61
3.3	INO specific digitisation . . . . .	63
3.4	Track Reconstruction Algorithm . . . . .	69
3.5	Fiducial volume and identification of events in fiducial volume . . . .	71
3.6	Calibration and Analysis of Fully Contained Tracks . . . . .	75
3.7	Summary . . . . .	78
<b>4</b>	<b>Hadron reconstruction in ICAL</b>	<b>81</b>
4.1	Reconstruction of hadronic shower using cluster algorithm . . . . .	83
4.2	Algorithm to remove ghost hits . . . . .	86
4.3	Analysis of hadron events and results . . . . .	87
4.4	Reconstruction of the direction of hadron shower . . . . .	93
4.5	Summary . . . . .	97
<b>5</b>	<b>mini-ICAL detector</b>	<b>99</b>
5.1	mini-ICAL magnet . . . . .	101
5.2	RPC Assembly . . . . .	108
5.3	Closed loop gas system . . . . .	111
5.4	Data Acquisition Systems . . . . .	114
5.4.1	Analog Front End . . . . .	115
5.4.2	Digital Front End . . . . .	116
5.4.3	Timing and Trigger System . . . . .	119



5.4.4	Back End Systems . . . . .	120
5.5	Summary . . . . .	121
<b>6</b>	<b>Analysis of mini-ICAL data</b>	<b>123</b>
6.1	Muon trajectory without magnetic field . . . . .	124
6.2	mini-ICAL simulation . . . . .	134
6.3	Track Reconstruction in magnetic field . . . . .	136
6.4	Explicit Track Model Fit . . . . .	138
6.5	Momentum spectra of cosmic ray muons . . . . .	142
6.6	Summary . . . . .	143
<b>7</b>	<b>Summary and future scope</b>	<b>145</b>
	<b>Appendices</b>	<b>149</b>
<b>A</b>	<b>Vavilov function</b>	<b>151</b>
	<b>Bibliography</b>	<b>153</b>
	<b>List of Abbrivations</b>	<b>160</b>



# Synopsis

The India-based Neutrino Observatory (INO), a multi-institutional collaboration, has been initiated in India to build a underground facilities for high energy physics particularly neutrino physics [1]. The planned magnetized Iron Calorimeter (ICAL) detector at INO would study the oscillations in the atmospheric neutrinos in the GeV range. The ICAL will consist of the Resistive Plate Chamber (RPC) detectors as the active elements [1], interspersed with 5.6 cm thick iron plates. There will be 151 horizontal layers of the iron plates, with 4 cm gaps to place the RPC units. ICAL will be magnetized with magnetic field of about 1.5 Tesla. The main goals of this experiment are precise measurement of neutrino oscillation parameters including the sign of the 2-3 mass-squared difference,  $\Delta m_{32}^2 (= m_3^2 - m_2^2)$  through matter effects, the value of the leptonic CP phase and, last but not the least, the search for any non-standard effect beyond neutrino oscillations.

Fast and precise timing information is mandatory to resolve the up-down ambiguity in the direction of muons, which in turn is one of the important experimental observations for the determination of the sign of the parameter,  $\Delta m_{32}^2$ . The Resistive Plate Chamber (RPC) chosen as the active detector element for ICAL detector has time resolution of about 1 ns. The first aim here is to improve the time resolution of the single gap RPC detectors using an offline calibration procedure.

The algorithm to improve the time resolution is tested and established using the 12 layer RPC stack at TIFR, Mumbai. The RPCs in the stack are of size  $1 \times 1 m^2$  and are placed with an interlayer gap of 16 cm. Each RPC is readout by

two orthogonal pickup planes - one on either side of its gas gap, labelled as X- and Y-planes. Signals in each plane is readout with 32 pickup strips of width 2.8 cm with an interstrip gap of 0.2 cm. The detector setup and DAQ has been described in detail in [2, 3]. Event data consist of two informations: (i) cosmic ray muon hits per layer and (ii) the corresponding time of arrival. Hit information is used to get the angular distribution of muons and details are described in detail in [2]. The trajectories in XZ and YZ planes are analysed independently in order to measure position and time resolution in X- and Y- readout planes of each RPC. A preliminary analysis of time of arrival was also performed and the overall time resolution of RPC was estimated to be 1.5 ns whereas the time resolution of individual RPC strips was found to be about 1.2 ns [3].

After correcting the muon arrival time (which used leading edge discriminator) for electronic offsets, it was observed that the average time delay between the strip charge induction to the front-end electronics input varies with the position of the particle interaction in the RPC which is not a linear function of with the position of the signal pickup strip with respect to the front-end electronics. Hence, the time measurement itself is used to make this offset correction. The average time delay is measured in  $32 \times 32$  pixels for both X- and Y-plane of the RPC. For each layer, the time is corrected using the offset corrections of the nearby four pixels.

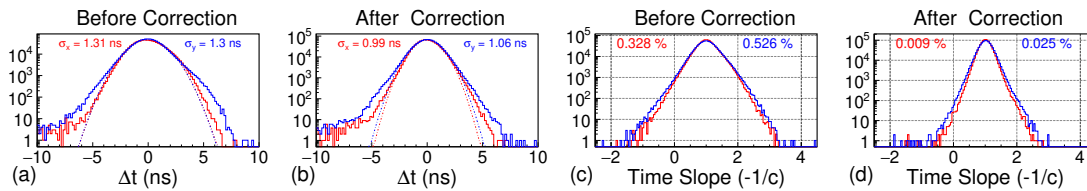


**Figure 1:** (a,c) shows the time resolution in layer-4 and measurement of muon direction without pixelwise offset correction and (b,d) shows the respective results with the correction. Here,  $\sigma$  is the gaussian fitted standard deviation and  $\sigma_{corr}$  is  $\sigma$  corrected for the extrapolation error.

The measured time resolution for one of the RPCs in the detector stack is shown in Figure 1(a) without any pixel-wise offset correction and in Figure 1(b) after applying the position dependent offset corrections. A substantial improvement can

be observed in the time measurements after using the corrections.

The position dependent gain of a RPC has been identified as the principal factor affecting its intrinsic time resolution. A technique of offline correction to improve the time measurement has been discussed and applied to a cosmic ray data sample from a detector stack. After correcting for this along with correction for time of flight of the signal in strips as well as for the delay in the electronic chains, most of the RPCs show a time resolution better than 1 ns in any part of the detector.

The various detector properties like position resolution, time resolution, efficiencies, multiplicities, etc are useful input to the simulation framework for any detector. For ICAL detector, its putative properties have been simulated using the GEANT4[4] package. To make the simulation more realistic, an INO specific digitization code was introduced in the simulation framework of ICAL detector, to have more realistic detector properties. Following this, the simulated response of ICAL detector to the final state particles produced in neutrino-nucleus interactions, predominantly muons and hadrons are studied.

The simulated response of ICAL to muons has been performed in [5]. In these studies, both fully and partially contained muon tracks were considered for analysis. If the muon trajectory is fully contained inside the detector, then the range of the muon is precisely known. Hence, the momentum measurement from the length of muon track inside the detector gives better estimation than the curvature fit for a fully contained track. Hence an algorithm is implemented to distinguish Fully Contained (FC) and Partially Contained (PC) muon tracks. The same algorithm is further applied along with position of the muon vertex to define fiducial volume.

In Figure 2(a), a scatter plot of the momentum of muon vs density weighted range of FC muon track in the detector is shown. The profile histogramme of the scatter plot (Figure 2(b)) shows the correlation between muon momentum and range which is fitted by second-order polynomial function. From the range information obtained from simulation of the passage of muons through ICAL detector

using GEANT4 and with the help of the polynomial function obtained in the previous step, the muon momentum is reconstructed for each event. Distribution of  $(p_{reco}/p_{true} - 1)^1$  (shown in Figure 2(c)) is fitted by Gaussian function and the fitted  $\sigma$  is treated as the resolution. The range-momentum correlation is observed in different  $\cos\theta_{true}$  bins and different calibration obtained for different bins to see the effect of polar angle on the calibration.

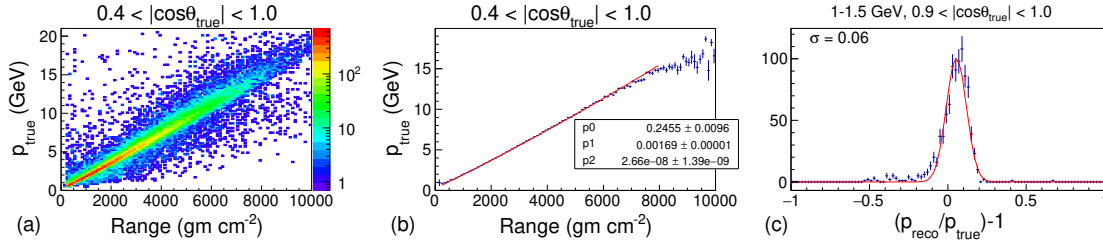


**Figure 2:** (a) Scatter plots of muon momentum with range of muons in the detector. (b) Fitted calibration function for relation between range of muons in the detector and momentum where  $p_0$ ,  $p_1$  and  $p_2$  are parameters of the second order polynomial function. (c) Resolution plots for a mean momentum of 1 to 1.5 GeV and  $1.0 > |\cos\theta_{true}| > 0.9$  for fully contained muon tracks.

The muons were generated using GEANT4, with the vertices smeared over the entire region of ICAL given by the coordinates  $(\pm 24, \pm 8, \pm 7.25) m^3$  in the momentum range from 0.5 to 20.5 GeV with uniform smearing over  $\cos\theta$  and  $\phi$ . The selection criteria for muon is that there should be only one reconstructed muon track with minimum 5 layers included in the Kalman fit. The momenta for fully contained events are reconstructed using the parameters of the second order polynomial function and the range of the muon track. The resolution plots for one of the momentum bins is shown in Figure 2(c) using the range calibration.

In Figure 3, resolution is plotted as function of momentum for different  $|\cos\theta_{true}|$  bins. The black points in the plot represent resolution for momentum reconstructed using curvature fit. The red and blue points in the plot are for momentum computed using the calibration described here for fully contained events. The small difference between Criteria 2 and 3 means that the impact of the more precise calibration

<sup>1</sup>Here, *true* is used for denoting the true information and *reco* for representing reconstructed information.

using individual  $\cos\theta_{true}$  bins is quite small. Also, at lower momentum, resolution is poorer because of multiple scattering whereas in the higher momenta bins, the number of events are less.

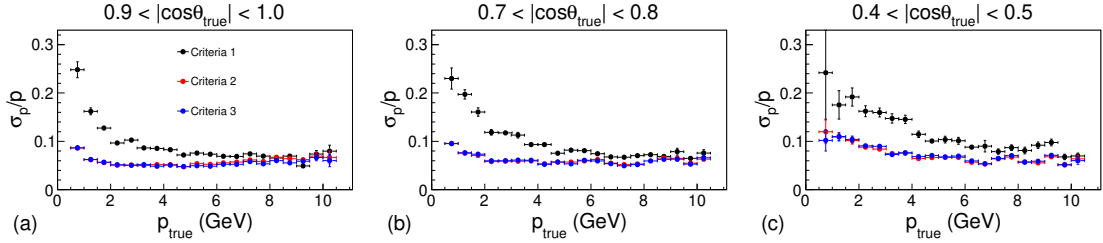


**Figure 3:** Momentum resolution as a function of momentum for fully contained muon tracks. Criterion 1 is for momentum estimated using curvature fit. Criterion 2 is for momentum estimated using range calibration in different  $|\cos\theta_{true}|$  bins. Criterion 3 refers to momentum computed using range calibration of muon tracks with all  $|\cos\theta_{true}|$  bins.

It is clearly observed that for fully contained events momentum reconstructed using the range of muons through the detector gives a better estimate than the curvature fit for a large range of momentum.

Muons, being minimum ionizing particles, typically register clean long tracks with just about one hit<sup>2</sup> per RPC layer in the detector whereas hadrons produce a shower with multiple hits per layer, due to the very different nature of their interactions. Also, in a typical neutrino interaction, more than one hadrons can be produced in a single neutrino interaction, due to which the response of the detector to different hadrons is overlapped. Hence, in principle, only an averaged information on the energy and direction of the hadrons is possible to estimate.

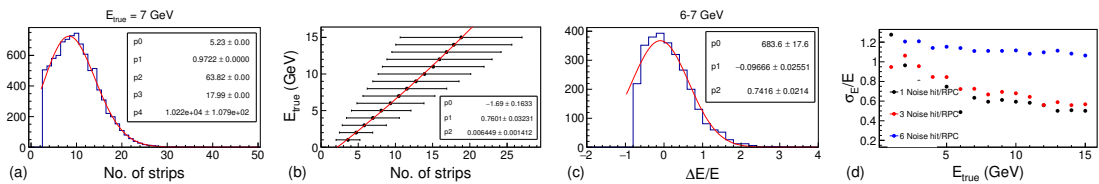


**Figure 4:** (a) Distribution of strip for a true energy of hadron ( $E_{true} = 7$  GeV) and fitted by Vavilov function. (b) Calibration curve for hadron energy reconstruction. (c)  $\Delta E/E_{true}$  distributions for energies 6 to 7 GeV fitted by gaussian distribution. (d) Energy resolution of hadron as function of true hadron energy for different simulated noise densities.

<sup>2</sup>Hits are all possible combination of X and Y strip for a particular RPC.

In the previous study [6], the detector response to hadrons propagating through it is investigated using the hadron hit multiplicity in the active detector elements. It shows some correlation of hit multiplicity with the energy of incident hadrons. However, as all possible combinations of X and Y strip hits are considered which leads to overcounting or ghost hits. Also, it would be necessary to distinguish noise hits from hadron shower hits which were missing in earlier studies. To achieve both above points, a clustering algorithm and a ghost hit removal algorithm are developed. In the algorithm, a unit ellipsoidal region is formed around a hit. The major axis of this unit ellipsoid corresponds to the number of z-layers whereas the minor axis corresponds to x- or y-strip numbers. The dimension of the ellipsoid for the cluster is supplied to the algorithm in terms of  $N_X$  strips,  $N_Y$  strips and  $N_Z$  layers (referred in this paper as  $(N_X, N_Y, N_Z)$ ). This formation of ellipsoid proceeds successively with new hits appeared in the previously formed ellipsoid and continued until all the hits in an event have been verified.

The basic aim of this work is to obtain a relation between the true energy,  $E_{true}$  vs the number of strips and apply it on simulated hadron events having energy distribution to reconstruct the energy of hadron,  $E_{reco}$ . The resolution of hadron energy is obtained from the distribution of  $(E_{reco} - E_{true})/E_{true}$ . To achieve this, single  $\pi^+$  events having uniform energy distribution from within 0-20 GeV have been generated using GEANT4 particle gun.

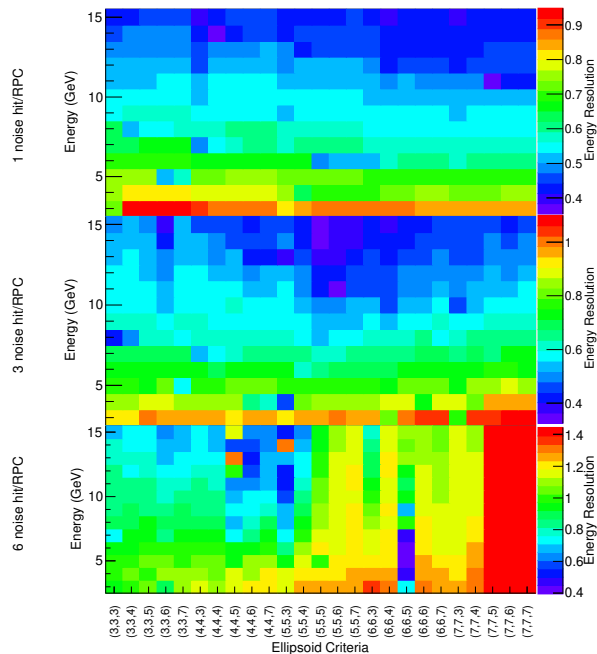


**Figure 5:** Energy resolution of hadrons for different noise rates.



Criteria $N_L \geq$	2	3	4	5
Using shower width	58.5 %	60.2 %	62.4 %	65.0 %
Using time information	75.5 %	78.5 %	82.9 %	87.1 %

**Table 1:** Fraction of events where the shower is developed in the direction of the true hadron.

These are distributed over the entire volume of the ICAL detector. The direction of  $\pi^+$  is uniformly smeared over zenith and azimuthal angles. The random noise hits were also simulated in the detector region near the vertex of the pion shower.

The distribution of strip for fixed hadron, energy,  $E_{true}$  is fitted by Vavilov distribution (shown in Figure 4(a)). The  $E_{true}$  is plotted as a function of the number of strips, which is the mean of the Vavilov distribution fitted to strip distribution. This plot is fitted by second-order polynomial function (shown in Figure 4(b)). From the strip information obtained from MC event or experimental data and with the help of the polynomial function obtained in the previous step, the hadron energy is reconstructed. The distribution of  $(E_{reco} - E_{true})/E_{true}$  is plotted for different ranges of  $E_{true}$  and fitted by Gaussian distribution (shown in Figure 4(c)). The variance of the fitted Gaussian function calculated using numerical integration is treated as  $\frac{\sigma}{E}$  of the particular  $E_{true}$  range.

The resolution also depends on the dimension of the ellipsoid chosen for the clustering algorithm as well as its efficiency to reject noise hits. The calibration and testing was performed on datasets with three different noise densities and with 25 different ellipsoid criteria. In Figure 4(d) the resolutions are plotted for the best cluster dimension for all the three noise densities. The algorithm has to be optimised for different noise densities as shown here.

The physics performance of atmospheric neutrino experiment is observed with  $L/E$  which is directly related to  $\cos\theta$  of incident neutrino. The reconstruction of the direction of hadron shower is required. The measurement of shower direction will also help in using the  $\nu_e$ -CC events in determining the neutrino mass hierarchy in ICAL detector.

The reconstruction of the direction of hadron shower has been performed for the cluster which contains minimum two z-planes (layers). An orientation matrix is calculated around the centre of the cluster (mean of co-ordinates of all the hits). The eigenvector related to the maximum eigenvalue of the orientation matrix gives the thrust axis, of the hadronic shower with 2-fold ambiguity in shower direction. To resolve the 2-fold ambiguity in shower direction, the shower width information is used as the hadron shower is expected to be narrower along the side towards which it is propagated.

Here, for different criteria of the minimum number of Z planes, the fraction of events where the shower is developed in the direction of the true hadron, i.e.  $\cos\theta_{true} \times \cos\theta_{reco} > 0$ , is shown in Table 1. It can be seen that using just the shower width information, the direction of a large fraction of events is misidentified. To resolve this, the time of hits is used to estimate the direction of the hadron shower. It is easy to understand that the hits obtained in the side from which the shower is generated are earlier in time than those which are present in the side towards which the shower is propagated. From the table, it can be seen that the fraction of events where the shower is developed in the true direction of the hadron improves significantly when using time of hits to resolve the two fold ambiguity in shower direction.

This improvement of energy/momentum measurement of muons and hadrons will improve the physics goal of the ICAL experiment. Also, for an ICAL like experiment, it is highly desirable to predict the absolute flux value and ratios among different kind of neutrinos precisely, and to understand their ‘‘systematic’’ uncertainties. M. Honda et.al [7, 8] shows the detailed calculation to estimate the atmospheric neutrino intensities. In their technique, the atmospheric muon flux is used to calibrate their calculation for estimating the atmospheric neutrino flux from the primary cosmic-ray flux. Hence, one of the motivation of mini-ICAL detector was to estimate the vertical muon flux at Madurai which is very near to the INO

site. The mini-ICAL detector also gives the opportunity to study the behaviour of detector, DAQ electronics, etc in the presence of magnetic field.

The mini-ICAL detector consisting of 11 layers of iron of size  $4\text{ m} \times 4\text{ m} \times 5.6\text{ cm}$  with interlayer gap of  $4.5\text{ cm}$  is built at IICHEP campus in Madurai. The copper conductors are wound in this set up similar to ICAL detector such that, in the central region (of  $2\text{ m} \times 2\text{ m}$  area), a uniform  $1.3\text{ T}$  magnetic field is obtained. Ten, large area RPCs (of dimensions  $174\text{ cm} \times 183.5\text{ cm}$ ) are placed in between the iron layers in this central region and act as active detector elements.

The atmospheric muons incident on the detector, registers clean tracks with just about one cluster (combination of nearby hits) per RPC layer in the detector. In the absence of magnetic field, the hits from muon (being minimum ionizing particle) will present a straight line pattern with small kinks appearing due to multiple scattering and strip multiplicity effect in the RPCs. Hence these tracks are fitted with straight line and various detector properties like efficiencies, strip multiplicities, electronic offsets for time measurements, etc are estimated. The mechanical alignment of the RPCs is also determined and perfected from these observations. These properties are further used as correction parameters and as inputs to the full detector simulation.

In presence of magnetic field, the hits from muon (experiencing Lorentz force), will show a curvature representing the bending of muon trajectory. The standard Kalman fit algorithm developed for the ICAL detector is used these trajectories. The momentum, zenith angle and the azimuthal angle of the incident muon can be estimated through this fit. To study the performance of the track fitting algorithm and further analysis, a GEANT4 based simulation package and INO specific digitization code are developed. The entire mini-ICAL detector geometry, along with the building in which it is installed, are included in the simulation framework to account for all the materials incident muon is passing through. The magnetic field is also an input to the simulation code.

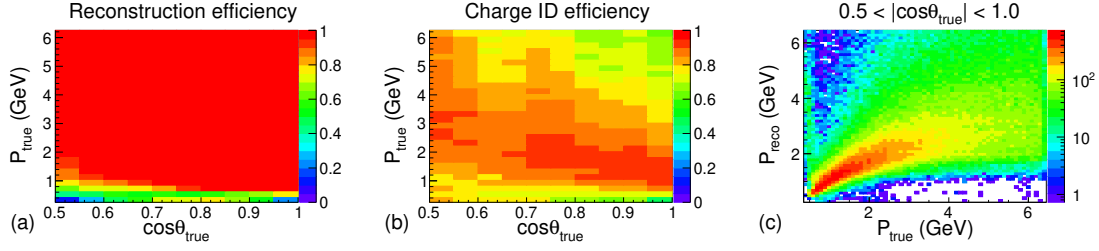


**Figure 6:** Figure about muon reconstruction  $P_{reco}$  v/s  $P_{gen}$ , (a) reconstruction efficiency (b) charge identification efficiency (c) Reconstructed momentum ( $p_{reco}$ ) v/s true input muon momentum ( $p_{true}$ ) for all combined  $\cos\theta_{true}$ .

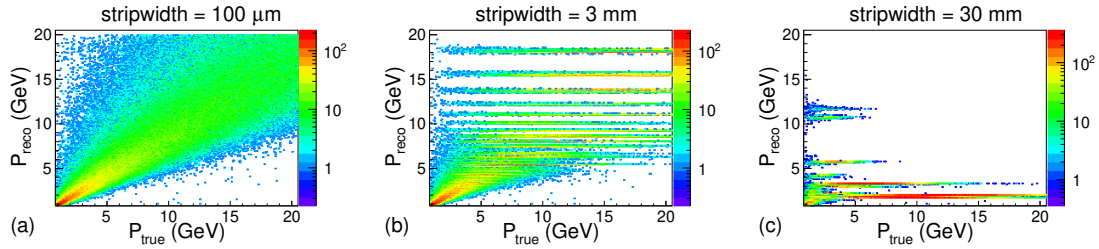


**Figure 7:** Reconstructed momentum ( $p_{reco}$ ) v/s true input muon momentum ( $p_{true}$ ) with different virtual strip width.

In order to study the momentum reconstruction, three lakh muons are generated from the center of the mini-ICAL detector just above the top most iron layer. The events were generated in momentum range 0.5–6.5 GeV with uniform smearing over  $\cos\theta$  (in the range of  $[-1.0, -0.5]$ ) and  $\phi$  in the simulation package described above. The detectors were assumed to be 100% efficient. The clusters obtained are reconstructed using Kalman fit based reconstruction algorithm. In Figure 6(a) and (b) the reconstruction efficiency the scatter plot of reconstructed muon momentum with the generated true momentum is shown. In Figure 6(c), the reconstructed momentum is plotted against the true muon momentum. In the figure, it is observed that beyond the true muon momentum of around 1 GeV, the reconstructed momentum starts showing some saturation and it is more at around 1.8 GeV.

Theoretically, it is known that the momentum resolution is inversely proportional to the magnetic field strength and the square of the length of track and directly proportional to the position resolution. The position resolution of the

RPC detector is around 7-8 mm. Hence, with 10 layers in mini-ICAL (giving limited number of measured points compared to ICAL detector), it is expected the position resolution will be poorer. But this doesn't explain the saturation of the reconstructed momentum as observed in this case. To check, that the Kalman filter technique was not adding any bias in the fit, the momentum was reconstructed using the explicit track model explained in [9]. In Figure 7, it can be observed that the reconstructed momentum shows saturation for various different strip widths. This saturation in reconstructed momentum is observed as a function of position resolution. It can be observed that there is a strong dependence of position resolution on the reconstructed momentum. When the position resolution is of the order of few hundred microns, there is no saturation observed in the reconstructed momentum. But, as the position resolution becomes poorer, the reconstructed momentum gradually starts to saturates at different momentum values.

The magnetic field in the mini-ICAL detector is along the Y-direction and the particle is moving along Z-direction. Hence, the bending of the track is supposed to be observed only along X co-ordinate. It is expected that the track will not show any deviation in Y co-ordinate except for multiple scattering. In Figure 7(f), it can be seen that the saturations is not only observed around one momentum value but, it is actually distributed for several different reconstructed momenta. For saturation band about 3 GeV, the hit pattern shows same Y- strip number for all the layers. In the XZ- plane, the X- strip number for layers 9 to 4 is 27 and for layers 3 to 0, is 28. Whenever this particular hit pattern is observed, the momentum is reconstructed at fixed value of 3.28 GeV. Similarly, for the saturation bands about 1.69, 1.97, 2.06, 5.76 GeVs, in the XZ- plane, the same X- strip number is observed for several layers and after that the observed X- strip number is deviated by  $\pm 1$  strip. The saturation about 1.97 and 2.06 GeVs in effect actually overlap each other. In all these cases, the Y- strip number remains the same for all the layers. For the saturation bands other than these five, they are observed when in

the hit pattern, there is also a deviation in Y co-ordinate. This deviation is mainly due to multiple scattering in iron layers. Hence, the different saturation bands observed in the reconstructed momentum corresponds to different hit patterns.

The cosmic-ray muons events recorded using the mini-ICAL detector were passed through the same reconstruction algorithm, where, the top four layers are used in the trigger cri-

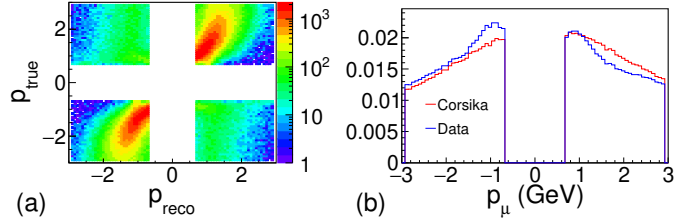


**Figure 8:** Unfolded Data with Corsika input.

teria. To compare the observed data with MC, discrete muons from the CORSIKA[10] event generator were passed through the GEANT4 based detector simulation. In the simulation, the muons are generated above the ceiling of the building. The various detector parameters like uncorrelated and correlated inefficiencies, trigger efficiencies, strip multiplicity, layer residuals and hardware trigger criterias were incorporated during the digitisation process of simulation. The detector parameters were calculated with the cosmic-ray muon events recorded in absence of magnetic field.

The measured momentum spectra of cosmic ray muons is distorted due to the finite resolution, limited trigger acceptance and other systematic effects of the detector. This leads to transfer of events between different momentum bins. Hence in order to allow a direct comparison of experimental measurement with theoretical predictions, the measurements are unfolded for the detector effects. The detector response matrix  $R$  (as shown in Figure 8(a)) in the unfolding procedure is derived using the Corsika events simulated using the detector simulation code as described above. The regularized unfolding method used and investigated for the current problem is iterative Bayesian Unfolding [11]. In the Bayesian technique, the background in each reconstructed momentum bin and efficiency of each true momentum bin is calculated. The reconstructed data and MC, are corrected for

the fake rate. During the unfolding, the efficiency is also corrected. After the unfolding, the observed muon spectra is presented in Figure 8(b). The observed spectra mainly shows the trend between experimentally observed and CORSIKA momentum spectra.





# List of Figures

1.1	Various sources of neutrinos. . . . .	3
1.2	Mass hierarchy for neutrinos . . . . .	10
1.3	Schematic representation of the ICAL detector . . . . .	14
1.4	The configuration of an RPC detector. . . . .	15
1.5	Horizontal component of geomagnetic field . . . . .	18
1.6	Neutrino Cross-sections . . . . .	19
1.7	Prototype RPC stacks for ICAL. . . . .	23
2.1	Elevation of the TIFR prototype stack . . . . .	29
2.2	Signal flow from RPC to back end . . . . .	30
2.3	Schematic of time stamps in the multi-hit TDC . . . . .	32
2.4	A muon trajectory . . . . .	33
2.5	Schematic of the time delay measurement circuit . . . . .	35
2.6	Time resolution and directionality of cosmic ray muon with only strip delay and electronic offset correction . . . . .	37
2.7	Efficiency map for X plane . . . . .	39
2.8	Efficiency map for Y plane . . . . .	40
2.9	Average time delay of muon signal for X-view . . . . .	41
2.10	Average time delay of muon signal for Y-view . . . . .	42
2.11	Schematic for pixelwise offset correction . . . . .	44
2.12	Time resolution and directionality of cosmic ray muon with the po- sition dependent time offset correction . . . . .	45
2.13	Strip multiplicity in X-view . . . . .	47

2.14	Strip multiplicity in Y-view . . . . .	48
2.15	Average delay time in X-view . . . . .	49
2.16	Average delay time in Y-view . . . . .	50
2.17	Time resolution and directionality of cosmic ray muon with all the corrections . . . . .	51
2.18	Corrected time with respect to the the expected time in the signal of X-plane as a function of Y-position . . . . .	53
2.19	Corrected time with respect to the the expected time in the signal of Y-plane as a function of X-position . . . . .	54
2.20	Time behaviour at button positions . . . . .	55
3.1	Schematic view of ICAL and a RPC unit in a tray . . . . .	59
3.2	Magnetic field in one of the ICAL module . . . . .	60
3.3	Database table for files . . . . .	61
3.4	Database for detector parameters . . . . .	62
3.5	Correlated and uncorrelated time resolution . . . . .	64
3.6	The signal propagation delay in the strip . . . . .	65
3.7	Correlated and uncorrelated inefficiency maps . . . . .	65
3.8	Correlated Noises . . . . .	66
3.9	Strip multiplicity . . . . .	68
3.10	An example typical event in ICAL . . . . .	70
3.11	Fiducial volume . . . . .	72
3.12	Various possible “fully” and “partially” contained events in ICAL .	73
3.13	Muon track in hadron shower . . . . .	74
3.14	Range momentum correlation for different $\cos\theta$ . . . . .	75
3.15	Range momentum correlation and calibration plot . . . . .	76
3.16	Calibration plots for different $\cos\theta$ . . . . .	76
3.17	Resolution plots for “fully” contained tracks . . . . .	77
3.18	Momentum resolution as function of true input momentum . . . . .	78

4.1	Ghost hits in RPC . . . . .	82
4.2	Two types of hadron events in ICAL . . . . .	83
4.3	Schematic diagram of trapezoid clustering . . . . .	84
4.4	Schematic diagram of ellipsoid clustering . . . . .	85
4.5	Schematic diagram of ghost hit removal algorithm . . . . .	87
4.6	Strip distributions for fixed hadron energies . . . . .	88
4.7	Calibration plot for hadron energy . . . . .	90
4.8	Hadron energy resolution plots for all energies . . . . .	91
4.9	Energy resolution of hadrons for different noise rates using various ellipsoid dimensions . . . . .	92
4.10	Energy resolution of hadrons for different noise rates . . . . .	93
4.11	Algorithm for estimating hadron direction . . . . .	95
4.12	Reconstructed shower direction using only shower width information	96
4.13	Reconstructed shower direction using only timing information . . .	96
5.1	mini-ICAL detector . . . . .	100
5.2	Iron plates and SS spacers . . . . .	102
5.3	Coil sections, coil brazing, hydraulic testing and interlayer gap mea- surements . . . . .	103
5.4	Magnet power supply and control software . . . . .	104
5.5	Fluxmeter for search coil based measurements . . . . .	105
5.6	Hall probe based measurement system . . . . .	106
5.7	Field map for mini-ICAL detector . . . . .	107
5.8	Onboard high voltage supply module for RPC . . . . .	110
5.9	Assembled RPC unit . . . . .	111
5.10	Flow diagram of closed loop gas recirculation system . . . . .	112
5.11	Gas recirculation system . . . . .	113
5.12	Schema for ICAL Data acquisition . . . . .	114
5.13	NINO front-end boards . . . . .	115

5.14	Anusparsh III front-end boards . . . . .	115
5.15	Block diagram of digital front-end . . . . .	117
5.16	Digital front-end module . . . . .	118
5.17	Trigger system for mini-ICAL detector . . . . .	120
5.18	Flow diagram of mini-ICAL's Data acquisition . . . . .	121
6.1	Cosmic muon events in mini-ICAL . . . . .	124
6.2	Signal rates for all channels for mini-ICAL . . . . .	125
6.3	Relative strip-hit profile of RPCs in mini-ICAL . . . . .	126
6.4	Layer hit multiplicities of RPCs in mini-ICAL . . . . .	127
6.5	Position resolution of RPCs in mini-ICAL . . . . .	128
6.6	Correlated inefficiency map for RPCs in mini-ICAL . . . . .	129
6.7	Uncorrelated inefficiency for X plane for RPCs in mini-ICAL . . . . .	130
6.8	Uncorrelated inefficiency for Y plane for RPCs in mini-ICAL . . . . .	131
6.9	Strip Multiplicity for X side of RPCs in mini-ICAL . . . . .	132
6.10	Strip Multiplicity for Y side of RPCs in mini-ICAL . . . . .	133
6.11	Time resolution of RPCs in mini-ICAL . . . . .	134
6.12	Magnetic field map in mini-ICAL simulation . . . . .	136
6.13	Muon reconstruction in mini-ICAL . . . . .	137
6.14	Reconstructed momentum $v/s$ true input muon momentum . . . . .	137
6.15	Reconstructed momentum for different stripwidth . . . . .	140
6.16	$(p_{reco} - p_{true})/p_{true}$ $v/s$ true input muon momentum ( $p_{true}$ ) . . . . .	141
6.17	Unfolding of data with CORSIKA simulation . . . . .	142

# List of Tables

1.1	Neutrino oscillation parameters . . . . .	11
1.2	Specifications of the ICAL Detector. . . . .	14
1.3	ICAL simulation framework . . . . .	21
2.1	Time resolution of RPCs in various experiments . . . . .	28
2.2	Time resolution with and without the position dependent offset correction . . . . .	52
2.3	Fraction of reconstructed up-going muons . . . . .	52
4.1	Different cases for simulation of single $\pi^+$ . . . . .	89
4.2	Energy resolution of the hadron in ICAL detector . . . . .	89
5.1	mini-ICAL magnet details . . . . .	102
5.2	Specifications of hall sensor . . . . .	107
5.3	INO RPC gas parameters . . . . .	112



# Chapter 1

## Introduction

The neutrino is one of the most interesting particles to study since it was postulated almost 90 years ago. It is the second most abundant particles in the universe after photons. It interacts with matter only via the weak force and detecting it is a challenging task. In the world, currently there are several experiments attempting to detect the neutrinos and not only study its various properties but also to use it to probe several novel physics concepts.

In this chapter, the concept of neutrino and its properties are discussed first. It is followed by the discussion on the neutrinos place in the Standard Model and the concept of neutrino oscillation. A brief introduction to the India-based neutrino observatory (INO) and the ICAL detector is presented here. This is followed by the contribution of this thesis to the ICAL R&D program is introduced in the later sections.

### 1.1 Neutrino - The Ghost Particle

In the nuclear two-body decays, mostly a discrete energy spectrum was observed for the daughter particles. In the early 20<sup>th</sup> century, in the nuclear  $\beta$ -decays, a continuous energy spectrum was observed. After repeated unsuccessful attempts by many experiments to find the missing energy [12], the law of conservation of energy

and momentum was started to question especially in the subatomic processes. In 1930, W. Pauli gave the idea of the  $\beta$ -decay being a three-body decay. The third neutral particle in this decay will be having the missing energy [13, 14]. In 1934, E. Fermi named this particle as “neutrino” and gave an theory of the  $\beta$ -decay assuming its a three-body decay [15–17].

Using the Fermi’s theory, The strength of the neutrino interactions with matter, i.e.  $\sigma \sim 10^{-44} \text{ cm}^2$  was estimated by H. Bethe and R. Peierls[18]. It was claimed that the neutrino may never be detected as this calculation gives a penetrating power of  $10^{16} \text{ km}$ . In 1950s, F. Reines and C.L. Cowan succeeded in detecting neutrino using the inverse  $\beta$ -decay process[19, 20].

However, a long wait of 26 years came to an end, when F. Reines and C.L. Cowan were successful in contradicting that prediction by detecting neutrino through the following inverse  $\beta$ -decay process [19, 20]

$$\bar{\nu}_e + p \rightarrow e^+ + n \tag{1.1}$$

In this experiment, they discovered the anti-neutrino of the electron type flavor. In 1962, the muon neutrino was detected by a high-energy accelerator neutrino experiment at the Brookhaven National Accelerator Laboratory[21]. They detected  $\nu_\mu$  produced from the decay of charged pions. The observation that the neutrinos arising from the charged pions decay mainly gave muons and not electrons when interacting with the nuclei gave the proof that muon neutrinos and electron neutrinos are different. When the  $\tau$  lepton was discovered and there was some missing energy in leptonic  $\tau$ decays[22], it immediately gave rise to speculation of the thrid flavor of neutrino. In 2000, the DONuT collaboration were able to successfully detect the  $\nu_\tau$  which completed the lepton family[23] in the standard model.



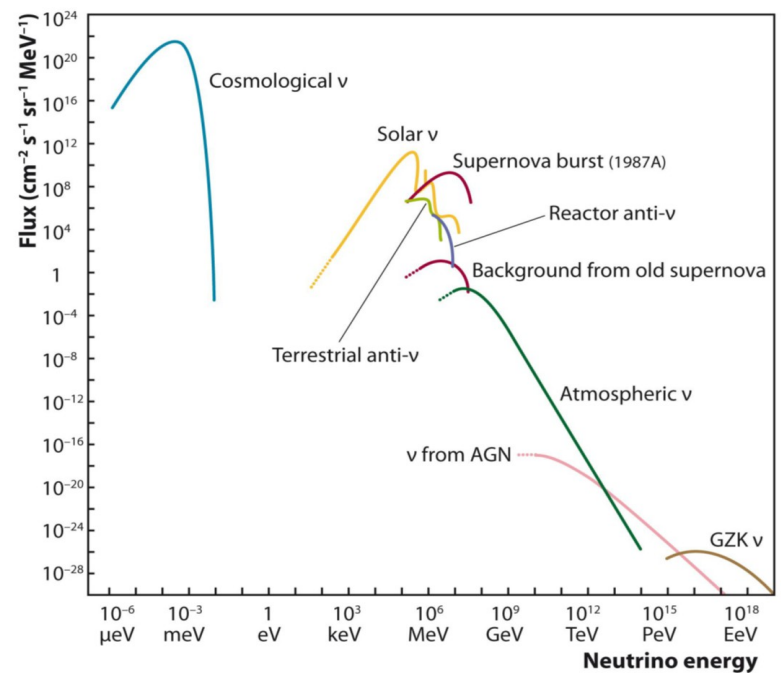
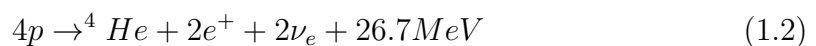


**Figure 1.1:** Various sources of neutrinos.

### 1.1.1 Sources of neutrinos

There are various sources, both natural and man-made, of neutrinos in several different energies. The important sources of the neutrinos and their energy ranges are shown in Figure 1.1 and discussed here. There is a significant correlation of the neutrino energy range and its several sources. In the nature, the principle sources of neutrinos on earth is mainly sun and the earth's atmosphere. Inside the sun, the exothermal thermonuclear fusion of four hydrogen into helium nuclei is the principal generator of energy according to the Standard Solar Model (SSM) [24]. The process can be shown by,



In this process, most of the released energy is in the form of thermal energy. The energy transferred to the neutrino is  $\sim 2\%$  from this process. There are two cycles of energy production inside the sun, namely; (i) Proton-Proton (PP) cycle,

and (ii) Carbon Nitrogen Oxygen (CNO) cycle. The solar neutrinos bombarding on the earth are in the range of few MeVs and their total flux on earth is  $\sim 6 \times 10^{10} \text{ cm}^{-2} \text{ s}^{-1}$ .

The atmospheric neutrinos are produced as by-products of the interactions of the cosmic rays with the nuclei of air molecules in the atmosphere. They were first reported in 1965 by an experiment in the underground laboratories at Kolar Gold Fields in India by a group from TIFR, Osaka University and Durham University [25, 26], and immediately afterward by Reines et al [27] in an experiment conducted in South African mines in 1965. The atmospheric neutrinos have been extensively studied in several underground laboratories. The evidence for oscillations [28] in the atmospheric neutrinos has also been observed.

The primary cosmic rays are high-energy particles bombarded on the Earth from several galactic and extragalactic sources. They are composed mainly of protons with about 9% helium nuclei and very small fractions of heavy nuclei. The energy spectrum of cosmic rays is very wide and goes beyond  $10^{10} \text{ GeV}$ , but falls off very rapidly with increasing energy. When the primary cosmic rays enter the earth's atmosphere, it interacts with the nuclei in the air molecules and produce secondary particles which mainly consist of pions with small mixture of kaons. The decay of these mesons to muons are principal source of atmospheric neutrinos as shown below;

$$\pi^- \rightarrow \mu^- + \bar{\nu}_\mu \quad \pi^+ \rightarrow \mu^+ + \nu_\mu \quad (1.3)$$

The kaons as well decay and contribute to the production of muons and muon neutrinos. These muons further decay to electrons which further contributes to muon neutrinos and also adding electron neutrinos to the source.

$$\mu^- \rightarrow e^- + \bar{\nu}_e + \nu_\mu \quad \mu^+ \rightarrow e^+ + \nu_e + \bar{\nu}_\mu \quad (1.4)$$

These atmospheric neutrinos are usually observed in the energies which range from a few hundreds of MeV to tens of GeV. These neutrinos can traverse the entire length earth. The wide energy range and baseline of atmospheric neutrinos (from 15 km to 13,000 km) help in the study of neutrino oscillations. Other than, solar and atmospheric neutrinos, the neutrinos can also be observed from supernova explosions, astrophysical sources, from the crust of the earth and relic neutrinos from the Big Bang.

In the supernova explosions, through the processes of electron capture of nuclei and free protons, a large number of neutrinos are produced. The resultant proto-neutron star also generates huge number of neutrinos in its hot core. As, the neutrinos are weakly interacting, they can easily escape the dense core. The neutrino burst from a supernova gives out a very high flux and is a very efficient source. The SN1987A is the only supernova that has been detected through the neutrino burst and has provided new results in the neutrino astronomy [29–31].

In the earth's crust, several radioactive isotopes like  $U^{238}$ ,  $Th^{232}$ ,  $K^{40}$ , etc are found. Through radioactive decay, they constantly emit antineutrinos [32–34]. The precision measurement of the geo-neutrino flux and its spectrum can provide important insight into the composition of the earth's core. Various astrophysical sources like active galactic nuclei (AGN) and gamma-ray bursts (GRB) emit neutrinos at very high energies. These neutrinos can reach the Earth from these distant sources without interacting with the CMB. The neutrinos don't get affected by the interstellar magnetic fields. The flux of these neutrinos is very low and it requires very large neutrino detectors. In 2013, The IceCube detector reported detection a number of such neutrinos [35–37].

The most prominent products of the Big Bang which survives even today are the relic neutrinos. After photons, they are the second most abundant particles in the universe. Their number density is approx. 336 neutrinos per cubic centimeter. The kinetic energies of the relic neutrinos is predicted to be in the range of few

ten's of keVs. This implies that they have a very weak interaction cross-section and it makes the direct detection of them a difficult challenge.

The neutrinos from man-made sources are obtained only from two places: nuclear reactors and accelerators. The first experimental detection of neutrinos was done by Cowan and Reines using anti-neutrinos from the nuclear reactor. The fission of neutron-rich isotopes like U, Th<sup>238</sup>, Pu<sup>239</sup> and Pu<sup>241</sup> generates power. The fission products emit a large number of anti-neutrinos via chain of  $\beta$ -decays. The energies of these anti-neutrinos vary from 0.1 to 10 MeV.

Like in atmospheric neutrinos, in accelerators charged pions and kaons are produced by a proton beam on a target. The decays of these charged mesons mainly produce a neutrino beam. In the accelerators, the pions and kaons can be focussed using magnetic horn and then sent into a decay tunnel where they produce muons and muon neutrinos. At the end of tunnel, the muons are absorbed into the earth and a neutrino beam is obtained. By selecting the charge of the mesons, a neutrino as well as anti-neutrino beam can be produced.

### 1.1.2 Neutrinos in the Standard Model

The Standard Model (SM) of Particle Physics, formulated in 1967, describes the elementary particles and the fundamental forces of nature[38, 39]. It is based on  $SU(2) \times U(1)$  gauge model which predicts the presence of weak neutral currents[40]. In 1973, the discovery of neutral-current neutrino interactions by the Gargamelle experiment at CERN and independently at Fermilab, is one of the initial proofs of the Standard Model [41–44]. It states that the universe is made up of fundamental building blocks of 12 spin  $\frac{1}{2}$  fermions (leptons and quarks) as well as its anti-particles. They interact among each other via gauge bosons of spin-1 which are called force carriers. In various experiments across the world, these particles were discovered out which the most famous being the latest discovery of a Higgs-boson at the ATLAS and CMS experiments at CERN [45, 46]. The invisible decay width

of Z boson was measured accurately by LEP experiment at CERN which puts a constraints on the number of neutrino flavors to three [47–50].

There are mainly two modes through which neutrinos can interact: charged current (CC) and neutral current (NC). The force carriers responsible for these two modes are W boson and Z boson respectively. In the standard model, all neutrinos have left-handed helicity whereas for the anti-neutrinos, the helicity is right-handed. They are massless and follow leptonic flavor conservation rules. Nonetheless, the discovery of neutrino oscillation shows the signature of neutrinos having non-zero mass. It is beyond the scope of standard model, to understand the mechanism of neutrino mixing. Hence, the neutrinos are very important objects to probe new physics beyond the standard model.

### 1.1.3 Neutrino oscillations and experiments

In 1950s, B. Pontecorvo made a proposal to this new phenomenon, where a neutrino can change its flavor [51, 52]. According to his hypothesis, the neutrino flavor eigenstates ( $\nu_e, \nu_\mu, \nu_\tau$ ) can be expressed as a superpositions of the mass eigenstates ( $\nu_1, \nu_2, \nu_3$ ) and during the weak interactions, only the flavor eigen states take part. This superpositions can be explained via a mixing matrix  $U$  which is named after Pontecorvo, Maki, Nakagawa and Sakata and called PMNS matrix[53, 54]. The mixing between the flavor and the mass eigenstates can be represented as

$$|\nu_\alpha\rangle = \sum_i U_{\alpha i}^* |\nu_i\rangle \quad (1.5)$$

where the PMNS matrix is given as,

$$U = \begin{bmatrix} c_{12}c_{13} & s_{12}c_{13} & s_{13}e^{-i\delta_{CP}} \\ -s_{12}c_{23} - c_{12}s_{23}s_{13}e^{-i\delta_{CP}} & c_{12}c_{23} - s_{12}s_{23}s_{13}e^{-i\delta_{CP}} & s_{23}c_{13} \\ s_{12}s_{23} - c_{12}c_{23}s_{13}e^{-i\delta_{CP}} & -c_{12}s_{23} - s_{12}c_{23}s_{13}e^{-i\delta_{CP}} & c_{23}c_{13} \end{bmatrix} \quad (1.6)$$

where,  $s_{ij}$  and  $c_{ij}$  represent the sine and cosine of the mixing angles  $\theta_{12}$ ,  $\theta_{13}$  and  $\theta_{23}$  whereas,  $\delta_{CP}$  is the complex phase which characterizes CP violation[55].

As the mass eigenstates have different masses, when the neutrino propagates in time, the mass eigenstates travel with different speeds. Due to this, the mass eigenstates get out of phase from a particular mixing ratio. This results in the transformation of the neutrino from a certain flavor to another flavor. This is only possible if the three mass eigenstates are distinct with different masses.

Using equation 1.5, the probability amplitude of the evolution of the flavor eigenstates in time can be obtained as:

$$P(\nu_\alpha \rightarrow \nu_\beta) = \delta_{\alpha\beta} - 4 \sum_{i>k} \text{Re}(\square) \sin^2 \left( \frac{\Delta m_{ki}^2 L}{4E} \right) + 2 \sum_{i>k} \text{Im}(\square) \sin \left( \frac{\Delta m_{ki}^2 L}{2E} \right) \quad (1.7)$$

where  $\square = U_{\beta i} U_{\alpha i}^* U_{\beta k}^* U_{\alpha k}$  and  $\Delta m_{ki}^2 = m_k^2 - m_i^2$ . Here, the neutrino is propagating in vacuum. If only the two flavor mixing is considered (where neutrino flavor  $\alpha$  changes to  $\beta$ ) then, the above equation is reduced to,

$$P(\nu_\alpha \rightarrow \nu_\beta) = \sin^2 2\theta \sin^2 \left( \frac{\Delta m^2 L}{4E} \right) \quad (1.8)$$

where E and L are the energy of the neutrino and distance traveled by it respectively. Both the last two equations represent the probability of neutrino oscillation in vacuum. However, when a neutrino is travelling in matter, although the neutrino interaction cross-sections are very low, the oscillation probabilities are significantly different due to coherent forward current interactions with electrons, protons and neutrons present in nature. This phenomenon is known as matter effect. Although, all the three flavors can interact with electron via neutral current, only the electron flavor neutrino can interact with electron via charged current interactions.

$$\nu_x + (e^-, p, n) \rightarrow \nu_x + (e^-, p, n) (NC) \quad (1.9)$$

$$\nu_e + e^- \rightarrow \nu_e + e^- (CC + NC) \quad (1.10)$$

Hence, the matter hamiltonian is,

$$H_m = H_0 + V_f \quad (1.11)$$

where,  $H_0$  is the free particle Hamiltonian and  $V_f$  is matter potential and in two flavor mixing case is given by,

$$V_f = \begin{bmatrix} V_{CC} + V_{NC} & 0 \\ 0 & V_{NC} \end{bmatrix} \quad (1.12)$$

where,  $V_{CC} = \sqrt{2}G_F n_e$  and  $V_{NC} = -\frac{\sqrt{2}}{2}G_F n_n$ . Here,  $n_e$  and  $n_n$  are the number density of electrons and neutrinos respectively and  $G_F$  is the Fermi coupling constant. In the case of two flavor mixing, the equation 1.8 is expressed as,

$$P(\nu_\alpha \rightarrow \nu_\beta) = \sin^2 2\theta_m \sin^2 \left( \frac{\Delta m_m^2 L}{E} \right) \quad (1.13)$$

where, the  $\Delta m_m^2$  and  $\theta_m$  are the matter affected mass squared difference and mixing angle respectively and given by,

$$\tan 2\theta_m = \frac{\Delta m^2 \sin 2\theta}{\Delta m^2 \cos 2\theta - A} \quad (1.14)$$

$$\Delta m_m^2 = \left[ (\Delta m^2 \cos 2\theta - A)^2 + (\Delta m^2 \sin 2\theta)^2 \right]^{1/2} \quad (1.15)$$

where,  $A = \pm 2\sqrt{2}G_F n_e E$  (+ neutrino – anti-neutrino) and  $n_e$  is electron number density. Here, when  $n_e \rightarrow 0$ , equation 1.13 becomes same as equation 1.8. It means that the mixing angles and the mass squared differences remains un-

changed from the values from its vacuum. When,  $n_e \rightarrow \infty$  or the energy is very large ( $E \rightarrow \infty$ ),  $\theta_m \rightarrow \frac{\pi}{2}$ . Here, even if the vacuum mixing angle is very small, maximum neutrino mixing is observed in matter. When  $A = \Delta m^2 \cos 2\theta$ , the equation 1.14 goes to zero. This gives rise to a resonance phenomenon which is called as the Mikheyev – Smirnov – Wolfenstein (MSW) resonance effect [56, 57]. In this case, depending on whether the  $\Delta m^2 > 0$  or  $\Delta m^2 < 0$ , the resonance occurs for neutrinos or antineutrinos respectively. For three flavor mixing and varying matter density the oscillation probabilities have to be solved numerically.

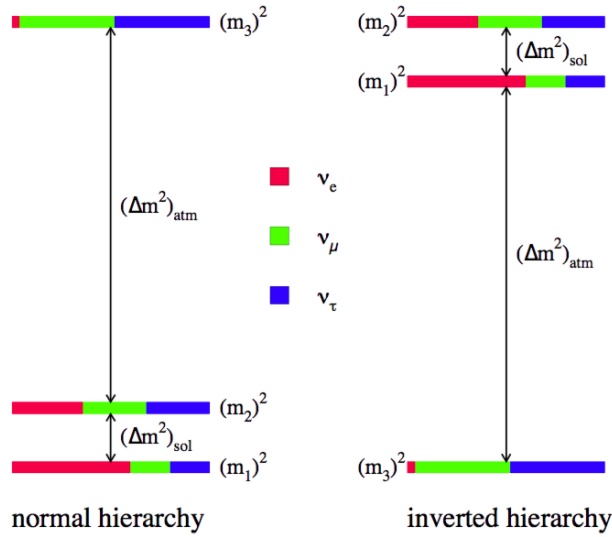


**Figure 1.2:** The normal (left) and inverted (right) mass hierarchy for neutrinos. The coloured bands signify the respective contributions of the flavour components in the mass eigen states.

In the neutrino oscillations, the amplitude of the probability is governed by the mixing angles whereas the frequency is affected by the mass squared differences. The overall probability is also dependent on the neutrino energy, the distance between the source and detector as well as the density of matter it is passing through. For a certain experiment, the distance (L), neutrino energy (E) and the matter density are very specific. e.g. For an accelerator neutrino experiment, the beam energy and hence the energy of neutrino has a specific bandwidth. Also, the source to detector distance as the well as the amount of matter the neutrinos travel through



is fixed. Hence, these factors determine the sensitivity of an experiment. There are several oscillation experiments which provide the information on the mixing angles and the mass squared differences. From several solar neutrino experiments, the  $\Delta m_{21}^2$  and  $\theta_{12}$  have been estimated. Hence, usually they are labelled as  $\Delta m_{sol}^2$  and  $\theta_{sol}$ . Similarly, the  $\Delta m_{32}^2$  and  $\theta_{23}$  are measured from the atmospheric neutrino experiments. So, usually they are referred to as  $\Delta m_{atm}^2$  and  $\theta_{atm}$ .

Parameter	Best fit $\pm 1\sigma$	$3\sigma$ range
$\Delta m_{21}^2 [10^{-5} eV^2]$	$7.39_{-0.20}^{+0.21}$	6.79–8.01
$\Delta m_{31}^2 [10^{-3} eV^2] (NO)$	$2.525_{-0.031}^{+0.033}$	2.431–2.622
$\Delta m_{31}^2 [10^{-3} eV^2] (IO)$	$2.512_{-0.031}^{+0.034}$	2.606–2.413
$\sin^2 \theta_{12}$	$0.310_{-0.012}^{+0.013}$	0.275–0.350
$\theta_{12}/^\circ$	$33.82_{-0.75}^{+0.78}$	31.61–36.27
$\sin^2 \theta_{23} (NO)$	$0.582_{-0.019}^{+0.015}$	0.428–0.624
$\theta_{23}/^\circ$	$49.7_{-1.1}^{+0.9}$	40.9–52.2
$\sin^2 \theta_{23}/10^{-1} (IO)$	$0.582_{-0.018}^{+0.015}$	0.433–0.623
$\theta_{23}/^\circ$	$49.7_{-1.0}^{+0.9}$	41.2–52.1
$\sin^2 \theta_{13}/10^{-2} (NO)$	$0.02240_{-0.00066}^{+0.00065}$	0.02044–0.02437
$\theta_{13}/^\circ$	$8.61_{-0.13}^{+0.12}$	8.22–8.98
$\sin^2 \theta_{13}/10^{-2} (IO)$	$0.02263_{-0.00066}^{+0.00065}$	0.02067–0.02461
$\theta_{13}/^\circ$	$8.65_{-0.13}^{+0.12}$	8.27–9.03
$\delta/^\circ (NO)$	$217_{-28}^{+40}$	135–366
$\delta/^\circ (IO)$	$280_{-28}^{+25}$	196–351

**Table 1.1:** The neutrino oscillation parameters summary from the global analysis [58]

From the several solar neutrino experiments, the magnitude as well as the sign of  $\Delta m_{21}^2$  is now well established. But for  $\Delta m_{31}^2$  (or,  $\Delta m_{32}^2$ ), from the experiments till date, only the magnitude is known. The absence of information about the sign of  $\Delta m_{31}^2$  gives rise to a 2-Fold ambiguity in the possible arrangements of neutrino mass eigen states as depicted in Figure 1.2. If the ordering is  $m_1 < m_2 < m_3$ , it is called the normal hierarchy (NH) and it is called the inverted hierarchy (IH) if the ordering is  $m_3 < m_1 < m_2$ . Once the sign of  $\Delta m_{31}^2$  is accurately known, in turn the hierarchy of the neutrino mass eigenstates will be confirmed. There are several experiments spread all across the world to explore the neutrino oscillation phenomena from various sources and energy ranges. In the current scenarios, the

best-fit values of the neutrino oscillation parameters, which are obtained from the global analysis [58, 59] of the various experiments around the world, have been summarized in Table 1.1.

## 1.2 The India-based Neutrino Observatory

As mentioned earlier, in 1960s, the reports of atmospheric neutrinos were reported by a group from TIFR, Osaka University and Durham University [25, 26]. These were the earliest effort of from India in the area of experimental neutrino physics. The first muon events coming from atmospheric neutrino interactions were observed in the detector placed underground at the Kolar Gold Field in the state of Karnataka. The India-based Neutrino Observatory (INO) [1] is multi-institutional collaboration with target to revive the Indian contribution to neutrino research. The principal aim is to build an underground facility at West Bodi Hills, in Pottipuram village, Theni district in the state of Tamilnadu. The facility will consist of an underground cavern with approximately minimum rock cover of  $\sim 1$  km in all direction. This will give a significant reduction in cosmic ray muon background can house several experiments.

The magnetized Iron Calorimeter (ICAL) detector is the flagship experiment at INO. It is a huge magnet weighing approximately 50 kt and will study the neutrino oscillation using atmospheric neutrinos. The uniqueness of ICAL, which makes it different from other atmospheric neutrino detector is its ability to differentiate between neutrinos and anti-neutrinos due its magnetic field. Although the main goals of this experiment are precise measurement of neutrino oscillation parameters including the sign of the 2-3 mass-squared difference,  $\Delta m_{32}^2 (= m_3^2 - m_2^2)$  through matter effects, the value of the leptonic CP phase and, last but not the least, the search for any non-standard effect beyond neutrino oscillations.

ICAL is a versatile detector, and hence a lot of new physics can be tested. For

example, using the energy measurement at ICAL, the violation of CPT or Lorentz symmetry in the neutrino sector can be estimated with precision [60]. Owing to the tracking capability at ICAL, the signatures magnetic monopoles passing through the detector may be detected through slowly moving, undeflected tracks [61]. The comparison of the flux from the sun with all other directions, the dark matter annihilation inside the sun can be investigated [62]. There are many other such scenarios which are being studied. The INO laboratory will also be home to other experiments like neutrinoless double beta decay, dark matter experiments, etc.

### 1.2.1 The ICAL Detector

The principle aim of ICAL is to study the neutrino oscillations along with matter effect in the atmospheric neutrinos. The main benefit of the atmospheric neutrinos is that they are present in a wide range of energies and while passing through earth they can travel through several different distances. These help to probe different physics concepts through neutrino oscillation in a wide range of  $E$  and  $L$ . The atmospheric neutrino flux is very low as compared to the accelerators. Hence to have a significant number of events, the atmospheric neutrino detectors have to be very large and massive. The ICAL is designed to measure not only the energy and direction of muons produced in the charged-current (CC) interactions of the neutrinos in the detector but also its charge. The ICAL is made up of alternating layers of Iron plates (which provide a target for neutrinos) and Resistive Plate Chamber (RPC) detectors (which are active detector elements to track the particles). The ICAL detector is mainly sensitive to muon neutrinos.

The CC interactions induced by atmospheric  $\nu_\mu$  and  $\bar{\nu}_\mu$  will be providing the main signal, the ICAL is going to detect. The ICAL detector is designed in the form of three identical modules of dimension  $16\text{ m} \times 16\text{ m} \times 14.5\text{ m}$  placed side by side. The detector modules are made up of 151 horizontal layers of 5.6 cm thick low carbon iron plates with 4 cm gap between them to place the RPCs. The total number

rof RPCs to be used in ICAL is  $\sim 28000$ . The schematic of the ICAL detector is depicted in Figure 1.3. The important detector specifications have been highlighted in Table 1.2.

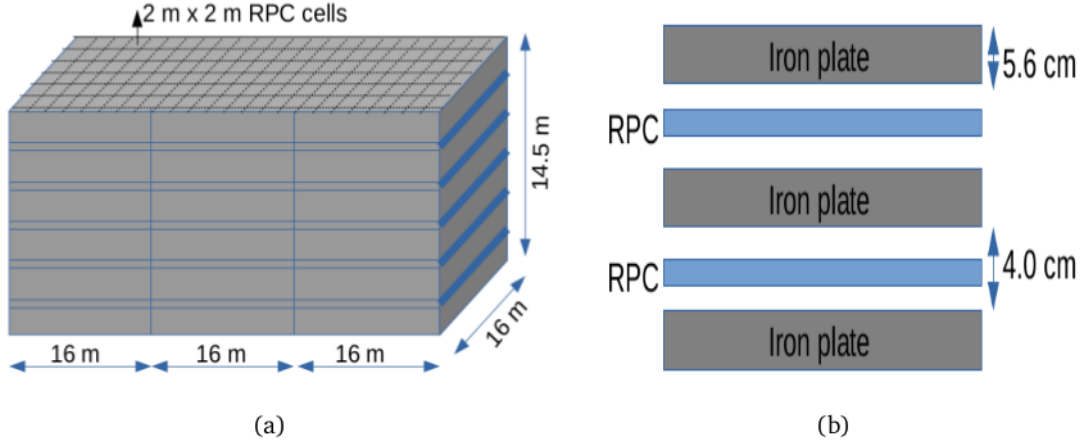


**Figure 1.3:** (a) The schematic representation of the ICAL detector with dimensions. (b) The placement of the iron plates and the RPC assembly in the ICAL. Each of the three modules of the ICAL consists of 151 such layers.

No. of Modules	3
Modular dimension	16 m $\times$ 16 m $\times$ 14.5 m
Total dimension	48 m $\times$ 16 m $\times$ 14.5 m
No. of iron layers	151
Iron plate thickness	5.6 cm
Gap for RPC assembly	4 cm
Magnetic field	1.4 T
RPC unit dimension	174 cm $\times$ 183.5 cm $\times$ 1.8 cm
Readout strip width	2.8 cm
No. of RPCs/Road/Layer	8
No. of Roads/Layer/Module	8
No. of RPC units/Layer	192
Total RPC units	28,800
No. of electronic channels	$\sim 3.7 \times 10^6$

**Table 1.2:** The specifications of the ICAL Detector.

## 1.2.2 Resistive plate chambers

In 1981, The concept of the resistive plate chambers was introduced as an alternative to the localized discharge spark counters [63]. These are basically parallel plate detectors made up of very high resistive material like glass or bakelite. The main benefits of the RPCs are its very good detection efficiency, good spatial resolution, wide-area coverage and low production cost.

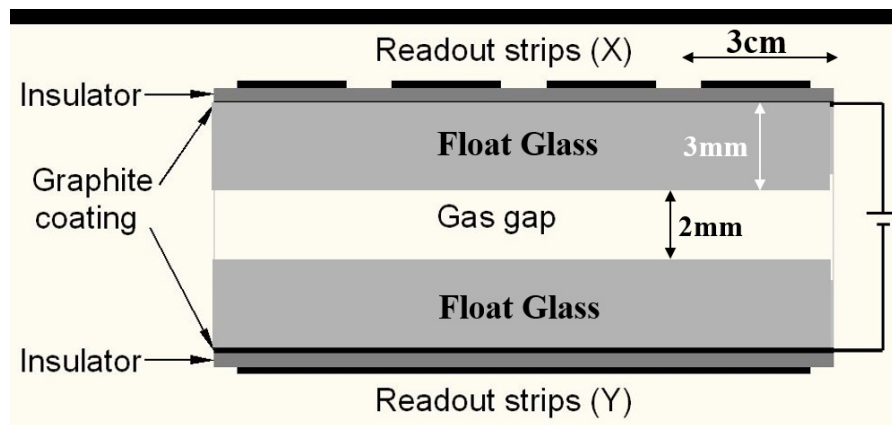


**Figure 1.4:** The configuration of an RPC detector.

A schematic diagram of an RPC configuration is presented in Figure 1.4. A gas mixture of R134a (95.2%), iso-butane (4.5%) and SF<sub>6</sub> (0.3%) is enclosed between two glass plates having a bulk resistivity of 10<sup>12</sup> Ωcm. The cylindrical polycarbonate spacers are glued between the two glass plates to maintain a uniform 2mm gas gap and a specially designed polycarbonate side spacers are used to seal the outer edges of the gap. There is provision of inlets and outlets for continuous gas flow. The outer surfaces of the two glass plates have a coating of graphite to maintain a uniform electric field ( $\sim 5$  kV/mm) across the gap.

The basic concept of signal formation in RPCs is based on the electron multiplication process. When a charged particle passes through the RPC, it ionizes the gas producing electron-ion pairs. The electrons are accelerated by the electric field and produces more electron-ion pairs. This process leads to electric signal formation inside the RPC. The RPCs can be operated in two different modes based on the gain

of the gas multiplication. These two modes are: streamer and avalanche. During the ICAL R&D program, the gas mixture mentioned earlier has been optimized to operate the RPCs in the avalanche mode [64].

The avalanche of electrons inside the RPC due to a passing charged particle starts a discharge. Due to the discharge, there is a drop in the electric field in the small area where the charge particle passed through. The recharging of this area is a slow process and the recovery time is  $\sim 2$  s. The electron avalanche induces a signal which is collected by copper pickup strips of width 2.8 cm placed outside the glass electrode. The copper strips are in the form of honeycomb pickup panels and are placed orthogonally on the either side of RPC. Due to this, the exact location of the particle where it crosses the RPC is measured in pixels of area  $2.8 \text{ cm} \times 2.8 \text{ cm}$ . The complete details of the working principle and design of the RPC detectors can be found in [65].

### 1.3 Neutrinos @ ICAL

The first evidence of neutrino oscillations in atmospheric neutrinos was observed at Super-Kamiokande detector at Kamioka, Japan [66]. The atmospheric neutrinos cover a wide  $L/E$  ( $=[\text{neutrino flight length}]/[\text{neutrino energy}]$ ) range, over four orders of magnitude. This is very much wider range as compared to the accelerator neutrino beam experiments. In atmospheric neutrino experiments, it is highly desirable to predict the absolute flux values and ratios among the different kinds of neutrinos precisely and to understand their systematic uncertainties. In order to calculate the atmospheric neutrino intensities, several models of particle interaction, atmospheric structures, and cosmic ray fluxes are used [7, 8].

In [7], they use detailed information about

1. the primary cosmic-ray spectra at the top of the atmosphere,
2. the hadronic interactions between cosmic rays and atmospheric nuclei,

3. the interaction of secondary particles inside the atmosphere,
4. the decay of the secondary particles,

in order to calculate the atmospheric neutrino flux intensities. Here, for primary cosmic spectra, there has been a reduction in the uncertainties due to recent measurements of primary cosmic rays. For the hadronic interaction models, the best method is to use the data from the accelerator experiments. The main drawback here is these data doesn't cover the desired phase space required for the calculation. In [7], they explore the hadronic interactions in the atmosphere, using the atmospheric muon flux. As the energy of  $\pi$  or  $K$  mostly goes to muons at their decay, the muons are considered to carry essential information of  $\pi$  and  $K$  production in the hadronic interactions.

For the muon flux, they use data from a series of precise measurements of atmospheric muons at various altitudes. The muon fluxes calculated using the HKKM04 scheme [67] with the observed density profile and compare it with the muon flux measurements. During the comparison, they observed a sizeable difference in the  $\mu^+/\mu^-$  ratio which was due to the errors in the hadronic interaction model used in the HKKM04 scheme. To correct this, they modify the DPMJET-III [68], hadronic interaction model with phenomenological considerations based on the quark parton model. Using this, they reproduce the observed muon flux.

In [69], using the same 3D scheme, the atmospheric neutrino fluxes are calculated for the proposed INO site at Theni, Tamilnadu. For this calculation, the JAM interaction model which is used in PHITS (Particle and Heavy-Ion Transport code System) [70] is for hadronic interactions at lower energies ( $< 32$  GeV). These calculations have been used to study the atmospheric muon flux at various altitudes for locations (GranSasso in Italy, SNO in Canada, Kamioka in Japan, etc) where accurate measurements exist [8, 67, 71]. In spite of using the same primary flux model and interaction model for the different sites, the calculated atmospheric

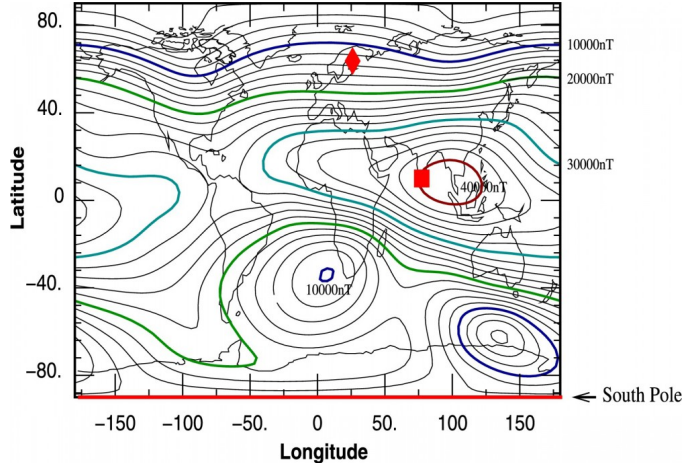


**Figure 1.5:** Magnitude of the horizontal component of geomagnetic field in IGRF2010 model. Square stands for the position of India-based Neutrino Observation (INO) site, diamond for the Pyhäsalmi mines, and bottom bar for the South Pole.

neutrino fluxes are different due to the geomagnetic field. The geomagnetic field affects cosmic rays both inside and outside of the atmosphere. Firstly, for low energy cosmic rays, it acts as a filter and secondly, it deflects the charged particles in the atmosphere. The strength of horizontal component of geomagnetic field obtained using IGRF2010 model [72] is shown in Figure 1.5. It can be seen that the INO site is close to the region where the strength of the horizontal component of the geomagnetic field is the largest on the earth. Hence, the neutrino flux at INO site is almost 30 % smaller at 1 GeV when compared with the flux at South Pole [69].

The relation  $\Delta\Phi_\mu/\Phi_\mu \approx \Delta\Phi_{\nu_\mu}/\Phi_{\nu_\mu} \approx \Delta\Phi_{\nu_e}/\Phi_{\nu_e}$  for the atmospheric lepton fluxes from the  $\pi$  decay, is useful in estimating neutrino fluxes. If the atmospheric muon flux with good accuracy is reproduced, the uncertainty of atmospheric neutrino flux due to the uncertainty of the  $\pi$  productions in the interaction model can be much better estimated.

The ICAL has been configured to make it primarily sensitive to the  $\nu_\mu$  induced charged-current CC events. Typically a 1 GeV muon can pass through 5–10 RPC layers in the detector depending on the angle of its incidence [5]. The electrons generated in  $\nu_e$  induced events will hardly cross a few layers, and suitable criteria on the number of layers crossed by the particle can be used to remove such events.



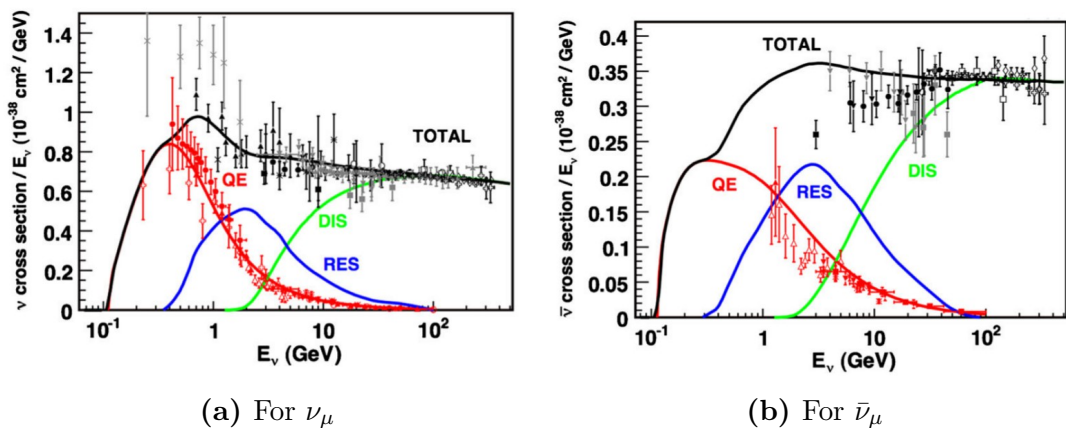


**Figure 1.6:** The cross sections of charged current neutrino interaction processes. [73]

The atmospheric  $\nu_\mu$  and  $\bar{\nu}_\mu$  interact with the iron target through quasi-elastic (QE), resonance scattering (RS) and deep inelastic scattering (DIS) processes as well as a negligible fraction of diffractive and coherent processes. The CC interactions produce muons as well as hadrons. Figure 1.6 presents the current knowledge on the cross-sections of the three prominent CC  $\nu_\mu$  and CC  $\bar{\nu}_\mu$  interactions [73]. As can be seen from these figures, in the sub-GeV range the QE processes dominate, and apart from the recoil nucleons, they do not have any other hadrons in the final state. As the energy increases RS and DIS processes start dominating and at a few GeVs, DIS becomes the most prominent process. Resonance events typically contain a single pion and a nucleon in the final state, though in a small fraction of events there are multiple pions along with the nucleon. DIS events produce multiple hadrons. In the neutral-current (NC) interactions, the final state consists of a neutrino and hadrons. The secondary neutrino would hardly interact with the target, and thus the hadronic parts are the only observables for those events. For the atmospheric neutrinos passing through the Earth's core, maximum matter effects would be experienced by the neutrinos in the energy range 4–6 GeV, which would have prominent fractions of RS and DIS interactions. Thus it is crucial to obtain information on all the final state particles to improve the sensitivity of ICAL in reaching its physics goals.

The ICAL detector would be optimized to be most sensitive to the atmospheric muon neutrinos in the energy range 1–10 GeV. The modular structure of the detector, with the horizontal layers of the iron plates and the RPC detectors, allows it to have a wide coverage to the direction of the incoming neutrinos, except the ones producing muons traveling almost horizontally. While the atmospheric neutrino flux provides a wide spectrum in the neutrino energy ( $E_\nu$ ), the detector structure enables it to be sensitive to a broad range of the path length (L) for the neutrinos penetrating through the Earth. The ICAL would be sensitive to both the energy and direction of the muons produced in the CC interactions of the atmospheric muon neutrinos and the antineutrinos with the iron absorber plates. The upward-going and downward-going muon events need to be identified which is one of the important experimental observations for the determination of the sign of the parameter,  $\Delta m_{32}^2$ . To achieve this, the fundamental requirement is obtaining fast and precise time information. The fast response time of the RPCs, which is of the order of nanoseconds, is helpful in determining the directionality of muons. The capability to up/down ambiguity in the direction of muons would allow the separation of the neutrinos with short path lengths from those with longer ones which is very useful to study neutrino oscillations, as the oscillation probability strongly depends on the path length L.

In addition, ICAL, being a magnetized detector, would be able to differentiate between muons and antimuons, which makes it capable of separating events induced by muon neutrinos and muon antineutrinos. Since the neutrinos and the antineutrinos experience different matter effects while propagating through the Earth, the ability to discriminate between neutrinos and antineutrinos makes the detector sensitive to the neutrino mass hierarchy, which is the main goal of the ICAL experiment. The presence of the magnetic field also improves the momentum resolution of the muons by measuring the extent of bending of the muon track in the local magnetic field.

Step 1: NUANCE or GENIE	<b>Neutrino Event Generation</b> $\nu_l + N \rightarrow l + X$ . Generates particles that result from a random interaction of a neutrino with matter using theoretical models for neutrino fluxes and cross-sections (i) Reaction Channel; (ii) Vertex and time information; (iii) Energy and momentum of all final state particles
Step 2: GEANT	<b>Event Simulation</b> $l + X$ through simulated ICAL Simulates propagation of particles through the ICAL detector with RPCs and magnetic field <b>Output:</b> (i) $x, y, z, t$ of the particles as they propagate through detector (ii) Energy deposited (iii) Momentum information
Step 3: DIGITIZATION	<b>Event Digitization</b> $(X, Y, Z, T)$ of final states on including noise and detector efficiency Add detector efficiency and noise to the hits <b>Output:</b> (i) Digitized output of the previous stage
Step 4: ANALYSIS	<b>Event Reconstruction</b> $(E, \vec{p})$ of $l, X$ (total hadrons) Fit the muon tracks using Kalman filter techniques to reconstruct muon energy and momentum; use hit in hadron shower to reconstruct hadron information <b>Output:</b> (i) Energy and momentum of muons and hadrons for use in physics analysis

**Table 1.3:** The simulation frame-work in the ICAL simulation package.

Though the ICAL is yet to be built, the physics reach of the ICAL has been studied using a simulation framework. The broad simulation framework for the ICAL, starting with event generation, is indicated schematically in Table 1.3. The events in the detector are generated using the GENIE Monte Carlo generator [4]. This uses the atmospheric neutrino fluxes [69] along with various possible neutrino-nucleus interaction cross-sections to generate the vertex and the energy-momentum of all final states in each event. These are then propagated through the virtual

ICAL detector using the GEANT4 simulation tool. The GEANT4 simulates the propagation of particles through the detector, including the effects of the iron, the RPCs, and the magnetic field. The information in the events is then digitized in the form of  $(X, Y, Z)$  coordinates of the hits in the RPCs and the timing corresponding to each of these 'hits'. This is the information available for the event reconstruction algorithms, which attempt, from the hit pattern, to separate the muon tracks from the showers generated by the hadrons, and reconstruct the energies and directions of these particles.

The simulation response of ICAL to the final-state particles produced in neutrino-nucleus interactions have been studied [5, 6, 74, 75]. In the previous studies of muon response, both fully contained and partially contained muon-events were considered for analysis. Also, the muon response in the central region [5] of the central module of the detector where the magnetic field is almost uniform and in the peripheral regions, [74] where it is non-uniform were studied separately. The detector response to hadrons, propagating through it, has been investigated using the hadron hit multiplicity in the active detector elements in [6]. In the study [6], no clustering algorithm was implemented and all the hits are used for calibration. In the real detector scenario, the hits from the signal as well as noise will be present in the detector output. In that case, it is difficult to use the hit multiplicity in estimating the hadron energy.

One of the targets in the current work is to improve the estimation of momentum/energy of the final state particles in the neutrino interactions. If the muon event is fully contained, then the range of the muon is precisely known. The momentum measurement from the range of the muon inside the detector gives a better estimation than curvature measurement. This is applicable only for the fully contained event. In this study, an algorithm to tag fully contained muon track is developed. A calibration scheme to estimate the momentum of these fully contained tracks is also explained and used. This will help in improving the mo-

momentum resolution substantially. Also, an attempt had been made to study the response of hadrons in the presence of detector noise. To achieve this an INO specific digitization code was introduced in the simulation framework of ICAL detector, to include more realistic detector properties like position resolution, time resolution, efficiencies, multiplicities, etc. In this work, a method to reconstruct the hadron shower direction using the width of the shower is developed. Using the direction of muon (estimated from curvature and fit) and hadron shower, the neutrino direction in CC-RS and CC-DIS events can be reconstructed.

## 1.4 Prototype Detectors

Successful completion of designing, building and characterizing large size glass RPCs have been done and reported in [64, 76]. As part of the ICAL detector R&D program, several prototype detector stacks have been successfully built to study the performance and long-term stability of the RPCs using cosmic-ray muons [64, 76, 77]. The first one of the stacks to be built was in TIFR, Mumbai. The detector is composed of 12 layers of glass RPCs of dimension  $1\text{ m} \times 1\text{ m}$ , stacked on top of each other with a vertical gap of 16 cm between them as shown in Figure 1.7. Another such identical 12 layer RPC stack has been built in the transit campus of IICHEP, Madurai with large area  $2\text{ m} \times 2\text{ m}$  RPCs [78].



(a) TIFR, Mumbai.

(b) IICHEP, Madurai.

**Figure 1.7:** Prototype RPC stacks for ICAL.

These stacks were used extensively to study various detector properties like position resolution, time resolution, detector efficiencies, strip multiplicities, etc. These properties are useful input to make the detector simulation more realistic. Fast and precise timing information is mandatory to resolve the up/down-going ambiguity of detected muons. The detector stack in TIFR was used to study the time resolution of RPC which was found to be 1.5 ns whereas the time resolution of individual RPC strips was found to be about 1.2 ns [3]. In this work, the uncertainties in the time measurement are studied with the reference to various detector properties. Also, an offline calibration procedure is developed to improve the time resolution of the single gap RPC using a large cosmic ray data sample, which can also be applied in a test beam setup. It is envisaged that the calibration strategy developed here will also be used for the INO-ICAL detector to improve its capability to discriminate the up/down-going muons.

## 1.5 miniICAL

The various tests to study the RPC performance and properties were done with different electronics including the final design for the INO-ICAL experiment [1]. Also, these were tested in the absence of a magnetic field. To study all the electronics in the fringe field of the magnet, a detector which is  $\sim 1/600^{th}$  the size of final ICAL detector in terms of volume is built-in IICHEP Campus in Madurai. The detector mainly consists of 11 layers of soft iron plates of thickness 5.6 cm having high magnetic permeability with an inter-layer gap of 4.5 cm. There are 2 coils made of copper conductors with 18 turns each and induction of 32,400 ampere-turns and maximum magnetic field of 1.5 T is achieved. The RPCs are placed in the interlayer gap and act as sensitive detectors. The data are collected using a coincidence signal in four layers, which are mainly due to cosmic ray muon.

Other than the test of electronics in presence of the magnetic field, these fol-

lowing items are also being tested in this setup, the magnetic field inside the iron is measured using the pick-up coil and hall probes and compared with the 2D simulation. This helps in validating the magnet design. This detector will soon be covered on all four sides and the top with three layers of extruded scintillator as cosmic muon veto detector. This will be the proof of principle test of the cosmic muon veto detector for the feasibility of a shallow ICAL detector.

The atmospheric muons incident on the detector registers clean tracks with just about one cluster (a combination of nearby hits) per RPC layer in the detector. In presence of the magnetic field, the hits from muon (experiencing Lorentz force), show a curvature representing the bending of muon trajectory. The standard curvature fit algorithm developed for the ICAL detector is used to fit these trajectories. The momentum, zenith angle and the azimuthal angle of the incident muon can be estimated through this fit. This helps in measurement of the charge-dependent muon flux up to  $\sim 1.5$  GeV and compare it with simulation [69]. Using the measured muon flux in the calculations demonstrated by M. Honda et.al [7, 8], the estimation of the atmospheric neutrino flux can be improved.

## 1.6 Chapter summary

First, a brief history of the particle physics along with the highlights of the neutrino experiments over the decade is discussed. The global picture of the neutrino oscillation as of today is then discussed. The aim of the INO project to perform a precise measurement of the neutrino oscillation parameters along with studies of several other physical phenomena and consequently requirements of the detector are discussed with necessary details. A brief summary of the Resistive Plate Chambers is discussed afterward. Then, the potentiality of ICAL detector for neutrino oscillations and the simulation of effort are discussed. Simultaneously, the scope of the present thesis along with the several prototype detectors are highlighted along

with the future outlook.



# Chapter 2

## Time resolution of RPC

One of the important experimental observations for the determination of the sign of the parameter,  $\Delta m_{32}^2$ , is the direction of muons produced in the CC interactions in ICAL. As the  $\nu_\mu$  and  $\bar{\nu}_\mu$  would experience separate matter effects for either of the possible mass ordering, while propagating through the Earth, it is mandatory to resolve the up–down ambiguity in the direction of muons. Fast and precise timing information is required to achieve this.

As part of the ICAL detector R&D program, several detector stacks have been successfully built to study the performance and long-term stability of the RPCs using cosmic-ray muons [1]. From the previous studies using an RPC cosmic ray telescope (1 m  $\times$  1 m) at TIFR, the time resolution of individual RPC strips was found to be about 1.2 ns [3]. The time resolution of large scale RPC in various high energy physics experiments are quoted in the range of 1.5–2.5 ns [79–82] and listed in Table 2.1. However, the best timing is obtained using a multigap RPC (MRPC) [83, 84]. The work presented in this chapter aims at improving the time resolution of the large area single gap RPC detectors using an offline calibration procedure.

In this chapter, Section 2.1 describes the experimental setup. The study of the muon trajectory is explained in brief in Section 2.2. The preliminary work on the time resolution and muon directionality[85], is summarized briefly in Section

Experiment	Time Resolution
L3	2.5-3.5 ns
BaBar	1.3-2.3 ns
BELLE	a few ns
ATLAS	1.2 ns

**Table 2.1:** Time resolution of RPCs in various experiments [79–82].

2.3. The correlation observed between the cosmic muon detection efficiency and the timing is described in detail in Section 2.4. In Section 2.5, the procedure of position-dependent time offset correction is discussed. The results on improvement in the time resolution after applying these corrections are presented in Section 2.6. The effect of RPC strip multiplicity on the measured time and a method to correct it is explained in Section 2.7. In Section 2.8, the observation of spurious large signals near button spacers is discussed. In Section 2.9, the major results of this work are summarized.

## 2.1 Experimental setup

The prototype stack (as shown in Figure 2.1) used in this study consists of 12 layers of glass RPCs of dimensions  $1\text{ m} \times 1\text{ m}$ , stacked on top of each other with a gap of 16 cm between them, thus resulting in a total stack height of 176 cm. The RPCs are labeled from 0 (bottom) to 11 (top) in the stack. These are float glass RPCs of size  $1\text{ m} \times 1\text{ m}$  with an active area of  $96\text{ cm} \times 96\text{ cm}$ . The glass thickness is 3 mm and the gap between two electrodes is 2 mm. The continuous flow of gas mixture, which is the active medium for the ionization, is maintained using an open-loop based gas recirculation system. A gas mixture of R134a, iso-butane, and  $\text{SF}_6$  in a proportion of 95.2 %, 4.5 % and 0.3 % respectively are used to operate these RPCs in avalanche mode. The RPCs are operated at 9.9 kV ( $\pm 4.95\text{ kV}$ ) in the avalanche mode with tracking efficiencies of  $(95.0 \pm 0.2)\%$  in the central region [2]. The chamber current drawn by these chambers, on an average, is 30-50 nA.

The surface resistivity of the graphite coating is maintained around  $1 \text{ M}\Omega/\square$ . For signal pick up, the plastic honeycomb panels (thickness 5 mm), with 30 mm wide copper strips on one side and  $100 \mu\text{m}$  thick aluminium sheet on the other (as ground plane) are used. The glass-gap is sandwiched between two pickup panels placed orthogonally. These panels also provide good mechanical support and are designed to have characteristic impedance of  $50 \Omega$ . To provide electrical insulation,  $50 \mu\text{m}$  thick mylar sheets are inserted between the pickup panels and graphite coating.

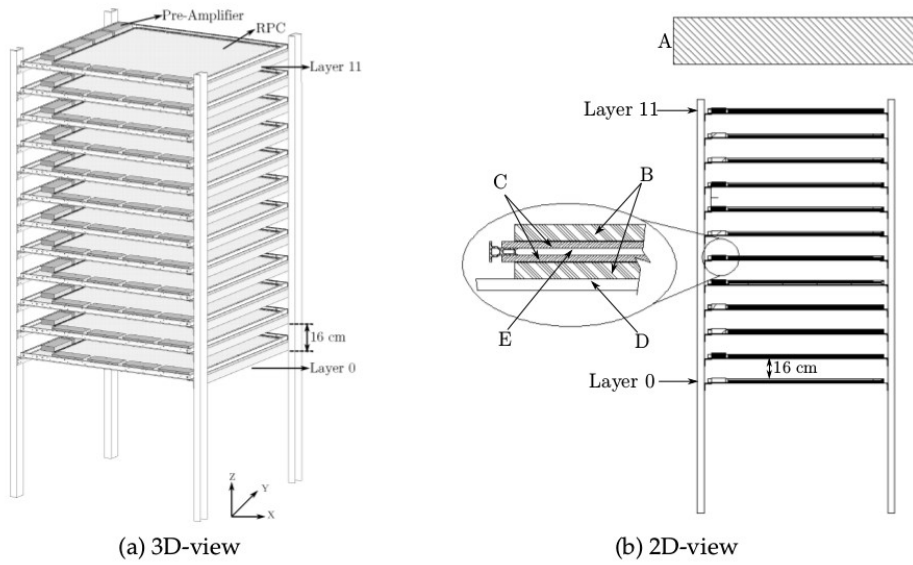


**Figure 2.1:** Elevation of the prototype stack in two dimensional (2D) and three dimensional (3D) view.

The flow of signals from the RPCs to the modules in the VME crate is shown in Figure 2.2. In avalanche mode of operation, a typical signal from RPC across a  $50 \Omega$  load is in the range  $0.5\text{--}2.0 \text{ mV}$  and rise time of about a few ns. The signals from each RPC strip are amplified by a two-stage Hybrid Micro Circuits (HMC) based high-speed high gain voltage pre-amplifiers. These amplifier provide a gain of  $\sim 80$ . Some of the design characteristics of the HMCs are: signal handling range ( $100\text{--}200 \text{ mV}$ ), bandwidth ( $350 \text{ MHz}$ ), rise time ( $2 \text{ ns}$ ), power rails ( $\pm 6 \text{ Volt}$ ) and power dissipation ( $120\text{--}140 \text{ mW}$ ) [85]. The length of cables going from the pre-amplifiers to the Analog Front End (AFE) boards is kept equal for all the channels

(1.7 m). The characteristic impedance of these cables is also  $50 \Omega$ .

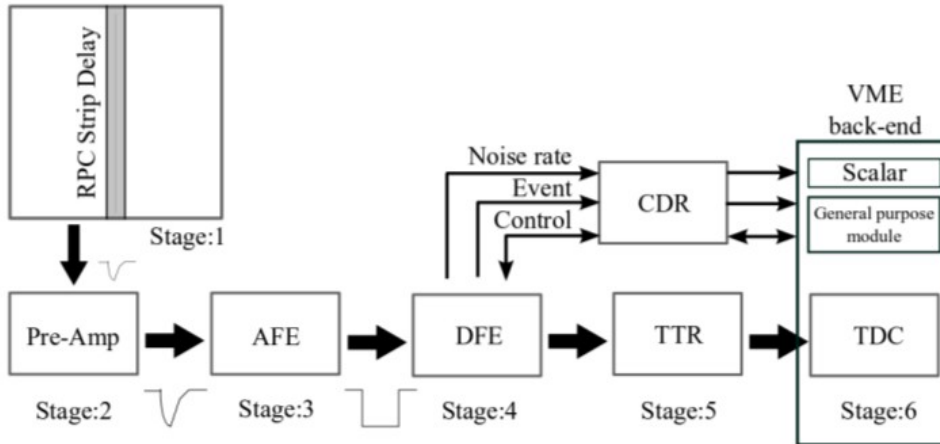


**Figure 2.2:** The data flow from the individual strips to the back-end VME DAQ system. The negative going pulses are only shown, whereas positive going pulses are also processed by similar electronics.

There are two AFEs per readout plane for each RPC. The main job of the AFE is to convert analog RPC signals to digital signals to make it for easy processing. To achieve this, the AFE contains adjustable threshold discriminators and ECL output signals. A fixed threshold of  $-20 \text{ mV}$  has been chosen based on the baseline noise[85]. An ultra-fast dual comparator (AD96687) has been used as a discriminator which gives differential ECL outputs. The AFE also contains the logic to generate primitive trigger logic where every  $8^{\text{th}}$  channel is ORed (wire ORed) and then the signal is shaped to  $100 \text{ ns}$  width. These are called the “level-0” trigger signals. The 32 strip signals per plane per RPC and the level-0 trigger signals are passed to the Digital Front End (DFE).

The main work of the DFE board is to collate the signals (strip signals as well as trigger signals) arriving from AFE and send them to the back-end. It has a decoder unit which controls the DAQ and noise monitoring. The Event section inside the DFE, handles the latching of the strip-hit information and serially flushes them out to the back-end via CDR on signal from Decoder unit. The Pre-trigger section generates the “level-1” trigger (1-Fold, 2-Fold, etc) signals from various

logical combinations of level-0 trigger signals. The level-0 signals from AFE are in differential ECL and are simply ORed to make an ECL 1-Fold signal for sending to backend TDC for timing measurement. The Noise Rate Monitoring section latches the noise rate of the active/calibration channel. These all four section are functioning parallelly and independently.

The four level-1 trigger signals and ECL 1-Fold signal for timing measurement from the DFE are routed to the VME backend via Time and Trigger Router (TDR) board. The trigger signals are sent to the Final Trigger Module (FTM) module for the generation of the trigger. The ECL 1-Fold signals are routed to the Time to Digital Converter (TDC) module in the VME backend. The CDR board accepts control signals from the INO DAQ Controller (from the back-end) via the address lines and accordingly to the commands from the controller, the monitoring and event signals are routed from each DFE board to the VME backend. The trigger address line carries the cosmic muon trigger information from FTM to each DFE module for latching of data. In the present configuration (with 12 layer RPC stack), one CDR board can not handle data routing for 12 layers. The processed signals from the DFE are transferred to the back-end DAQ system as Event or Monitoring data, which are finally recorded on the basis of a valid trigger.

- The Event data, i.e., the  $(x, y)$  strip hit patterns in the layers due to the passage of cosmic muons, is read by an I/O Module (Customised CAEN V1495). This I/O Module also manages the latching of the data from the appropriate DFE boards using the control lines in the CDR. The timing data from each of these layers, from the TTR unit, is read by a multi-hit TDC (CAEN V1190)
- The Monitoring data which contains strip noise rate, the four calibrating fixed frequencies and fold signals, are read by a 24 bit scalar (CAEN V830) at regular intervals.

The cosmic-muon flux measurement and the directionality study of muons are done using 1-Fold signals from layers 2, 4, 7 and 9. This particular choice was made just to gain in the detector solid angular coverage. On an average trigger rate of 22 Hz has been observed in this case. Tracking efficiency measurements of RPC layers using muons were done with a different set of trigger criteria to gain in the solid angular coverage. The coincidence trigger generates an interrupt via the TDC module and is sent to DFE to read out the Event Data. The I/O module manages the periodic readout of noise rates. The DAQ back-end process has been designed to have a multi-threaded structure so that it can support parallel processing of several jobs with different priority. The QThread class (from Qt) has been used to implement the threads are used here.

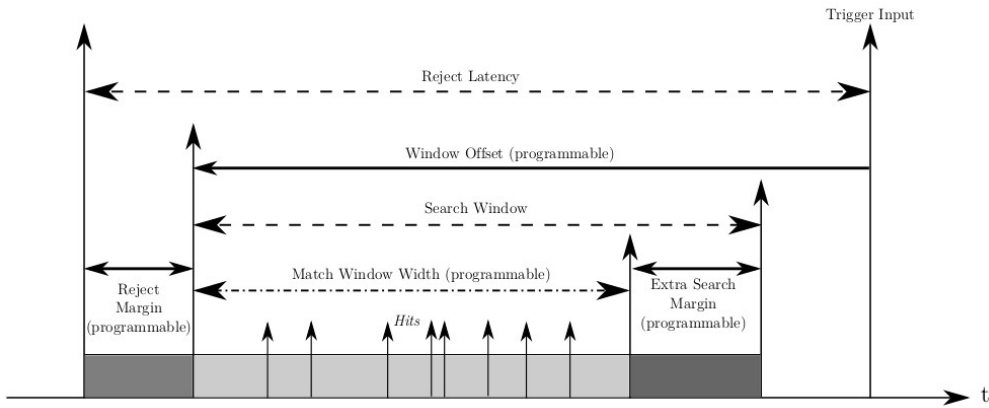


**Figure 2.3:** Schematic of time stamps in the multi-hit TDC.

The formal start-stop information is not available in the multi-hit VME-TDC. Hence, depending on the trigger a programmable match window is opened with an extra search and reject margins (Figure 2.3). The timestamps due to the signals from different layers are expected to be inside the match window for a genuine event. Hence, the relative timestamps, i.e., time of a layer with respect to another layer has been used for any timing measurements. In general, the bottom ( $0^{th}$ ) layer is used as a reference. But during time offsets estimation or in the directionality study, the lowest selected layer based on the muon hit selection criteria is chosen as the reference layer. The arrival times of the intercepting particle at various RPC

planes are recorded by a TDC (100 ps LSB) using the 1-Fold signal of that plane and the global trigger signal as a reference. Further details about the DAQ system are discussed in [85, 86].

## 2.2 Study of muon trajectory

The cosmic ray muons are the only source of charged particles in the laboratory for this study. They arrive from all directions at the top of the detector stack. RPC strips are fired due to the passage of these muons. An event data typically consists of a hit pattern of strips (one logic bit per strip) from X- and Y-planes as well as one timing information per plane. Thus, judicious selection criteria are necessary to choose good events over the background noise. This study is based on the trigger criteria, where at least one strip in the X-plane of 2<sup>nd</sup>, 4<sup>th</sup>, 7<sup>th</sup>, and 9<sup>th</sup> RPC layers have simultaneous hits within 100 ns time window. Figure 2.4 shows a typical event observed in this experimental setup. The trajectories in XZ and YZ planes are analyzed independently in order to measure time resolution in X- and Y- readout planes of each RPC.

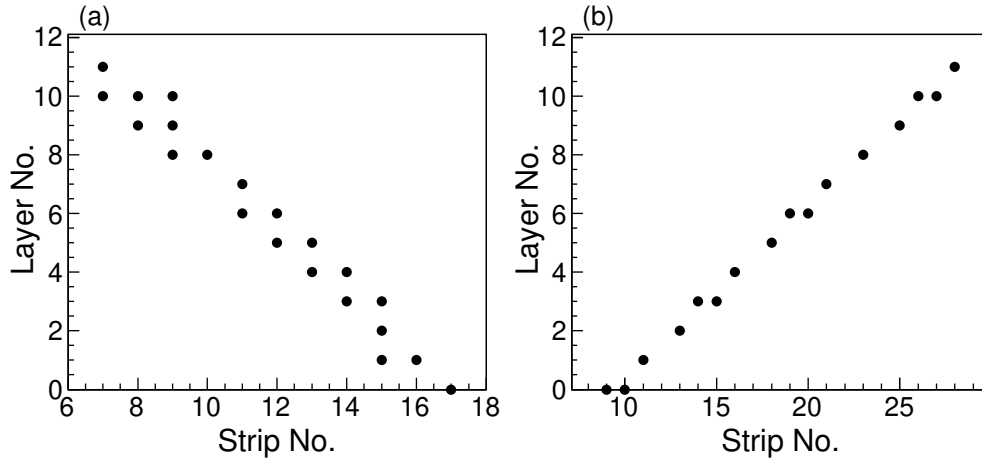


**Figure 2.4:** A muon trajectory, (a) in XZ-view and (b) in YZ-view.

The typical average strip multiplicity, number of strips simultaneously fired (signal above discrimination threshold,  $V_{th} = -20$  mV) in a layer varies from 1.73

to 2.10 [2]. About 3.50–5.64% of the cases the strip multiplicity is found to be more than three, which is mainly due to correlated electronic noise or simultaneous passage of more than one charged particles within the detector stack. There is also a small contribution from streamer pulses in the RPC to the increased multiplicity. A layer which has at most three-strip signals and all of which are consecutive are included in the analysis. The selected hit points in XZ and YZ planes are fitted separately with a straight line using equation 2.1.

$$x(/y) = a \times z + b \quad (2.1)$$

where  $x$  or  $y$  is the hit position (average strip position) from the X or Y plane respectively for  $z^{th}$  layer,  $a$  is the slope,  $dx(/y)/dz$  and  $b$  is the intercept. Using these four parameters, one can obtain the exact position of the muon trajectory in all the RPC layers. The detailed analysis along with the selection criteria as well as the alignment procedure can be found in [2]. There are at least six layers with selected hit position (time) for this fit and events with normalized  $\chi^2 < 2.0$  are used in the study. These same criteria are also applied during the alignment and all timing offset corrections. Due to the good mechanical accuracy and by using alignment corrections derived using muon tracks, an overall chamber alignment accuracy of better than  $100 \mu\text{m}$  is obtained.

## 2.3 Study of timing measurements

There is a time delay between the development of the detector analog signal and its arrival to the TDC module. The total time delay may be divided into two parts:

- delay from signal propagation in the pickup strip;
- time delays due to all the electronics elements from preamplifiers to the TDC



module.

The first stage delay can be easily measured by knowing the muon hit position on the strips. The propagation delay in the RPC strips is approximately 4.7 ns/m. For studying the delay from the second stage, in the previous studies [85], the calibrations were done using pulse generator, wherein a signal is simultaneously sent to two AFEs for two different layers among which one is the reference and the other is to be calibrated. A schematic of this calibration method is shown in Figure 2.5. Using this method, the time delay's of electronics elements can be measured but to calibrate the entire detector is cumbersome and time-consuming. Nonetheless, the results obtained from these measurements give an idea of the order of magnitude of the delays.

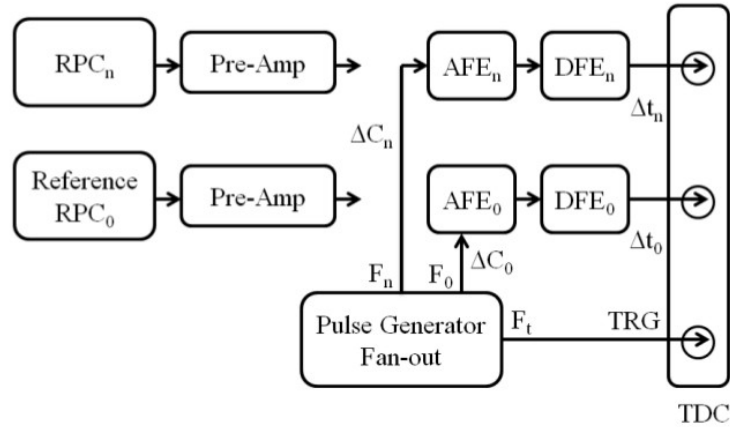


**Figure 2.5:** Schematic of the time delay measurement circuit.  $F$ 's denote fan-out of the signal from pulse generator.  $\Delta t$  denotes the time delay from AFE to TDC and  $\Delta C$  is the cable delay from pulse generator to the corresponding AFE input. Here the time delay of  $n^{th}$  layer with respect to the  $0^{th}$  layer is defined as  $\Delta t_n - \Delta t_0$ .

In view of the shortcomings seen in using the pulse generator, an alternative method was adopted using muon tracks as a source of time calibration by S. Pal et.al [3]. In that study, events with only single hit multiplicity were used to avoid uncertainty in timing due to time ORing among all the strips in a layer[85]. The raw TDC timing is first corrected for the time delay due to propagation in the

RPC strips and then used to determine the relative delays of each strip due to the electronics using the formula

$$t_i = \frac{1}{c} \ell_i + \delta \quad (2.2)$$

where  $t_i$  is the relative time of  $i^{\text{th}}$  layer with respect to the lowest layer in the stack with a valid hit and  $\ell_i$  is the cosmic muon track length in the  $i^{\text{th}}$  layer with respect to the same lowest layer. With the assumption that the particle is moving with velocity,  $c$ , the only free parameter in the Equation (2.2), the intercept ( $\delta$ ) is estimated using the track length and timing information from other layers. To calculate the time offset of a layer/strip, the expected time is compared with the measured time in that layer/strip. This process is repeated iteratively for all the channels to calculate the delay corrections from the electronics. This iterative method is described in detail in [3]. Also, in that study, data from three strips on the boundaries of pickup panels were excluded, as the inclusion of the same was found to drastically worsen the time resolution. Hence, the fiducial volume was reduced to about 66 % of that of the detector stack. After these corrections, the estimated time resolution in the central region of these chambers is found to be 0.97–1.77 ns. The observed time resolution of an RPC is obtained from the difference in the measured time with corrections in that layer and the time of the muon crossing that is expected to the layer/RPC. The latter is calculated from the time measurements in the remaining layers.

The time resolution observed for different layers of RPCs in the study is shown in Figure 2.6. The measured slope of the selected events after the pixel-wise offset correction is shown in Figure 2.6 (m) and (n). The misidentification rate for muon trajectories as up-going are estimated to be  $\sim 0.3\%$  for X-plane and  $\sim 0.5\%$  for Y-plane. One of the aims of this study is to understand the position-dependent

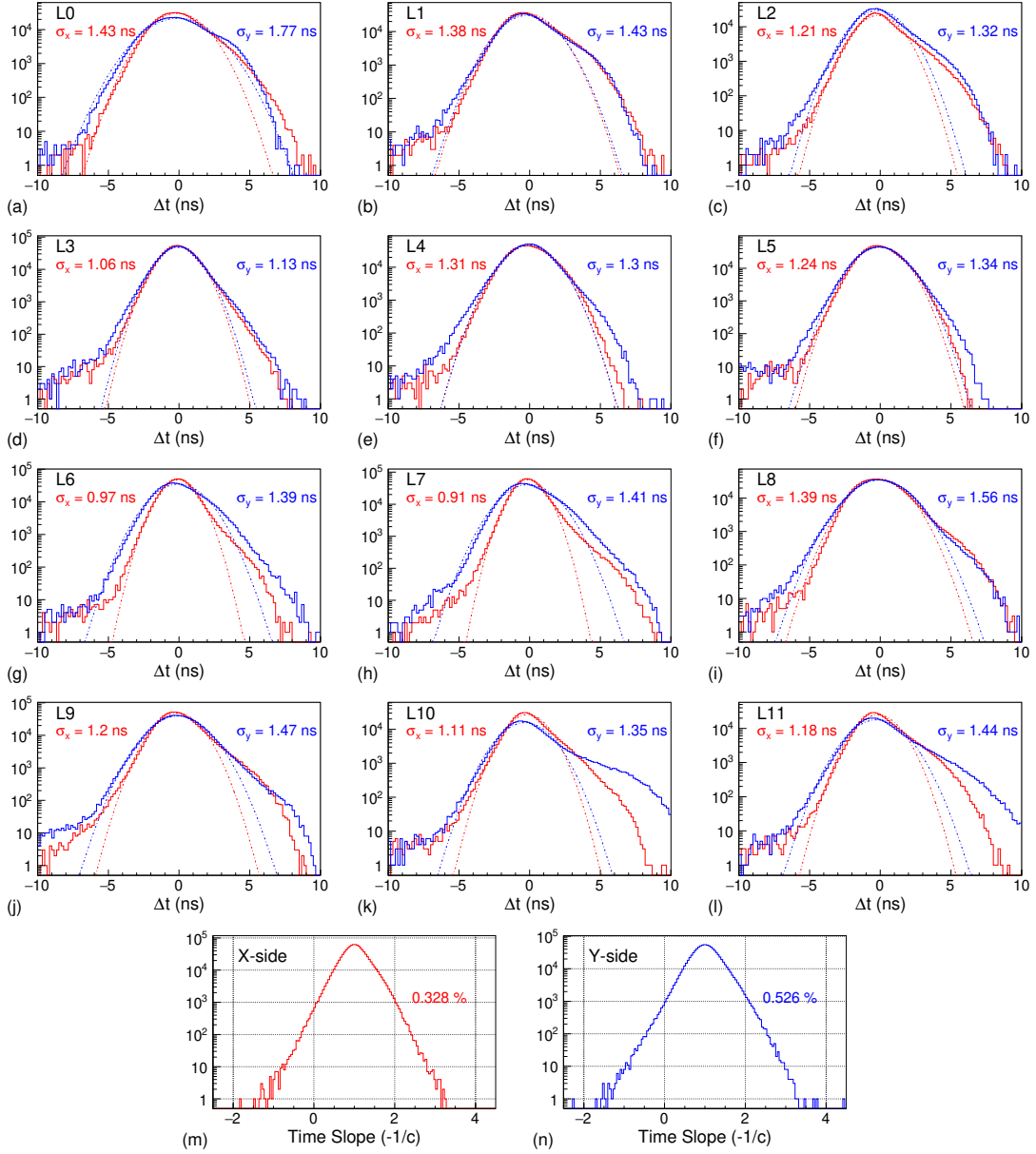


**Figure 2.6:** (a-l) Time resolution in all 12 layers and (m) and (n) directionality (fitted slope in eqn 2.2) of cosmic ray muon using timing information with only strip delay and electronic offset correction. Red colour for X-view and Blue colour for Y view. Dashed line represents the Gaussian fitted function. Here  $c = 29.979$  cm/ns.

time resolution of the RPC detector so that the whole detector can be used for precise time measurements.

## 2.4 Position dependent efficiency versus time delay

For each event, the muon trajectory information from the other eleven layers is used to identify the intersection (both x and y coordinates) of the muon trajectory in  $L_i$ . The efficiency of each layer is calculated by excluding that layer in the straight-line fit of the muon trajectory. The efficiency plots have  $32 \times 32$  of 2D pixels, where each pixel is of size  $3 \text{ cm} \times 3 \text{ cm}$ . Here, the efficiency of a layer is defined as the ratio of number of events where a hit is found within 6 cm of the expected position of muon in that layer, without any hit in other parts of that layer, to the expected number of muons using the fit of hits in all other layers. The inefficiency is caused by charged particles that did not produce a signal larger than the discriminator threshold. The detailed description of the calculations of the efficiency maps is given in [85]. The X- and Y-plane efficiency maps for all the layers of RPCs are shown in Figures 2.7 and 2.8 and the following features are observed in the efficiency plots:

- (a) Efficiency map is exactly the same in X- and Y-planes of the respective RPC.
- (b) The inefficiency matrix of spots is due to spacer buttons located at these positions.
- (c) Efficiency of the area covered by the first X-strip is almost zero in many layers.
- (d) Large region of inefficiency near the corners (Y-strip number,  $N_Y = 0-5$ ) in many RPCs.

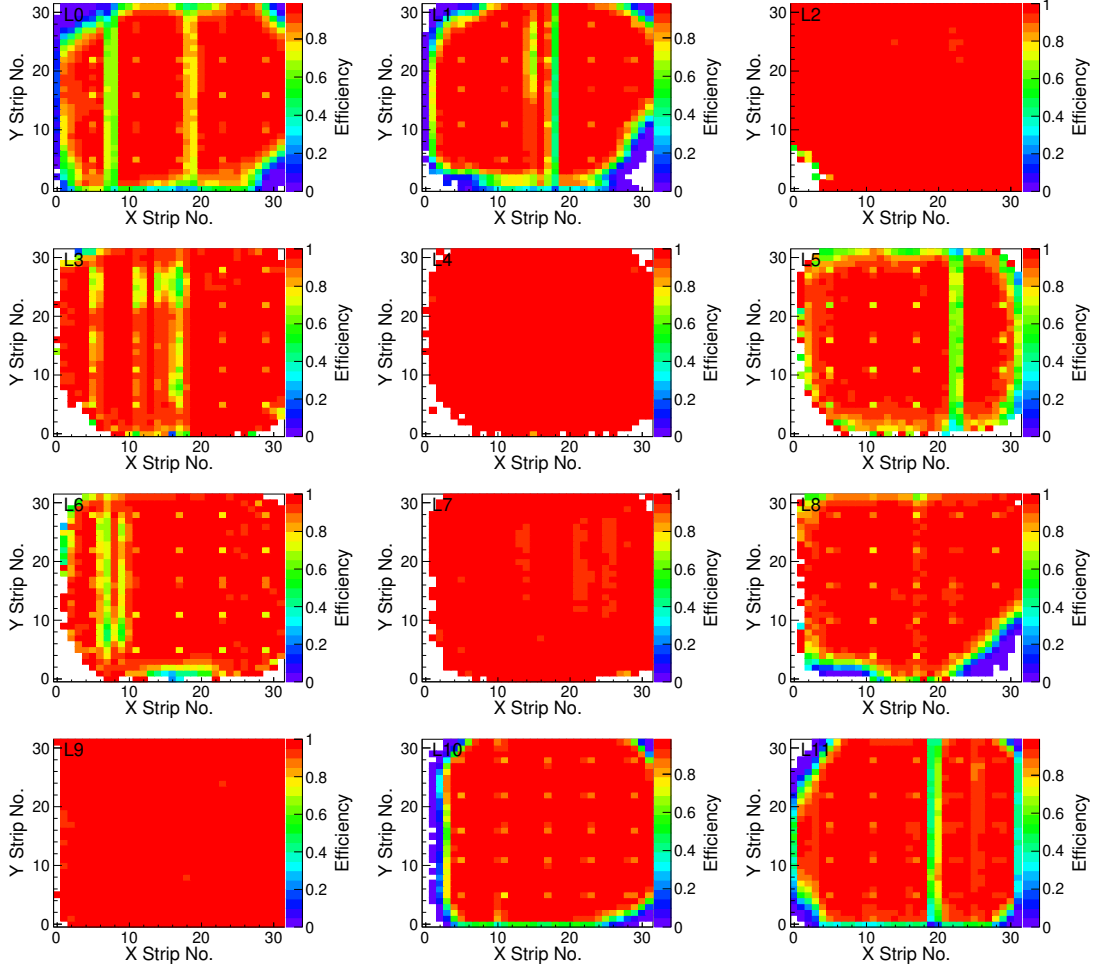


**Figure 2.7:** Efficiency for all 12 layers for the X-view.

- (e) In some RPCs, there are entire strips in either X- or Y-plane which shows lower efficiencies.
- (f) Layers 2, 4, 7 & 9 show nearly 100 % efficiency throughout the region as these are the hardware trigger layers.

The possible sources of the position-dependent variation in the efficiency are,

- Variation in the preamplifier gains across different strips: In this case, a correlation of efficiencies in the X- and Y-planes is not expected. The variation may be visible either in X- or in Y-plane for a whole length of the strips (described in Point “e”). Thus, this possibility may be excluded. Similarly, the effect due to mismatch of the characteristic impedance of readout strips

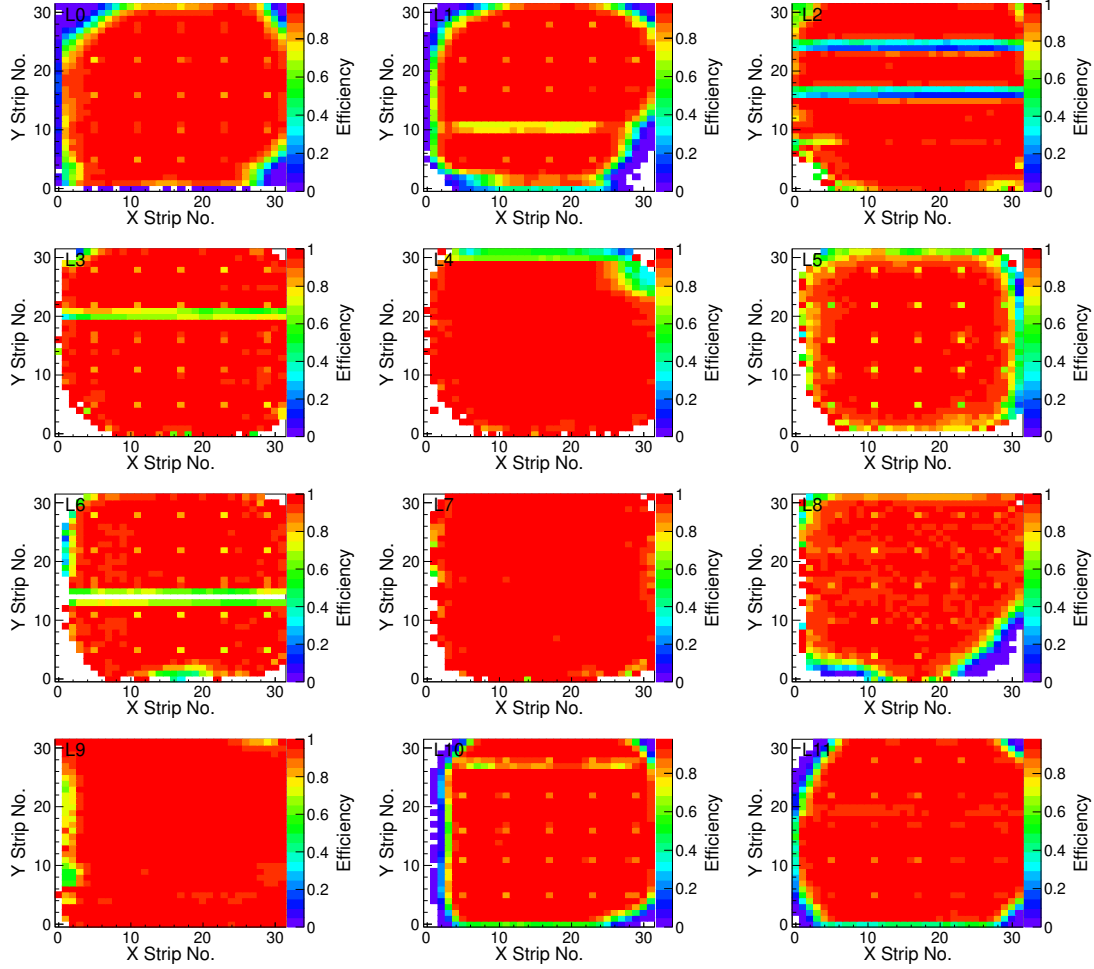


**Figure 2.8:** Efficiency for all 12 layers for the Y-view.

and the input impedance of preamplifiers is also ruled out due to the same argument.

- Dead zones in the gas gap due to the non-uniform flow of gas: The efficiencies in X- and Y-planes should be correlated due to this effect and it indeed matches with the observation. But there are two gas inlets at  $N_X = 31$  and  $N_Y = 0 \& 31$  and two outlets at  $N_X = 0$  and  $N_Y = 0 \& 31$ , which implies that the observed pattern on inefficiency is not due to the effect of non-uniform gas flow. Here  $N_X$  and  $N_Y$  indicates the strip number in X- and Y- plane respectively. Besides, with the same connectivity of gas lines, the observed efficiency maps are different in different RPC chambers.

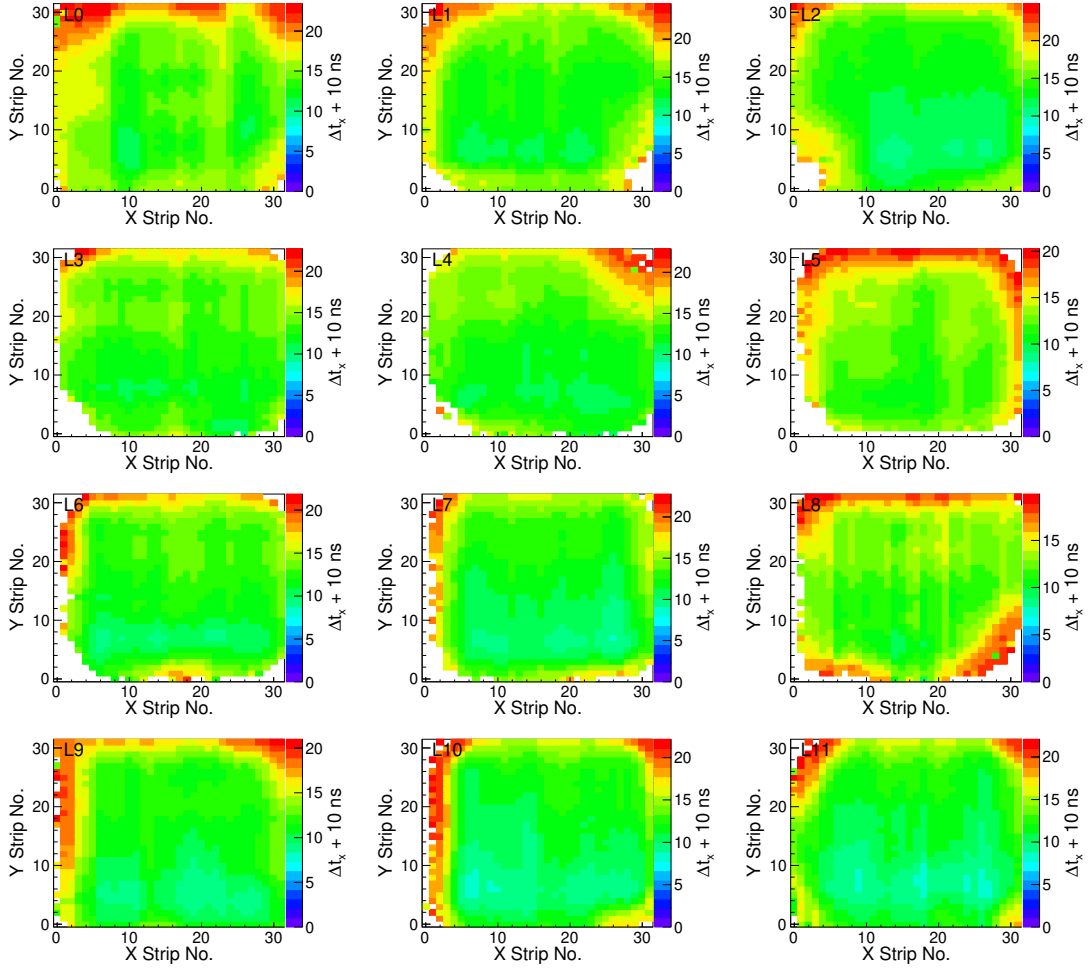


**Figure 2.9:** Average time delay of muon signal in all 12 layers for X-view.

- Variation in the surface resistivity of the paint on the electrodes: Surface resistivity maps of two sides of the RPC gas gap are different due to different screening of induced signal, but the observed efficiency map is similar on both X- and Y-planes, thus the effect of variation of surface resistivity is also ruled out.
- Variation in the thickness of glass electrodes or gas gap spacers: This would result in variation of the electric field in the gas chamber and consequently the gas gain of the RPC. The observed efficiency maps indicate that this could be the dominant contribution for variation of efficiency across the RPC area. The thickness of glass used for RPC fabrication is  $3.1 \pm 0.1$  mm, whereas the

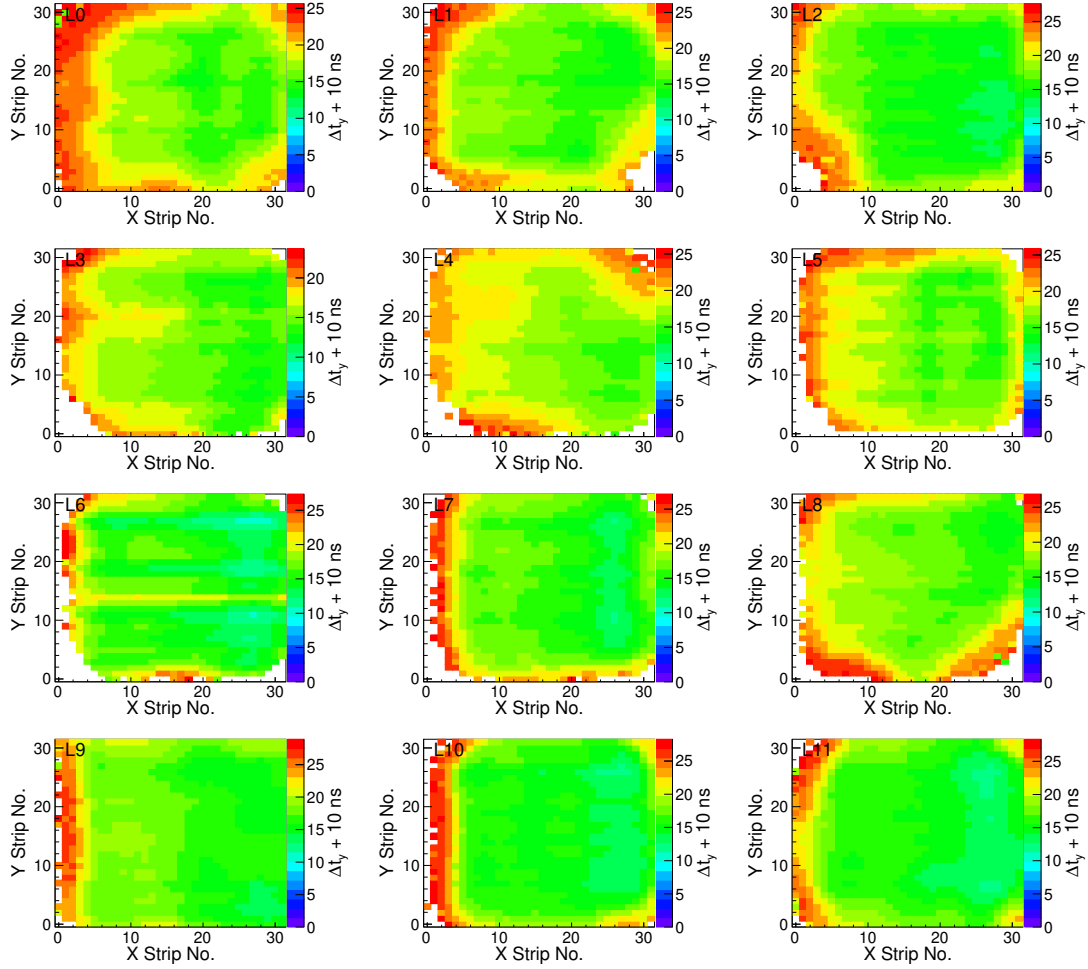


**Figure 2.10:** Average time delay of muon signal in all 12 layers for Y-view.

thickness of spacers is  $2.0 \pm 0.2$  mm. But the observed efficiency map indicates that the difference in the spacer and/or gluing at the edges is the dominant source of inefficiency. It is difficult to improve the tolerance in glass thickness, as regular commercially produced glass is used for the RPC fabrication.

Using the same muon tracks in the detector stack, the timing studies of the RPCs were carried out. Before performing further studies using the timing data, the known sources of time delays were corrected, which are:

- Correction for delay of signal propagation in the pickup strip, which is 4.7 ns/m.
- Average signal delays in electronics and cables between the RPC strip and the DAQ system. The channel by channel corrections are obtained using an



iterative method of offset correction, details of which are given in [3].

The average time delay of the avalanche signals in X- and Y-planes with respect to the expected time in all 12 layers are shown in Figures 2.9 and 2.10. The expected arrival time is computed by the fit of corrected time measurement in all other layers excluding the layer under study. Comparing the Figures 2.8 & 2.9 and Figures 2.8 & 2.10, a correlation can be observed between the the inefficient regions of RPC and the regions where the time delay is large. This shows a variation in time delay due to the variation of avalanche gain in different parts of the RPC, particularly in the regions of low efficiency. The average gain is less in the less efficient region which implies that on average, the signal in that region is low. The large signals cross the leading edge discriminator earlier than the small signals consequently giving an earlier timestamp. Also, from the figure, it can be observed that in the region of 100% efficiency, there is a very small variation in time delay.

This variation in time delay can be avoided by using constant fraction discriminator (CFD), but considering the advanced state of electronics design and implementation, this is a difficult proposition for ICAL detector. In absence of such hardware, an attempt has been made to correct the gain dependent time delay using offline calibration in order to achieve performance similar to CFD.

## **2.5 Position dependent pixel-wise time offset correction**

From the previous section, it can be seen that the average time delay between the production of the signal and time stamp at the discriminator varies with the position where the particle interacts in the RPC. The average values of these delays can be corrected using the efficiency plot. However, this correction cannot be applied in the region where the efficiency of the RPC is  $\sim 100\%$ . The second option is to use the average time measurement itself to perform this offset correction. The

average time delay is measured in  $32 \times 32$  pixels (each of about  $3 \text{ cm} \times 3 \text{ cm}$ ) for both X- and Y-planes of the RPC. For a position in each layer, the time is corrected using the offset corrections of the nearby four pixels.

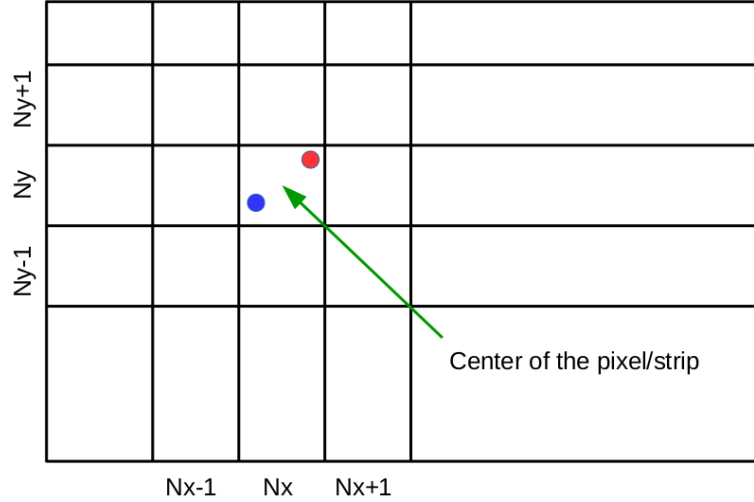


**Figure 2.11:** Schematic for pixelwise offset correction.

In Figure 2.11, if the muon passed through the pixel  $(N_x, N_y)$  and within the pixel if the muon passed through the position marked with a red dot. For the strips on the X plane, the time offset is computed using the interpolation of the delay correction in pixels  $(N_x, N_y)$  and  $(N_x, N_y + 1)$ . If within the pixel, the muon passed through the position marked with a green dot, then the offset is calculated using the pixels  $(N_x, N_y)$  and  $(N_x, N_y - 1)$ . Similarly, for Y-plane, the offset is computed with the delay correction in pixels  $(N_x, N_y)$  and  $(N_x \pm 1, N_y)$  depending on the position within the pixel with respect to its center.

## 2.6 Improvement of time resolution and reduction of up/down ambiguity

In Figure 2.12, the measured time resolution after applying the position-dependent pixel-wise offset correction is presented. Comparing Figures 2.6 and 2.12, it can

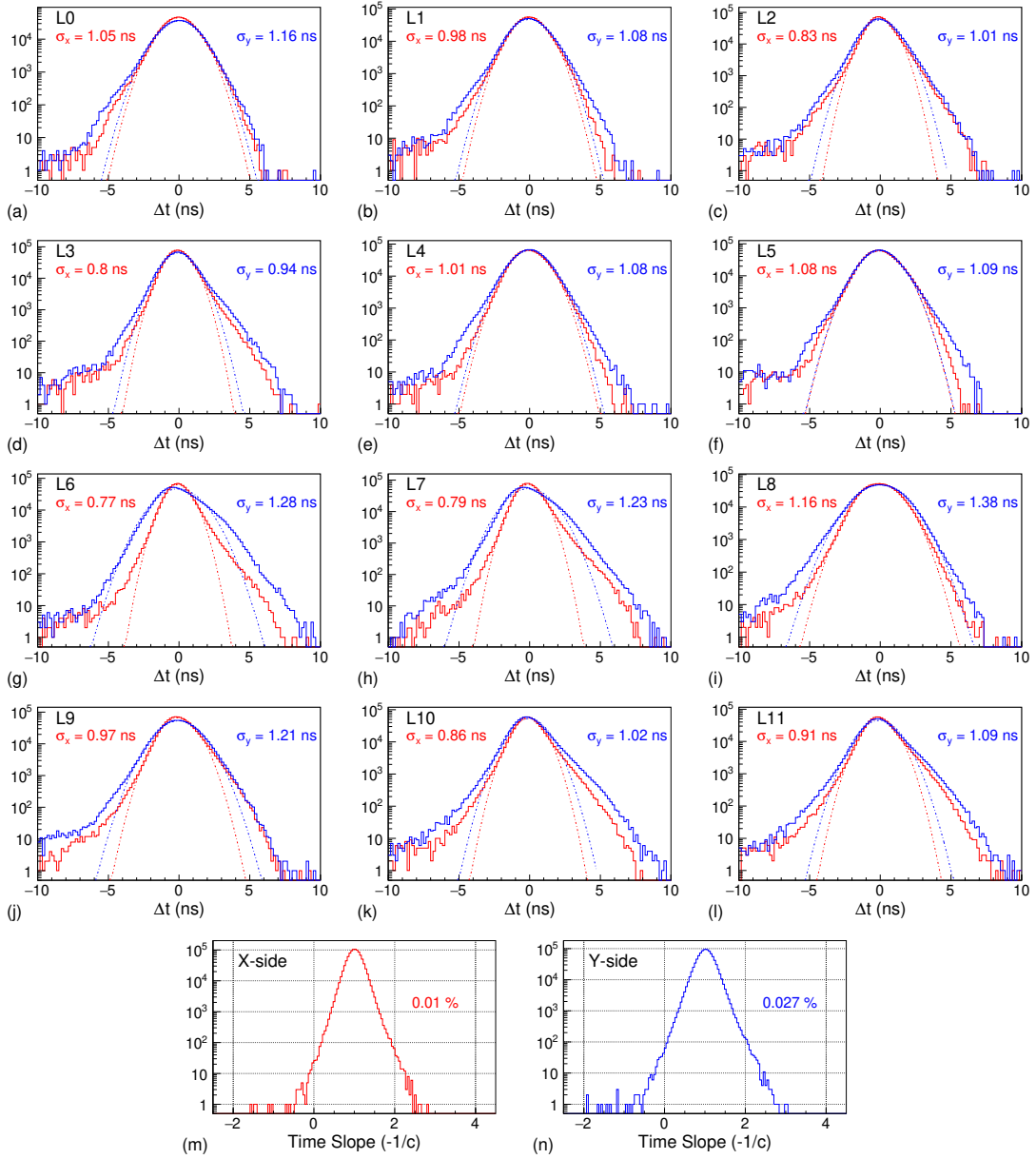


**Figure 2.12:** (a-l) Time resolution in all 12 layers and (m) and (n) directionality (fitted slope in eqn 2.2) of cosmic ray muon using timing information with the position dependent time offset correction. Red colour for X-view and Blue colour for Y view. Dashed line represents the Gaussian fitted function. Here  $c = 29.979$  cm/ns.

be clearly observed that there is a considerable improvement in the time measurement. For example, for layer-2 X-plane, the time resolution improved from 1.21 ns to 0.83 ns. So, the estimated error due to position-dependent time variation is 1.11 ns, which is nearly equal to the resultant time resolution from all other factors. Therefore, it can be concluded that this is the primary source of uncertainty in time resolution in the earlier result of S. Pal et.al [3].

As discussed in Section 2.2, the recorded events are due to cosmic ray interactions in the atmosphere above the detector stack. The probability, that a fraction of these recorded events is due to muons entering from the bottom the detector, is insignificant. So, the expected slope of equation 2.1 should always be negative in this case as the arrival time of muon in the top layer (with the largest layer number, 11) is earlier than that in the bottom layer (with the smallest layer number, 0). The measured slope of the selected events after the pixel-wise offset correction, is shown in Figure 2.12 (m) and (n). The estimated misidentification rate for muon trajectories as up-going reduces from 0.3 % to 0.01 % for X-plane and from 0.5 % to 0.03 % for Y-plane. To compensate for the effects of noise, inefficiency and trigger acceptance, the minimum number of layers used in this measurement is 9 as against 12 layers of the detector stack.

## **2.7 Effect of lateral hit position on strip for time measurement**

It is expected that if the avalanche occurs near the center of a strip, the induced signal in that strip is much larger than those on the neighboring strips. As the pitch of pickup strips being 30 mm, and an inter-strip gap of 2 mm, it is expected that a much larger fraction of events to show up with a strip multiplicity of one. In the second case, if the avalanche occurs in between the two strips, the induced signal will be shared by both the strips. The observed average strip multiplicity of

these RPCs is 1.9. The strip multiplicity as a function of muon position in a strip for different layers is shown in Figures 2.13 and 2.14. The position is measured with respect to the center of the strip. It can be clearly observed in the data, that the idea of induced charge sharing between neighboring strips is correct.

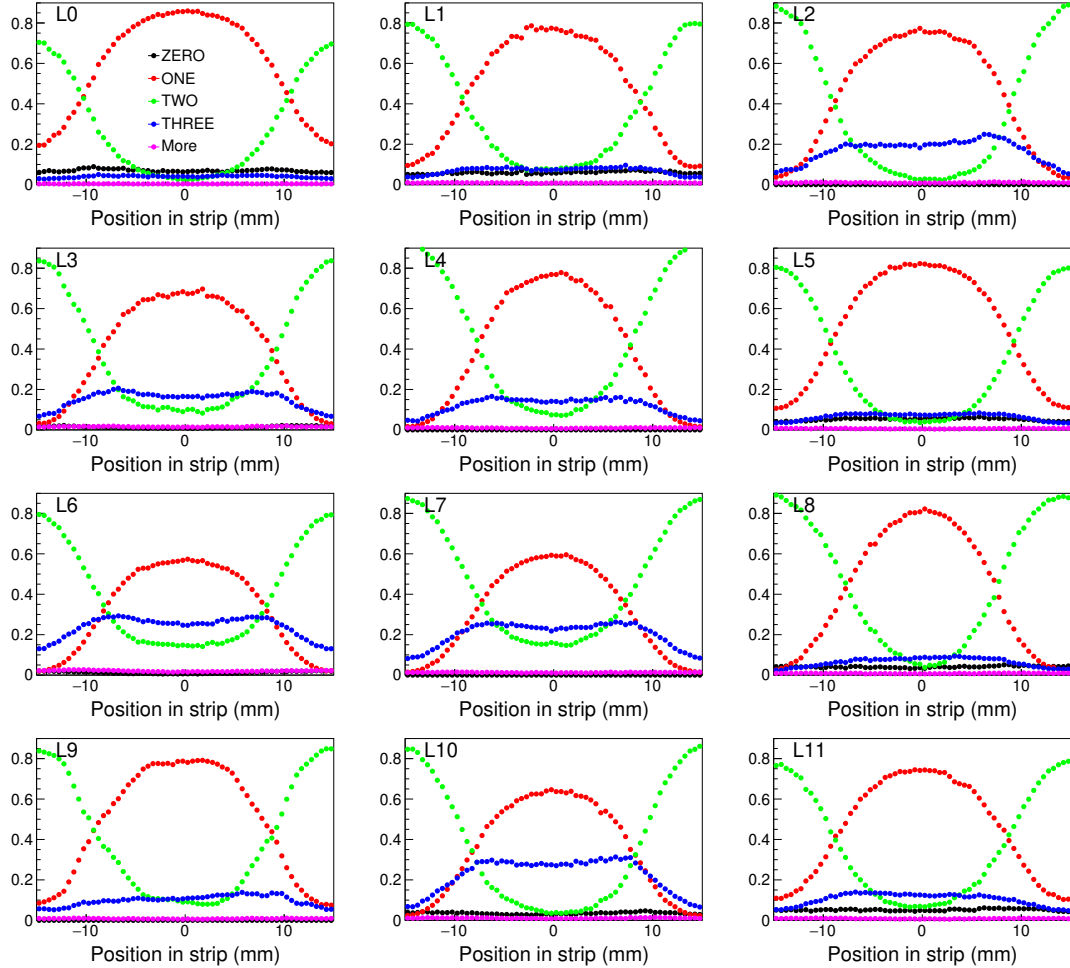


**Figure 2.13:** Strip multiplicity as a function of muon position in the strip for all 12 layers in X-view.

As seen in these plots, there are almost no events with strip multiplicity of two, when the muon trajectory is at the center of the strip and similarly almost no events with strip multiplicity one, when the muon trajectory is at the boundary between two strips. The position of maxima and minima of the strip multiplicity distributions at the center and edge of the strips respectively also indicates that the position alignment of RPCs in the detector stack is accurate. It should also

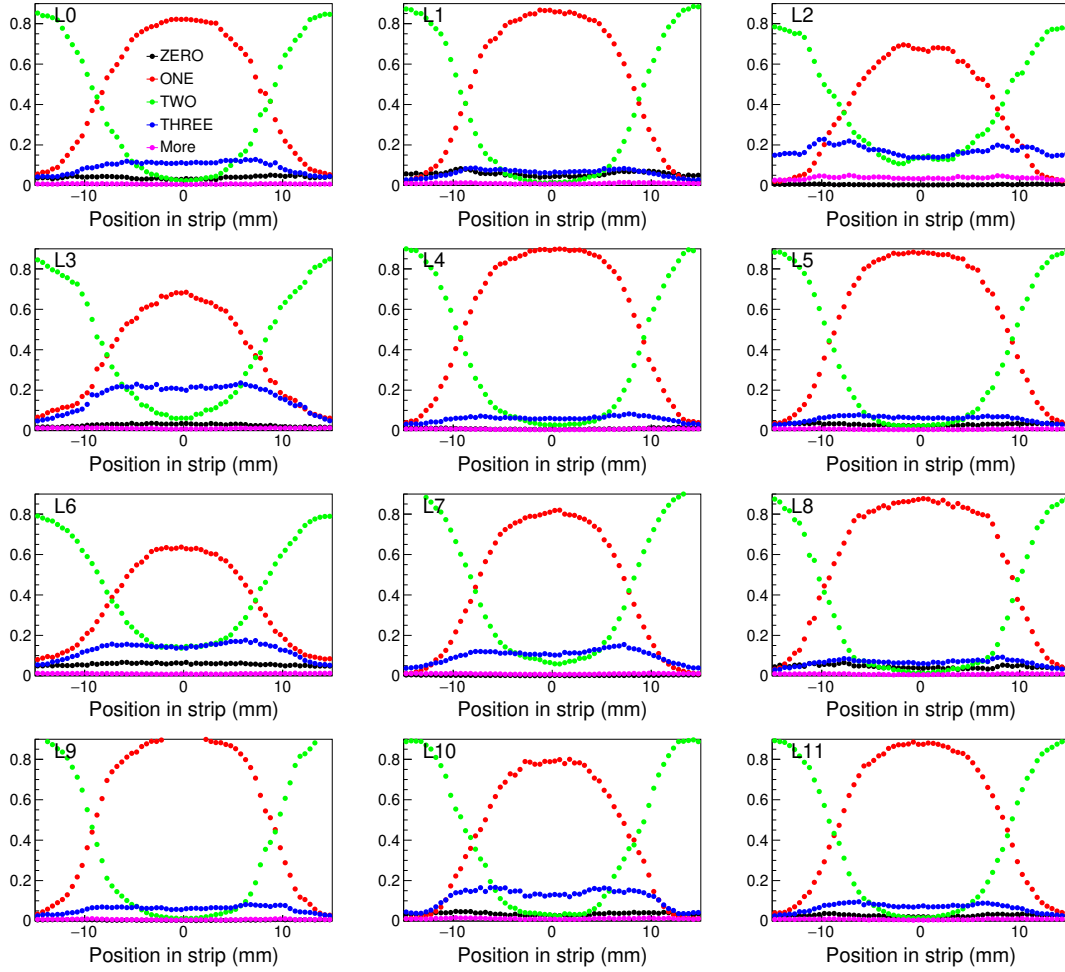


**Figure 2.14:** Strip multiplicity as a function of muon position in the strip for all 12 layers in Y-view.

be noted that on an average the charge induced on one strip for an event with strip multiplicity of two is more than the charge induced for an event with strip multiplicity of one. The sharing of an induced signal on multiple strips depends on the position of the muon trajectory.

The average offset of measured signal arrival times in a layer with respect to the expected arrival times (obtained using the arrival times of other layers) as a function of strip position for different multiplicities for Y-plane is shown in figures 2.15 and 2.16. The shapes of the offset for X- and Y-plane are the same, implying that they depend only on the gains of RPCs as well as on the differences in electronics signal paths, if any, between layers. No correlation between time delay and muon position

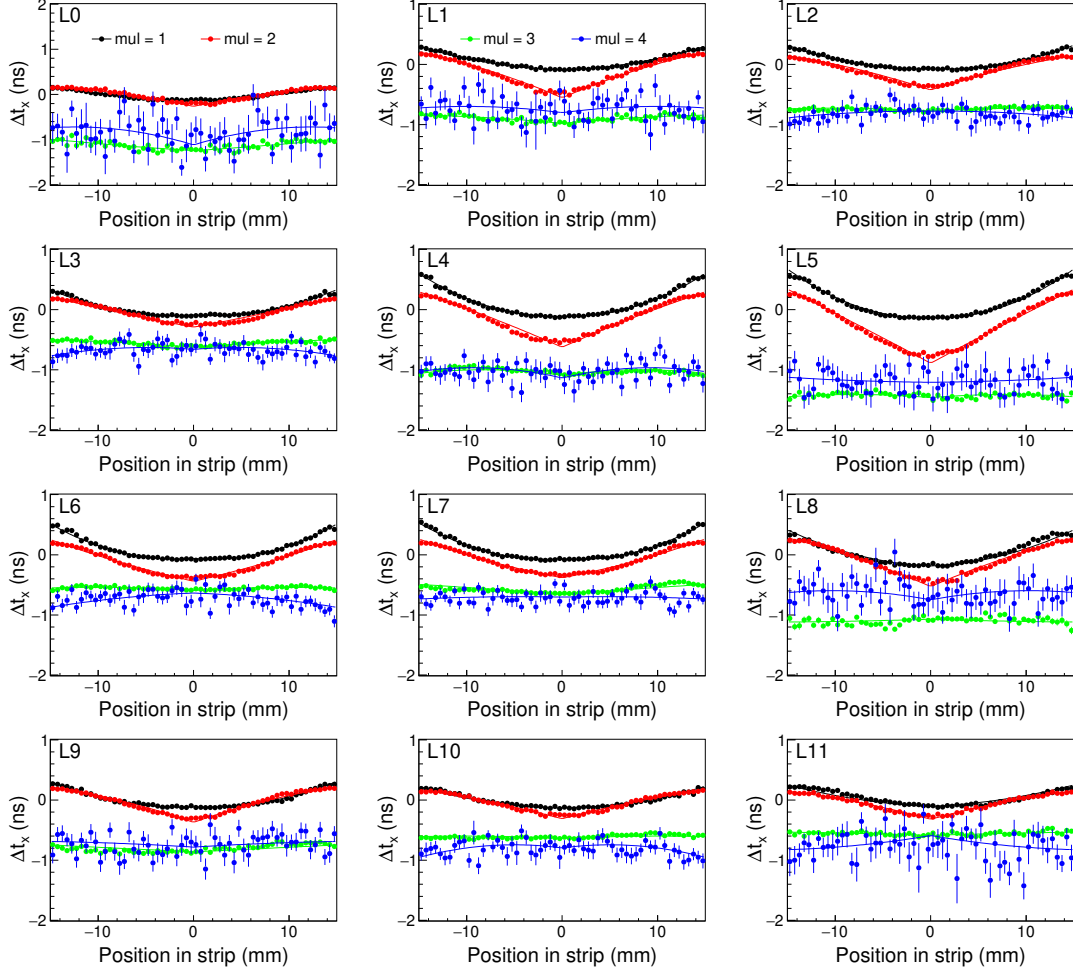


**Figure 2.15:** Average delay time as a function of muon position in strip for all 12 layers in X-view.

has been observed in events with strip multiplicity of three and above. The offsets observed in Figures 2.15 and 2.16 can be fitted using a second-order polynomial function as shown below:

$$\Delta t(x) = P_0 + P_1|x| + P_2x^2 \quad (2.3)$$

where  $x$  is the muon hit position with respect to the center of the strip and  $P_0$ ,  $P_1$  and  $P_2$  are appropriate coefficients determined by the fit. So, based on the lateral position of muon hit on a strip and observed strip multiplicity, this offset correction can be computed and applied. The time resolution of the RPCs with

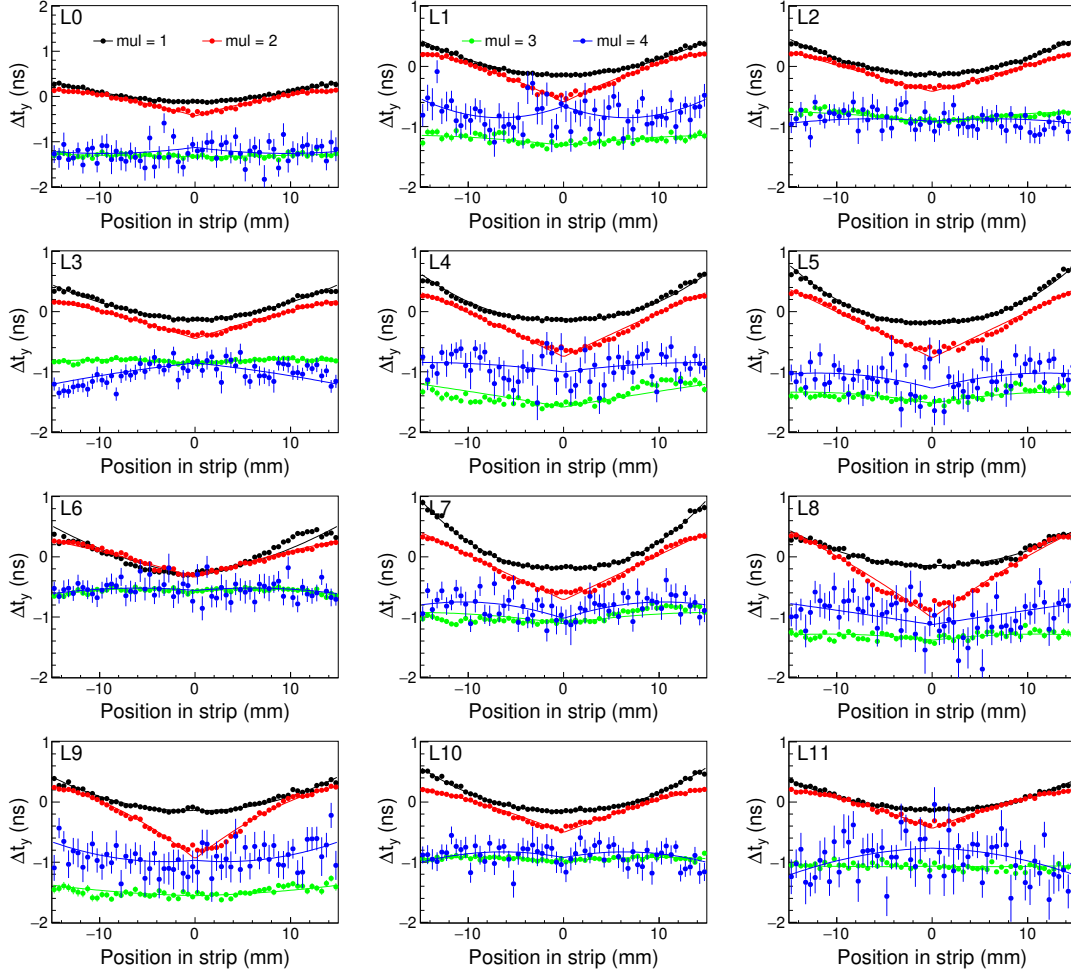


**Figure 2.16:** Average delay time as a function of muon position in strip for all 12 layers in Y-view.

this additional corrections is shown in Figure 2.17 and there is a clear improvement in time resolution with this additional time corrections, but this is not a significant improvement.

The observed time resolution of an RPC is obtained from the difference in the measured time with corrections in that layer and the time of the muon crossing that is expected to the layer/RPC. The latter is calculated from the time measurements in the remaining layers, as a consequence, this expected time has some uncertainty. Thus, the time resolution of a layer is obtained by quadratically subtracting the expected error due to extrapolation from the observed resolution. The measured time resolutions in all layers are given in Table 2.2. This table indicates that



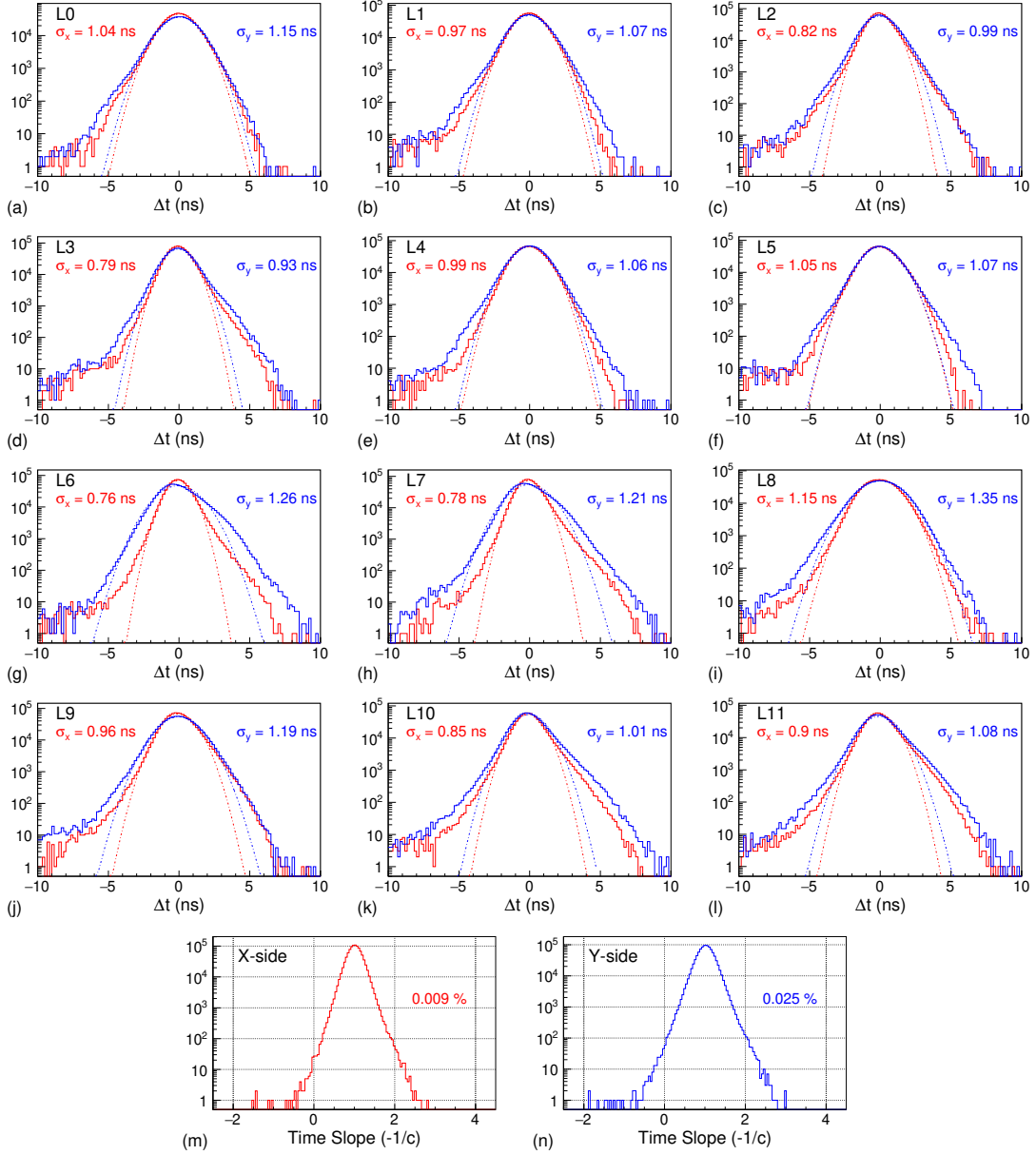


**Figure 2.17:** (a-l) Time resolution in all 12 layers and (m) and (n) directionality (fitted slope in eqn 2.2) of cosmic ray muon using timing information with all the corrections. Red colour for X-view and Blue colour for Y view. Dashed line represents the Gaussian fitted function. Here  $c = 29.979$  cm/ns.

after this offset correction, the time resolution of all the RPC detectors, except the Y-plane of layers 6-9 improves to better than 1 ns.

In order to compare the improvement of this misidentification rate with a previous work by S. Pal et.al [3], a table (Table 2.3) is prepared with the same selection criteria. There are improvements on this misidentification rate by a factor of four

#	X-plane					Y-plane				
	Mean	RMS	$\mu$	$\sigma$	Corr $\sigma$	Mean	RMS	$\mu$	$\sigma$	Corr $\sigma$
0	0.007	1.078	0.009	1.043	0.885	0.01	1.191	0.024	1.151	0.965
1	0.006	1.008	0.005	0.97	0.846	0.009	1.127	0.014	1.073	0.916
2	0.006	0.931	-0.023	0.829	0.692	0.008	1.068	0.000	0.999	0.850
3	0.005	0.875	-0.023	0.798	0.710	0.007	1.035	-0.03	0.932	0.825
4	0.005	1.018	0.000	0.995	0.946	0.006	1.109	0.008	1.064	1.000
5	0.004	1.087	0.000	1.058	1.021	0.004	1.13	-0.001	1.072	1.018
6	0.004	0.845	-0.028	0.762	0.707	0.004	1.37	-0.063	1.263	1.218
7	0.003	0.894	-0.047	0.783	0.721	0.003	1.308	-0.041	1.213	1.159
8	-0.008	1.169	-0.007	1.152	1.104	0.002	1.384	0.013	1.358	1.297
9	0.002	1.052	-0.033	0.967	0.875	-0.015	1.244	-0.016	1.199	1.091
10	-0.011	0.99	-0.062	0.855	0.713	0.001	1.181	-0.064	1.016	0.833
11	0.000	1.055	-0.065	0.909	0.696	0.000	1.238	-0.061	1.085	0.843

**Table 2.2:** Time resolution (ns) of all twelve layers with and without the position dependent offset correction. Statistical errors on these mentioned are in 4<sup>th</sup> decimal place. Here Mean and RMS is the statistical mean and RMS of the  $\Delta t$  distribution,  $\mu$  and  $\sigma$  are gaussian fitted mean and sigma and corr  $\sigma$  is resolution after quadratic subtraction of extrapolation error from the fitted  $\sigma$ .

as compared to the earlier work [3]. The observed improvement is less than the expected one, which is mainly due to the tail part of the resolution plots, e.g., events beyond  $\pm 3$  ns as shown in Figure 2.17. Though there is a substantial improvement of the overall time resolution in the combined sample, this tail is not reduced to the same extent.

Layer # $\geq$	6	8	10	11
X-plane	$9.70 \pm 0.99$	$1.14 \pm 0.38$	$0.27 \pm 0.27$	$0.60 \pm 0.60$
Y-plane	$25.26 \pm 1.59$	$4.33 \pm 0.72$	$0.67 \pm 0.39$	$0.88 \pm 0.62$

**Table 2.3:** Fraction ( $\times 10^{-5}$ ) of reconstructed up-going muons with different criteria on the number of used RPC layers in the fit.

## 2.8 Spurious noise near spacer buttons

As mentioned in the previous sections, there are large tails in the time resolution plots of all layers of the detector, which is not easily corrected by any known logic. These tails result from the inherent noise in the electronic chain and due to a sharp change in the electric field of the RPC detector affecting its gain particularly near

buttons and side spacers. Figure 2.18 shows corrected time with respect to the arrival time ( $\Delta t$ ) of the signal of X-plane as a function of Y-position for all layers. Similarly, Figure 2.19 shows the same for the signal of Y-plane as a function of X-position for all layers. It can be seen that most of the events have very small  $\Delta t$  with a small tail. But in a small fraction of events, a large variation in  $\Delta t_x$  ( $\Delta t_y$ ) is observed at particular Y-(X-) positions. The positions show a periodicity of  $\sim 18$  cm (6 strips).

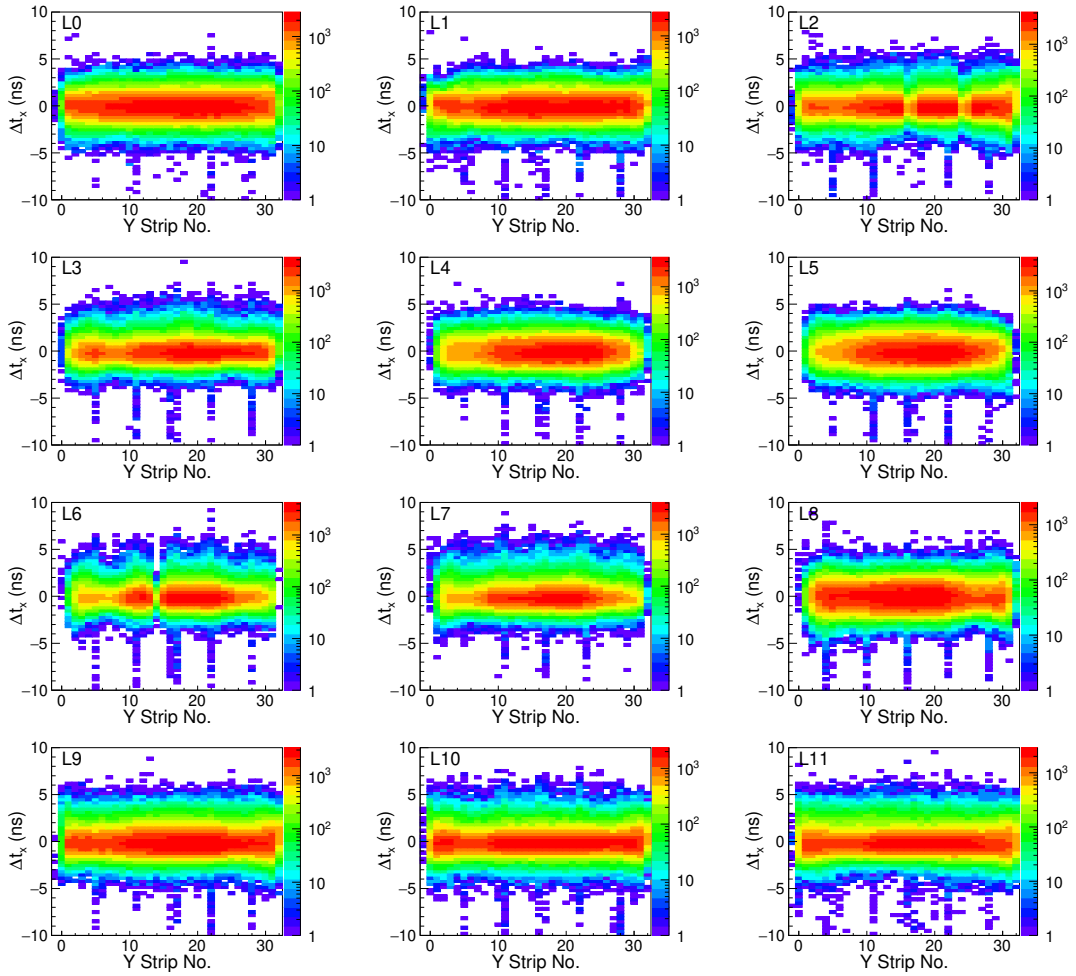


**Figure 2.18:** Corrected time with respect to the the expected time ( $\Delta t$ ) in the signal of X-plane as a function of Y-position.

These Y- and X-positions correspond to the positions of the polycarbonate spacer buttons, which are used for maintaining a uniform gap between the glass electrodes. The buttons are glued to the glass with epoxy (3M DP190 epoxy). The

peripheries of these glued buttons remain sharp after the glue is set, and the electric field is enhanced locally due to which larger and hence faster signals are produced. On the other hand, the position where the spacer button is glued to the glass electrodes constitutes almost dead space for avalanche multiplication. Therefore, the efficiency from these regions is low which was observed in Figure 2.7 and 2.8.

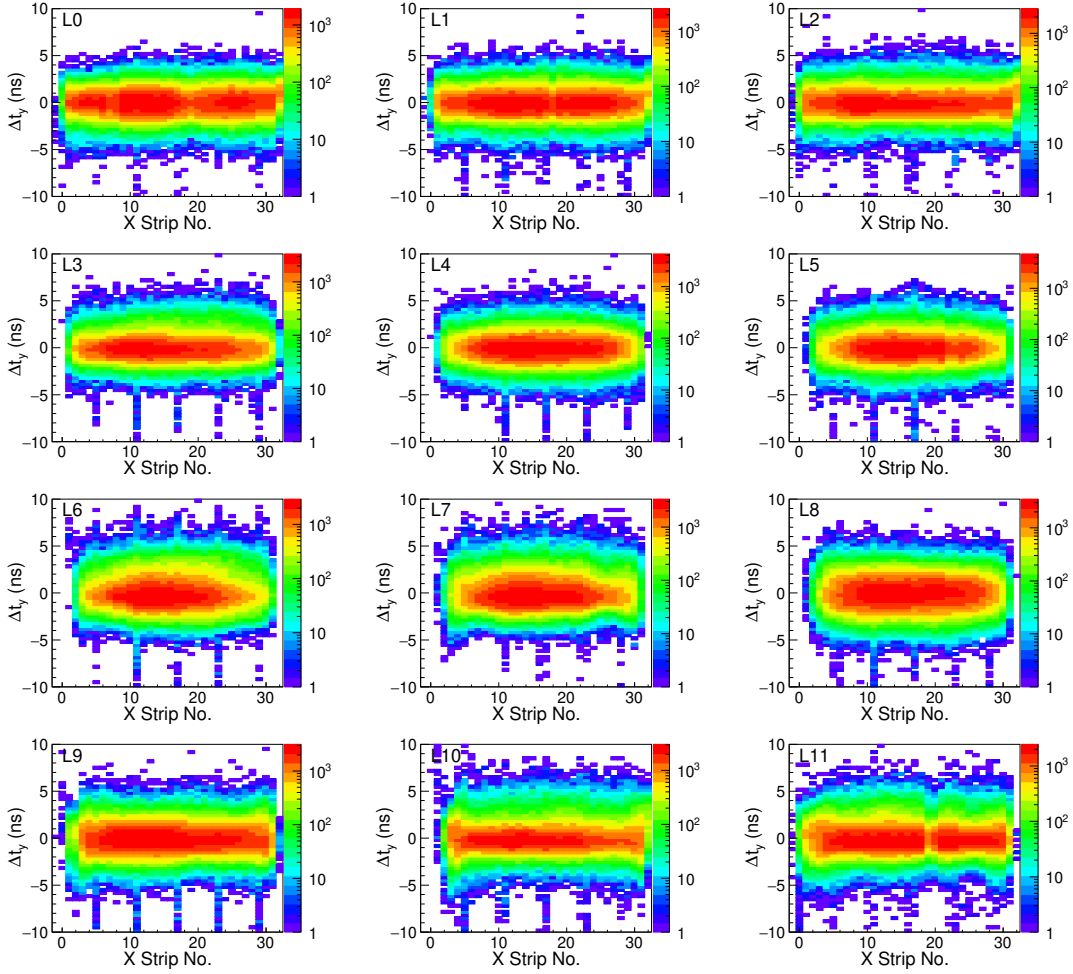


**Figure 2.19:** Corrected time with respect to the the expected time ( $\Delta t$ ) in the signal of Y-plane as a function of X-position.

Figure 2.20(a) shows correlations of  $\Delta t_x$  and  $\Delta t_y$  for positions of muon within 1 cm of button centres, for events selected with criteria,  $|\Delta t_x| > 4$  ns and  $|\Delta t_y| > 4$  ns. A clear correlation of the arrival times between X- and Y-plane strips and in particular for large signals (fast signals) is seen. Figure 2.20(b) shows the positions of muon trajectories in the RPCs (combination of all 12 layers), where  $\Delta t_x < -8$  ns

and  $\Delta t_y < -8$  ns. Clusters of these positions match with the positions of spacer buttons. Button positions in all the RPC chambers are not exactly identical, thus the combined distribution shows a wider spot of buttons. There is also a band of positions meeting the above condition for a lower value of X in the layer-7 and layer-10, which is due to the gluing of the side spacer, not the button. But, smaller signals, consequently delayed ( $\Delta t_x > 8$  ns and  $\Delta t_y > 8$  ns) do not show any correlation with position, which is evident in Figure 2.20(c).

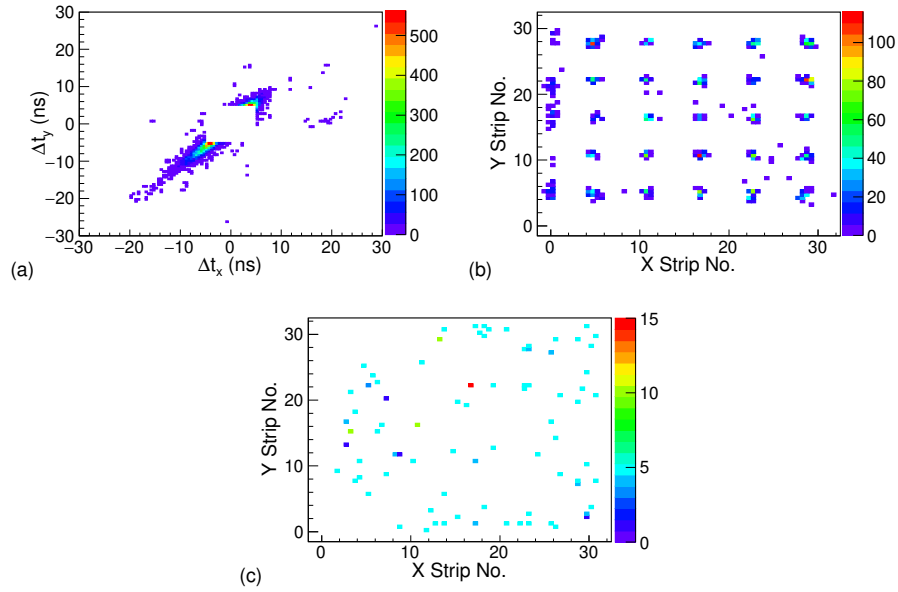


**Figure 2.20:** (a)  $\Delta t_x$  vs  $\Delta t_y$  for a position of muon within 1 cm of button centre, (b) Combined position of muon in all layers, where  $\Delta t_x < -8$  ns and  $\Delta t_y < -8$  ns, and (c) Combined position of muon in all layers, where  $\Delta t_x > 8$  ns and  $\Delta t_y > 8$  ns.

It may be noted that it is very difficult to achieve a perfect quality of the various manufacturing procedures of the RPC detectors, and in particular of the gluing process. Perhaps the best solution to this problem is by characterizing these imperfections and incorporate them in Monte Carlo simulation or veto that region.

## 2.9 Summary

In this chapter, it is observed that the dominant factor affecting the time resolution of a large scale single gap RPC is its position dependent gain. There are many

sources that contribute to position-dependent gain variations, e.g., a variation of glass thickness, variation in button and spacer dimensions, non-uniformity of gas composition due to improper flow of gas, leakages in the gas circuit, etc. This chapter also describes a technique of offline correction of time resolution of RPCs using a large cosmic ray data sample, which can be done in a test beam setup also. Also, there is a variation of recorded timing information as a function of strip multiplicity as well as the lateral position of the trajectory. After correcting for these two factors along with correction for the time of flight of the signal in strips as well as for the delay in the electronic chains, most of the RPCs show a time resolution better than 1ns in any part of the detector.

In summary, we conclude that by using offline corrections, large-area single gap RPCs can be operated with detection efficiency better than 95% and timing resolution better than 1ns.

## Chapter 3

# The ICAL detector simulation and muon reconstruction

The ICAL detector is mainly sensitive to the interactions due to the atmospheric  $\nu_\mu$ s which are arising from  $\nu_\mu \rightarrow \nu_\mu$  and  $\nu_e \rightarrow \nu_\mu$  oscillation channels. The accurate determination of the energy and direction of the final state particles, i.e., the muons and the hadrons, in these interaction events are critical to accomplish the physics goals of the ICAL. The  $\nu_\mu$  and  $\bar{\nu}_\mu$  experience separate matter effects for either of the possible mass ordering while propagating through the Earth. Hence, by observing the individual event rates for  $\nu_\mu$  and  $\bar{\nu}_\mu$  through the distinction of the final state  $\mu^+$  and  $\mu^-$  in the CC events, the mass ordering can be determined. The additional information on the final state hadrons will provide an enhancement in the physics sensitivity of the detector [87]. In order to achieve the physics goals, the ICAL detector has to be properly calibrated to reconstruct the energy and direction of the muons and hadrons, as well as the identification of the charge of the muons.

To calibrate the ICAL response to the muon and hadrons, a detector simulation framework [1, 88–90] has been developed using the GEANT4 simulation package. This framework work has been described in Section 3.1. For easy sharing of geometry parameters and various other inputs, a database is a must. For ICAL simulation

framework, a database is set up using “PostgreSQL” and is described in Section 3.2. The INO specific digitization algorithm which is implemented to convert the GEANT4 output to the detector observed output has been discussed in Section 3.3. The muon reconstruction algorithm is then described in Section 3.4. If the muon event is fully contained (FC) within the detector, then the range of muon is precisely known. The momentum measurement from the range of muon inside the detector gives a better estimate than the one measured using the curvature, however, this is applicable only to the FC event. In section 3.5, an algorithm to tag a fully contained (FC) muon track is presented. Some observations about the *fiducial volume* for ICAL detector are also discussed in the same section. In the case of  $\nu_\mu$  ( $\bar{\nu}_\mu$ ) CC-RS or CC-DIS interaction, along with a muon track, a hadron shower will also be observed with a cluster of hits in the vicinity of the vertex. This same algorithm has also been adapted to extrapolate the muon track in the hadron shower. The calibration scheme and analysis of the FC events using the range of the muon track is presented in Section 3.6. In Section 3.7, the major results of this work are summarized.

### 3.1 ICAL detector simulation framework

The muons and hadrons, which are generated in neutrino interactions, pass through the dense detector material and an inhomogeneous magnetic field in the ICAL detector. The simulation of such particles through the detector geometry is performed by a package based on the GEANT4 [4, 91] toolkit and an INO specific digitization code. In the GEANT4 simulation framework, the ICAL detector includes the geometry as well as the magnetic field. The layout of the ICAL detector geometry is shown in Figure 3.1(a).

The 50kt ICAL detector has a modular structure of three modules, each of size  $16\text{ m} \times 16\text{ m} \times 14.5\text{ m}$ , with a gap of 20 cm between the modules. The ICAL



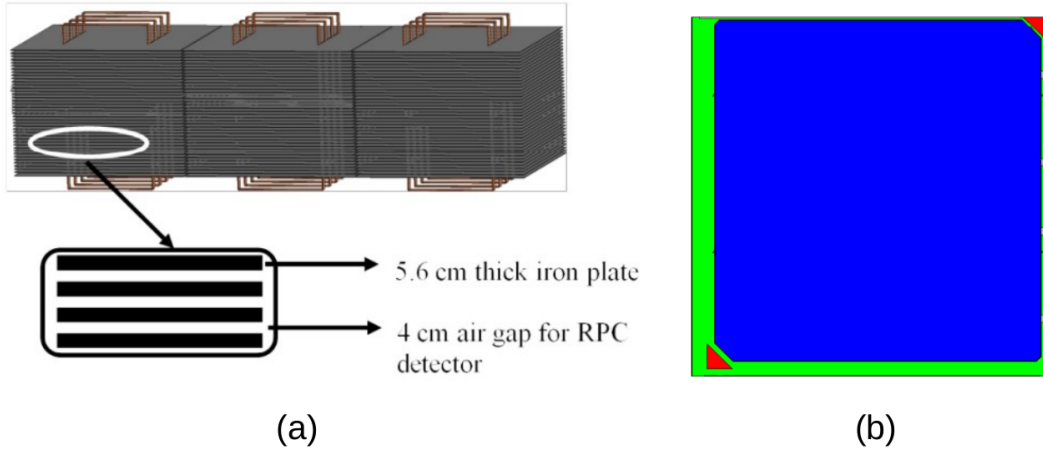


**Figure 3.1:** (a) Schematic view of the 50 kt ICAL detector and (b) A basic RPC unit along with the tray.

coordinates are defined as follows: the direction along which the modules are placed is labeled as the x-direction with the remaining horizontal transverse direction being labeled y. As the final orientation of the ICAL detector is not yet finalized, the “x” is currently considered to coincide with the geographical south. The z-axis points vertically upwards so that the polar angle equals the zenith angle  $\theta$  while the zero of the azimuthal angle  $\phi$  points south. In the geometry, the origin is taken to be the center of the second module. Each ICAL module consists of 151 layers of iron plates with thickness of 5.6 cm. The area of each module is  $16\text{ m} \times 16\text{ m}$ , while the area of each iron plate is  $2\text{ m} \times 4\text{ m}$ . There is a vertical gap of 4 cm between the two layers. Hence, the vertical separation between the two RPC layers is 9.6 cm. The iron sheets are supported every 2 m in both the x and y directions, by steel support structures. The basic RPC units are placed in a grid format within the air gaps.

Vertical slots at  $x = x_0 \pm 4\text{ m}$  (where  $x_0$  is the central x value of each module) extending up to  $y = \pm 4\text{ m}$  and cutting through all layers are provided to accommodate the four copper coils that wind around the iron plates, providing a magnetic field in the x-y plane. The magnetic field map as obtained from simulations using MAGNET6.26 software[92] is shown in Figure 3.2 [93]. In the central region of

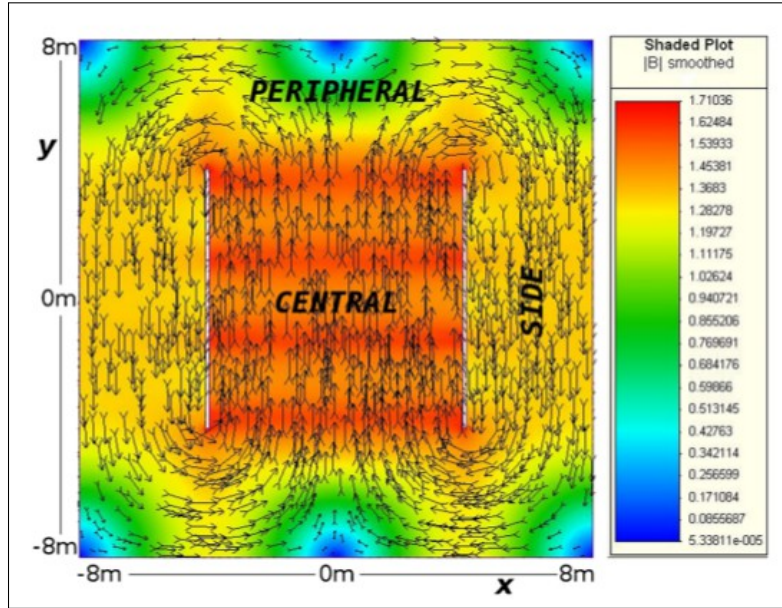


**Figure 3.2:** The magnetic field lines in the central iron layer of the central module ( $z = 0$ ). The length and direction of the arrows indicate the magnitude and direction of the field; the magnitude (in T) is also shown according to the colour-coding indicated on the right.

each module, typical values of the field strength are about 1.5 T in the y-direction.

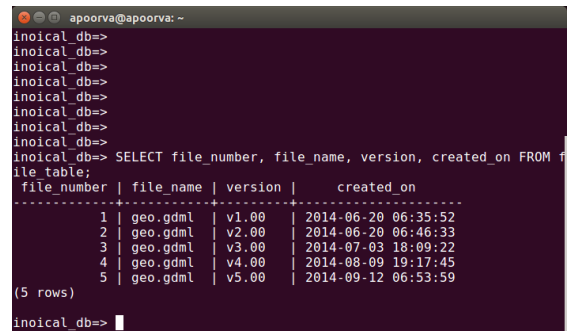
In the old geometry, the total RPC dimension was  $184 \text{ cm} \times 184 \text{ cm} \times 1.88 \text{ cm}$ . As per the detector design at that time, the electronics board was to be kept on top of the RPCs. To accommodate that in the detector geometry, the electronic board material (G10) was uniformly spread over the entire RPC. Hence, the thickness of RPC (in the geometry) was larger by an extra cm. In the new RPC design implemented in the current geometry, the RPC size is  $174 \text{ cm} \times 183.5 \text{ cm} \times 1.8 \text{ cm}$ . There are two triangular cuts on two diagonal corners to accommodate two electronic boards (one for DAQ and another for H.V. power supply) as shown in Figure 3.1(b). The RPC is kept in a tray made of Fibreglass Reinforced Plastic (FRP) material along with the two triangular electronic boards. The RPC is not kept at the center of an FRP Tray but slightly off-center. The DAQ Board is right angle triangle with side length 12.5 cm and thickness 0.5 cm and H.V. Power Supply Board is also right angle triangle with side length 10 cm and thickness 0.5 cm. The RPC

tray size is 191 cm × 194 cm × 3.4 cm. This is the main difference in geometry in the simulations framework as compared to previous works. The width of the readout strip of RPC is 3 cm. The ICAL geometry is written to a machine-readable GDML file that can be read off by other associated packages, like the event reconstruction and GENIE event generator [94, 95].

## 3.2 Database for ICAL simulation framework

The role of commercial and home-made database systems in HEP experiments is reviewed in [96]. In this review, a database is defined as “*A system for the storage and retrieval of data in which the data are identified by the attributes which are most relevant to the user or application.*” The typical applications to use database in INO collaboration include the list of RPCs, DAQ electronic boards, etc and its electrical and mechanical properties, delivered for ICAL experiment. For such applications, the database has already been setup. In this section, the main aim is to use a database system in HEP collaboration activities like simulation, reconstruction, and analysis software. The insertion and retrieval of bulky data, mainly by the C++ based software for these activities is the major area. Alignment and calibration information for ICAL like detectors can be both bulky and frequently changing. These parameters are regular inputs to the detector simulation and reconstruction algorithms. These data may be created and accessed by many different processes, often operating simultaneously.

For the more specialized HEP applications for ICAL detector, the needs are:



```

apoorva@apoorva: ~
inoical_db=>
inoical_db=>
inoical_db=>
inoical_db=>
inoical_db=>
inoical_db=>
inoical_db=>
inoical_db=>
inoical_db=> SELECT file_number, file_name, version, created_on FROM file table;
file number | file_name | version | created_on
-----|-----|-----|-----
1 | geo.gdml | v1.00 | 2014-06-20 06:35:52
2 | geo.gdml | v2.00 | 2014-06-20 06:46:33
3 | geo.gdml | v3.00 | 2014-07-03 18:09:22
4 | geo.gdml | v4.00 | 2014-08-09 19:17:45
5 | geo.gdml | v5.00 | 2014-09-12 06:53:59
(5 rows)
inoical_db=>

```

**Figure 3.3:** Database table for files with various versions.

parameter_number	parameter_name	value_g1	comments	units	created_on	revision
1	iron thickness	5.6	Set the thickness of iron layer	cm	2013-11-18 22:31:44.077361	r-01-00
2	airgap thickness	4.0	Set the thickness of Air volume between to Iron layers, >2.9cm	cm	2013-11-18 22:31:44.077361	r-01-00
3	x_strip_width	1.96	stripwidth - X	cm	2013-11-18 22:31:44.077361	r-01-00
4	y_strip_width	1.96	stripwidth - Y	cm	2013-11-18 22:31:44.077361	r-01-00
5	n_layer	158	Number of layers in Z direction	cm	2013-11-18 22:31:44.077361	r-01-00
6	n_chamber	8	Number of RPCs per chamber	number	2013-11-18 22:31:44.077361	r-01-00
7	n_module	8	Number of columns of modules	number	2013-11-18 22:31:44.077361	r-01-00
8	n_iron	8	Number of iron plates in a module	number	2013-11-18 22:31:44.077361	r-01-00
9	n_ironmodule	4	Number of iron plate modules	number	2013-11-18 22:31:44.077361	r-01-00
10	n_ironlayer	151	Number of iron layers	number	2013-11-18 22:31:44.077361	r-01-00
11	n_spacer1	4	Number of spacers of type 1 in a layer	number	2013-11-18 22:31:44.077361	r-01-00
12	n_spacer2	8	Number of spacers of type 2 in a layer	number	2013-11-18 22:31:44.077361	r-01-00
13	n_spacer3	6	Number of spacers of type 3 in a layer	number	2013-11-18 22:31:44.077361	r-01-00
14	n_spacer4	21	Number of spacers of type 4 in a layer	number	2013-11-18 22:31:44.077361	r-01-00
15	n_spacer5	28	Number of spacers of type 5 in a layer	number	2013-11-18 22:31:44.077361	r-01-00
16	n_spacer6	14	Number of spacers of type 6 in a layer	number	2013-11-18 22:31:44.077361	r-01-00
17	n_coil	4	Number of coils in a module	number	2013-11-18 22:31:44.077361	r-01-00
18	n_coilsupport	3	Number of supports per coil	number	2013-11-18 22:31:44.077361	r-01-00
19	gap_ino	28.0	Gap between two INO module (full length)	cm	2013-11-18 22:31:44.077361	r-01-00
20	n_ino	3	Number of INO modules	number	2013-11-18 22:31:44.077361	r-01-00
21	par_chm	188.0	Chamber size	cm	2013-11-18 22:31:44.077361	r-01-00
22	par_ino	888.0	INO size	cm	2013-11-18 22:31:44.077361	r-01-00
23	par_lay	888.0	RPC layer	cm	2013-11-18 22:31:44.077361	r-01-00
24	par_coilspacerpc	4.0	Space for coil in RPC layer	cm	2013-11-18 22:31:44.077361	r-01-00
25	par_mod	188.0	RPC module	cm	2013-11-18 22:31:44.077361	r-01-00
26	par_iron	288.0	Iron plate	cm	2013-11-18 22:31:44.077361	r-01-00
27	par_ironmod	288.0	Iron module	cm	2013-11-18 22:31:44.077361	r-01-00
28	par_ironlay	888.0	Iron layer	cm	2013-11-18 22:31:44.077361	r-01-00
29	par_coilspaceliron	4.8	Space for coil in iron layer	cm	2013-11-18 22:31:44.077361	r-01-00
30	par_airgap1	799.5	Space for horizontal air gap in iron layer	cm	2013-11-18 22:31:44.077361	r-01-00
31	par_airgap2	8.25	Space for vertical air gap in iron layer	cm	2013-11-18 22:31:44.077361	r-01-00
32	par_airgap3	0.25	Space for air gap between coil in iron layer	cm	2013-11-18 22:31:44.077361	r-01-00
33	par_spacer1	12.5	Spacer1	cm	2013-11-18 22:31:44.077361	r-01-00
34	par_spacer2	25.25	Spacer2	cm	2013-11-18 22:31:44.077361	r-01-00
35	par_spacer3	25.25	Spacer3	cm	2013-11-18 22:31:44.077361	r-01-00
36	par_spacer4	25.25	Spacer4	cm	2013-11-18 22:31:44.077361	r-01-00
37	par_spacer5	25.8	Spacer5	cm	2013-11-18 22:31:44.077361	r-01-00
38	par_spacer6	12.5	Spacer6	cm	2013-11-18 22:31:44.077361	r-01-00
39	par_gas	91.999	RPC gas (2mm)	cm	2013-11-18 22:31:44.077361	r-01-00
40	par_g10	92.0	g10 which includes g10, qr2 and gas (5mm)	cm	2013-11-18 22:31:44.077361	r-01-00

Figure 3.4: Database table for detector parameters.

1. Efficient retrieval of bulky and/or numerous data according to simple search criteria.
2. Reasonably efficient insertion of bulky and/or numerous data.
3. C++/Fortran access (essential).
4. Terminal access (desirable).
5. Concurrent write access. It must be possible to lock (ideally automatically) an adequately small fraction of the database.
6. Portability, both for the Fortran/C++ base codes and the database contents.
7. Robustness.
8. Security to reduce accidental damage or hacking.
9. Cost-effective. This is almost mandatory for any system which must be installed at many institutes or with a large number of users.

The online database for the ICAL simulation code is set up by using “PostgreSQL” based database management system. PostgreSQL has a good easy interface with C++ which is currently the programming language used in software for INO. At present, the database has been set up for the detector geometry parameters (Figure 3.4), magnetic field map and a file table for various input files (Figure 3.3) having alignment and correction parameters, strip health information, geometry file for reconstruction, etc. The database is set up to implement different versions of the parameters using tags and distribute them to the users. For the future, the various tables can be easily migrated to store the run data like the trigger, DAQ parameters, high voltage, channel maps, noise rates, thresholds, etc.

### 3.3 INO specific digitisation

When a charged particle passes through the RPC gas volume, the GEANT4 framework provides the energy deposited at that position, its coordinates (x,y,z) and an exact timestamp. These coordinates of the signals are then translated through digitization code into information of the  $X^{th}$  strip and the  $Y^{th}$  strip at the  $Z^{th}$  plane<sup>1</sup>. For the time information, a constant time resolution was applied on the time stamp obtained from GEANT4 and then stored along with the strip information. The detector was assumed to have a uniform efficiency of 95 % and applied as such during the digitization. Also, the implementation of strip multiplicity was uniform all over the RPC which is not in the real detector.

As observed in Chapter 2, in the actual detector, the time resolution of RPC is around 1 ns. This time resolution can be further split into correlated (common for both X- and Y- side) and uncorrelated (independent for X- and Y- side) time resolution. In the current study, the correlated time resolution of about 0.7 ns is applied to the time stamp and an independent uncorrelated time resolution of

---

<sup>1</sup>Pick up panels in top and bottom sides are aligned orthogonally and readout strips in top panel is defined here as Y-strips and bottom one is X-strips.

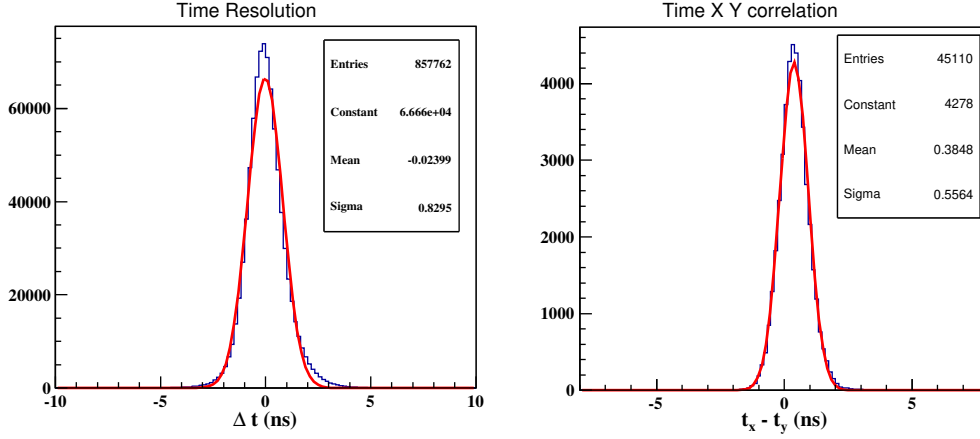


**Figure 3.5:** Correlated and uncorrelated time resolution.

about 0.7 ns is applied to get time  $t_x$  for  $x$  strip and  $t_y$  for  $y$  strip. Figure 3.5b shows the difference between the time measured using the strip on X and Y plane. When the difference in time measured through X plane and Y plane is taken, the uncertainties in time due to factors common for both planes cancel each other. So, only the uncertainties due to factors not common can be measured. This is calculated in Figure 3.5 (b). It is called uncorrelated time resolution and is defined as:

$$\sigma_{uncor} = \frac{\sigma_{t_x - t_y}}{\sqrt{2}} \quad (3.1)$$

$$\sigma_{corr} = \sqrt{\sigma_{measured}^2 - \sigma_{uncor}^2} \quad (3.2)$$

If the uncorrelated time resolution is quadratically subtracted from measured time resolution, the uncertainties in time due to factors common for both planes can be measured. It is called correlated time resolution. For the distributions in Figure 3.5, the uncorrelated time resolution is 0.4 ns and measured time resolution is 0.83 ns. So, the correlated time resolution is 0.73 ns. The propagation time of the signal in a strip will add a delay of around 5 ns/m. This delay depends on the X and Y position of the hit.

For the time recorded from the X- strip, the delay is computed from the corresponding Y- strip in the hit and applied. Similarly for the time recorded for the Y- strip, the corresponding X- strip in the hit is used to calculate the delay. In the end, the time is stored in a digitized format as it would be in the TDC, i.e. with the least count of 200 ps. The  $x$  and  $y$  strip information is stored independently in the precise way as the data will be stored in the detector.

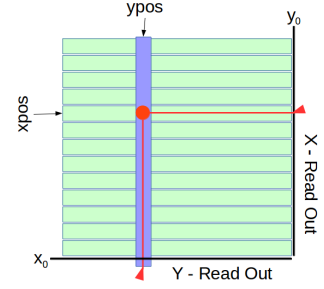


**Figure 3.6:** The signal propagation delay in the strip.

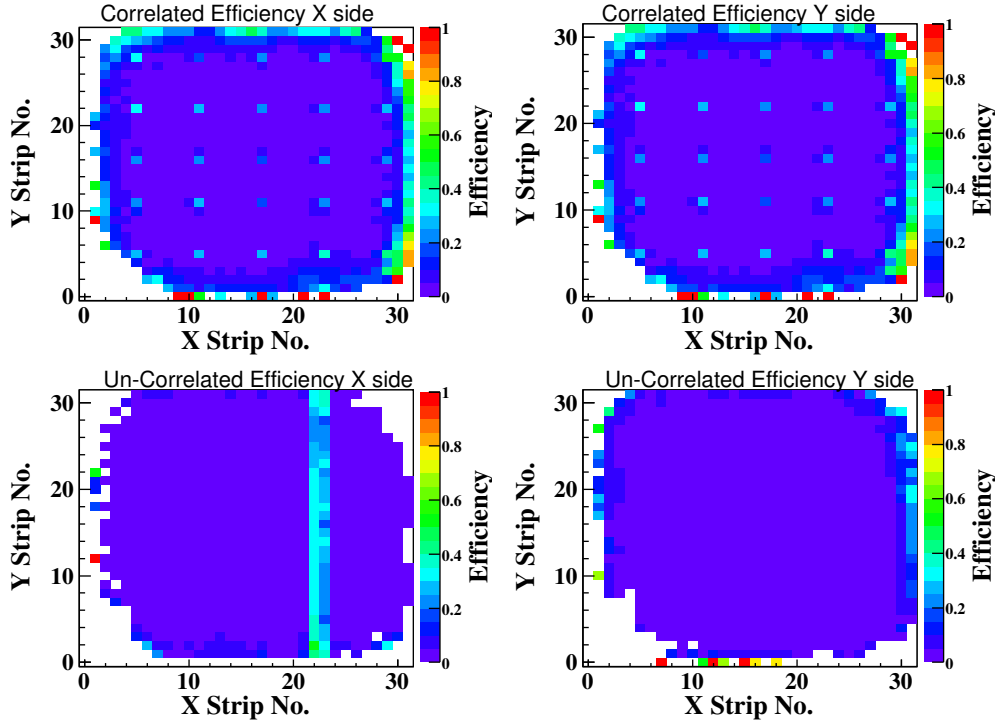


**Figure 3.7:** Correlated and uncorrelated inefficiency maps.

The inefficiency is caused by the trajectories of charged particles that didn't produce any avalanche signal larger than the discriminator threshold in the RPC. The efficiency maps for  $1 \times 1 m^2$  RPCs, were discussed in Section 2.4. In Figure 3.7, the efficiency maps for a typical layer are shown. Here, it can be observed that a part of the efficiency is contributed due to the electronics including the strips which will be different for X- and Y- sides. But a major component of the efficiency

which is due to variation in the thickness of glass electrodes or spacers is common to both sides. Using this observation, the efficiency was divided into correlated and uncorrelated components. The correlated component of the efficiency is applied to both X and Y signal for particular hit coming from GEANT4. The uncorrelated component of the efficiency is applied to X and Y signal independently. Once the ICAL detector is built, the future plan is to apply the observed efficiency map (Figure 3.7).

In the real detector, along with the hits due to the propagation of charged particles, a lot of hits will be recorded due to noise signals. There can be two kinds of noise: (i) uncorrelated and (ii) correlated noise. The first kind of noise is random in nature and can give hits in any region of the detector. The rate of random noise in a signal strip is measured to be  $\sim 200$  Hz. In ICAL detector there are approximate,  $4 \times 10^6$  electronic channels. The coincidence window for trigger generation is 100 ns. Hence, the total number of noise hits, in any event, can be estimated using the equation,

$$\text{No. of noise hits} = 4 \times 10^6 \times 200 \times 10^{-7} = 80 \quad (3.3)$$

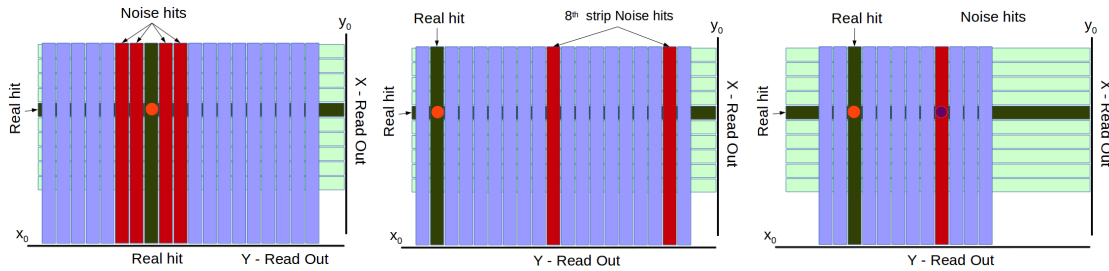


**Figure 3.8:** Different types of correlated noises.

Hence, we simulate around 100 noise spread uniformly throughout the ICAL detector. A timestamp is generated for the noise hits, which is digitized and saved. Currently, the probability of random noise in both strips is kept to be 50% and for in any one (either X- or Y-) strip is 25%. The correlated noise is the noise signals generated due to the signal in a particular strip. In the ICAL code, three such



kinds of correlated noise have been included and listed below:

1. Consecutive 5 strips get hit (Figure 3.8a).
2. Every 8<sup>th</sup> strip get hit (Figure 3.8b).
3. Correlated X & Y strip hit (Figure 3.8c).

These correlated noises occur only when there is a signal in that RPC. There can be other correlated noises that may need to be included in the future. In the first case, for signal in any strip, two strips on either side also give a signal. This type of signal is mostly due to streamer signals in RPCs, or when there is a large avalanche. The second type of noise is due to the electronic readout. As explained in Section 2.1, every 8<sup>th</sup> strip is OR'ed to get Level-0 trigger signals. This contributes to this kind of noise. The third kind of noise is observed, when a particular X or Y strip gives a signal, there is a signal observed in some other particular X or Y strip. At present, the probability of getting correlated for any hit is kept to be 10%. In the future, the noise simulation will be based on the noise observed during the testing of the RPCs. The observed noise will be used to simulate the noise in that particular RPC. A preliminary algorithm to simulate this noise has been implemented for the mini-ICAL detector simulation.

The spatial resolution in the horizontal plane is of the order 10 mm [2](due to the strip width and sharing of induced signal in multiple strips) while that in the z-direction is of the order of mm (due to the nonuniformity of passive material mainly iron support structure). The number of strips has induced signal above threshold due to the passage of a muon is called strip multiplicity. The multiplicity observed in the prototype RPC stack at TIFR, Mumbai is discussed in detail in Section 2.7. It is expected that if the location of avalanche is at the center of a strip, the induced signal in that strip is much larger than those on the neighboring strips. On the other hand, if the avalanche has occurred in the middle of two strips, both strips will share the induced signal. Noting that the pitch of pickup

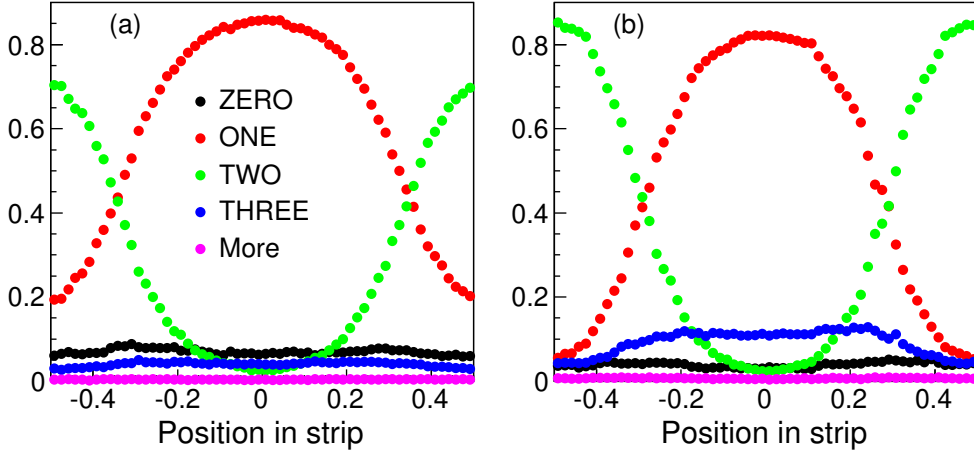


**Figure 3.9:** Strip multiplicity as a function of muon position in the strip, (a) X-plane and (b) Y-plane.

strips is 30 mm, with an inter-strip gap of 2 mm, it is expected that a much larger fraction of events will show up with a strip multiplicity of one. Figure 3.9 shows the normalized strip multiplicity as a function of muon position with respect to the center of the strip and in the unit of strip width. The data clearly support the simple idea of induced charge sharing between the neighboring strips. There are almost no events with strip multiplicity of two, with muon trajectory is at the center of the strip and similarly, there are almost no events with strip multiplicity one, with muon trajectory at the boundary of two strips. The strip multiplicity distribution observed in Figure 3.9, are fitted with Gaussian deconvoluted form of equation 3.4.

$$f(x) = Ae^{-\frac{1}{2}\left(\frac{x}{\sigma}\right)^2} \quad (3.4)$$

where  $x$  is the extrapolated position within the strip. Using these observations, the concept of strip multiplicity is implemented in the digitization part of the ICAL code. The X- and Y- position where the particle passed through inside the RPC, is translated to the position inside the strip width and based on the probability of one, two or even three-strip hit multiplicity is calculated. The “Zero” multiplicity is accommodated by the inefficiency factor.

During the reconstruction, in the first step all possible pairs of nearby X and Y strips in a plane are combined to form a cluster of hits. In a typical neutrino interaction, only an averaged information on the energy and direction of the hadrons is in principle possible to estimate. As in a single event, more than one hadrons can be produced, the response of the detector to all of them is overlapped. Muons, on the other hand, being minimum ionizing particles, leave long clean tracks. They can be easily recognised in the ICAL detector from all the other particles. The muon momentum can be determined from the curvature of its trajectory as it propagates in the magnetized detector, and also by measuring its path length. The nanosecond time resolution of the RPCs also allows the distinction between up-going and down-going muons <sup>2</sup>. The track is identified in the collection of hits by using a track finder package and the muon momentum is computed by a track fitting algorithm. This algorithm reconstructs both the momentum and charge of the muons. The track finder package and track fitter algorithm developed for track reconstruction are discussed in detail in [88, 97] and are summarized in the next sections of this chapter.

### 3.4 Track Reconstruction Algorithm

The muons being minimum ionizing particles, leave long clean tracks as shown in Figure 3.10, and hence are easy to identify in the ICAL detector. But in the collection of hits, the first step is to identify a track-like feature in the topology of the hits. This is achieved by a track finder package. In short, the track finder uses clusters, i.e., the combinations of all possible pairs of nearby X and Y hits in a Z-plane, as its basic elements. A set of clusters found in three out of five layers which satisfy a track-like criteria is combined and identified as a tracklet. The “track-like” criteria is basically a simple straight-line algorithm along some flexibility to include bending. The “three out of five plane” requirement allows for

some missing hits (due to inefficiency) in a given plane. For the ICAL detector, in a  $\nu_\mu$ -CC event, a single long track due to muons and a shower from hadrons near the vertex is usually observed. As muons leave only about one or two hits per layer they traverse ( $\sim 1.6$ – $2.1$  on average from Chapter 2) as opposed to hadrons that leave several hits per layer, the hadron showers are separated by using criteria on the average number of hits per layer in a given event.

The ends of overlapping tracklets are matched allowing for bending to form longer tracks, and the longest possible track is found [97] by iterations of this process. The track finder package thus forms muon tracks as an array of three-dimensional clusters. In the rare cases when there are two or more tracks, the longest track is identified as the muon track. The direction

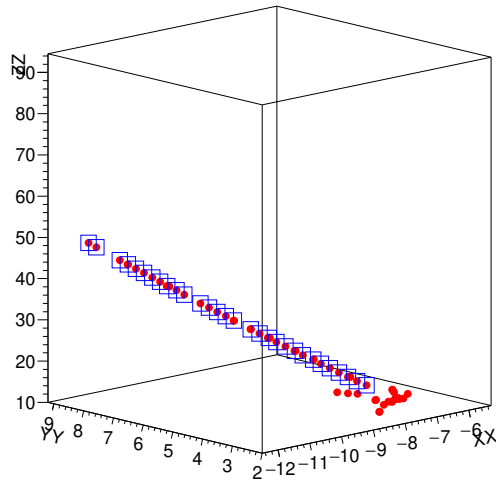


**Figure 3.10:** An example typical event in ICAL.

(up/down) of the track is calculated from the timing information which is averaged over the X and Y timing values in a plane. For muon tracks that have at least 5 hits in the event, the clusters in a layer yield an average hit position per layer with X, Y and timing information. These coordinates of the hits in the track, along with the direction calculated from timing information are sent to the track fitting algorithm for further analysis.

The track fitter which is a Kalman-filter based algorithm, is used to fit the tracks based on the bending of the tracks in the magnetic field. In this algorithm, every track is initiated by a state vector  $X_0 = (X, Y, dX/dZ, dY/dZ, q/p)$  which contains the position of the starting hit  $(X, Y, Z)$  as recorded by the finder, along with the charge-weighted inverse momentum  $q/p$  taken to be zero. As the tracks

don't show much bending near the vertex, the initial direction (the slopes  $dX/dZ$ ,  $dY/dZ$ ) is estimated from the first two layers. This initial state vector is then extrapolated to the next layer using an extrapolation algorithm which propagates the track using the state vector information, geometry information (materials the track crosses) and the local magnetic field inside the iron (from magnetic field map). The extrapolated state vector is filtered and the estimation is improved using a standard Kalman-filter based algorithm, which calculates the Kalman gain matrix.

In the existing algorithm, the state prediction is based upon equation of motion of a particle in a magnetic field. The Kalman filter algorithm and the corresponding error propagation is performed by a propagator matrix [97]. The Kalman filter takes into account the process noise due to multiple scattering as described in [98] and energy loss in the matter, mainly iron, according to the Bethe formula [99]. The extrapolated point is compared with the actual location of a hit in that layer if any, and the process is iterated.

The best fit for the track is also obtained from this iteration. After the complete iterations, the track is then extrapolated backward to another half-layer of iron (the neutrino interaction is most probable to take place inside the iron) to determine the vertex of the interaction and the best fit value of the momentum at the vertex. While  $q/p$  determines the magnitude of the momentum at the vertex and charge of muon, the direction is reconstructed using  $dX/dZ$  and  $dY/dZ$ , which yield the zenith and the azimuthal angles, i.e.,  $\theta$  and  $\phi$  respectively.

### 3.5 Fiducial volume and identification of events in fiducial volume

For a “fully” contained event, the momentum measurement from the range of muon inside the detector gives a better estimate than the one measured using the curvature. The simple assumption for an FC event is that the vertex and endpoints of

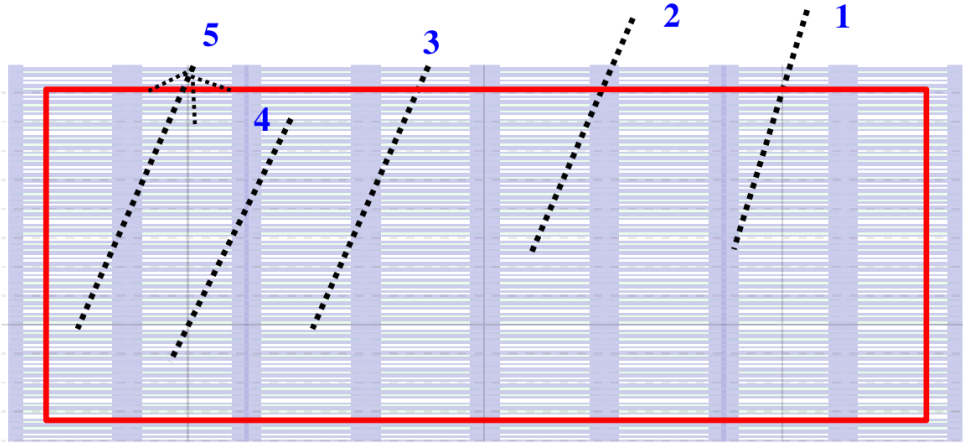


**Figure 3.11:** Fiducial volume for ICAL detector.

the trajectory are inside the fiducial volume. Also, the Fiducial Volume is needed to distinguish events produced in the rock from the events produced inside the ICAL detector. The fiducial volume for ICAL detector is taken by excluding 2 RPC layers from top and bottom and 3 strips on either side of X and Y direction. To check the validity of these criteria, single  $\mu^-$  events are generated in simulation. In the generated dataset, there are two types of events, (i) Generated within Fiducial volume(FGEN) and (ii) Generated outside of Fiducial volume(OGEN). After reconstruction, extrapolation is needed to analysis the reconstructed position of the vertex of the tracks to check whether it is within the fiducial volume or not. The events are observed in the following criteria:

- FF – Generated fiducial and reconstructed fiducial –  $0.975 \pm 0.001$ .
- FO – Generated fiducial and reconstructed outside –  $0.025 \pm 0.001$ .
- OF – Generated outside and reconstructed fiducial –  $0.035 \pm 0.001$ .
- OO – Generated outside and reconstructed outside –  $0.964 \pm 0.001$ .

Now, the number of FO and OF combinations is quite small which implies the reconstruction is quite accurate. But, it is not as simple as it is assumed. In

Figure 3.11, a few types of possible events, which can be observed in the ICAL detector, are depicted. The *event 1* is clearly coming from the outside and the criteria mention above will clearly tag this as coming from outside the Fiducial volume. The *event 2* is also coming from outside, but as the first hit is well within the detector volume, it will be tagged as the event inside the Fiducial volume. The *event 3* appears similar to *event 1*. The *event 4* will be tagged as well within the Fiducial volume. The *event 5* starts from the 1<sup>st</sup> layer of ICAL, but along with hadron shower. In principle, this event should be considered within the Fiducial volume but just applying the criteria will not permit it. Looking at these events, it is clear that the simple criterion of excluding some fixed number of strips and layers from the boundaries of the ICAL detector is insufficient to tag an event as inside fiducial volume or not.

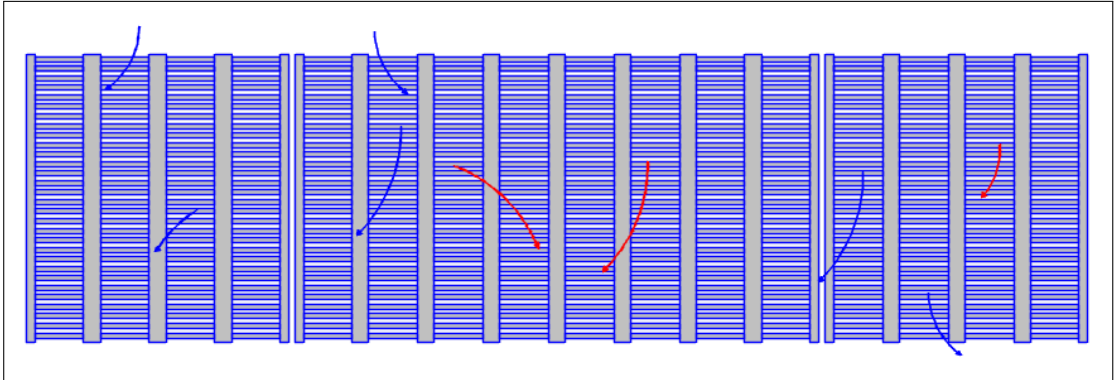


**Figure 3.12:** Various possible “fully” and “partially” contained events in ICAL.

The algorithm presented here can only be applied to muon tracks. Figure 3.12 presents some examples of fully and partially contained muon tracks possible in the ICAL detector. In the algorithm, the track is extrapolated back to two layers in the backward direction from the vertex and in the forward direction from the endpoint. If the extrapolated points from one of the ends of the track are in the dead region of the detector, then it is tagged as *Partially Contained(PC)* track. If the extrapolated points are in the sensitive region RPC i.e. the gas volume, then it is tagged as a *FC* track. In Figure 3.12 the red track is only fully contained,

the remaining others are all partially contained. For FC tracks, the range of the muons is calculated easily as the vertex and endpoint are within the sensitive region of the RPC. Using the range of muons to estimate the momentum will provide a better estimate than the curvature in the magnetic field. For the current analysis, the description of simulation and the conditions on event selection and cuts are discussed in the following section.

A typical CC-RS or CC-DIS event is shown in Figure 3.10. Here in the vicinity of the vertex, there is a hadron shower overlapping the muon track. An example of such an event is shown in Figure 3.13 where the *green* colored hits in the figure are from muon and fitted as a track by track fitting algorithm. The remaining hits are due to signal from the passage of both muons and hadrons. The track fitting algorithm can reconstruct the track up to the hadron shower layers. Beyond that, it cannot fit the track.

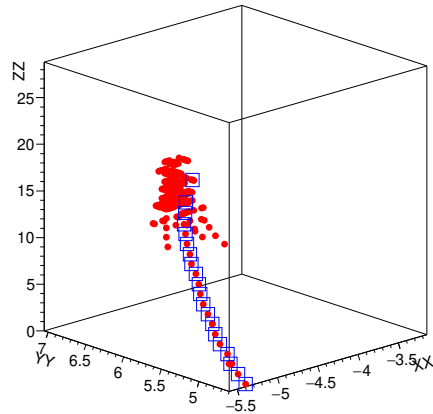


**Figure 3.13:** Muon track in hadron shower.

To reach the vertex, the track is extrapolated up to the end of the shower planes. During the extrapolation, for any layer, if a hit is found to be within two strip distance of the extrapolated position, it is tagged as a track (*blue* colored) hit and the track is extended. For two consecutive layers, if no hit is found, the extrapolation is stopped.



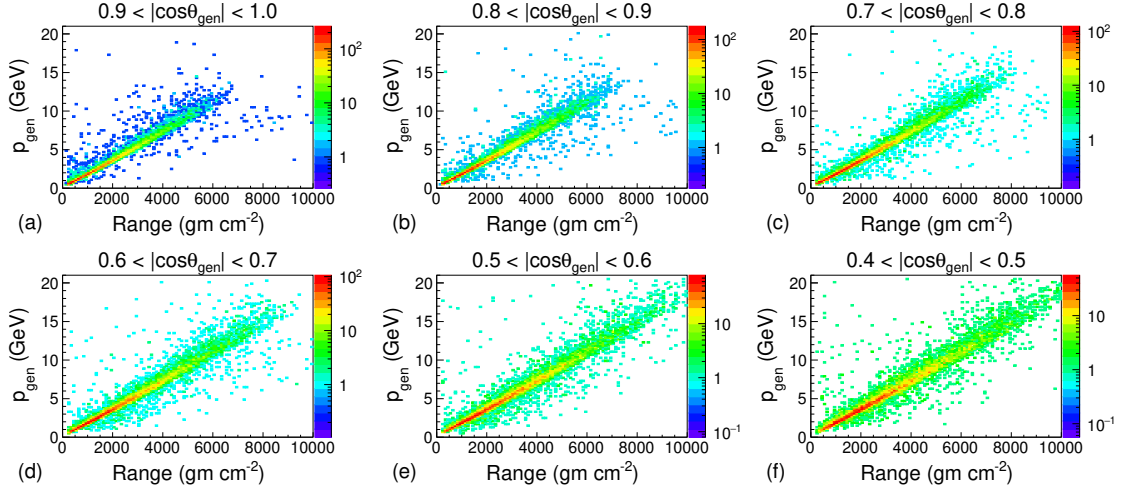


**Figure 3.14:** Scatter plots of muon momentum with range of muons in the detector for different  $\cos\theta_{gen}$ .

## 3.6 Calibration and Analysis of Fully Contained Tracks

In this study, one million muon events are simulated in the ICAL detector. The vertices of these events are uniformly spread over the entire volume of the detector. The events were generated in the momentum range from 0.5 to 20.5 GeV and their momentum direction were smeared uniformly in polar ( $\cos\theta_{gen}$ ) and azimuthal ( $\phi$ ) angle. In the calibration and analysis, only the events with one reconstructed track having a minimum of five layers in the track fit are selected. The events are segregated in different  $|\cos\theta_{gen}|$  bins for calibration and analysis.

To obtain the calibration relation of momentum as a function of the length of the track, the first step is getting the scatter plot of the true momentum of muons vs the density-weighted pathlength of fitted tracks in the detector for selected events. In Figure 3.15(a), for the events with all  $|\cos\theta_{gen}|$  bins and in Figure 3.14(a) to (f), the scatter plot is presented for different  $|\cos\theta_{gen}|$  bins. As for events with  $|\cos\theta_{gen}| < 0.327$ , the reconstruction efficiency is low, these events are not considered in this analysis.

To observe the calibration curve, the profile histogramme of the scattered plot is constructed as shown in Figure 3.15(b). In this study, for each  $|\cos\theta_{gen}|$  bin, a different cali-

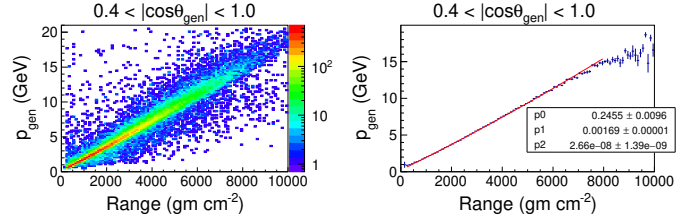


**Figure 3.15:** (a) Scatter plot and (b) calibration for muon momentum with range of muons for all  $\cos\theta_{gen}$ .

bration is obtained (Figure 3.16(a) to (f)) as well as for the events will all  $|\cos\theta_{gen}|$  bins to observe if there is any bias in the calibration due to the zenith angle. These plots show the correlation between muon momentum and density-weighted range. They are fitted by second-order polynomial functions.

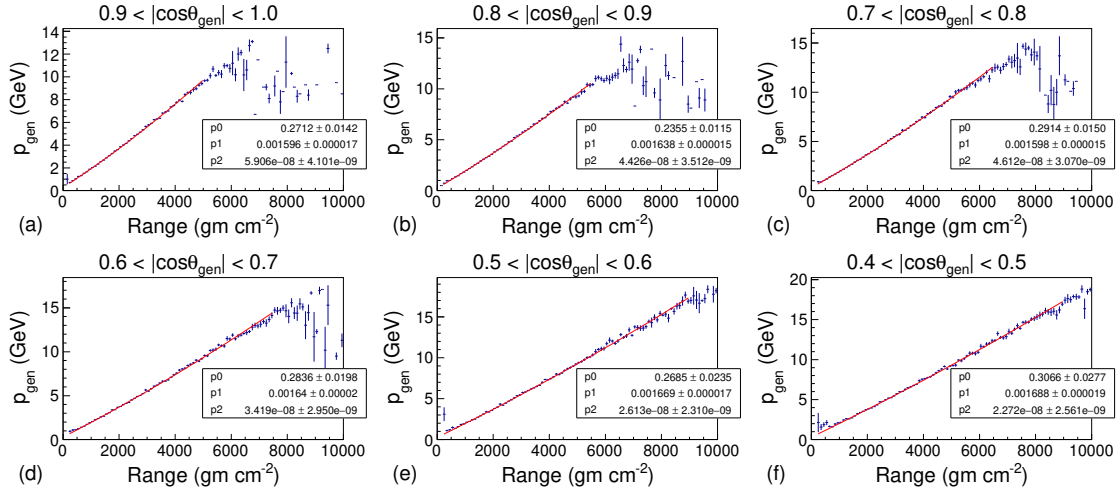


**Figure 3.16:** Calibration plots of muon momentum with range of muons in the detector.

From the range information obtained from fitted tracks and the polynomial functions obtained in the previous step, the muon momentum is reconstructed for each event for two different calibrations ( $\cos\theta_{gen}$  dependent and all events). The distribution of  $\frac{p_{reco} - p_{gen}}{p_{gen}}$  is plotted for different ranges of  $p_{gen}$  and fitted by Gaussian function as shown in Figure 3.17. The sigma ( $\sigma$ ) of the fitted Gaussian function is treated as the resolution for the mean muon momentum of the particular momentum range. In Figure 3.17, the  $\frac{p_{reco} - p_{gen}}{p_{gen}}$  distribution are for three different  $(p_{gen}, \cos\theta_{gen})$  bins, for three different methods of estimating the momentum is

presented. For the plots, in Figure 3.17(a), (d) and (g), the momentum is estimated from the curvature fit. Figure 3.17(b), (e) and (h) is for momentum estimated using range calibration in different  $|\cos\theta_{gen}|$  bins. And Figure 3.17(c), (f) and (i) refers to momentum computed using range calibration of muon tracks with all  $|\cos\theta_{gen}|$  bins.

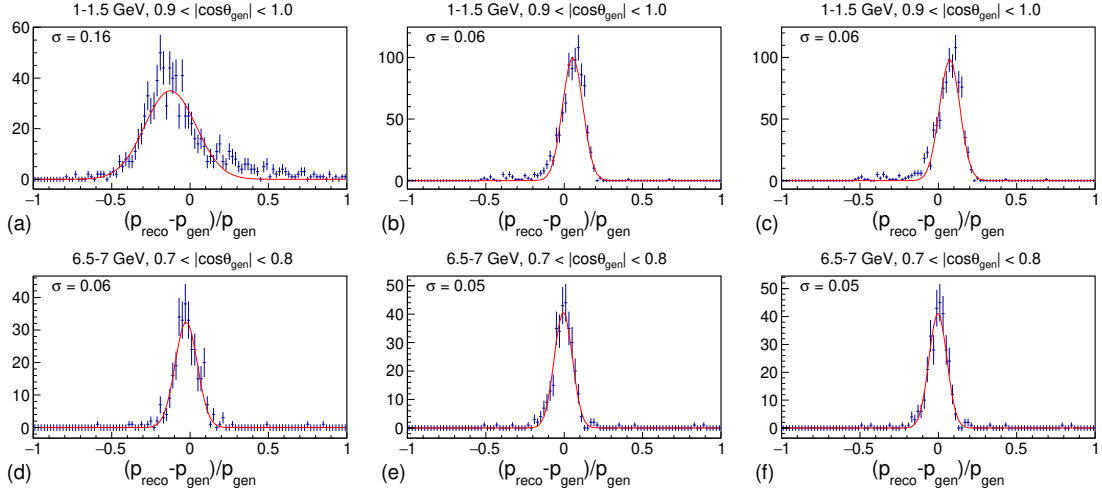


**Figure 3.17:** Resolution plots for FC events. (a) and (d) for momentum estimated from curvature fit. (b) and (e) for momentum calculated from calibration for corresponding  $\cos\theta_{gen}$  bins (Figure 3.16). (c) and (f) for momentum calculated from combined calibration from Figure 3.15.

In Figure 3.18, resolution is plotted as function of momentum for different  $|\cos\theta_{gen}|$  bins. The black points in the plot represent a resolution for momentum reconstructed using curvature fit. The red and blue points in the plot are for momentum computed using the calibration described here for fully contained events. The small difference between Criteria 2 and 3 means that the impact of the more precise calibration using individual  $\cos\theta_{gen}$  bins is quite small. Also, at lower momentum, the resolution is poorer because of multiple scattering. It is clearly observed that for fully contained events momentum reconstructed using the range of muons through the detector gives a better estimate than the curvature fit for a large range of momentum. But out of total reconstructed tracks only  $\times 10\%$  are fully contained. So, the overall impact is small. There is a need to improve the algorithm to identify more “Fully Contained” events for better performance of the

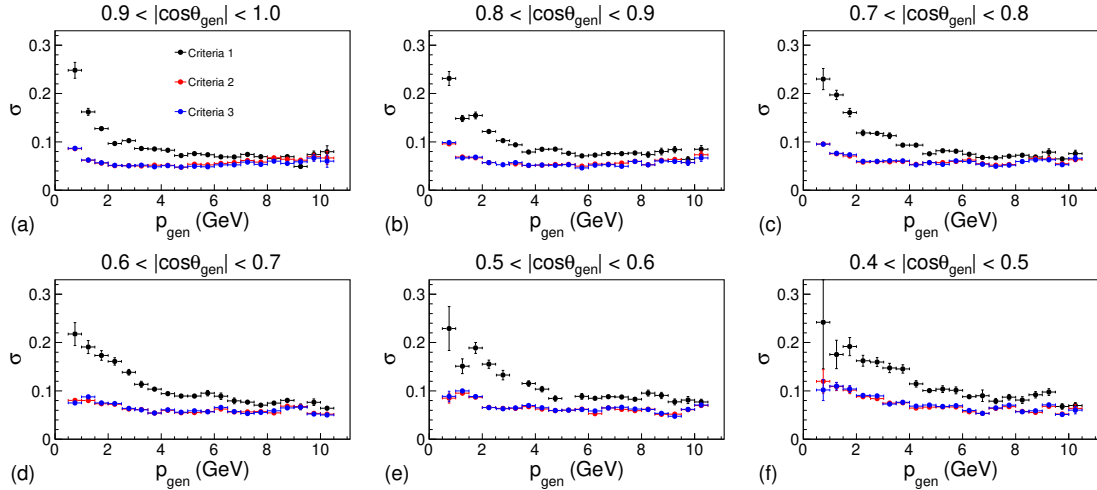


**Figure 3.18:** Momentum resolution as a function of momentum for fully contained muon tracks. Criteria 1 is for momentum estimated using curvature fit. Criteria 2 is for momentum estimated using range calibration in different  $|\cos\theta_{gen}|$  bins. Criteria 3 refers to momentum computed using range calibration of muon tracks with all  $|\cos\theta_{gen}|$  bins.

INO experiment.

### 3.7 Summary

In this chapter, the ICAL detector simulation framework is discussed. The RPC geometry is modified in the simulation according to the latest detector design. The database for the distribution of various detector parameters and several other properties for the ICAL simulation has been set up. An INO specific digitization algorithm is implemented for including detector properties like detector inefficiencies, strip multiplicities, time resolution, detector noise, etc to make the simulation more realistic. The muon reconstruction algorithm is described briefly. The fiducial volume for the ICAL detector is discussed. An algorithm, to tag “fully contained” muon tracks, is described. A method of calibration, to estimate momentum from the pathlength of the track for fully contained muon trajectories is described. For the fully contained charged particle, there is a substantial improvement of momentum resolution from the measurement of pathlength in comparison with the result

from the Kalman filter technique and the ICAL experiment will use the pathlength technique for the fully contained events.



# Chapter 4

## Hadron reconstruction in ICAL

The reach of the ICAL detector for studying various physics goals using atmospheric neutrinos using the information of muon energy and direction has been presented in [1, 100, 101]. The ICAL detector is sensitive to hadrons over a wide energy range. The reconstruction of the energy of the incoming muon neutrino in a CC-event is possible by combining the energies of the muon and the hadrons. It also enables the ICAL detector to neutral-current events, CC-DIS events generated by  $\nu_e$  interactions, and CC- $\nu_\tau$  events where the  $\tau$  decays hadronically. The information obtained from all these events adds crucially to our knowledge of neutrino oscillations. The CC-events helps in the direct measurement of the oscillation probabilities where as, the NC events which are not affected by active neutrino oscillations, help in flux normalization, as well as in the search for oscillations to sterile neutrinos [102]. Also, it has been observed that by combining the muon and hadron information the sensitivity to neutrino parameters at INO is enhanced [87, 103]. Also, the contribution of the  $\nu_e$ -CC events in determining the neutrino mass hierarchy in ICAL detector has been studied [104, 105]. It is therefore important to characterize the response of the ICAL to hadrons.

In the previous study [6], the detector response to hadrons propagating through it is investigated using the hadron hit multiplicity in the RPC. They first studied

the detector response to charged pions of fixed energy, followed by the average response to the hadrons produced in atmospheric neutrino interactions using events simulated with the NUANCE event generator [89, 90]. In [75], the hadron energy resolution was studied as the function of the thickness of the iron plates. In these studies, however, no clustering algorithm was implemented and all the hits are used for calibration. During the detector operations, along with hits from muons and hadrons, hits due to noise signals will also be present in the data which was ignored in those studies. Hence, the approach discussed in [6] cannot be directly applied to reconstruct hadron energy. The algorithm to remove hits belonging to the muon track from the hadron shower has been discussed in the previous chapter (refer Section 3.5).

In the present study, the first step is to develop a clustering algorithm to identify all the hits due to hadron shower (after identifying all the hits of muon track during track fitting) which is explained in Section 4.1. A muon usually leaves one or two hits per layer and so the hits from both X and Y strips can easily be combined to obtain the number of hits and their position coordinates  $(x, y)$  in a given layer. However a hadron shower consists of multiple hits per layer and combining all possible X and

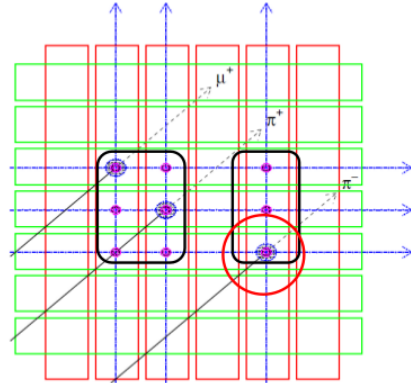


**Figure 4.1:** Ghost hits in RPC.

Y strip hits leads to overcounting, resulting in what is termed as *ghost hits* (Figure 4.1). Hence, an algorithm is required to remove these ghost hits. In this study, an attempt has been made to develop one such algorithm which will be discussed in Section 4.2. Using the strip distributions for different energies, a correlation between the mean number of strips and energy of the hadron is observed which is used as calibration to reconstruct the hadron energy. The hadron energy res-



olution obtained using this calibration technique is presented in Section 4.3. In this study, the effect of noise hits on the hadron energy resolution has also been discussed in the same section. The technique to reconstruct the direction of the hadron shower has been established and its results are presented in Section 4.4. Finally, the chapter is summarised in Section 4.5.

## 4.1 Reconstruction of hadronic shower using cluster algorithm

The reconstruction of the hadron shower is required for two different cases listed below and shown in Figure 4.2.

- Type 1 : Event having good reconstructed track
- Type 2 : Event having no reconstructed track

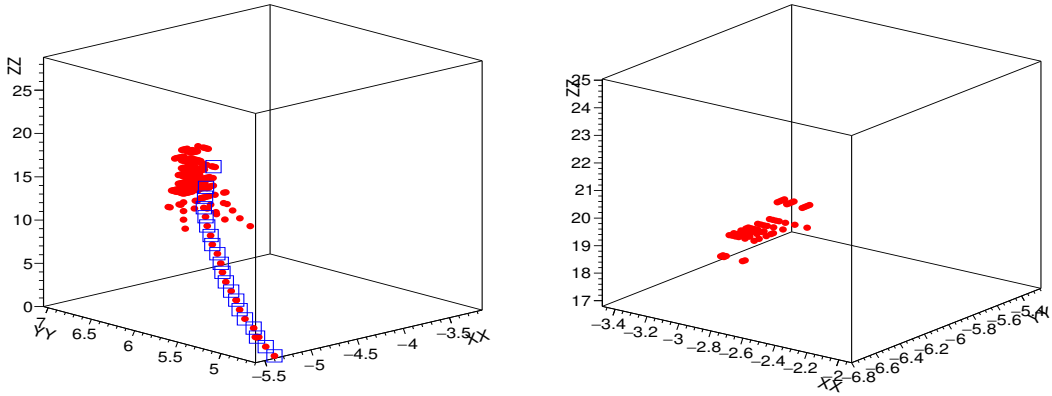


**Figure 4.2:** Two types of hadron events in ICAL.

For INO, the "Type-1" event consists of  $\nu_\mu$  CC-DIS and CC-RS interactions when there are a clean muon track and hadron shower near the vertex. The "Type-2 event" consists of all the remaining neutrino events, ie. all NC events,  $\nu_e$ -CC events and most of the  $\nu_\tau$ -CC events interactions. The algorithms described in this study can easily be applied to the "Type-2" event.

As shown in Figure 4.3 when there is a good reconstructed track, a trapezoidal region is formed around the vertex of the track, having one plane in the backward direction and five planes in the forward direction with a base of the trapezoid of length 10 cm. All the hits within the trapezoidal region, which are not associated with the track, are chosen as hits from hadron shower. By this procedure, the noise hits which are far from the actual hits due to hadron shower in the data are rejected.

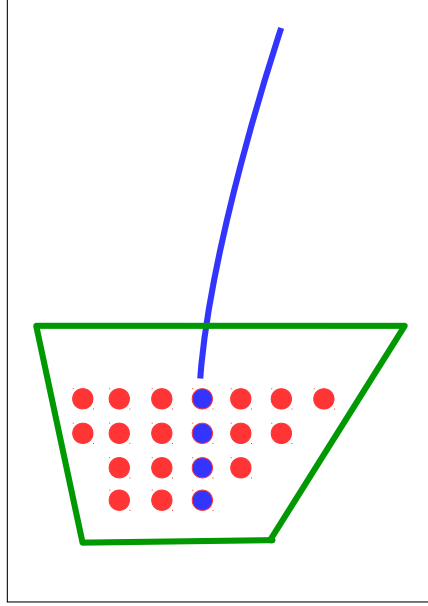


**Figure 4.3:** Schematic diagram of trapezoid clustering for Type-I event with the reconstructed track and hits associated with the track shown in *blue* colour.

For an event in which there is no good reconstructed track (i.e type II event), a clustering algorithm is applied to collect all the nearby hits to make clusters of hits and find the cluster that is formed in ICAL detector due to hadron shower. In this algorithm, a unit ellipsoidal region is formed around a hit. The major axis of this unit ellipsoid corresponds to the number of z-layer whereas the minor axis corresponds to x- or y-strip number. The semi-major/minor axes of the ellipsoid for the cluster is supplied to the algorithm in terms of  $N_X$  strips,  $N_Y$  strips and  $N_Z$  layers (referred in this paper as  $(N_X, N_Y, N_Z)$ ). Hence, if the cluster dimension is  $(3, 3, 4)$ , it means the cluster size semi-axes are of dimension 3 strip width in the X-dimension, 3 strip width in the Y-dimension and 4 layers in the Z-dimension. This formation of ellipsoid proceeds successively with new hits appeared in the previously formed ellipsoid and continued until all the hits in an event have been verified. In the ICAL experiment, the neutrino interaction rate is very small. Thus in an event, it is not expected to have two independent interaction. Thus it is expected to have only one cluster in an event. But there is a possibility that an event has more than one cluster. In

such a case among all of the clusters, the cluster containing the largest number of hits is chosen as the cluster formed in the ICAL detector due to hadron shower.

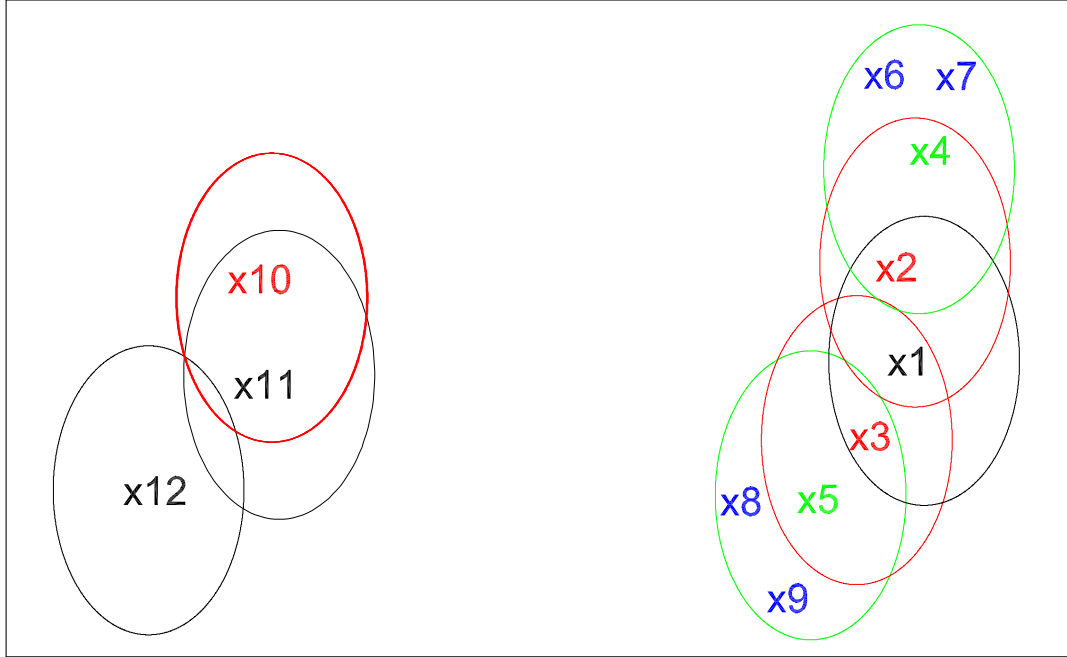


**Figure 4.4:** Schematic diagram of cluster algorithm. In the diagram there are three clusters containing nine, two and one hits. The cluster containing nine hits is considered as the cluster due to hadron shower.

It is to be noted that in Figure 4.4, there are three clusters irrespective of the choice of the starting hit. From Figure 4.4, it is also observed that the unit cluster around hit  $X_{12}$  does not contain any new hit, thus this is the smallest cluster having only one hit. Whereas the unit cluster surrounding the hit  $X_{11}$  contains hit  $X_{10}$  as well, so this creates the cluster having two hits. For the largest cluster, a unit ellipsoid around  $X_1$  contains hits  $X_2$  and  $X_3$ . In the next step, a unit ellipsoid around the hit  $X_2$  includes  $X_1$  as well as  $X_4$ . Similarly, for hit  $X_3$ , it includes the hit  $X_1$  and  $X_5$ . Hence, now hits  $X_4$  and  $X_5$  are also taken into the cluster associated with the hit  $X_1$ . Similarly, a unit ellipsoid surrounding the  $X_4$  includes hits  $X_2$ ,  $X_6$  and  $X_7$ . Also, a unit ellipsoid around  $X_5$  includes hits  $X_3$ ,  $X_8$  and  $X_9$ . Hence all these hits are also associated with cluster surrounding the hit  $X_1$ . Thus the final clusters around these all hits contain nine, two and one hits respectively. As a result, the cluster around hit  $X_1$  is the largest one and

chosen as the cluster formed due to hadron shower. For the largest cluster, it can be observed that the composition of the cluster doesn't change, even if the starting point is other than hit  $X1$ .

## 4.2 Algorithm to remove ghost hits

The ghost hit removal (GHR) algorithm is applied to the hits obtained from the largest cluster of the clustering algorithm. At the beginning of this algorithm, layers having only one hit are identified. These hits are considered as a 'true' hit from hadron shower. When there is no noise during the experiment, this type of hits should not be a 'ghost' hit. In contrast, practically there will be noise during the experiment and there is a probability that such hits are generated actually due to noise event. But this possibility has been ignored in the present algorithm. Starting from those single 'true' hit in a layer, the nearest hits in the successive upper and lower layers are identified in the next step of the algorithm. For this purpose, the difference between x- and y- strip's numbers of a true hit in a layer and each hit in one layer above and below are calculated and these two differences (difference in x-strip numbers and y-strip numbers) are added for each hit. Among all of the hits in a layer, the hit having with the smallest sum of the differences is chosen as 'true' hit that is formed due to hadron shower in that layer. A hit in a layer is identified as a 'ghost' hit if its x and y-strip numbers correspond to more than one hit of that RPC and x- or y-strip number is the same as that of 'true' hit of the same layer. This process of identifying 'true' hit and 'ghost' hit will be continued until all layers are verified. The addition of all hits, except 'ghost' hits, is considered as the total number of hits due to hadron shower.

In Figure 4.5, layer 2 has only one hit named 'E' having x and y -strip numbers 5 and 3 respectively. So, starting from this hit the nearest hits are found in layers 1 and 3. In layer 1, among four hits, the hit named 'B' having x and y-strip numbers

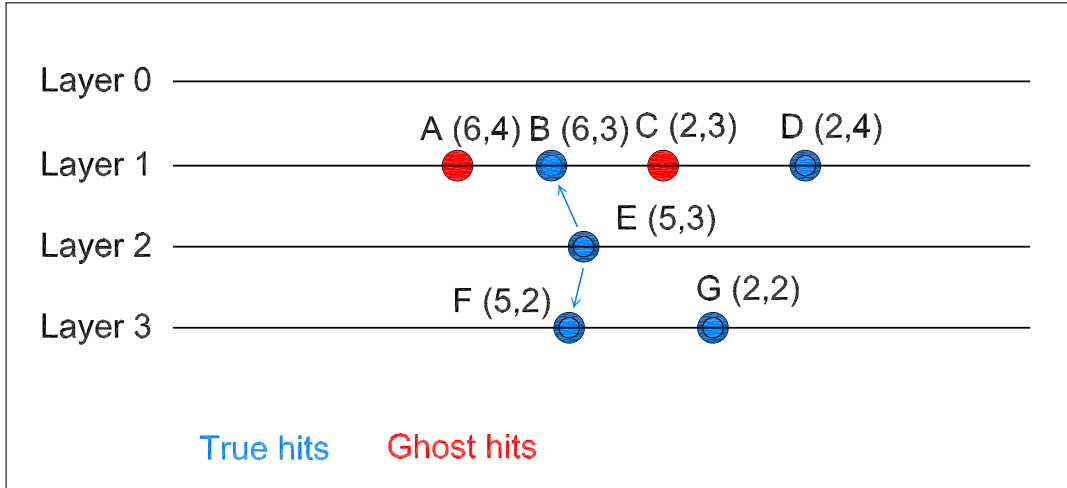


**Figure 4.5:** Schematic diagram of ghost hit removal algorithm.

6 and 3 respectively is the nearest one. It can be observed that in layer 1, there is another hit (D) which have x and y-strip number 2 and 4 respectively. Thus the two hits named ‘A’ and ‘C’ of layer 1 are the ‘ghost’ hits of that layer because their strip numbers could be generated due to a combination of the strip numbers of hit ‘D’ and true hit ‘B’ of that layer. The hit ‘D’ is considered as a hit from hadron shower. In layer 3, the nearest hit combination is (5,2), hit obtained with x and y strip combination (2, 2) cannot be ghost hit because there is only one hit having x-strip number 2. Thus in Figure 4.5, out of seven hits, five hits are considered in the measurement of the hadronic shower.

### 4.3 Analysis of hadron events and results

The clustering algorithm is tested here with single  $\pi^+$  generated in the GEANT4 detector simulation. In the work [6], the energy resolution is obtained directly from the strip distribution of each fixed energy. In that method, the strip finding algorithm was directly applied to all the obtained hits in the detector. The distribution of the number of strips for fixed pion energy was obtained as shown in Figure 4.6. It was observed that the position of the peak of this distribution moves towards the higher value with an increase in the pion energy. It was further observed that the

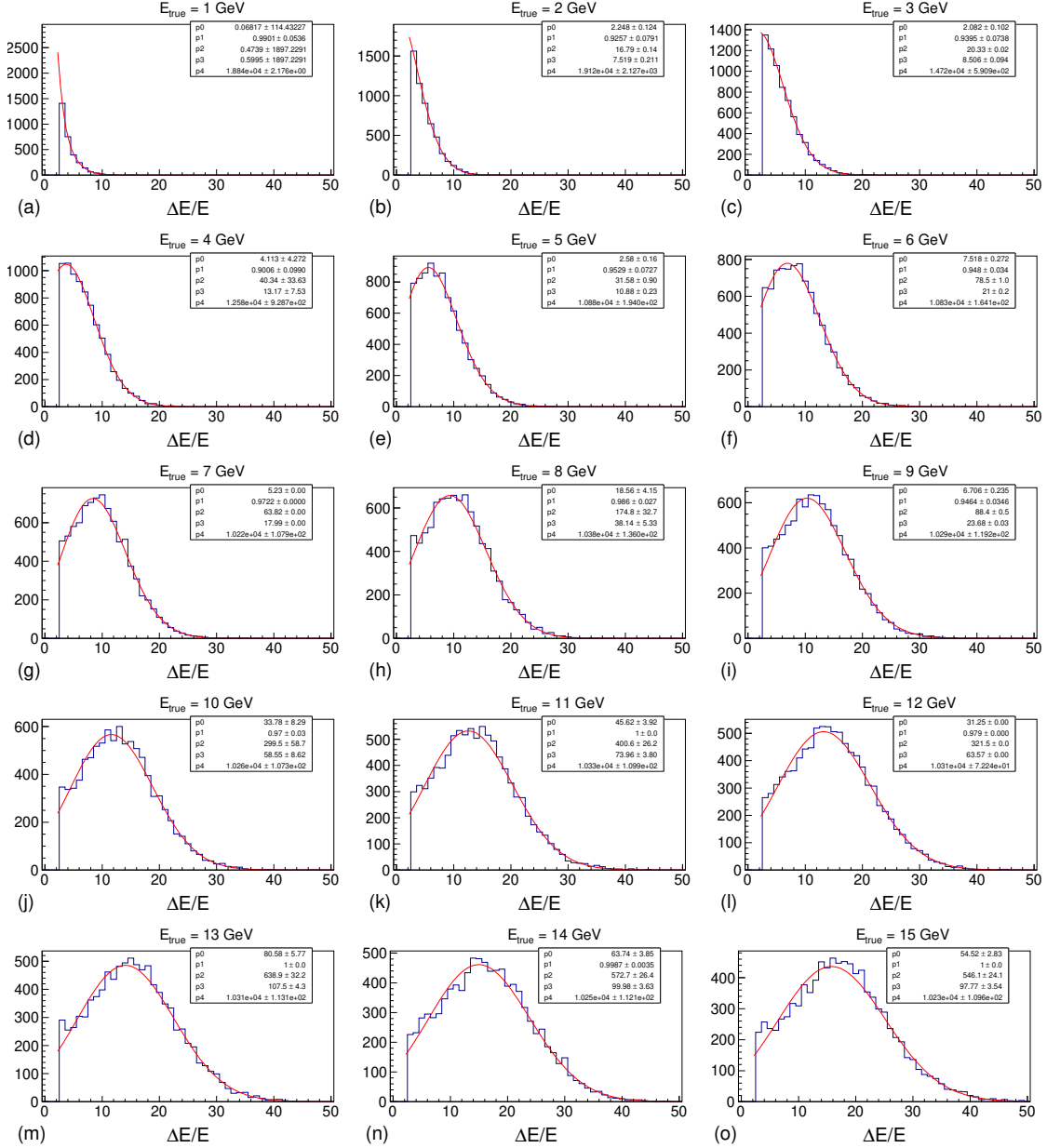


**Figure 4.6:** Strip distributions for all hadron energies.

distribution was asymmetric along with a long tail on the positive side. Hence, this distribution was fitted with modified Vavilov distribution (given in Appendix A). The energy resolution of the hadron was calculated from the following expression;

$$\frac{\sigma}{E} = \frac{\Delta n(E)}{n(E)} \quad (4.1)$$

where,  $(\Delta n)^2$  and  $n(E)$  are variance and mean of the Vavilov distribution

respectively. From the distributions, in Figure 4.6, the energy resolution of the hadron has been obtained and compared with the results from Devi et.al in Table 4.2 (Case V). The results show that there is a significant worsening of the energy resolution when compared to the previous work. To understand this, a systematic study of the energy resolution was conducted looking at the different differences between in the ICAL detector simulation software versions. The several cases which were studied for this are listed in Table 4.1 and it clearly indicates that the current result is consistent with the earlier result but due to change in strip width and detector size at the present the resolution is worse.

Case	RPC size ( $cm^2$ )	Strip width ( $cm$ )	Inefficiency	Algorithm
I	$192 \times 192$	1.96	No	Strip finding
II	$192 \times 192$	1.96	No	Clustering + Strip finding
III	$174 \times 183.5$	1.96	Yes	Only Strip finding
IV	$174 \times 183.5$	3.0	Yes	Only Strip finding
V	$174 \times 183.5$	3.0	Yes	Clustering + Strip finding

**Table 4.1:** Different cases with single  $\pi^+$  distribution over the central region of the ICAL detector.

$E_{had}$ (GeV)	$\sigma/E$					
	Ref. [6]	Case I	Case II	Case III	Case IV	Case V
1	0.907	0.747	0.779	0.876	0.868	0.916
2	0.671	0.595	0.649	0.714	0.712	0.764
3	0.571	0.529	0.592	0.622	0.628	0.682
4	0.514	0.482	0.543	0.588	0.574	0.650
5	0.479	0.453	0.510	0.546	0.538	0.612
6	0.449	0.434	0.482	0.517	0.519	0.582
7	0.429	0.430	0.481	0.497	0.503	0.565
8	0.413	0.412	0.460	0.486	0.481	0.557
9	0.401	0.392	0.454	0.477	0.474	0.542
10	0.390	0.398	0.453	0.471	0.463	0.528

**Table 4.2:** Energy resolution of the hadron in ICAL detector.

During the actual experiment, only the hit information is available for analysis, not the total energy. Therefore, this procedure cannot be applied to reconstruct the hadron energy from the experimental result. Hence, the basic aim of this work is to obtain a relation between the true energy  $E_{gen}$  vs the number of strips and

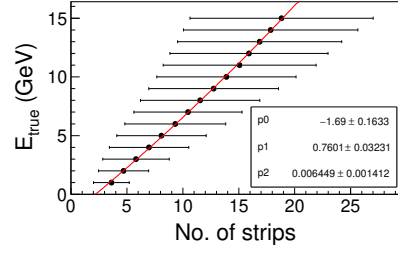


**Figure 4.7:** Calibration plot for hadron energy.

apply it on simulated hadron events having energy distribution to reconstruct the energy of hadron,  $E_{reco}$ . The resolution of hadron energy is obtained from the distribution of  $(E_{reco} - E_{gen}) / E_{gen}$ .

In the current study, single  $\pi^+$  having uniform energy distribution from (0-20) GeV has been generated using GEANT4 particle gun. These are distributed over  $(\pm 24m, \pm 8m, \pm 7.25m)$  the entire region of the ICAL detector. The direction of  $\pi^+$  is uniformly smeared over zenith angle  $0 \leq \theta \leq \pi$  and azimuthal angle  $-\pi \leq \phi \leq \pi$ . The random noise hits were simulated in the detector region near the vertex of the pion shower. Also, inefficiency was introduced in the detector simulation while generating the dataset for this analysis. It must be noted that in the current study, the events having signals in more than one layer are only considered for the analysis. The following steps are performed to get the resolution of the reconstructed energy of hadron:

1. Distribution of strip for fixed hadron, energy,  $E_{gen}$  is fitted by Vavilov distribution (as shown in Figure 4.6).
2.  $E_{gen}$  is plotted as a function of the number of strips, which is the mean of the Vavilov distribution fitted to strip distribution in the previous step. This plot is fitted by second-order polynomial function (as shown in Figure 4.7).
3. From the strip information obtained from MC event or experimental data and with the help of the polynomial function obtained in the previous step,



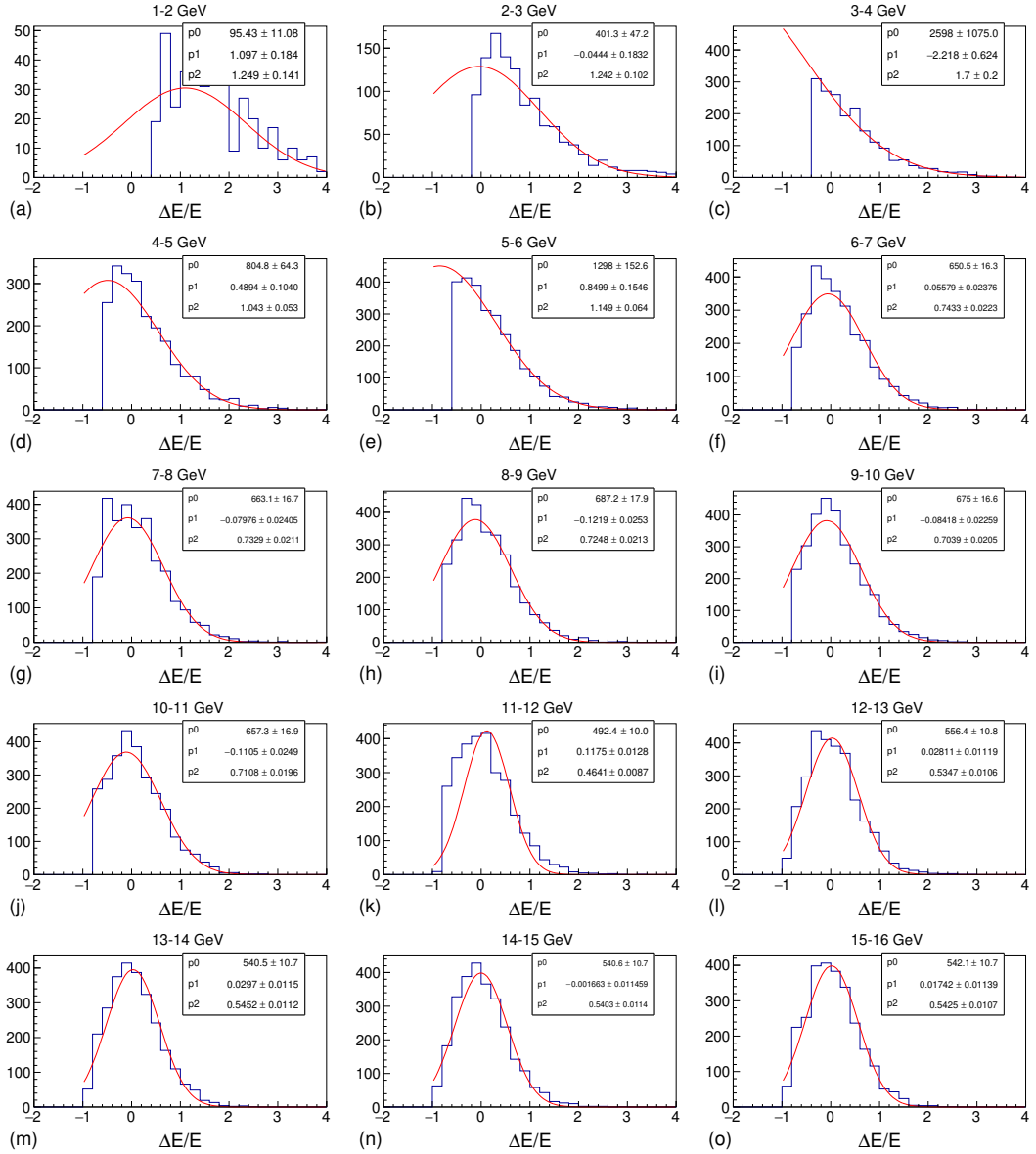


**Figure 4.8:** Resolution Distributions for all the energies 1–15 GeV.

the hadron energy is reconstructed.

4. Distribution of  $(E_{reco} - E_{gen})/E_{gen}$  is plotted for different ranges of  $E_{gen}$  and fitted by Gaussian distribution (as shown in Figure 4.8).
5. The variance of the fitted Gaussian function calculated using numerical integration is used for  $\frac{\sigma}{E}$  of the particular  $E_{gen}$  range.

The resolution also depends on the dimension of the ellipsoid chosen as well as its efficiency to reject noise hits. This study is presented in the next section.

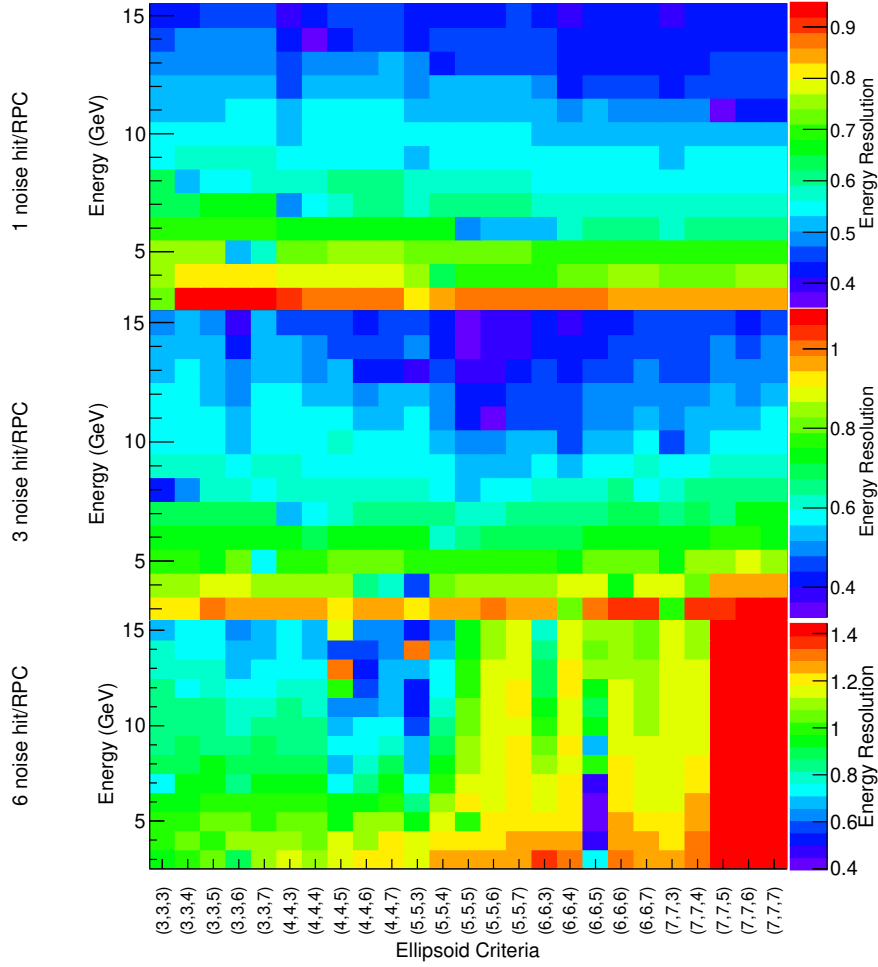


**Figure 4.9:** Energy resolution of hadrons for different noise rates. The energy resolution is estimated using various ellipsoid dimensions, to select the best possible ellipsoid dimension for particular noise rate.

The dimension of the ellipsoid for the cluster is supplied to the algorithm in terms of  $N_X$  strips,  $N_Y$  strips and  $N_Z$  layers. The effect of noise hits on these various ellipsoid dimensions is also studied in the current analysis. The study has been performed using various ellipsoid dimensions listed on the X-axis of Figure 4.9 and for different noise density. The noise density included are 1, 3 and 6 noise hits per RPC and the noise is considered only in the 10 layers around the vertex in the direction of hadron. The resolutions observed are presented in Figure 4.9. It is clearly observed that  $(5, 5, 5)$  option shows the best possible resolution for a noise density of 3 hits/RPC. The reason for some island is due to the imperfect shape

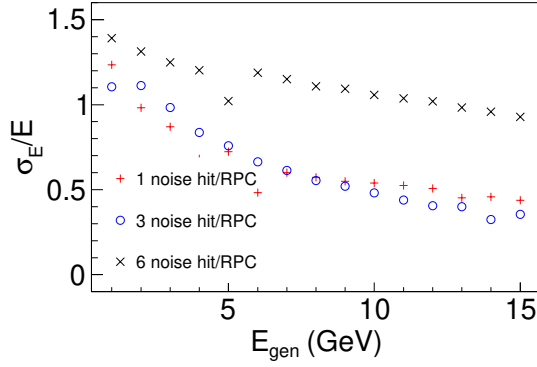


**Figure 4.10:** Hadron energy resolution for different noise rate for optimal ellipsoid size.

of  $\Delta E/E$  distribution. For those energy bins, the shape of  $\Delta E/E$  distribution not gaussian due to which it is not possible to estimate the energy resolution. In Figure 4.10, the resolutions are plotted for the best cluster dimension for all the three noise densities. The algorithm has to be optimized for different noise densities as shown here.

## 4.4 Reconstruction of the direction of hadron shower

The reconstruction of the direction of hadron shower has been performed for the cluster which contains a minimum of two z-planes (layers). The coordinates of the center of the cluster, say,  $O(x, y, z)$  is the mean of the coordinates of hits in the cluster.

$$\bar{x} = \frac{\sum(x_i)}{n}, \bar{y} = \frac{\sum(y_i)}{n}, \bar{z} = \frac{\sum(z_i)}{n} \quad (4.2)$$

where co-ordinates of each hit is  $(x_i, y_i, z_i)$ . Distance between that center of the cluster  $(\bar{x}, \bar{y}, \bar{z})$  to each hit  $(x_i, y_i, z_i)$  has been calculated. The matrix obtained using these distances is following,

$$M = \begin{bmatrix} \sum_{i=1}^n (x_i - \bar{x})^2 & \sum_{i=1}^n (x_i - \bar{x})(y_i - \bar{y}) & \sum_{i=1}^n (x_i - \bar{x})(z_i - \bar{z}) \\ \sum_{i=1}^n (x_i - \bar{x})(y_i - \bar{y}) & \sum_{i=1}^n (y_i - \bar{y})^2 & \sum_{i=1}^n (y_i - \bar{y})(z_i - \bar{z}) \\ \sum_{i=1}^n (x_i - \bar{x})(z_i - \bar{z}) & \sum_{i=1}^n (y_i - \bar{y})(z_i - \bar{z}) & \sum_{i=1}^n (z_i - \bar{z})^2 \end{bmatrix} \quad (4.3)$$

where  $n$  is the total number of hits in the largest cluster. The eigenvalues and eigenvectors of the matrix are calculated. The eigenvector related to the maximum eigenvalue gives the thrust axis, of the hadronic shower with a 2-fold ambiguity in shower direction. To confirm whether the direction of the hadron shower is in the same or opposite direction of that of the eigenvector, the average width of the hadron shower has been calculated. The hadron shower is expected to be narrower along the side towards which it is propagated. For this purpose it is needed to identify the hits in the following two regions:

- Region I :  $\cos \Psi > 0$ .
- Region II :  $\cos \Psi < 0$ .

where  $\Psi$  is the angle between the eigenvector ( $\vec{a}$ ) and the vector connecting the center of the cluster and a particular hit ( $\vec{b}$ ) as shown in Figure 4.11. In Region-I the value of  $\cos \Psi$  is positive while in Region II the value of  $\cos \Psi$  is negative. For each region, the distance of hits in that region from the eigenvector is calculated and an average distance is obtained. If, 'h' is the distance of hit from eigenvector ' $\vec{a}$ ', ' $\vec{b}$ ' is the vector connecting a hit to the center of the cluster,

$$h = \frac{|\vec{a} \times \vec{b}|}{|\vec{a}|} \quad (4.4)$$

The average of ' $h^2$ ' has been calculated separately for Region I and II. The region which has a higher value of the average of  $h^2$  is the region from which the hadron shower has started. If the average value of ' $h^2$ ' is greater for Region

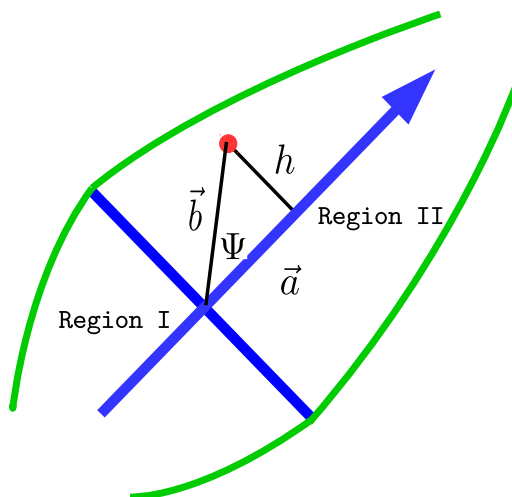


**Figure 4.11:** Algorithm for estimating hadron direction.

I (i.e.  $\cos \Psi > 0$ ), the hadron shower direction is the same as the direction of the previously mentioned eigenvector, otherwise, it will be made opposite to the direction of the eigenvector. In order to find the direction of hadron shower, the events are selected based on the minimum number of planes in the shower.

The physics performance of an atmospheric neutrino experiment is observed with  $L/E$  which is directly related to  $\cos \theta$  of incident neutrino. Hence, there is more emphasis on the performance of  $\cos \theta$  in the study. The distributions of the cosine of zenith angle of reconstructed hadron shower, w.r.t. true hadron direction, are shown in Figure 4.12 for different conditions on a minimum number of Z planes in the cluster. Here, for different criteria of the minimum number of Z planes, the fraction of events where the shower is developed in the direction of the true hadron, i.e.  $\cos \theta_{gen} \times \cos \theta_{reco} > 0$  is only 55-56 %.

The time of hits is also used to estimate the direction of the hadron shower. It is easy to understand that the hits obtained in the side from which the shower is generated are earlier in time than those which are present in the side towards which the shower is propagated. When the time of hits in the Region I is greater than that in Region II, the direction of hadron shower is the same as the direction of

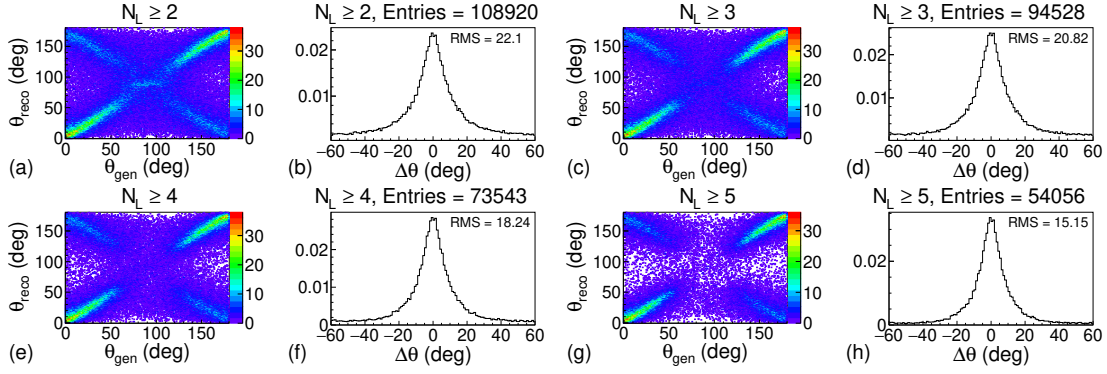


**Figure 4.12:** The reconstructed shower direction vs true hadron direction (a,c,e,g) and the distribution of difference of cosine of zenith angle of reconstructed shower direction and true hadron direction (b,d,f,h) using only shower width information. Here,  $N_L$  is minimum number of Z planes in the reconstructed shower.

the eigenvector, otherwise, it is made opposite to the direction of the eigenvector.

The distributions of the cosine of zenith angle of reconstructed hadron shower w.r.t. that of true hadron direction using the time of hits are shown for different conditions on the minimum number of Z planes in the cluster. Here, for different criteria of the minimum number of Z planes, the fraction of events where the shower is developed in the true direction of the hadron is around 75–76 %.

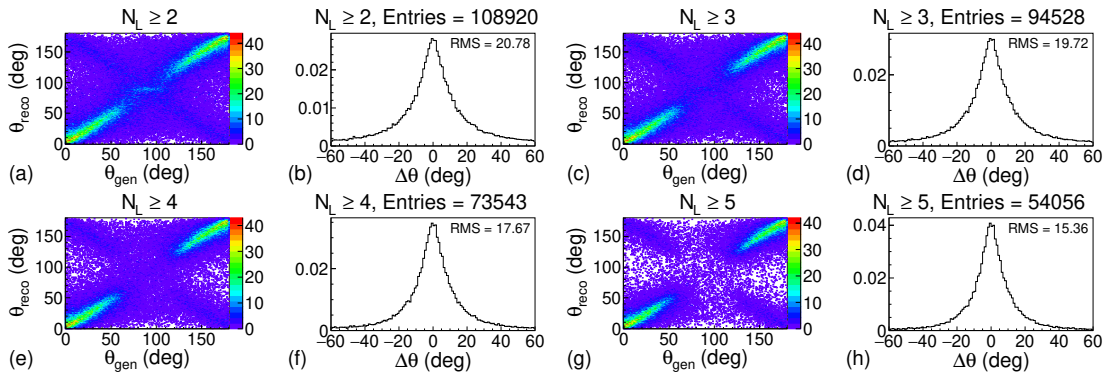


**Figure 4.13:** The reconstructed shower direction vs true hadron direction (a,c,e,g) and the distribution of difference of cosine of zenith angle of reconstructed shower direction and true hadron direction (b,d,f,h) using only timing information. Here,  $N_L$  is minimum number of Z planes in the reconstructed shower.

## 4.5 Summary

The new clustering algorithm is developed for the measurement of energy and direction of neutral hadrons. For the charge current neutrino interaction, the direction of neutrino can be measured from the direction of the muon, but this algorithm is also able to have a crude measurement of the direction of hadrons in neutral current neutrino interaction. The measurement of shower direction will also help in using the  $\nu_e$ -CC events in determining the neutrino mass hierarchy in ICAL detector [104]. Detector noise had a very small impact on the momentum measurement of the muon but had a significant effect on the measurement of the hadronic shower. This improvement of energy/momentum measurement will improve the physics goal of the ICAL experiment.





# Chapter 5

## mini-ICAL detector

During the detector R&D phase of ICAL, several RPC detector stacks were constructed and operated by the collaboration for many years with the main goal of studying the long term performance of the RPC detectors. The long term stability of Resistive Plate Chamber (RPC) detectors has already been tested using a 12 layer stack of RPCs having  $1 \times 1 \text{ m}^2$  area each at Mumbai as well as a 12 layer stack of RPCs having  $2 \times 2 \text{ m}^2$  area each at Madurai. Before proceeding to construct the  $3 \times 17 \text{ kton}$  Iron Calorimeter detector modules, it is necessary to build a scaled-down version, called mini-ICAL (shown in Figure 5.1) hereafter, at the transit campus of Inter-Institutional Centre for High Energy Physics (IICHEP) at Madurai.

The size of the mini-ICAL detector,  $4 \text{ m} \times 4 \text{ m} \times 11$  layer weighing about 85 tons, was dictated by the size of the experimental hall at IICHEP. Building and operating the mini-ICAL detector would allow issues of electromagnetic interference (EMI), long term performances of the front end electronics in presence of the fringe magnetic field, DC-DC HV module, trigger, data acquisition systems, and closed-loop gas system, to name a few, to be evaluated and problems addressed. The experience thus gleaned would be useful in setting up and operating the engineering module of ICAL which in turn, would help in building the ICAL modules. Other



**Figure 5.1:** mini-ICAL detector.

than the engineering issues, these following items are being tested in this setup;

- (a) the validation of magnet design by measuring the magnetic field using pickup coil and Hall probes and comparing it with 2D simulation by MAGNET[92] software,
- (b) the performance of RPC including DC-DC power supply, on-board electronics, closed loop gas system, etc,
- (c) the feasibility study of using Muon Spin Rotation technique to measure B-field which can be complementary to pickup coil and Hall probe data,
- (d) the measurement of momentum spectra of the charge-dependent muon flux up to  $\sim 1.5$  GeV and compare it with MC simulation,
- (e) the proof of principle test of the cosmic muon veto detector for the feasibility of a shallow ICAL detector[106] etc.

The major components of the mini-ICAL detector discussed in the following sections of this chapter are:

1. The 85 ton electromagnet, including the mechanical tiling of the 11 layers of iron, the spacers maintaining the required gaps for insertion of the active particle detectors, RPCs, the magnetic field measurement system, a DC power supply (PS) and the copper coils for energizing the magnet.
2. A closed-loop low conductivity chilled water system to cool the magnet power supply and the copper coils.
3. The RPC based muon detectors.
4. A closed-loop gas system to circulate the specified gas mixture in the RPCs.
5. Electronics for data acquisition, trigger, and control system.

## 5.1 mini-ICAL magnet

The building of mini-ICAL magnet has helped in standardizing and qualifying manufacturing processes of magnet components, their handling, inspection as well as the installation. It also helped in identifying the problems, if any, with the integration of magnet with auxiliary systems and during the commissioning of the detector. The experience gained in building the mini-ICAL detector will help for the final construction of the ICAL detector.

The mini-ICAL magnet consists of 11 layers of iron, with thickness 56 mm with an interlayer gap of 45 mm. The RPC, which is sensitive to charged particles, is placed in this interlayer gap. The details of the magnet are given in Table 5.1.

Each iron layer in mini-ICAL is made up of four different tiles (shown in Figure 5.2 (a)) of soft iron (with chemical composition: C (0.015 %), Mn (0.37 %), P (0.012 %), S (0.008 %), Si (0.188 %), Al (0.001 %), N (50 ppm) and remaining is

Parameter	Value (Mini ICAL Magnet)
Magnet Size (only iron stack)	4 m × 4 m × 1.06 m
Magnet Weight	85 Ton
Magnetic field uniformity	F > 1 T for 90 % area
No. of Layers	11 layers
Gap between two plate layers	45 mm
No. of copper coil/No. of turns in each coil	02/18
Induction (AT rating)	32,400 (Nominal)
Coil	
Conductor cross section (mm)	30 × 30 × $\phi$ 17 bore
Conductor material	Oxygen free copper
Coil cooling	Low conductivity DM water
Coil slot length & width	800 mm & 80 mm at coil
Distance between two copper conductors	40 mm

**Table 5.1:** mini-ICAL magnet details.

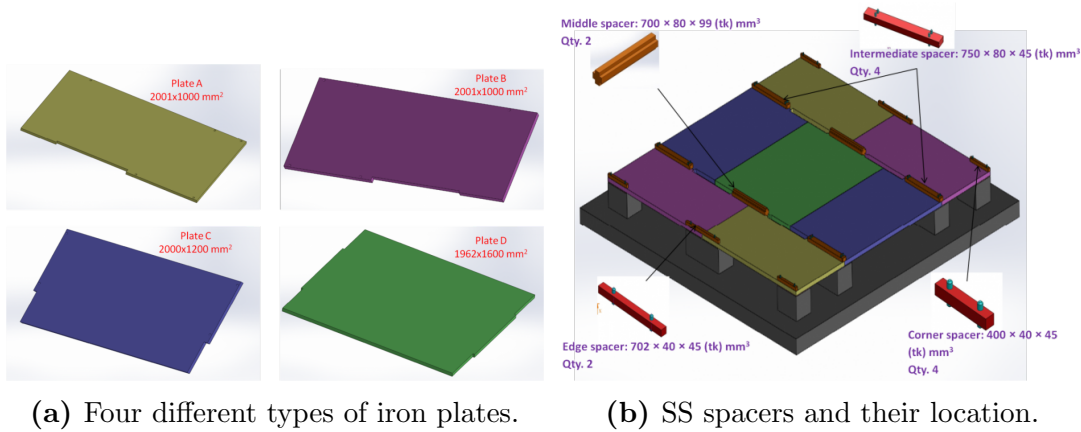


**Figure 5.2**

iron). These plates have high magnetic permeability with knee point at 1.5 T. They have low carbon percentage but sufficient mechanical strength. The iron tiles are cut at the designed location where the copper conductors for coil pass through. The spacers (Figure 5.2 (b)) used to create the 45 mm gap are made of non-magnetic stainless steel (SS-304). The positions of the spacers are designed to support the iron plates with minimum possible deflection. The mini-ICAL's magnet coil is made of pure OFE grade copper (oxygen content less than 10 ppm), with high electrical ( $58.3 \text{ m}/\Omega\text{-mm}^2$ ) and thermal ( $390 \text{ W}/\text{m-K}$ ) conductivity. The conductor used for coil has a cross-section of  $30 \text{ mm} \times 30 \text{ mm}$  with a bore diameter

of 17 mm. The coil is fabricated in two parts called “bottom U” and “upper C” sections.



(a) Bottom “U” coil sections.

(b) Brazing of coil.



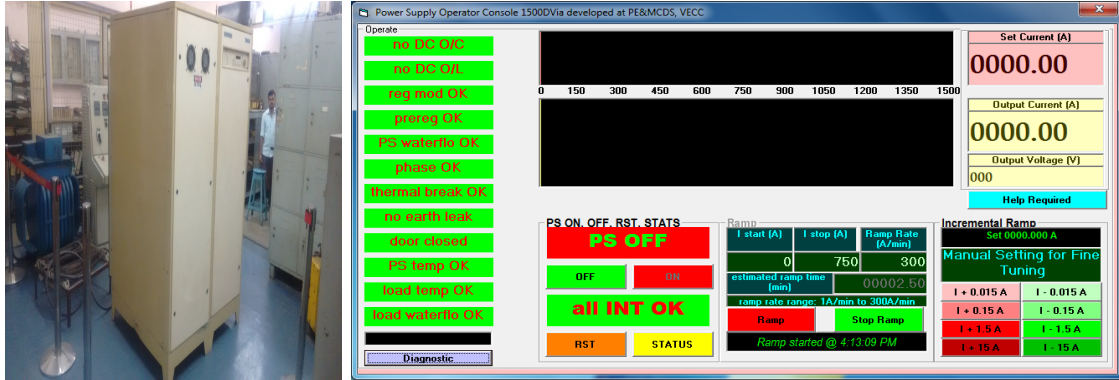
(c) Hydraulic testing of brazed joint.

(d) Measurement of inter-layer gaps.

**Figure 5.3**

During the construction of the mini-ICAL detector, first the “bottom U” sections of the coil are placed as demonstrated in Figure 5.3 (a) and the first layer is tiled with the iron plates. After tiling the iron layer, 45 mm thick SS spacers are mounted on the layers at the designated locations. Likewise, all eleven layers of iron plates are assembled. After tiling the final iron layer, the “upper C” sections of the copper conductor are brazed with the “bottom U” sections to complete the coils (Figure 5.3 (b)). The pressure holding test is performed on the brazed joints for 1 hour at 12 bar (Figure 5.3 (c)). The resistance less than  $5 \mu\Omega$  was achieved across brazed joint thus ensuring the electrical integrity of the coil at the joints.

This is the qualifying test for the brazing of copper coils. To qualify the inter-layer gap, the gap measurement device shown in Figure 5.3 (d) is used.



(a) Magnet power supply.

(b) Software for power supply.

Figure 5.4

After completing all the tests, the coils are connected in series electrically. An SCR based linear regulated power supply manufactured by “Danfysik” is used to energize the magnet (Figure 5.4 (a)). It can supply current up to 1500 A with a maximum output voltage of 30 V. The current stability is better than 100 ppm. The GUI based software allows operating the power supply remotely from the control room. A screenshot of the operating panel is shown in Figure 5.4 (b). The software also presents the status of various interlocks, monitoring of current, voltage, etc. During the operation, a high current ( $\sim 900$  A) will be passing through the coil. Hence, a closed-loop low conductivity water cooling system (LCWCS) has been designed and installed. The two coils are connected independently to this system, for cooling. This system is also connected with the power supply for the magnet which requires cooling as well.

The mini-ICAL magnet has been energized up to 1000 A and the functionalities of the auxiliary systems like power supply, LCWCS, etc are monitored for approximately 12 hours. Thereafter, the current is reduced to 800 A and magnetic field data were recorded with the field measurement system. The magnetic measurement system adopted for the mini ICAL has got two components:

1. **Search coil-based magnetic measurement:** It measures the average field inside the cross-sectional area of the iron plate covered by the coil during dynamic conditions of the magnet, ramping up and ramping down. The locations of the search coils are transverse to the field direction.
2. **Hall probe-based magnetic measurement:** It measures the field during steady-state and ramping of the magnet. Hall probes placed in the air gap between the iron plates will measure the field in the transverse direction.

In the mini-ICAL magnet out of 11 iron layers,  $0^{th}$ ,  $5^{th}$  and  $10^{th}$  (bottom, middle and top) layers have provisions for magnetic field measurement. Search coil-based magnetic measurement: All the type A, B and D plates of  $0^{th}$ ,  $5^{th}$  and  $10^{th}$  layers are wound with search coils. Each search coil consists of a single turn of Teflon coated flexible wire of approximately  $0.25\text{ mm}^2$  cross-section. Signals from each search coil will be amplified and integrated over the time period in the fluxmeter (shown in Figure 5.5) to get the field value.

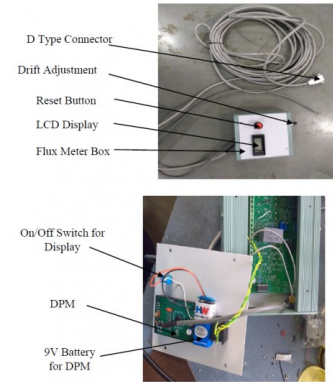
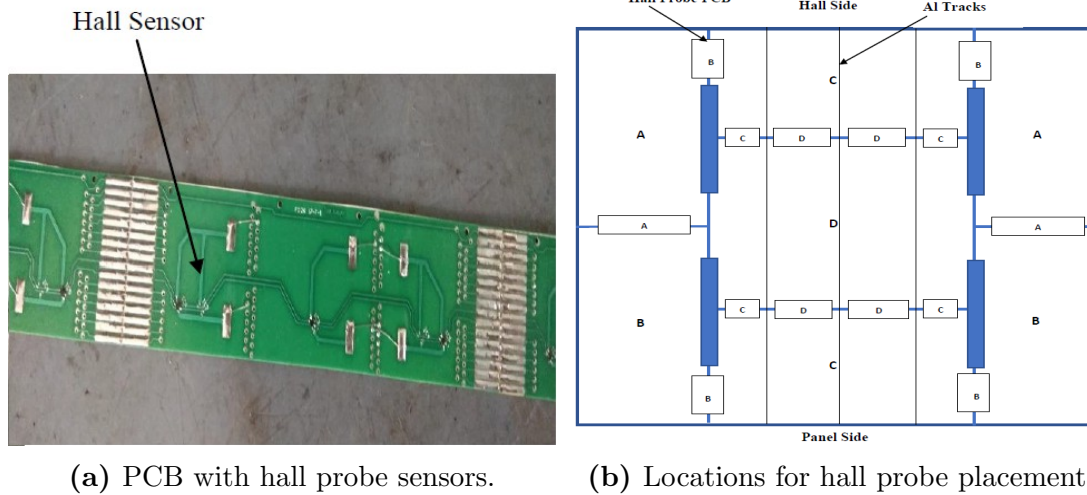


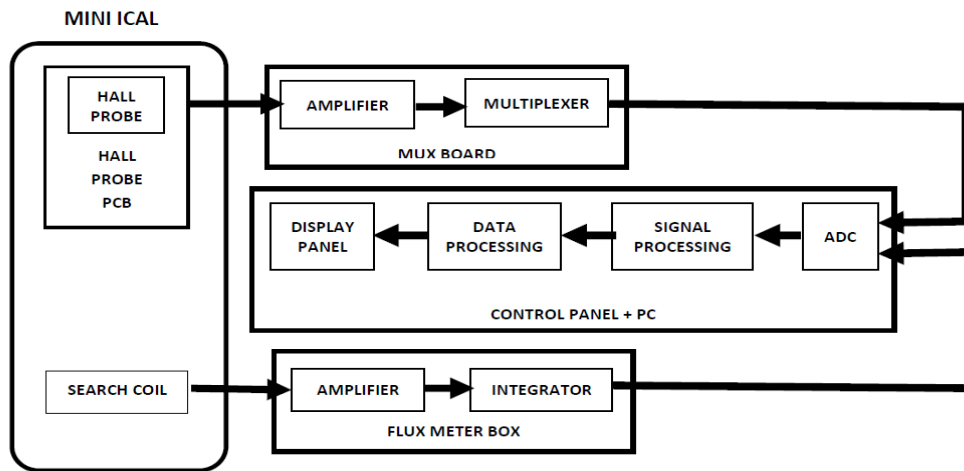
**Figure 5.5:** Fluxmeter for search coil based measurements.

A hall probe-based magnetic measurement system is developed to measure the field during steady-state and ramping of the magnet. The hall probes are placed in the air gap between the iron plates in layer – 0, 5 and 10. In these layers, between the iron plates, SS shims are placed during the installation to maintain the gap for inserting the hall probes. The hall probes measure the magnetic field in the traverse direction. A sample hall probe PCB, as well as the placement of hall probe PCBs in an iron layer, are shown in Figure 5.6.

The specifications of the hall sensors are listed in Table 5.2. All the hall sensors are calibrated before they are inserted into the gap. The block diagram of the



(a) PCB with hall probe sensors. (b) Locations for hall probe placement.



(c) Block diagram for magnetic field measurement system.

**Figure 5.6**

magnetic measurement system is shown in Figure 5.6 (c). In the control unit, the voltage sensors from hall probe sensors are digitized with 16-bit ADC with (100 ms digitization) and processed in the back end computer. The limitation of Hall sensors is that it can only measure the magnetic field in the gap between the iron plates. For the physics requirement to reconstruct a muon track, the magnetic field inside the iron is the necessary input. This information is obtained from the magnetic field simulation.

The magnetic field simulation of the mini-ICAL is carried out using MAGNET software[92]. The simulation is performed using Finite Element Method (FEM)



Parameter	Value
Basic sensor material	Mono-crystal GaAs
Type of probe	For transverse field measurement
Measurement range	up to 3 T
Accuracy	0.2 % of full scale
Non-linearity	< 1 %
Max. input current/voltage	30 mA/10 V
Max. input power	150 mW
Hall output voltage at B=100 mT, I=8 mA, V=6 V	110–150 mV
Offset voltage	$\pm 11$ mV
Input resistance	650–800 $\Omega$
Output resistance	650–800 $\Omega$
Temperature co-efficient of hall output voltage	0.06 %/ $^{\circ}$ C
Temperature co-efficient of input outpt resistance	0.3 %/ $^{\circ}$ C

**Table 5.2:** Specifications of hall sensor.

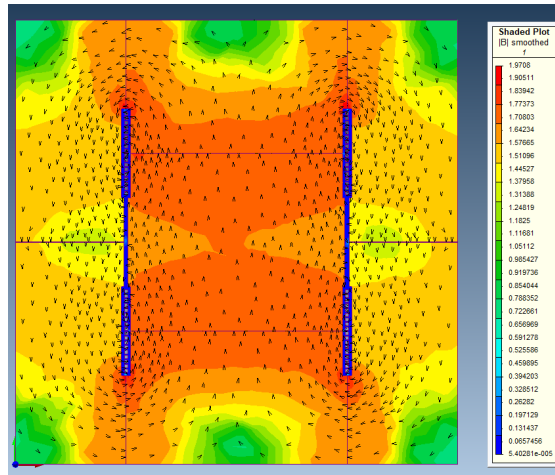


**Figure 5.7:** Field map obtained from magnetic field simulation.

based solvers. For the field simulations, the measured magnetic property of the core material is an important input. The B–H curve of the soft iron plate is measured. The simulations were carried out for different coil currents and the simulated field values are compared with the measured values, in the gap where the hall probes are located. The variation between hall sensor measurements and simulated results is within  $\pm 10\%$ . A simulated field map for a layer of iron is shown in Figure 5.7 for coil current of 900 A.

## 5.2 RPC Assembly

The sensitive detectors for mini-ICAL are large area RPCs. They are constructed using gas gaps made using two float glasses of size  $1.74\text{ m} \times 1.87\text{ m} \times 3\text{ mm}$ . These gas gaps were manufactured by Saint Gobain Glass Industries Pvt. Ltd., Chennai. The outer surface of the glass electrodes in this gas gap is coated by graphite paint to permit uniform application of the high voltage. The graphite coating is applied by the screen printing technique. An  $8 \times 8$  matrix of polycarbonate buttons (of 11 mm diameter) is glued to the inner surfaces of the glass electrodes to maintain the 2 mm gap between them. Finally, the gap is sealed on all sides by gluing side spacers along with inlet and outlets for gas flow specially designed for ICAL RPCs. Before the gas gaps are used for making RPCs, they are tested for surface resistivity of the graphite coat and leak tightness of gap volume. The surface resistivity of glasses selected for mini-ICAL is in the range of  $0.6\text{--}1.5\text{ M}\Omega/\square$ .

In the mini-ICAL detector, a closed-loop gas recirculation system (CLS) is used to distribute the gas mixture to the RPCs. The leakage of the gas mixture from the CLS or the distribution network will increase the cost of operation. Also, the leakage of the outside atmosphere into the system will contaminate the gas mixture by water vapor and oxygen which may affect the performance of RPCs or damage the gas gaps. The fluorine present in the gas mixture will react with water vapor from the atmosphere producing hydrofluoric acid which will damage the inner surfaces of the glass electrodes. The oxygen gas having an affinity to electrons can affect the performance of the detector. Due to the aforementioned reasons, a proper leak test is performed on all the gas gaps. A technique for leak test of gas gaps by monitoring the absolute pressure inside the gap has been designed and tested. The detailed description of the leak test set up and quantification of the leak are described in [107]. The gas gaps were tested for a leak for a duration of 7–8 hours. The leak rate for the selected gas gaps was found to be less than

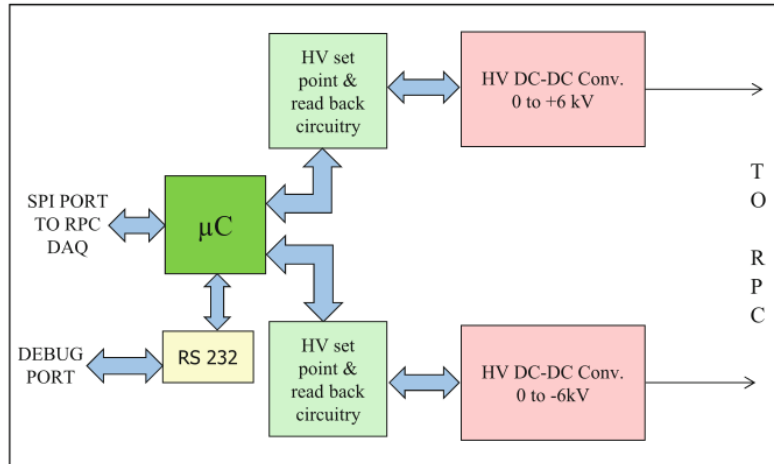
0.02 ml/hr-mmWC<sup>1</sup>.

Honeycomb panels of 5 mm in thickness, which was fabricated using polypropylene as a dielectric, laminated on one side by 70  $\mu\text{m}$  thick aluminum sheet and another side by 70  $\mu\text{m}$  thick copper sheet are used for the electronic signal pickup. Also, for trial purposes, a few pick-up panels were made using PVC foam of 3 mm thickness as the dielectric medium. The readout strips of 28 mm width are realized by machining 2 mm wide gaps on the copper sheet at 30 mm pitch. The aluminum acts as the signal reference layer/ground plane. The honeycomb pick-up panels provide good mechanical support and its characteristic impedance is  $\sim 50 \Omega$ . The pickup panels are of the same dimension as that of gas gaps. Before packing the gas gaps with the pickup panels, the dimensions of these panels are verified as part of the quality check. Also, these panels were tested to check, if the strip width and pitch of 28 mm and 30 mm respectively are maintained along the length of the panel. The characteristic impedance of each of the strip is tested and is found to be 47–50  $\Omega$ . After certifying all these tests, one end of each of the strips is terminated with 50  $\Omega$  resistor. The electrical wires to connect the other end of the strips with the preamplifiers are then soldered.

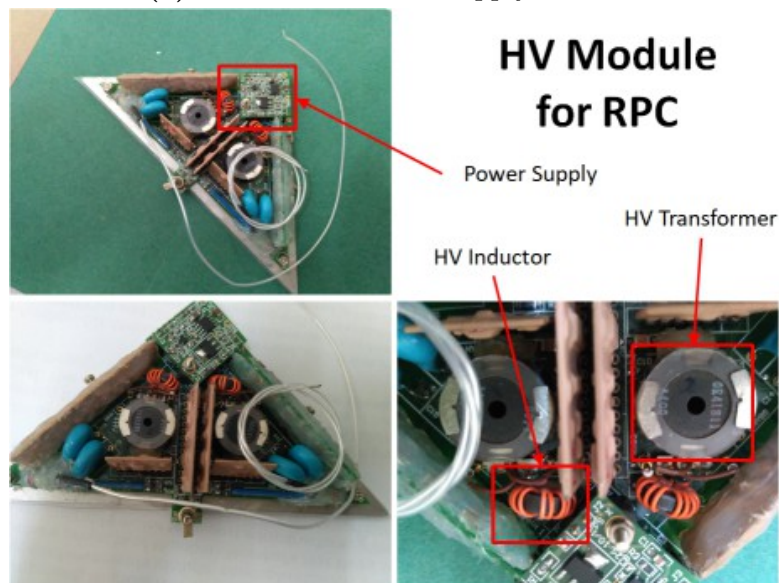
To minimize the HV leakage on the chamber surface, the RPC bias supply is designed as  $\pm (0-6)$  kV differential supply as shown in Figure 5.8. The two HV outputs are obtained using two low noise, HV DC–DC convertors which are based on a current fed resonant Royer circuit minimizing the harmonic generation and RFI. It is constructed in a right angle triangular shaped PCB having dimensions 105 mm  $\times$  105 mm. It is mounted on one corner of RPC as shown in Figure 5.9. The output voltage is adjustable in the range of  $\pm 0.1$  to  $\pm 6$  kV, with a resolution of 2 V. The output ripple and noise is less than 200 mV<sub>p-p</sub>. The load current read back is 0–2000 nA with a measurement resolution of 1 nA. It provides an adjustable ramp rate of 1–100 V/s. It has an onboard Atmel AVR microcontroller which receives

---

<sup>1</sup>Millimetres water column, abbreviated to mmWC, is a unit of pressure. It is the pressure required to support a water column of the specified height. 1 mmWC = 0.098 mbar.



(a) Schematics for HV supply for RPC.



(b) Assembled HV supply module.

**Figure 5.8**

all the HV control commands from the onboard Digital Front-end unit, through a four-wire SPI interface.

For the final assembly of the RPC unit, both the sides of gas gaps are covered with two layers of insulator (mylar material) sheets and the pickup panels are placed on both sides of the gap such that the strips in the two panels are orthogonal to each other. This packed RPC unit is placed in a tray along with all the front end electronics and gas supply connections. For mini-ICAL, trays made from aluminum honeycomb are used. For one layer (Layer-2), a tray made from Fibre

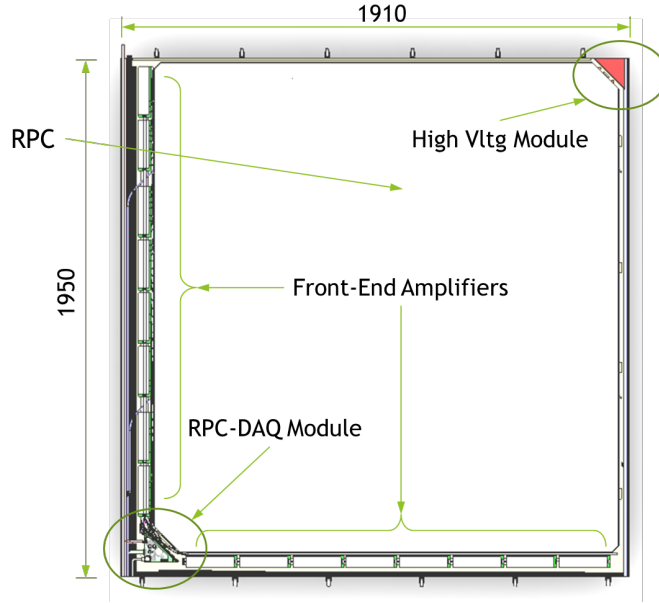


**Figure 5.9:** Assembled RPC unit in a tray along with front end electronics and HV module.

Reinforced Plastic (FRP) which was designed for ICAL is used for trial purposes. The placement of RPC along with front-end electronics (explained in Section 5.4) and the H.V. supply module in the tray is shown in Figure 5.9.

### 5.3 Closed loop gas system

The RPC can be operated in two modes viz, avalanche mode and streamer mode. The INO RPCs are planned to be operated in the avalanche mode and hence the gas mixture is in the ratio of about 94.5% R134a ( $C_2H_2F_4$ , 1,1,2,2-Tetrafluoroethane), 4.5% isobutane (iso- $C_4H_{10}$ ) and about 0.3% Sulphur hexafluoride ( $SF_6$ ). The mixed gas will be input into the RPC at a few mbar above the atmospheric pressure. If the RPC is operated in streamer mode, then the gas mixture will have Argon gas at appropriate concentration but doesn't contain  $SF_6$ . In the closed-loop system (shown in Figure 5.11), designed for RPCs, a provision is made to add Argon gas in the system.

The basic function of the gas system is to mix the three gas components in

Gas volume (10 RPCs)	$10 \times 8 \text{ litres} = 80 \text{ litres}$
Gas mixture composition	$R134a:iso-C_4H_{10}:SF_6 = 95.2:4.5:0.3$
Normal flow rate	few $0.01 \text{ m}^3/\text{h}$
Gas renewal rate	atleast $\sim 0.3 \text{ volume/hour}$ even without radiation
Purity requirement	$O_2 < 1000 \text{ ppm}$ , $H_2O < 1000 \text{ ppm}$ , $N_2 < 1 \%$

Table 5.3: INO RPC gas parameters.

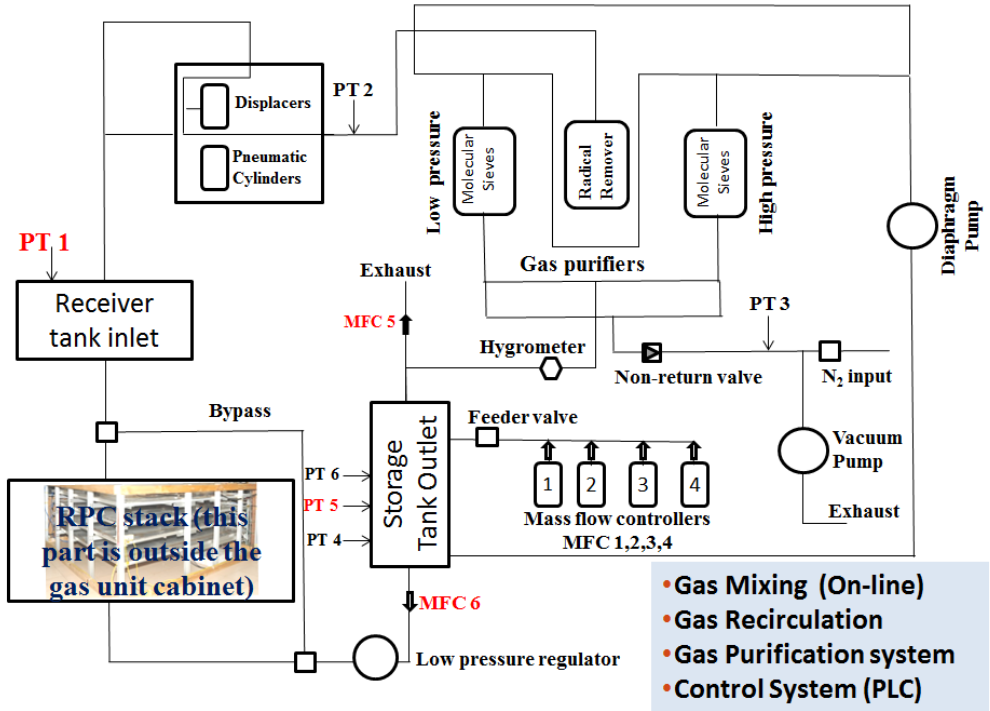


Figure 5.10: Flow diagram of closed loop gas recirculation system.

the appropriate proportions and to distribute them to the individual chambers. To economize the consumption of the gas mixture and to reduce the release of effluents into the atmosphere, a closed-loop gas recirculation system was designed, fabricated and installed at TIFR, Mumbai. The performance and integrity of RPCs in this pilot experiment were monitored to study the effect of periodic fluctuations and transients in the atmospheric pressure and temperature, room pressure, flow pulsations, etc. Due to its satisfactory performance, the same system was deployed for the mini-ICAL detector to study its capabilities of handling a stack of 10 large area RPCs. Although the system is designed to provide gas recirculation for 12 RPCs, it will be upgraded to handle 20 RPCs which is the final configuration of



(a) Back view.

(b) Front view.

**Figure 5.11:** Gas recirculation system.

mini-ICAL detector.

The flow diagram of the closed-loop system is shown in Figure 5.10. A pneumatically operated positive displacement pump sucks the gas mixture from a receiver tank connected to the RPC outlets. This pump operates at pressures between 2 to 5 mbar above atmospheric pressure. It delivers the gas mixtures to the storage tank at 1.65 bar after passing it through the purifiers. The mass flow controllers (MFCs) labeled 1,2,3 and 4 collect the individual gases from the storage cylinders and deliver them to the main storage tank when the pressure drops below 1.35 bar. The MFCs maintain the ratios of the gas mixture at 95.2:4.5:0.3% of R134a, iso-C<sub>4</sub>H<sub>10</sub> and SF<sub>6</sub> respectively. The pressure in the main storage tank is maintained between 1.35 bar and 1.65 bar.

The pressure of the gases at six different locations as well as the atmospheric

pressure are monitored by solid-state transmitters. The flow and pressure throughout the loop are controlled by Siemens PLC with input and output modules, actuators and SCADA interface. The various data parameters are logged periodically for remote monitoring of the system.

## 5.4 Data Acquisition Systems

The DAQ system performs a large number of tasks mainly, identifying the physics events in the detector by forming a trigger and tracking the particles traversing through the detector by storing the detector state during an event. Simultaneously, the health of the RPC detectors is also monitored by recording noise rates, chamber currents, etc periodically. The broad schematic of the DAQ for the ICAL detector is shown in Figure 5.12. The same scheme is used in the mini-ICAL detector with 10 RPCs present (20 RPCs in the final design) instead of 28,800 RPCs in the ICAL.

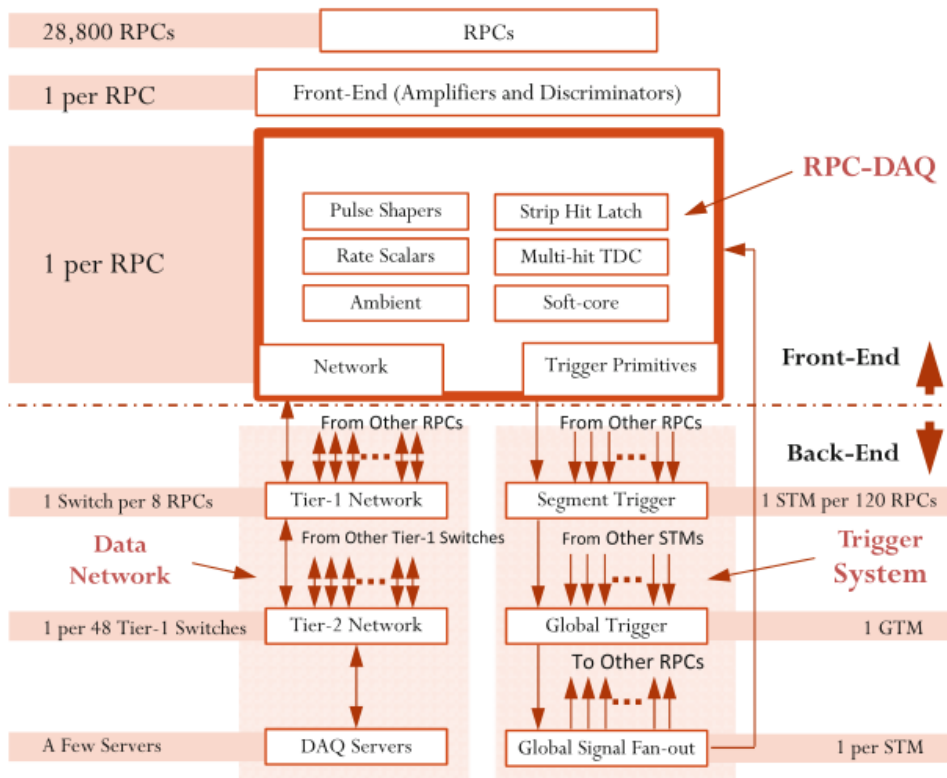


**Figure 5.12:** Schema of ICAL Data acquisition which is used in mini-ICAL.



### 5.4.1 Analog Front End

The RPC detector signals are of around 1–5 mV in amplitude with the rise time of the order of 1 ns. Also, the pulse profiles are extremely narrow viz; 5–10 ns. For mini-ICAL, analog front end (AFE) boards using NINO ASIC (shown in Figure 5.13) have been designed and deployed. NINO[108, 109] is an ultrafast low noise 8-ch FE preamplifier cum discriminator chip developed at CERN to be used mainly in ALICE time of flight detector. It is a fully differential chip featuring 4 differential amplifier stages with built-in hysteresis control. For mini-ICAL, a 6 layer AFE board (Figure 5.13) using NINO ASIC and 8 differential drivers of unity gain with threshold control is designed with track separation of 5 mil and board dimensions of 200 mm  $\times$  23 mm. The power consumption of the board is  $\sim$  560 mW. The NINO based AFE were extensively tested and characterized on RPC detectors. The RPC signal detection efficiency of 92% and stable noise rates of  $\sim$  45 Hz were achieved for an RPC with a threshold of 80 fC. The full details about NINO front end boards are explained by Kaur et.al [110].

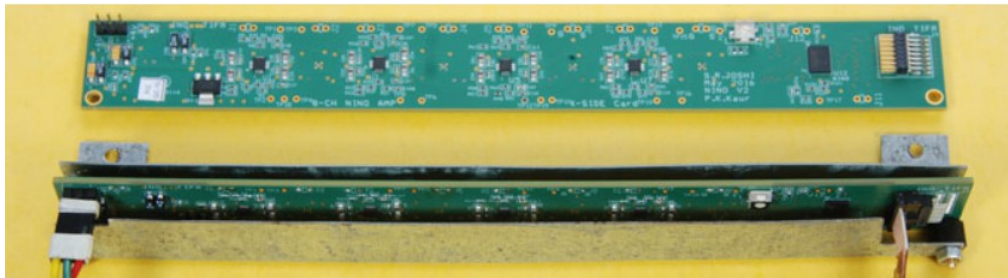


**Figure 5.13:** NINO front end boards with mounts.

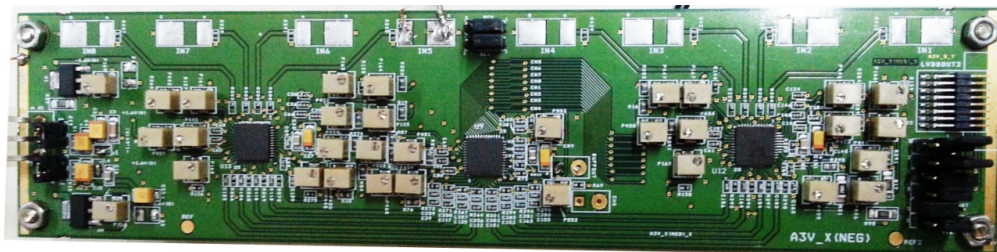


**Figure 5.14:** Anusparsh III chip along with its PCB.

One of the layers in mini-ICAL, ie. Layer-1 is populated with ANUSPARSH

[111] front end ASIC (Figure 5.14). It is a CMOS, 8-channel, high speed, low power amplifier-discriminator designed for avalanche mode of operation for RPCs. It was extensively tested in the  $1\text{ m} \times 1\text{ m}$  RPC stack at TIFR, Mumbai. It is designed to meet the readout requirements of RPC detectors for the ICAL experiment. Its total channel gain is  $6\text{ mV}/\mu\text{A}$  with an amplifier rise time of  $1.2\text{ ns}$  and input impedance is matched to the pick-up strips ( $\sim 47\ \Omega$ ). The performance of single-ended inputs of both polarities (X- and Y- pickup strips of an RPC has opposite polarity) is identical. It also provides the output of an amplified detector signal for profile analysis. And last but not the least, it has a low power consumption of  $45\text{ mW}$  per channel at  $3.3\text{ V}$  supply.

### 5.4.2 Digital Front End

The digital front-end module (DFE) (Figure 5.16) is located at one corner of the RPC tray. It's design is based such that RPC along with the electronics on the FRP tray can serve as a minimum standalone unit. It consists several functional blocks required to not only receive signals from AFEs but also record them in the ICAL data format. It also takes care of the data transfers between the RPC units and the back end servers. In ICAL data format, the signals to be recorded are strip hit information, time of arrival of signals and monitoring the signal rates in all the channels. The various functional blocks on the DFE module are Time to Digital convertor (TDC) (to measure time of arrival of signal), strip-hit latch (to record the strips giving the signals), rate monitors (to monitor signal rates in all channels), logic to generate pre-trigger (Level-0) signals, ambient parameter monitor (to record pressure, temperature and humidity), etc. Most of the DFE's functionalities have been implemented inside a Field Programmable Gate Array (FPGA) [112]. Figure 5.15 shows a simplified block diagram of the DFE module. The module is centered on an FPGA. Most of the data acquisition functionality is built into it. A soft-core processor has been used to supervise the data acquisition,

data collection and sending the data to the back-end over the network interface.

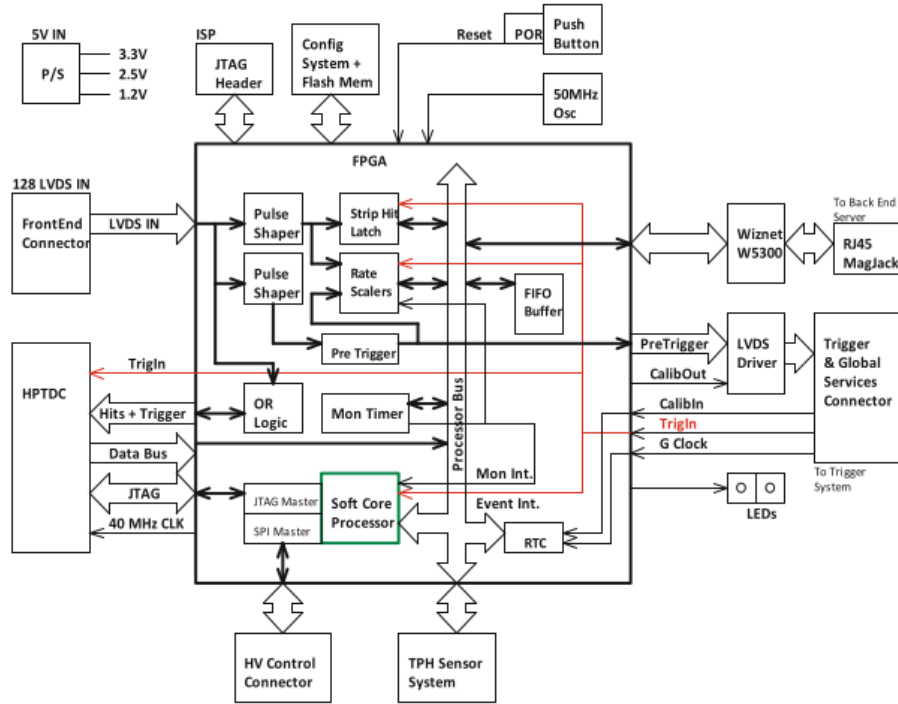
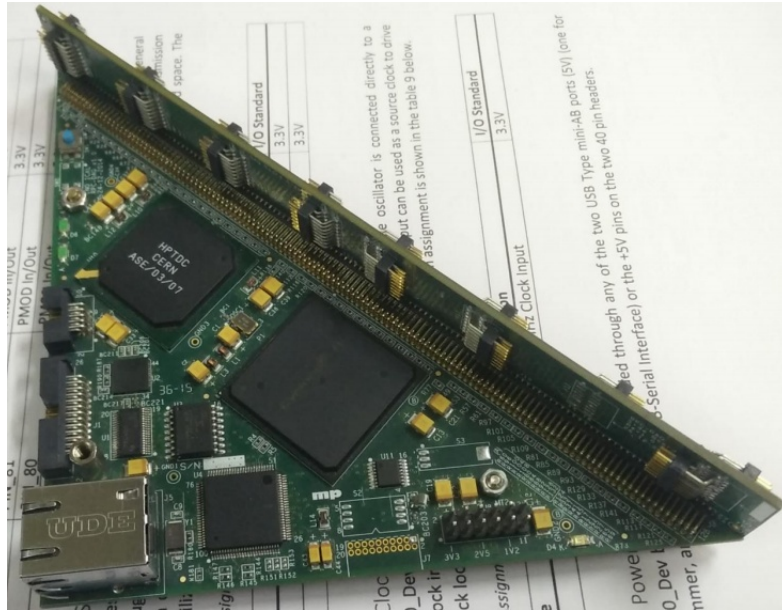


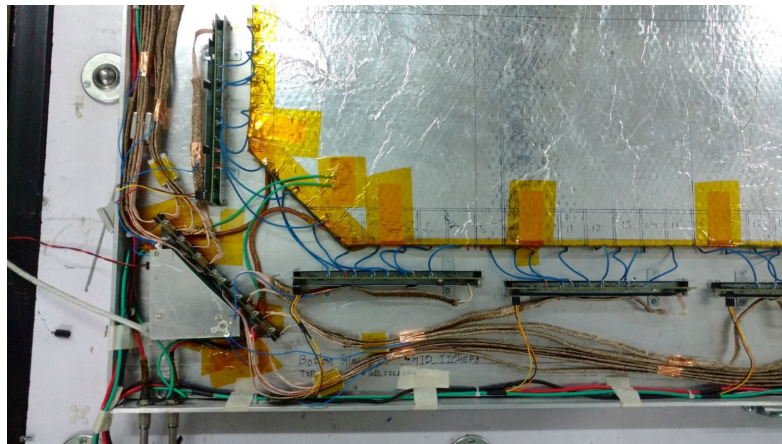
**Figure 5.15:** Block diagram of FPGA based digital front end module.

The FPGA has been configured for data acquisition and data transfer functionality of the DFE. For the DFE module, Altera Cyclone IV E series CE115 FPGA has been selected. It has 114,480 logic elements, 486 kB of embedded memory and up to 528 user I/Os [113]. As explained in Chapter ??, to determine the up/down directionality of the particles tracks recorded using the RPCs, the relative arrival times of the signals in the detector have to be measured. In order to record precise timing information, high-resolution TDC ASICs are mostly used. To resolve the up/down ambiguity in directionality, the timing measurement should be made with a least count of atleast 200 ps. For the current DFE module, High-Performance TDC (HPTDC) ASIC developed at CERN is being used [114]. In the future, a TDC ASIC which is being developed within the ICAL collaboration is expected to be deployed.

A central microcontroller unit (MCU) is required to control various components



(a) Assembled DFE module with the FPGA.



(b) DFE module in assembled RPC unit

**Figure 5.16**

of the data acquisition, acquire data from them, pack and send it to the backend. In the DFE module, NIOS-II soft-core processor is used as the MCU. The NIOS-II is a 32-bit general-purpose RISC processor. It can be configured to use a variety of on-chip peripherals as well as off-chip memories and peripherals [115]. The event data mainly includes strip hit pattern, TDC timing data and event timestamp. In parallel, the DFE module logic, carries out monitoring tasks periodically in the background, wherein it measures the RPC strips' background count rates as well as the trigger primitives' rates and also ambient temperature, humidity pressure,

and the RPC's high voltage and chamber currents. The end of the monitoring cycle interrupts the processor software, whose interrupt service routine reads out all the monitoring data and sends it to the backend server. A detailed explanation about the module and its functionalities is given in Saraf et.al [112].

### 5.4.3 Timing and Trigger System

The multi-level trigger system generates the global trigger signal based solely on event topology information. Trigger logic is essentially defined as  $(m \times p) / n$ , i.e. trigger is generated when out of a group of  $n$  consequent layers, at least  $p$  layers have  $m$  channels each with simultaneous signals in them. The pre-trigger signals from DFEs are fed to Signal Router Boards (SRBs) which bunch signals and redistribute them to the Trigger Logic Boards (TLBs). The second-level trigger logic is implemented in the TLBs and the boundary coincidences are resolved by the Global Trigger Logic Boards (GTLBs). The hardware components are shown in Figure 5.17. The entire control of the trigger system, monitoring of various signal rates, etc. is handled by the Trigger Control and Monitor (TCAM) module. Further, the Control and Monitoring (CAM) module provides an interface between the trigger and backend data concentrator units. In the mini-ICAL with 10 RPCs in the current condition, (20 RPCs in the final design) is a much smaller version of the ICAL (28,800 RPCs) or the Engineering Prototype (with 320 RPCs). The expected trigger rates for the mini-ICAL is 250 Hz (on the surface). So, the trigger system hardware inventory for mini-ICAL consists of: 1 Signal Router Board (SRB), 2 Trigger Logic Boards (TLBs) with 1 TLB for X-Orientation and 1 TLB for Y-Orientation, 1 Global Trigger Logic Board (GTLB), 1 Control and monitoring Board (CAM) and 1 Trigger Time Stamping Board (TCAM)

Calibration and auxiliary (CAU) services sub-system mainly interfaces with trigger system and DFE boards and performs functions of distribution of global clocks and trigger signals as well as the measurement of time offsets due to disparate

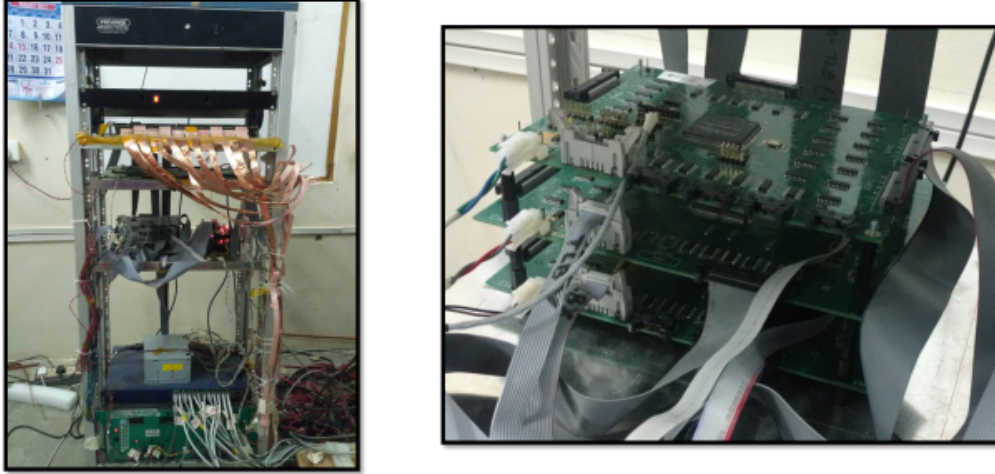


**Figure 5.17:** Trigger system for mini-ICAL detector.

signal path lengths. The local TOF in each DFE is then translated to a common timing reference by adding the respective offsets for the reconstruction of particle trajectories. The CAU unit was tested extensively on the RPC stacks and was found to provide offset corrections of better than 100 ps. The Real-Time Clocks (RTCs) of all the DFEs are pre-loaded with epoch time and synchronized up to a microsecond using pulse per second signal and global clock. The events are built in the backend using these RTC time stamps.

#### 5.4.4 Back End Systems

The data acquired by the DFE needs to be dispatched to the backend data concentrator hosts on receipt of the trigger signal. To achieve this, each DFE unit has an Ethernet controller. In every event, an event trigger is generated by the global trigger system and is fanned out to all the RPCs (DFE modules) as shown in Figure 5.18. On receiving the trigger signal, the participating DFEs will collect event data (Event time stamp, strip hit and time of flight) from their respective RPCs and push the event packet to transmit buffer. The integral number of event packets are sent to (one or more) Data Concentrator(s) at the back end over dedicated and pre-established TCP connections. Each DFE module is capable of handling

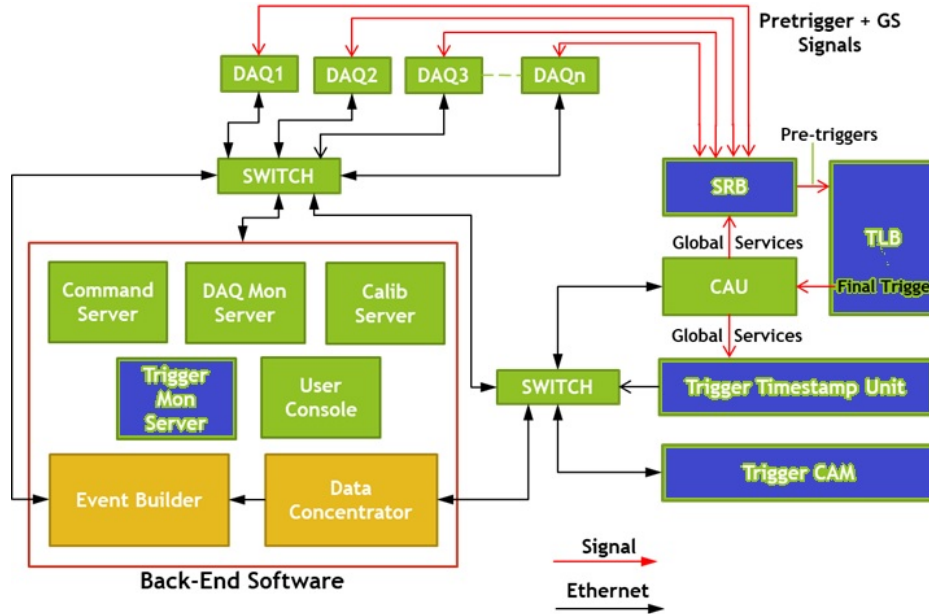


**Figure 5.18:** Flow diagram of mini-ICAL's Data acquisition.

38 Mbps data throughput.

The Data Concentrator in backend acts as a server and the DFEs act as clients in terms of the network protocol. The Data Concentrator(s) gather the RPC data packets and attach an event number to each of the data packets belong to the event based on event timestamp comparison before transmitting the data to another server, the Event-Builder.

UDP based command interface was implemented in MULTICAST and UNICAST modes to control DFE functionality. Suitable handshaking and checksum schemes are implemented to ensure the reliability of command and acknowledgment. The average cycle time of a command is 1 ms.

## 5.5 Summary

The experimental set up of the mini-ICAL detector along with a brief discussion on individual detector components and basic building blocks of the data acquisition electronics are discussed in this chapter. The mini-ICAL detector is commissioned

with 10 layers of RPCs and is operational since May 2018 with 1.5 T field. The magnetic field measurement has been closely matched with the simulation using MAGNET software. There is no unexpected noise in the RPC electronics due to the fringe field.



# Chapter 6

## Analysis of mini-ICAL data

The atmospheric muons incident on the detector, register clean tracks with just about one cluster (a combination of nearby hits) per RPC layer. In the absence of a magnetic field, the hits from the muon (being minimum ionizing particle) will present a straight line pattern with possible small kinks appearing due to multiple scattering and strip multiplicity effects. In presence of the magnetic field, the hits from muon (experiencing Lorentz force) will show a curvature representing the bending of muon trajectory. The curvature of the bending helps in estimating the momentum of an incident muon. Hence, the momentum distribution of atmospheric muons is observed in mini-ICAL. Figure 6.1 shows some cosmic muon events observed in mini-ICAL detector at 900 A current which corresponds to magnetic field of  $\sim 1.5$  T in the central region.

The magnetic field in the central region of the mini-ICAL detector is along the Y-direction and the particle is moving along Z-direction. Hence, the bending of the track is supposed to be observed only along X co-ordinate. It is expected that the track will not show any deviation in Y co-ordinate except for multiple scattering.

First, the muons observed in the detector in absence of the magnetic are fitted with a straight line and its various properties like detector inefficiencies, strip multiplicities, electronic offsets for time measurements, position alignment, etc are

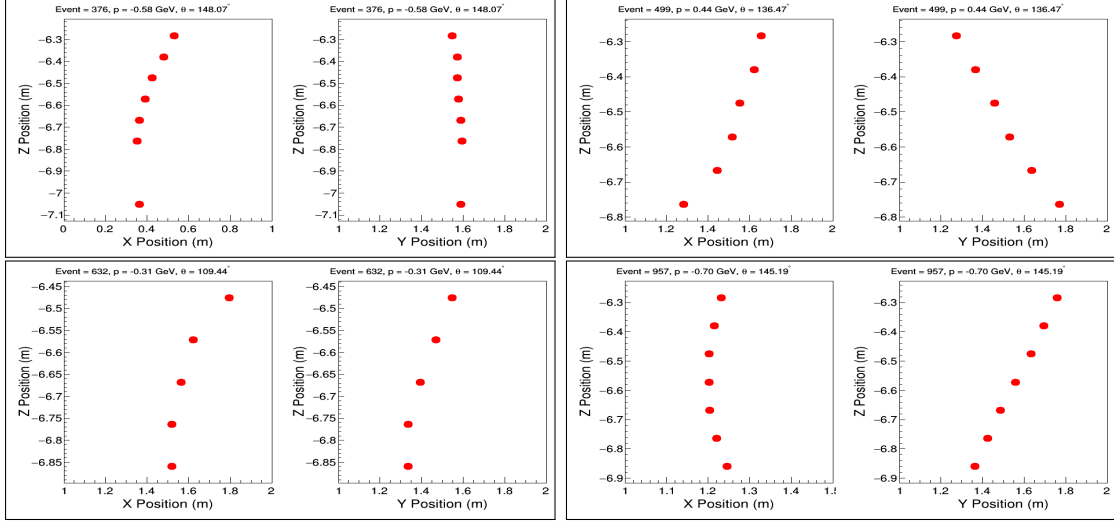


**Figure 6.1:** Typical cosmic muon events in miniICAL with magnetic field  $\sim 1.5$  T.

estimated. These properties will be further used as correction parameters and also as inputs to full detector simulation.

## 6.1 Muon trajectory without magnetic field

The detector performance is dependent on ambient conditions. Hence, the detector health needs to be monitored over a long period of time. For the RPCs, the signal rate in the strips is an important observation to monitor detector performance. The Noise Rate Monitoring section in the DFE latches the noise rate of the active strips as well as Fold signals on receipt of a clock signal from the back end and switches over to the next strip. In Figure 6.2, the average signal rates in all the channels in the DAQ which are monitored are presented. Here, The various layers with their X- and Y- planes are represented on the X-axis, all the strips and the Fold signals are denoted on the Y-axis and the average signal rates are presented on the color axis in Hz. From the plot, it can be observed that the average signal rate in strips is in the range of 30–250 Hz.

The atmospheric muons arrive from all directions at the top of the detector stack. The RPC strips are fired due to the passage of these muons. The strip

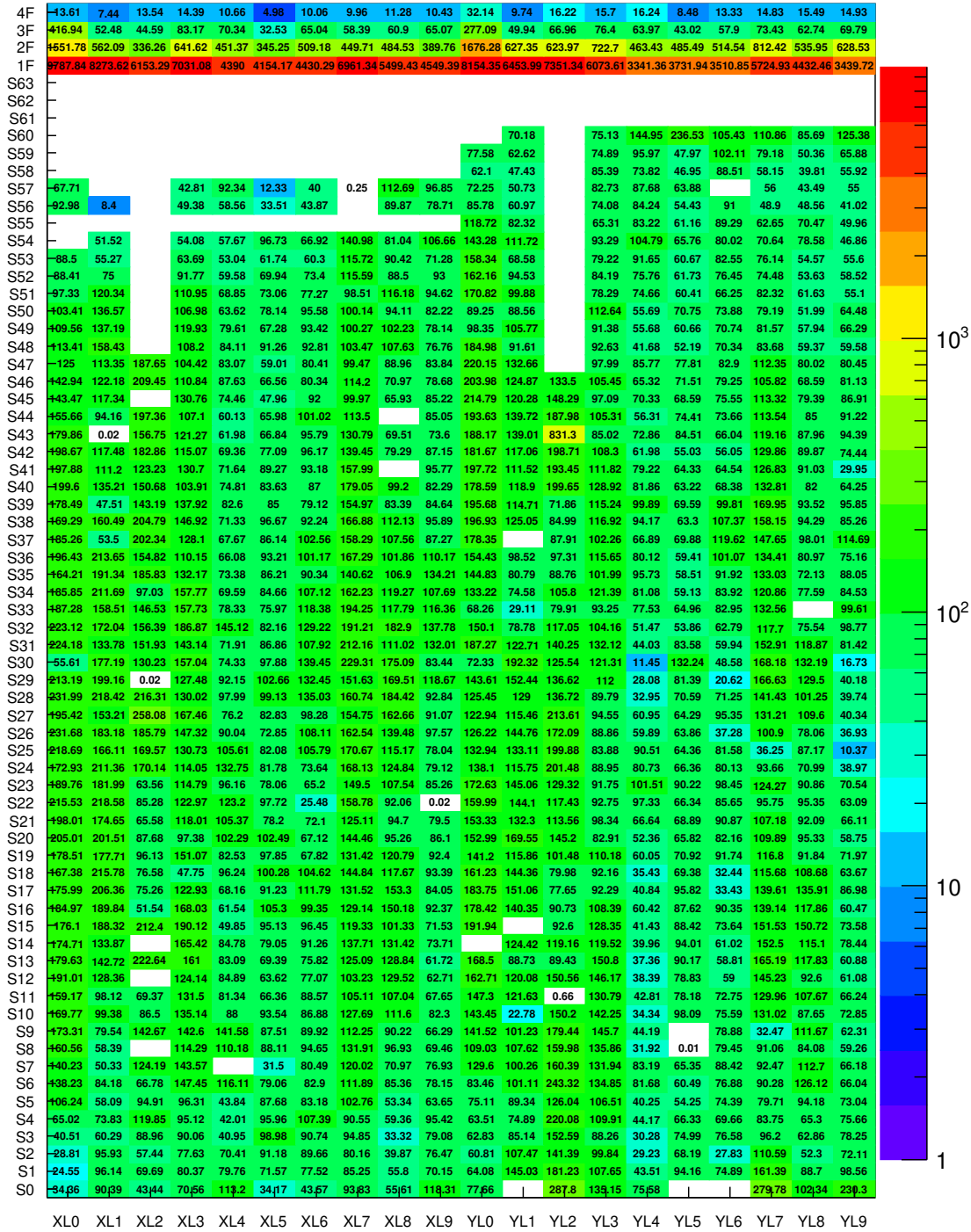


**Figure 6.2:** Signal rates (in Hz) for all channels in mini-ICAL including different trigger rates.

hit distribution (shown in Figure 6.3) for a layer is expected to be uniformly distributed. In practice, the strips at the edges have fewer events than those in the middle. This particular behavior is due to the in-situ trigger condition. Usually, a

top and bottom layers are present in the trigger formation and due to this geometry solid angular coverage is restricted for in between layers. A strip is rejected if its counting rate is very high and is not considered in the fit. For example, the strip number 43 in layer-2 on Y-side is rejected as its counting rate is too high compared to others. Similarly, the strip numbers 42 and 43 in layer-8 on X-side are rejected.

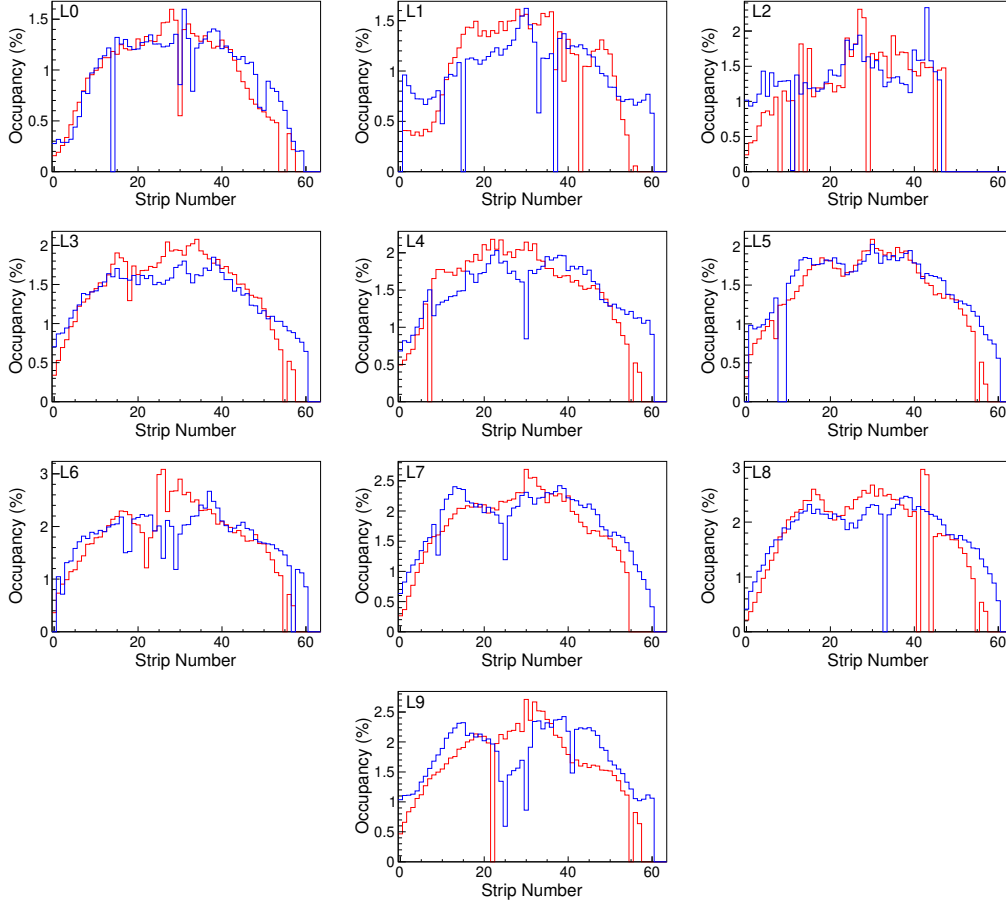


**Figure 6.3:** Relative distribution of strip occupancy. Distributions are normalised with respect to total number of events acquired. Red colour for X-view and Blue colour for Y view.

The typical nature of strip multiplicity is shown in Figure 6.4. Though the peak of the distribution is around one or two, a long tail exists due to many strips in a layer giving signals. The primary ionization inside the RPC gas gap and flow of the charged particles towards their respective electrodes produces signals in the readout strips. The principle of signal induction by moving charges to the respective electrodes are relevant here to discuss. A detail discussion in this context is given

in [116]. The primary ionization takes place within a very small area  $0.1 \text{ cm}^2$  inside the gas chamber. The area of a pixel formed by the overlap of the X and Y strip is about 100 times larger than this. Hence only, a single multiplicity in the RPC is expected. But there are many other factors due to which higher multiplicity is observed in RPC.

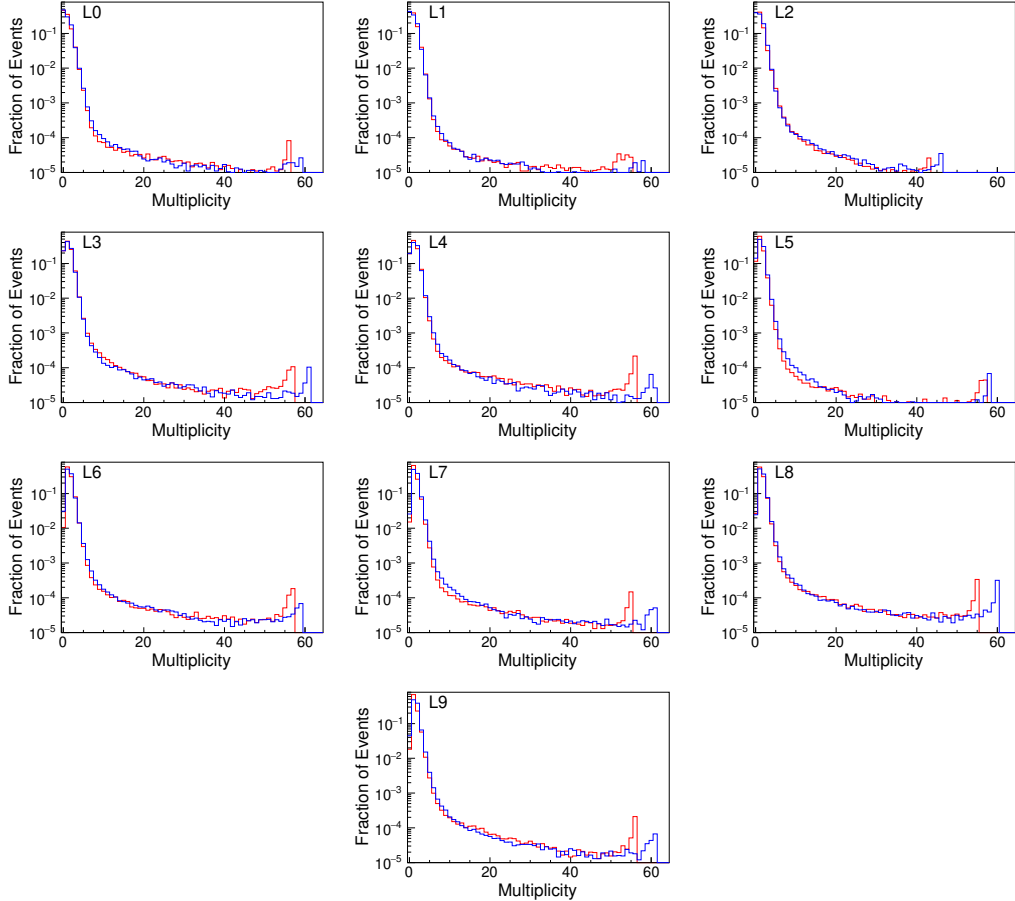


**Figure 6.4:** Relative distributions of layer hit multiplicities for all ten layers of mini-ICAL. Distributions are normalised with respect to total number of events acquired. Red colour for X-view and Blue colour for Y view.

One of the main reasons is the production of the secondary avalanches due to photons inside the gas gap. But using iso-butane in the gas mixture this possibility is reduced. The surface resistivity due to graphite coating is not exactly uniform over the entire electrode surface. In the region where the ionization took place, if the resistivity is less, the signal induction may spread over a wider region which can produce multiplicity more than one. Moreover, the cross-talk between two adjacent

RPC read-out strips also produces higher multiplicities. An RPC readout strip is electronically a transmission line. Hence, when a high-frequency signal is passing through a strip, it also induces signals in nearby strips. Except these, all RPCs strips share a common electrical ground. In such a scenario, if the net current is high, then it may induce signals in many strips. The long tail observed in Figure 6.4 is mainly due to correlated electronic noise in that layer. The intermediate region in Figure 6.4 is mainly due to the streamer formation inside the RPC. Overall, an average strip multiplicity of 1.6 is observed in mini-ICAL.

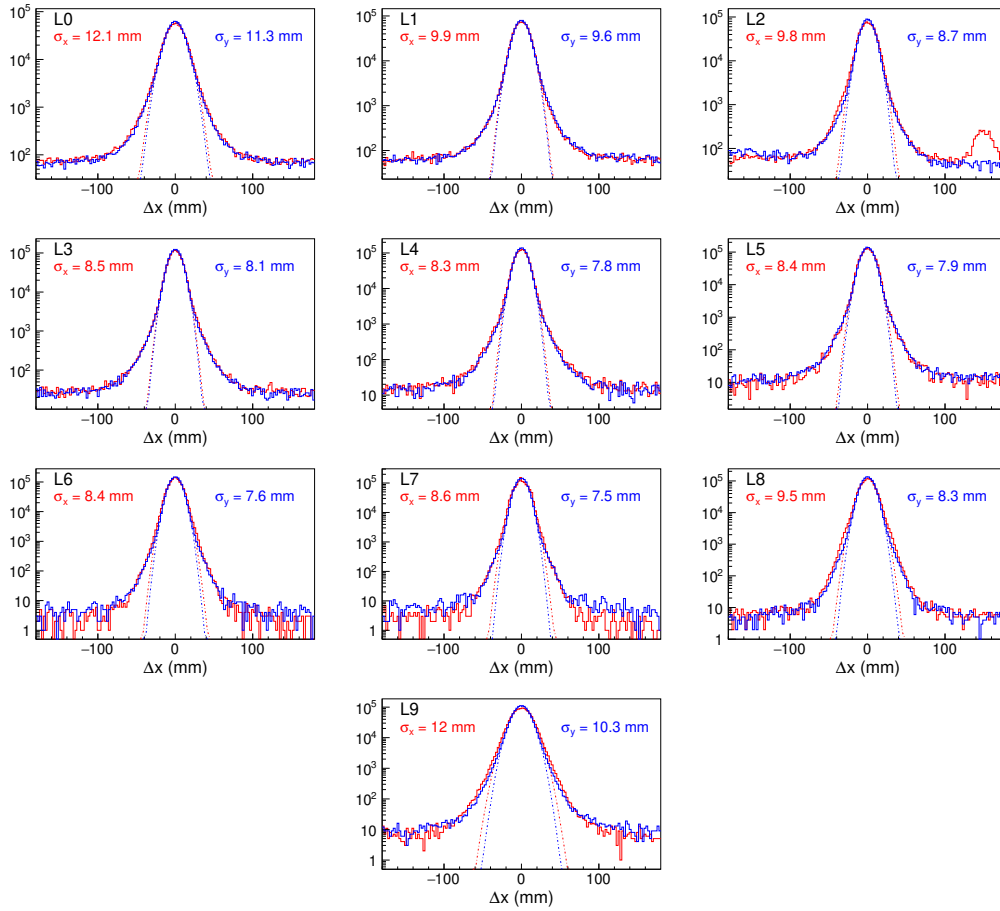


**Figure 6.5:** Position resolution in all ten layers of mini-ICAL. Red colour for X-view and Blue colour for Y view. Dashed line represents the Gaussian fitted function.

In the absence of a magnetic field, the muon tracks show linear behavior. The selected strips in the X- and Y- view are fitted separately with the straight-line fit which is explained in Chapter 2. The residual ( $\Delta R$ ) is defined as the difference

between a hit and the fit position. A hit in a layer is rejected, if it is more than seven strips away than the fit position in that layer ( $|\Delta R| > 7$ ). To avoid bias in determining the residual the calibrating layer is excluded from the fitting. The typical position residue distributions are shown in Figure 6.5. These distributions are fitted with Gaussian function and the Gaussian “ $\sigma$ ” is considered the position resolution. The distribution is peaking at zero, which shows the good mechanical alignment and an overall chamber alignment accuracy of better than  $100\ \mu\text{m}$  is obtained.

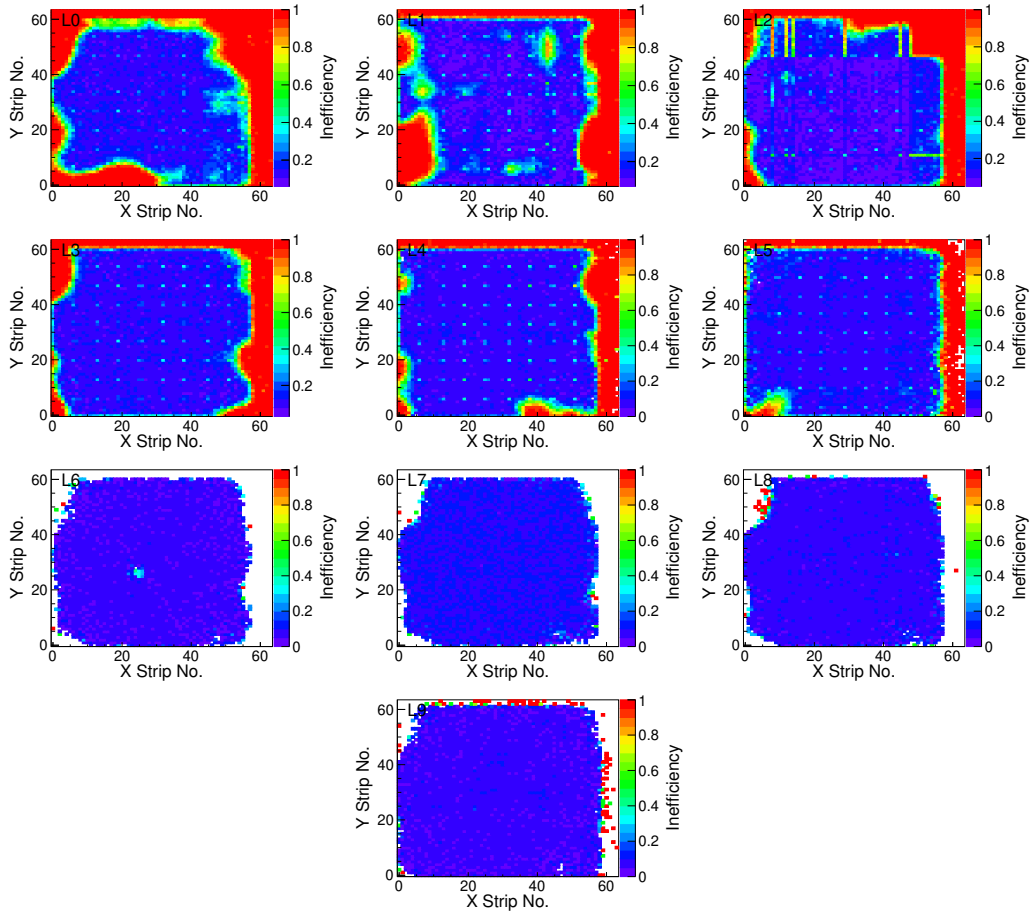


**Figure 6.6:** Correlated inefficiencies for all ten layers.

For each event, the muon trajectory information from the other nine layers is used to identify the intersection (both x and y coordinates) of the muon trajectory in  $L_i$ . The efficiency of each layer is calculated by excluding that layer in the straight-line fit of the muon trajectory. The efficiency plots have  $58 \times 62$  of 2D

pixels, where each pixel is of size  $3\text{ cm} \times 3\text{ cm}$ . Here, the efficiency of a layer is defined as the ratio of number of events where a hit is found within  $6\text{ cm}$  of the expected position of muon in that layer, without any hit in other parts of that layer, to the expected number of muons using the fit of hits in all other layers. The inefficiency is caused by charged particles that did not produce a signal larger than the discriminator threshold. The detailed description of the calculations of the efficiency maps is given in [85].

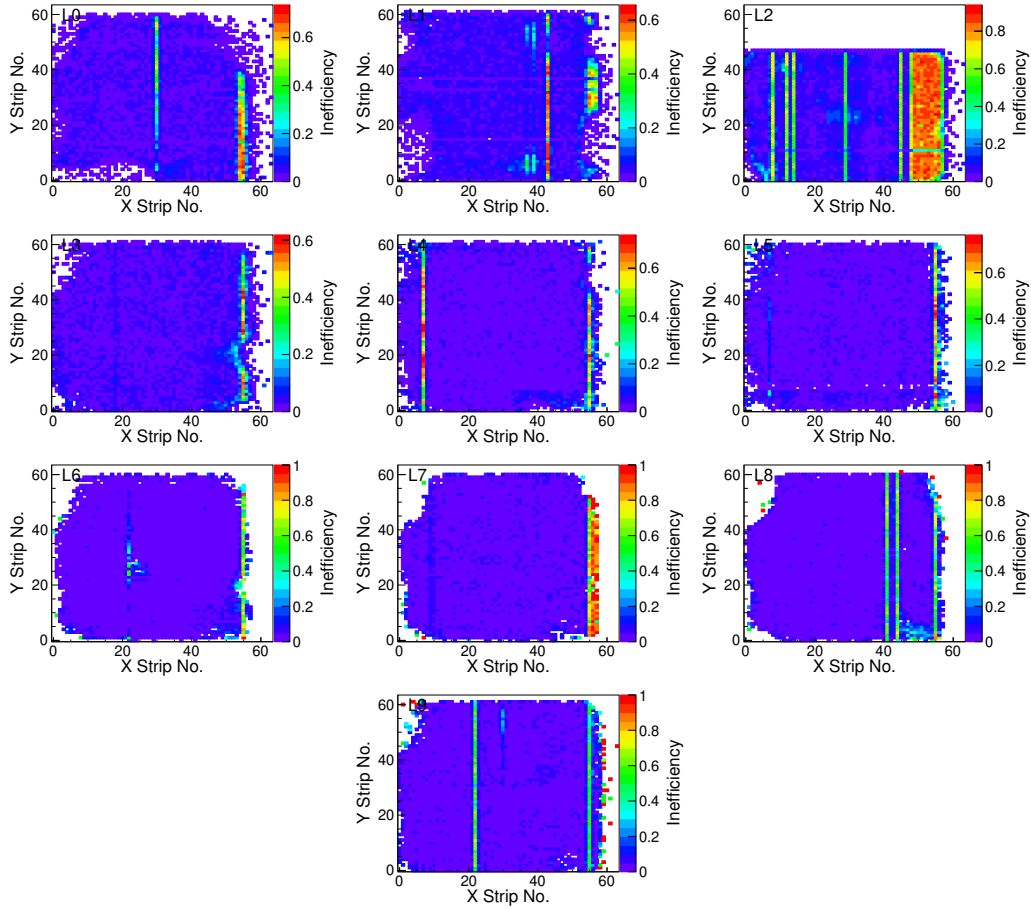


**Figure 6.7:** Uncorrelated inefficiency for all ten layers of mini-ICAL for the X-view.

For plots in Figure 6.6, the muon hit is checked in both X- and Y- view. Hence, it shows the inefficiency which is common to both X- and Y- view. The inefficiency matrix of spots is observed in layers- 0–5 is due to the spacer buttons located at these positions. This matrix is not visible in layers- 6–9. Also, it can be seen that Layers 6, 7, 8 and 9 show nearly 0% inefficiency throughout the region as these



are the hardware trigger layers. Also, there is a large region of inefficiency near the corners in many RPCs. As explained in Chapter 2, the difference in spacer height and/or thickness of glue at the edges is the dominant source of this inefficiency.

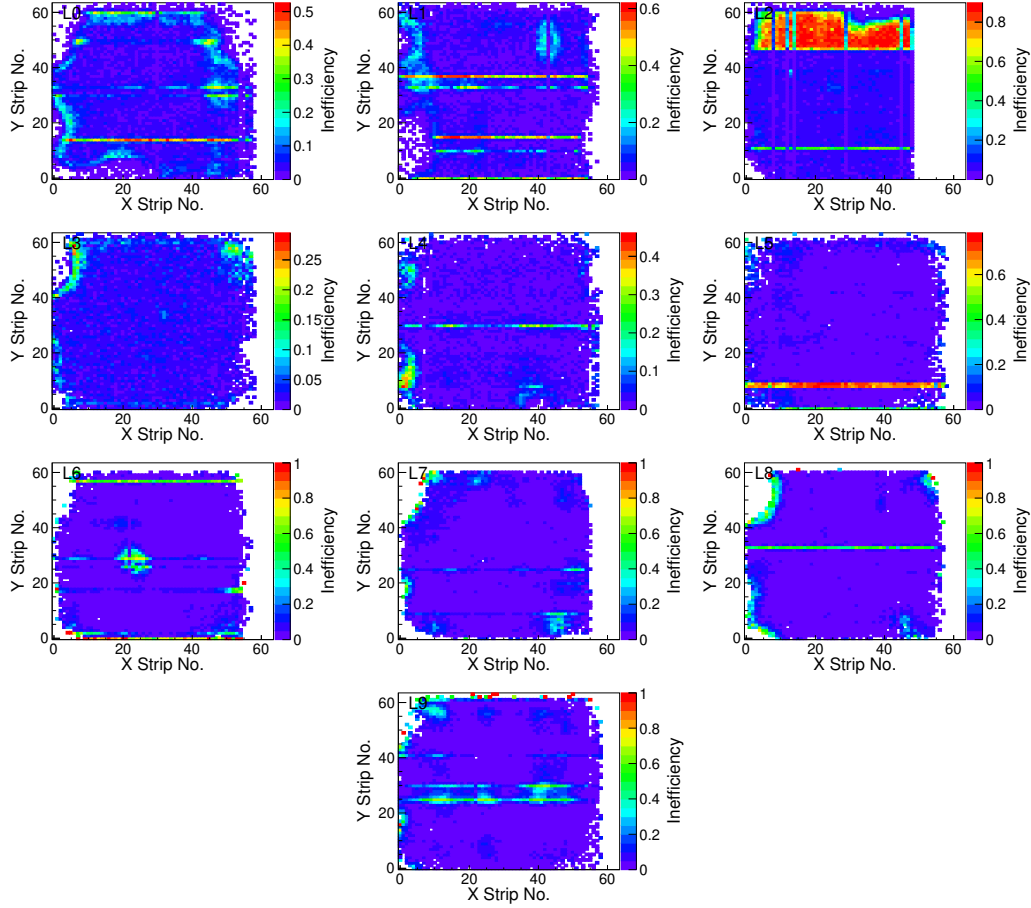


**Figure 6.8:** Uncorrelated inefficiency for all ten layers of mini-ICAL for the Y-view.

In Figure 6.7 and 6.8, the uncorrelated inefficiencies in X- and Y- plane for all layers are presented. Here, in some RPCs, there are entire strips in either X- or Y-plane which shows lower efficiencies. Also, in layer-2, there is inefficiency information beyond strip number 48 in both X-side and Y-side or it is shown highly inefficient, as there are on 6 ANUSPARSH-III AFE boards (8 channel per board) per side. Hence, the last 10/14 X/Y- strips are not connected.

It is expected that if the avalanche occurs near the center of a strip, the induced signal in that strip is much larger than those on the neighboring strips. As the pitch of pickup strips being 30 mm, and an inter-strip gap of 2 mm, it is expected

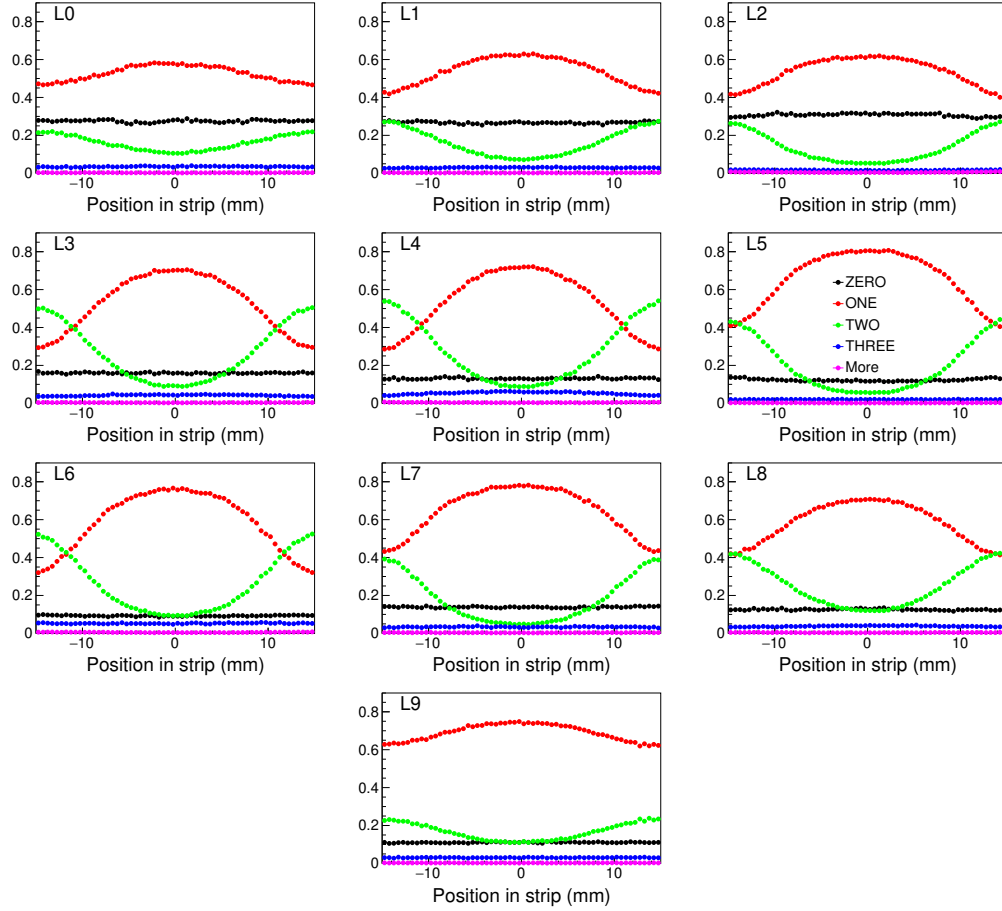


**Figure 6.9:** Strip multiplicity as a function of muon position in the strip for all 10 layers in X-view.

that a much larger fraction of events to show up with a strip multiplicity of one. In the second case, if the avalanche occurs in between the two strips, the induced signal will be shared by both the strips. The observed average strip multiplicity of these RPCs is 1.9. The strip multiplicity as a function of muon position in a strip for different layers is shown in Figures 6.9 and 6.10. The position is measured with respect to the center of the strip. It can be clearly observed in the data, that the idea of induced charge sharing between neighboring strips is correct.

As seen in these plots, there are almost no events with strip multiplicity of two, when the muon trajectory is at the center of the strip and similarly almost no events with strip multiplicity one, when the muon trajectory is at the boundary between two strips. The position of maxima and minima of the strip multiplicity

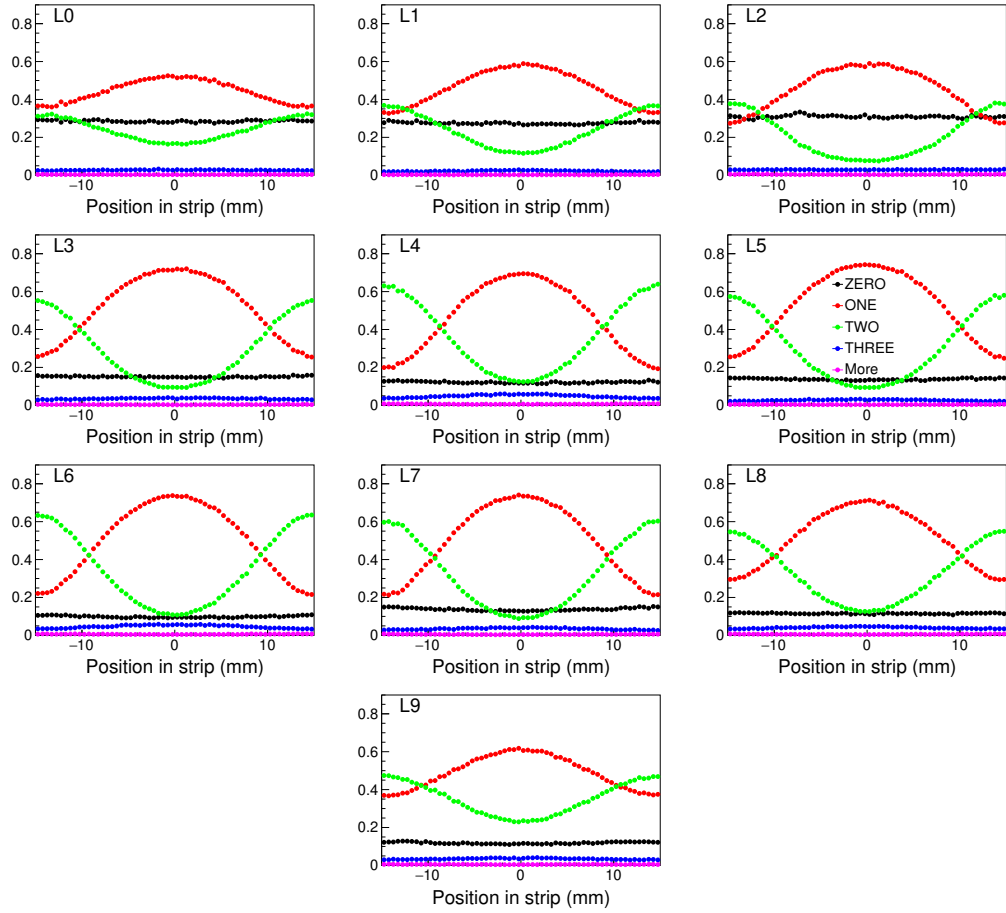


**Figure 6.10:** Strip multiplicity as a function of muon position in the strip for all 10 layers in Y-view.

distributions at the center and edge of the strips respectively also indicates that the position alignment of RPCs in the detector stack is accurate. It should also be noted that on an average the charge induced on one strip for an event with strip multiplicity of two is more than the charge induced for an event with strip multiplicity of one. The sharing of the induced signal on multiple strips depends on the position of the muon trajectory.

The observed time resolution of an RPC is obtained from the difference in the measured time and the time of the muon crossing that is expected to the layer/RPC. The corrections discussed in Chapter 2, have been applied to the measured time. The measured time resolutions in all layers are in the range of 0.9–1.1 ns and are presented in Figure 6.11.

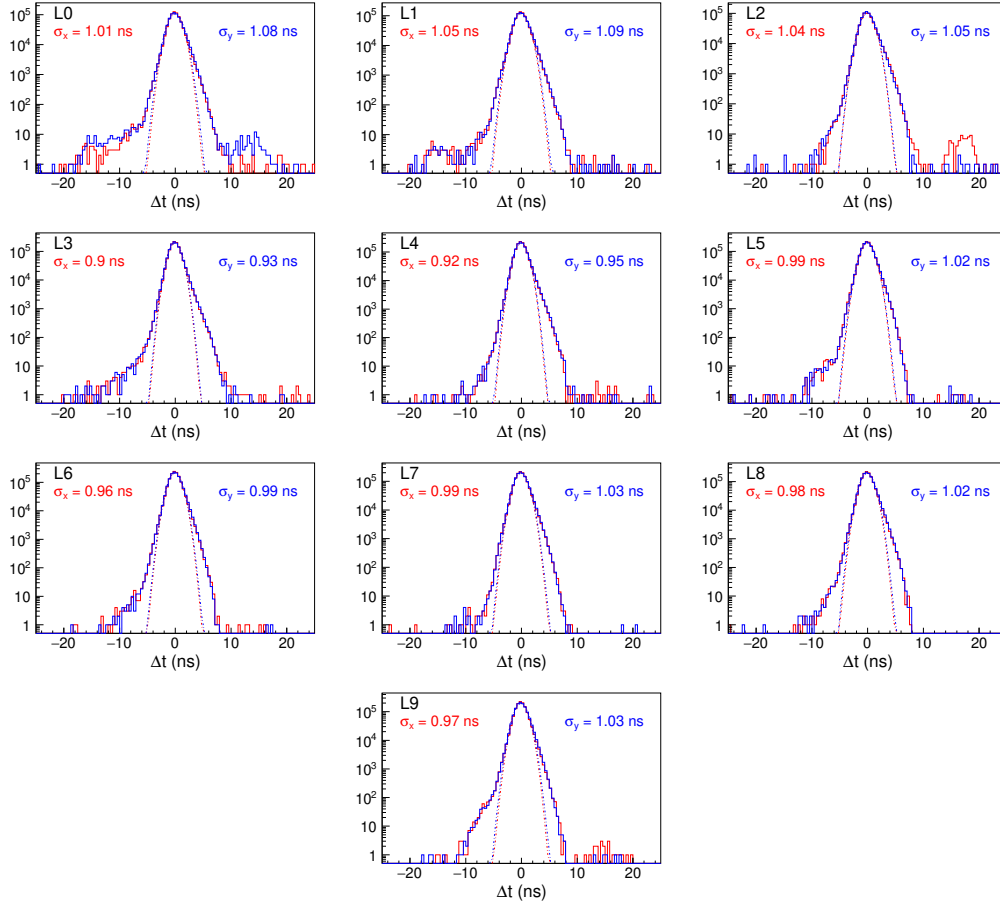


**Figure 6.11:** Time resolution for all 10 layers in mini-ICAL. Red colour for X-view and Blue colour for Y view. Dashed line represents the Gaussian fitted function.

## 6.2 mini-ICAL simulation

The atmospheric muon analysis is verified through an MC simulation. The CORSIKA[10] generator is used to generate the secondary particle at an experimental site. In the CORSIKA simulation, 20 million primary protons and 2 million Helium from 10 GeV to 1 PeV with spectral index  $-2.7$  is generated from the top of the atmosphere. The low energy and high energy interaction models used in CORSIKA generation are GEISHA and SIBYLL respectively. The generated primary proton energy is compared to the rigidity cutoff at different  $(\theta, \phi)$  bins. The primaries having energy above the rigidity cutoff is allowed to progress, otherwise, a new primary was generated. The kinematic information of the secondary particles which reach earth surface in the simulation is stored.

The simulation of secondary particles (in this case muons) through the detector geometry is performed by a package based on the GEANT4[4, 91] toolkit and INO specific digitization code. The entire mini-ICAL detector geometry, along with the building in which it is installed, is included in the simulation framework to account for all the materials incident muon is passing through. The magnetic field obtained from Finite Element simulation (Chapter 5) is also an input to the simulation code. Here, the z-component of the magnetic field ( $B_z$ ) is negligible. Hence, only the x- and y- component of the magnetic field (shown in Figure 6.12) are considered

In the GEANT4 simulation, the secondary particles are generated above the ceiling of the building. The various detector properties like uncorrelated and correlated inefficiencies, trigger efficiencies and strip multiplicity, that are estimated from analysing the cosmic ray muon data in absence of magnetic field (see Section 6.1) are incorporated during the digitization process of simulation. The various steps followed in the MC event generation are; the momentum ( $P_x, P_y, P_z$ ) of the particle (muon) from CORSIKA dataset and position is generated within the RPC region of the topmost trigger layer (i.e., layer-9). Using the co-ordinates of this point and the direction obtained from the momentum is extrapolated to the bottom trigger layer (layer-6 in this case) to test the trigger acceptance condition. If the extrapolated point in the bottom trigger layer is within the sensitive region of RPC, then the point is extrapolated on a plane on top of the ceiling to get the co-ordinate of the vertex for the simulation of the passage of a particle through the detector geometry.

When the particle, passes through an RPC (sensitive detector volume), the GEANT4 provides the (x, y, z) co-ordinate and the exact timestamp for that point. This information obtained from GEANT4 is translated into the strip information<sup>1</sup> for the corresponding Z plane. The pixel-wise correlated inefficiency map discussed in the previous section is used to incorporate the correlated inefficiencies in the sim-

---

<sup>1</sup>X and Y strip number and digitized time stamp according to the time smearing and TDC least count

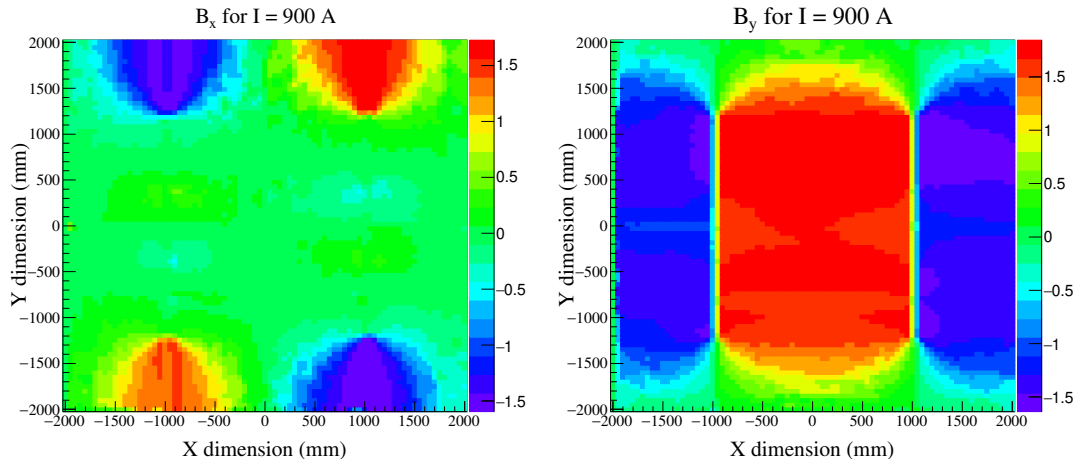


**Figure 6.12:** Magnetic field map at 900 A current, (left)  $B_x$  and (right)  $B_y$  in Tesla. Length in X- & Y- axis are in mm.

ulated event. The position (hit position with respect to the strip centre) dependent strip multiplicity, as shown in Figure 6.10 and 6.9 is used to implement the multiplicity effect. The uncorrelated inefficiencies for X and Y strips are incorporated independently based on strip multiplicity using the inefficiency map discussed in the previous section. The trigger efficiencies are incorporated only for the trigger layers (namely layers 6, 7, 8 and 9) in the X- or Y- plane to accept an event according to trigger condition during data acquisition. The simulated events and the events from the real data are passed through the same reconstruction algorithm.

### 6.3 Track Reconstruction in magnetic field

In presence of the magnetic field, the hits from muon (experiencing Lorentz force), will show a curvature representing the bending of muon trajectory. The standard Kalman fit algorithm developed for the ICAL detector is used for these trajectories. The momentum, zenith angle and the azimuthal angle of the incident muon are estimated through this fit. In order to study the performance of the algorithm, three lakh muons are generated from the center of the mini-ICAL detector just above the topmost iron layer. The events were generated in momentum range 0.5–6.5 GeV with uniform smearing over  $\cos\theta$  (in the range of  $[-1.0, -0.5]$ ) and  $\phi$

in the simulation package described above. The detectors were assumed to be 100% efficient. The clusters obtained are reconstructed using Kalman fit based reconstruction algorithm.

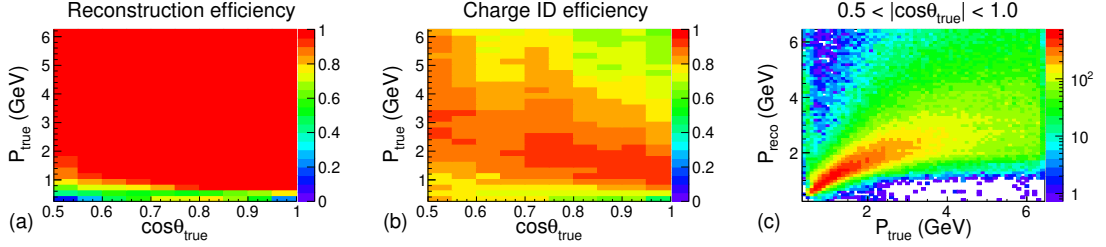


**Figure 6.13:** Muon reconstruction in mini-ICAL (a) reconstruction efficiency (b) charge identification efficiency (c) Reconstructed momentum ( $p_{reco}$ ) v/s true input muon momentum ( $p_{true}$ ) for all combined  $\cos\theta_{true}$ .

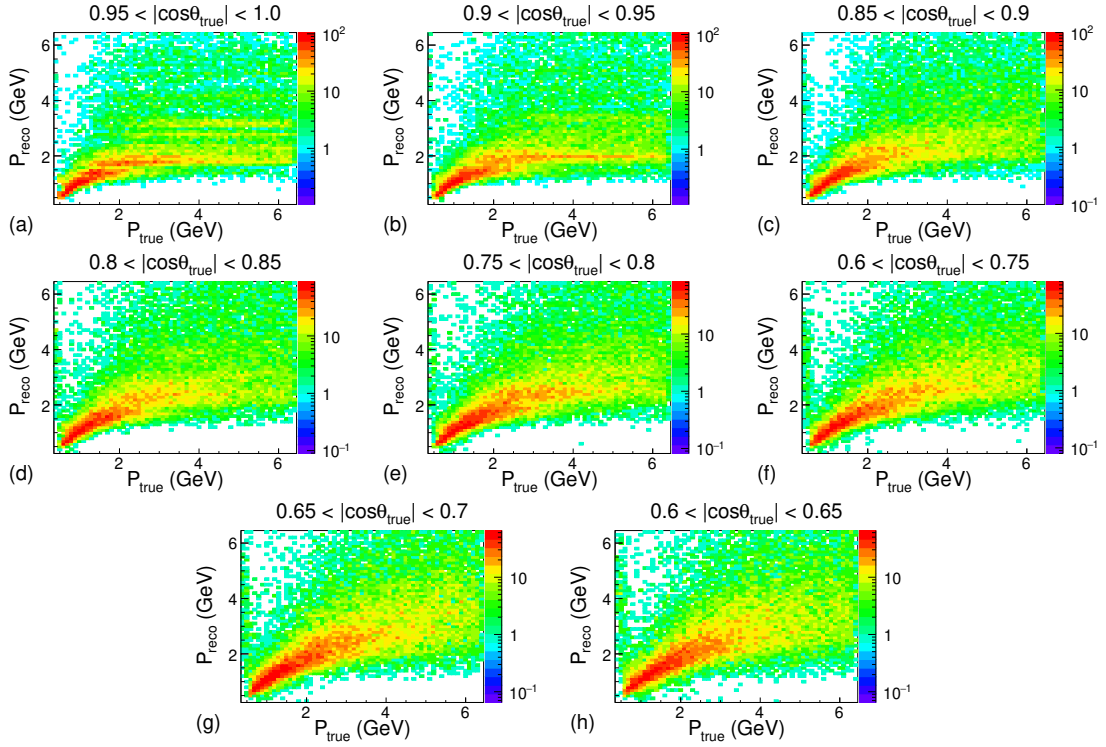


**Figure 6.14:** Reconstructed momentum ( $p_{reco}$ ) v/s true input muon momentum ( $p_{true}$ ) with different  $\cos\theta_{gen}$  bins.

In Figure 6.13(a) and (b) the reconstruction efficiency and the charge identification efficiency are shown. In Figure 6.13(c), the reconstructed momentum is plotted against the true muon momentum. In the figure, it is observed that beyond the true muon momentum of around 1 GeV, the reconstructed momentum starts

showing some saturation and it is dominant from 1.8 GeV.

In Figure 6.14, the reconstructed momentum is plotted against the true muon momentum for different  $\cos\theta_{gen}$  to understand the saturation. Here, it is observed that there is a mild dependence of saturation on the angle at which the muon is incident on the detector. As the  $\cos\theta_{gen}$  decreases, the saturation becomes less prominent.

## 6.4 Explicit Track Model Fit

To check, that the Kalman filter technique was not adding any bias in the fit, the momentum was reconstructed using the global track fitting by the least-squares method (LSM) which is explained in detail in [9]. The method's important statistical properties, together with its numerical simplicity, form the basis of the wide range of its application.

If the track model can be sufficiently well approximated by a linear model in the neighborhood of the measurements, and if the errors vary sufficiently little with the track parameters that they can be considered as being constant in the neighborhood of an individual track's path, then the LSM estimation has minimum variance among the class of linear and unbiased estimates.

The track model is, in general, the set of solutions of the equations of motion, whereas the track model in the LSM is the linear expansion of the functions  $f(p)$ , where  $f$  is a deterministic function of the 5-vector of track parameter  $p$ . At a reference surface  $Z_\Gamma$ ,  $p$  is defined by  $(x, y)$  coordinates and the momentum 3-vector. At a first approximation,

$$f(p) = f(p_0) + A \cdot (p - p_0) + O \cdot (p - p_0)^2 + \dots \quad (6.1)$$

with,  $A = \partial f(p) / \partial p$  at  $p = p_0$ .

In addition to the track model, the 'weight matrix'  $W$ , which is defined as the



inverse of the covariance matrix (“error matrix”)  $V$ , must be evaluated.

$$W = V^{-1} \quad (6.2)$$

In simple cases the measurement errors are uncorrelated, i.e.  $W$  is of the form,

$$(W)_{ij} = \frac{\delta_{ij}}{\sigma_j^2} \quad (6.3)$$

where  $\sigma_j$  is the standard deviation of  $j^{\text{th}}$  measurement  $\varepsilon_j$ . In general, mainly in the cases of multiple scattering,  $W$  will also have off-diagonal terms and matrix inversion is necessary to obtain it numerically. The LSM tries to minimize the function,

$$\chi^2 = [f(p_0) + A \cdot (p - p_0) - m]^T \cdot W \cdot [f(p_0) + A \cdot (p - p_0) - m] \quad (6.4)$$

where  $m$  is “realization” of specific measurements, in this case vector of measurements,  $(x, y)$  ( $2 \times N$ , number of track points). Differentiating  $\chi^2$  with respect to  $p$  and putting  $\partial\chi^2/\partial p = 0$  yields,

$$p = p_0 + (A^T W A)^{-1} A^T W (m - f(p_0)) \quad (6.5)$$

Theoretically, it is known that the momentum resolution is inversely proportional to the magnetic field strength and the square of the length of track and directly proportional to the position resolution. The position resolution of the RPC detector is around 7–11 mm. Hence, with 10 layers in mini-ICAL (giving a limited number of measured points compared to ICAL detector), it is expected that the momentum resolution will be poorer. But this doesn’t explain the saturation of the reconstructed momentum as observed in this case.

In order to understand, the saturation in the reconstructed momentum muons

are generated from the center of the mini-ICAL detector just above the topmost iron layer with  $\cos\theta_{gen} = -1$  (going vertically straight downwards). The events were generated in the momentum range of 0.5–20.5 GeV. These same events were digitized by different strip width, to study the effect of position resolution on the momentum measurement.

In Figure 6.15, it can be observed that the reconstructed momentum shows saturation for various different strip widths. This saturation in reconstructed momentum is observed as a function of position resolution. It can be observed that there is a strong dependence of position resolution on the reconstructed momentum. When the position resolution is of the order of a few hundred microns, there is no saturation observed in the reconstructed momentum. But, as the position resolution becomes poorer, the reconstructed momentum gradually starts to saturate at different momentum values. The magnetic field in the mini-ICAL detector is along the Y-direction and the particle is moving along Z-direction. Hence, the bending of the track is supposed to be observed only along X co-ordinate. It is expected that the track will not show any deviation in Y co-ordinate except for multiple scattering.

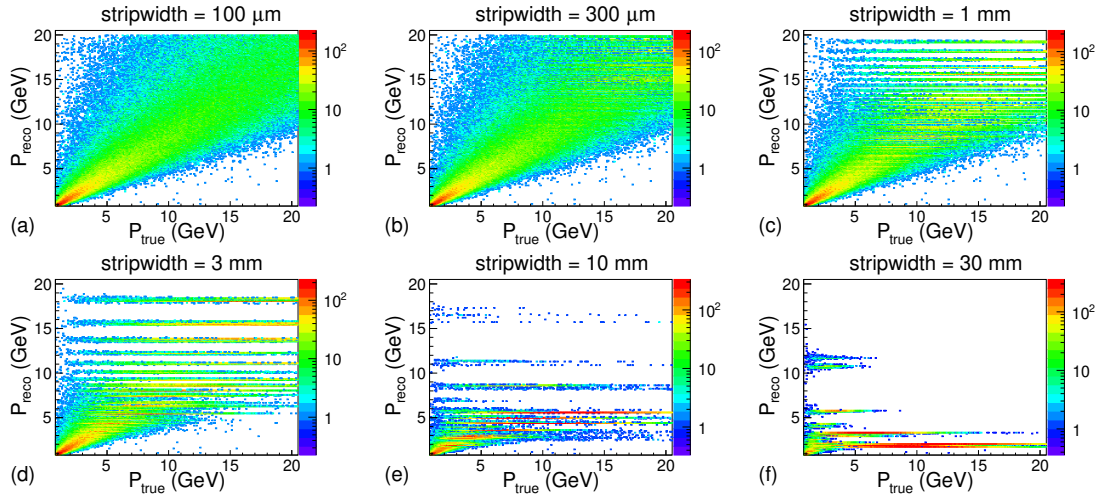


**Figure 6.15:** Reconstructed momentum ( $p_{reco}$ ) v/s true input muon momentum ( $p_{true}$ ) with different virtual strip width.

In Figure 6.15(f), it can be seen that the saturation is not only observed around

one momentum value but, it is actually distributed for several different reconstructed momenta. For the saturation band about 3 GeV, the hit pattern shows the same Y- strip number for all the layers. In the XZ- plane, the X- strip number for layers 9 to 4 is 27 and for layers, 3 to 0, is 28. Whenever this particular hit pattern is observed, the momentum is reconstructed at a fixed value of 3.28 GeV. Similarly, for the saturation bands about 1.69, 1.97, 2.06, 5.76 GeVs, in the XZ- plane, the same X- strip number is observed for several layers and after that, the observed X- strip number is deviated by  $\pm 1$  strip. The saturation at about 1.97 and 2.06 GeVs in effect actually overlap each other. In all these cases, the Y- strip number remains the same for all the layers. For the saturation bands other than these five, they are observed when in the hit pattern, there is also a deviation in Y co-ordinate. This deviation is mainly due to multiple scattering in iron layers. Hence, the different saturation bands observed in the reconstructed momentum corresponds to different hit patterns.

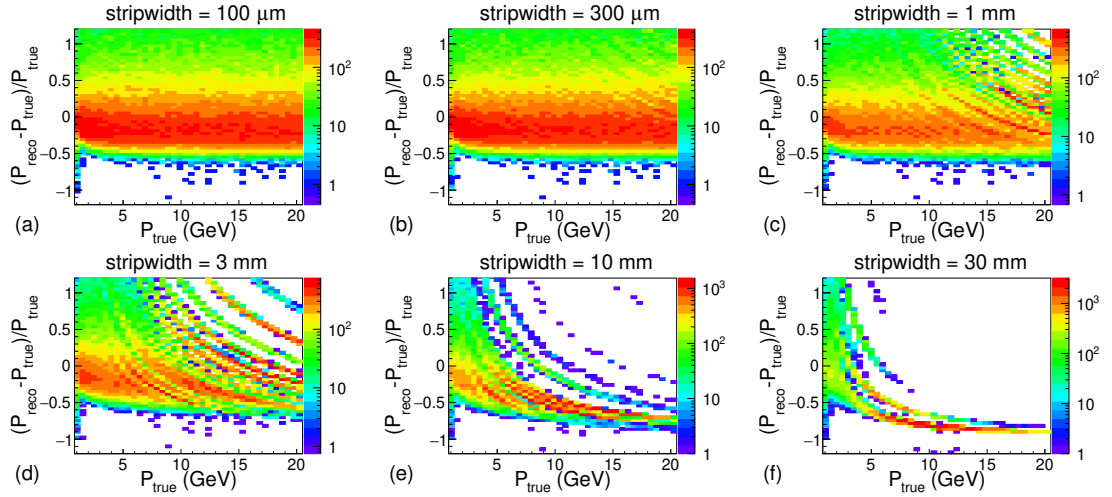


**Figure 6.16:**  $(p_{reco} - p_{true})/p_{true}$  v/s true input muon momentum ( $p_{true}$ ) for different virtual strip width.

To observe, the momentum resolution,  $(p_{reco} - p_{true})/p_{true}$  is plotted against true input muon momentum. In Figure 6.16, it can be observed that there are formation of bands (curvature in shape) when the stripwidth 1mm and above. Also, the saturation bands intensify as the stripwidths increases. In Figure 6.16

(f), the saturation is so prominent 1.8 GeV that if the slice of the plot is taken for true input momentum of 1.8–8 GeV in Y-axis, three different peaks are observed in the  $(p_{reco} - p_{true})/p_{true}$  distribution. For the true input momentum beyond 8 GeV, one or peaks are observed in the  $(p_{reco} - p_{true})/p_{true}$  distribution. In such a scenario, it is very difficult to determine the momentum resolution of muon tracks.

## 6.5 Momentum spectra of cosmic ray muons

The measured momentum spectrum of cosmic ray muons is distorted due to the finite resolution, limited trigger acceptance and other systematic effects of the detector. This leads to the transfer of events between different momentum bins. Hence in order to allow a direct comparison of experimental measurement with theoretical predictions, the measurements are unfolded for the detector effects. The detector response matrix  $R$  (as shown in Figure 6.17(a)) in the unfolding procedure is derived using the CORSIKA events simulated using the detector simulation code as described above. The regularized unfolding method used and investigated for the current problem is iterative Bayesian Unfolding [11].

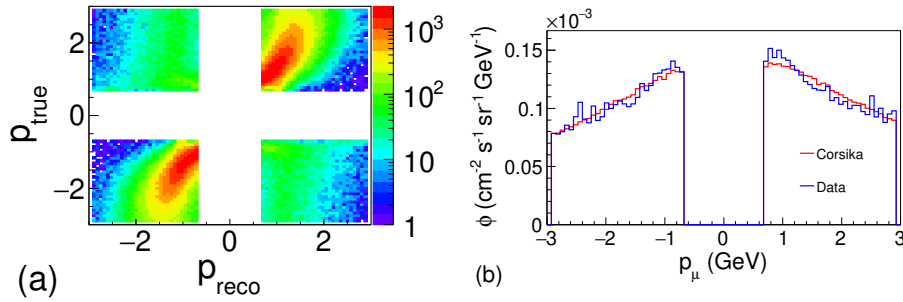


**Figure 6.17:** Unfolding of data with CORSIKA simulation.

In the Bayesian technique, the background in each reconstructed momentum bin and efficiency of each true momentum bin is calculated. The reconstructed data and MC, are corrected for the fake rate. During the unfolding, the efficiency is also corrected. After the unfolding the distribution is normalized to calculate the flux by using the following formula;

$$\Phi_i = \frac{N_i}{\epsilon_{daq} \times T_{tot} \times \lambda} \quad (6.6)$$

where,  $\Phi_i$  is the muon flux in  $i^{th}$  bin,  $N_i$  is the number of reconstructed muon per GeV in  $i^{th}$  bin,  $\epsilon_{daq}$  is the efficiency due to the dead time in data acquisition system,  $T_{tot}$  is the total time taken to record the data (in seconds) including DAQ's dead time (0.5 ms/event) and  $\lambda$  is accepted solid angle times the surface area (A) which is given as;

$$\lambda = A \times \int_{\theta_1}^{\theta_2} \sin\theta d\theta \times \int_{\phi_1}^{\phi_2} d\phi \quad (6.7)$$

This is carried out for each momentum bin and the result is compared with the CORSIKA flux as presented in Figure 6.17(b).

## 6.6 Summary

The observations of atmospheric muons from the mini-ICAL detector are summarized here. Also, the detector simulation of mini-ICAL is briefly explained. The saturation of reconstructed muon beyond a 1.8 GeV of input momentum is observed. It can be concluded that the dominant reason for the saturation effect in reconstructed is the poor position resolution of RPCs and the limited number of tracker layers in the mini-ICAL. Using the unfolding technique, the muon momentum spectrum is observed and the results are compared with the CORSIKA model.



# Chapter 7

## Summary and future scope

The INO collaboration plans to study the neutrino oscillations in the atmospheric sector with a 50 kt magnetized ICAL detector. The ICAL detector R&D program is running at full pace and several prototype detectors have been successfully built. These stacks have been extensively used to study the performance and long term stability of the RPCs using cosmic-ray muons. The various detector properties like position and time resolution of RPCs, detector inefficiencies, strip multiplicities, detector noise, etc are studied using these RPC stacks.

One of the most important experimental observations of the sign of the parameter  $\Delta m_{32}^2$  is to distinguish upward-going and downward-going muon events as well as charge of muons in both cases. An offline calibration procedure has been developed to improve the time resolution of large-area single gap RPCs. Using this method, the RPCs can be operated with the detection efficiency of more than 95% and timing resolution of better than 1 ns can be achieved. During the commissioning phase of the ICAL detector, before installing, all the RPCs will be in a test facility on the surface in a detector stack. A cosmic ray muon data collected for 3-4 days is enough to estimate all the offset corrections to achieve better than 1 ns time resolution of all channels. However, it is important to note that the correction factors obtained are valid only for a particular set of operating parameters

of the RPCs. The correction factors will not be valid if the operating HV, gas composition or pressure are changed. In the electronics design, the pulse width at the discriminator threshold is recorded along with the arrival time of the signal. This information, which is called Time over Threshold (ToT) is a function of the width of the avalanche gain, using which the timing information can be corrected in offline analysis. This technique has the advantage that it can be applied, and is independent of the RPC operating conditions at the surface. It is expected to obtain timing resolution better than 1 ns in ICAL detector using the offline correction for timing information using the ToT technique.

The ICAL detector is sensitive to detect the interactions of atmospheric  $\nu_\mu$ s arising from  $\nu_\mu \rightarrow \nu_\mu$  and  $\nu_e \rightarrow \nu_\mu$  oscillation channels. The accurate determination of the energy and direction of final state particles (muons and hadrons) in these interactions is crucial to achieving the physics goal of the ICAL. To calibrate the ICAL response to the muons and hadrons, a detector simulation framework has been developed using the GEANT4 toolkit. For easy sharing of geometrical parameters and various other inputs like magnetic field map, strip health information, etc, a database using “PostgreSQL” language is implemented in the simulation framework. The database helps in handling different versions of parameters using tags and distributes them to all the users. An INO specific digitization algorithm has been implemented in the simulation framework of the ICAL detector. This helps in including various detector properties like position resolution, time resolution, strip multiplicities, detector inefficiencies, electronic and detector noises, etc into the simulation.

In the reconstruction algorithm, a Kalman filter algorithm is used to fit the track-like hits and estimate the momentum of the muon from the curvature. If the vertex and endpoint of a muon track are within the fiducial volume of the detector, then the range of muons is precisely known. The momentum measurement from the range of muons inside the detector gives a better estimation than curvature



measurement. To improve the estimation of the momentum/energy of muons an algorithm to tag fully contained muon track has been implemented. A method of calibration has been developed using the correlation of the range of muons and its momentum. For fully contained muon track, there is a substantial improvement observed in the momentum resolution using the calibration from pathlength.

An important feature of the ICAL detector is its sensitivity to hadrons over a wide range of energies. This allows the reconstruction of energy and direction of incoming muon neutrino in CC events by combining reconstructed energies and directions of muons and hadrons. It also enables the detection of neutral current events (for all three flavors), CC-DIS events by  $\nu_e$  and a fraction of CC events of  $\nu_\tau$ . The information contained in all these events adds crucially to our knowledge of neutrino oscillations. The response of ICAL to hadrons has been studied. A clustering algorithm has been implemented to identify all the hits due to hadron shower. An algorithm to remove ghost hit has been developed to avoid over counting. A calibration technique is developed to estimate hadron energy using the number of hits from the shower. Using the width of the shower, a method to reconstruct hadron shower direction has been implemented. The clustering algorithm has been tested in the presence of noise to test its ability to reject noise hits.

The various tests to study the RPC performance and its properties were done with different electronics including the final design for the ICAL experiment. Also, these were tested in the absence of a magnetic field. To study the behavior of electronics in the fringe field of the magnet as well as to understand various mechanical challenges in building the ICAL magnet, a scaled-down version ( $\sim 1/600^{th}$  size) of the ICAL detector has been built. The mini-ICAL detector has been commissioned with 10 layers of RPC and has been operational since May 2018 with 1.5 T magnetic field. The magnetic field has been closely matched with the simulation using MAGNET software.

The performance of the RPCs along with front-end electronics has been studied

in the mini-ICAL detector using cosmic muon data sample. A full simulation of the mini-ICAL detector has been developed using the GEANT4 toolkit. The Kalman filter based reconstruction algorithm already developed for ICAL detector has been adapted to reconstruct cosmic muon events in the mini-ICAL data. During the testing of the algorithm, a saturation effect has been observed in the reconstructed momentum of muons beyond the true momentum of 1.8 GeV. From the study presented here, it can be concluded that the dominant reason for the saturation effect in the reconstructed muon momentum is the poor position resolution of the RPCs (as compared to the other tracking system in the experiment of high energy physics) and the limited number of RPC layers in the mini-ICAL detector. Due to these limitations, the momentum spectrum of atmospheric muons is observed up to 3 GeV and the results are compared with the CORSIKA model.

# Appendices



# Appendix A

## Vavilov function

The Vavilov PDF in the standard form is defined by [117]

$$P(x; \kappa, \beta^2) = \frac{1}{2\pi i} \int_{c-i\infty}^{c+i\infty} \phi(s) e^{xs} ds, \quad (\text{A.1})$$

where

$$\phi(s) = e^C e^{\psi(s)}, C = \kappa(1 + \beta^2\gamma), \quad (\text{A.2})$$

and

$$\psi(s) = s \ln \kappa + (s + \beta^2\kappa) \cdot \left[ \int_0^1 \frac{1 - e^{-st/\kappa}}{t} dt - \gamma \right] - \kappa e^{-s/\kappa} \quad (\text{A.3})$$

where  $\gamma = 0.577\dots$  is the Euler's constant. The parameters *mean* and *variance* ( $\sigma^2$ ) of the distribution in equation A.1 are given by,

$$\text{mean} = \gamma - 1 - \ln \kappa - \beta^2; \sigma^2 = \frac{2 - \beta^2}{\kappa} \quad (\text{A.4})$$

For  $\kappa \leq 0.05$ , the Vavilov distribution may be approximated by the Landau distribution, while for  $\kappa \geq 10$ , it may be approximated by Gaussian distribution with corresponding mean and variance.

To fit the hit distributions in Chapter 4, the Vavilov function  $P(x; \kappa, \beta^2)$  which is built into the ROOT package, has been modified to the form,

$$\frac{a_4}{a_3} P\left(\frac{x - a_2}{a_3}; a_0, a_1\right) \quad (\text{A.5})$$

This has been done to account for the x-scaling ( $a_3$ ), normalization ( $a_4$ ) and the shift of the peak to a non-zero value ( $a_2$ ). Clearly,  $a_0 = \kappa$  and  $a_1 = \beta^2$ . The modified mean and variance for the Vavilov distribution are,

$$Mean_{vavilov} = (\gamma - 1 - \ln a_0 - a_1) a_3 + a_2, \sigma_{vavilov}^2 = \frac{2 - a_1}{2P_0} a_3^2 \quad (\text{A.6})$$

# Bibliography

- [1] A. Kumar, A. M. Vinod Kumar, Abhik Jash, et al. *Pramana*, 88(5):79, Apr 2017.
- [2] S. Pal, B.S. Acharya, G. Majumder, et al. *Journal of Cosmology and Astroparticle Physics*, 2012(07):033, 2012.
- [3] G. Majumder et al. *Nucl. Instrum. Meth. A*, 735:88–93, 2012.
- [4] S. Agostinelli, J. Allison, K. Amako, et al. *Nucl. Instrum. Meth. A*, 506(3):250 – 303, 2003.
- [5] A Chatterjee, K K Meghna, R Kanishka, et al. *Journal of Instrumentation*, 9(07):P07001, 2014.
- [6] M M Devi, A Ghosh, D Kaur, et al. *JINST*, 8(11):P11003–P11003, nov 2013.
- [7] T. Sanuki, M. Honda, T. Kajita, K. Kasahara, and S. Midorikawa. *Phys. Rev. D*, 75:043005, Feb 2007.
- [8] M. Honda, T. Kajita, K. Kasahara, S. Midorikawa, and T. Sanuki. *Phys. Rev. D*, 75:043006, Feb 2007.
- [9] R. Frühwirth, M. Regler, R.K. Bock, H. Grote, and D. Notz. *Chapter 3, Data Analysis Techniques for High-Energy Physics*. Cambridge Monographs on Partic. Cambridge University Press, 2000.
- [10] D. Heck, J. Knapp, J. N. Capdevielle, G. Schatz, and T. Thouw. CORSIKA: A Monte Carlo code to simulate extensive air showers. Technical report, Institute of Nuclear Physics (IK), 1998.
- [11] G. D’Agostini. *Nucl. Instrum. Meth. A*, 362(2):487 – 498, 1995.

- [12] L. Meitner and W. Orthmann. *Z. Phys.*, 60:143–155, 1930.
- [13] Pauli W. Letter to the participants of workshop at tübingen, germany, 1930.
- [14] W. pauli, 2000.
- [15] E. Fermi. *La Ricerca Scientifica*, 2:12, 1933.
- [16] E. Fermi. *Z. Phys.*, 88:161, 1934.
- [17] E. Fermi. *Nuovo Cimento*, 11:1–19, 1934.
- [18] H. Bethe and R. Peirels. *Nature*, 133:532, 1934.
- [19] C. L. Cowan, F. Reines, F. B. Harrison, H. W. Kruse, and A. D. McGuire. *Science*, 124(3212):103–104, 1956.
- [20] F. Reines and C. L. Cowan. *Nature*, 178:446–449, 1956.
- [21] G. Danby, J-M. Gaillard, K. Goulianos, et al. *Phys. Rev. Lett.*, 9:36–44, Jul 1962.
- [22] M. L. Perl, G. S. Abrams, A. M. Boyarski, et al. *Phys. Rev. Lett.*, 35:1489–1492, Dec 1975.
- [23] K. Kodama, N. Ushida, C. Andreopoulos, et al. *Physics Letters B*, 504(3):218 – 224, 2001.
- [24] John N. Bahcall. *Phys. Rev. Lett.*, 12:300–302, Mar 1964.
- [25] C.V. Achar, M.G.K. Menon, V.S. Narasimham, et al. *Physics Letters*, 19(1):78 – 80, 1965.
- [26] C.V. Achar, M.G.K. Menon, V.S. Narasimham, et al. *Physics Letters*, 18(2):196 – 199, 1965.
- [27] F. Reines, M. F. Crouch, T. L. Jenkins, et al. *Phys. Rev. Lett.*, 15:429–433, Aug 1965.
- [28] Y. Fukuda, T. Hayakawa, E. Ichihara, et al. *Phys. Rev. Lett.*, 81:1158–1162, Aug 1998.
- [29] K. Hirata, T. Kajita, M. Koshiba, et al. *Phys. Rev. Lett.*, 58:1490–1493, Apr 1987.
- [30] R. M. Bionta, G. Blewitt, C. B. Bratton, et al. *Phys. Rev. Lett.*, 58:1494–



- 1496, Apr 1987.
- [31] E. N. Alekseev, L. N. Alekseeva, V. I. Volchenko, and I. V. Krivosheina. *JETP Lett.*, 45:589–592, 1987.
  - [32] T. Araki et al. *Nature*, 436:499, 2005.
  - [33] G. Bellini, J. Benziger, S. Bonetti, et al. *Physics Letters B*, 687(4):299 – 304, 2010.
  - [34] G. Bellini, J. Benziger, D. Bick, et al. *Physics Letters B*, 722(4):295 – 300, 2013.
  - [35] M. G. Aartsen, R. Abbasi, Y. Abdou, et al. *Phys. Rev. Lett.*, 111:021103, Jul 2013.
  - [36] IceCube Collaboration. *Science*, 342(6161), 2013.
  - [37] M. G. Aartsen, M. Ackermann, J. Adams, et al. *Phys. Rev. Lett.*, 113:101101, Sep 2014.
  - [38] Steven Weinberg. *Phys. Rev. Lett.*, 19:1264–1266, Nov 1967.
  - [39] Abdus Salam. *Conf. Proc.*, C680519:367–377, 1968.
  - [40] Sheldon L. Glashow. *Nuclear Physics*, 22(4):579 – 588, 1961.
  - [41] F.J. Hasert, H. Faissner, W. Krenz, et al. *Physics Letters B*, 46(1):121 – 124, 1973.
  - [42] F.J. Hasert, S. Kabe, W. Krenz, et al. *Physics Letters B*, 46(1):138 – 140, 1973.
  - [43] F.J. Hasert, S. Kabe, W. Krenz, et al. *Nuclear Physics B*, 73(1):1 – 22, 1974.
  - [44] A. Benvenuti, D. C. Cheng, D. Cline, et al. *Phys. Rev. Lett.*, 32:800–803, Apr 1974.
  - [45] S. Chatrchyan, V. Khachatryan, A.M. Sirunyan, et al. *Physics Letters B*, 716(1):30 – 61, 2012.
  - [46] G. Aad, T. Abajyan, B. Abbott, et al. *Physics Letters B*, 716(1):1 – 29, 2012.
  - [47] B. Adeva, O. Adriani, M. Aguilar-Benitez, et al. *Physics Letters B*, 231(4):509 – 518, 1989.

- [48] D. DeCamp, B. Deschizeaux, J.-P. Lees, et al. *Physics Letters B*, 231(4):519 – 529, 1989.
- [49] M.Z. Akrawy, G. Alexander, J. Allison, et al. *Physics Letters B*, 231(4):530 – 538, 1989.
- [50] P. Aarnio, P. Abreu, W. Adam, et al. *Physics Letters B*, 231(4):539 – 547, 1989.
- [51] B. Pontecorvo. *Sov. Phys. JETP*, 6:429, 1957. [Zh. Eksp. Teor. Fiz.33,549(1957)].
- [52] B. Pontecorvo. *Sov. Phys. JETP*, 7:172–173, 1958. [Zh. Eksp. Teor. Fiz.34,247(1957)].
- [53] B. Pontecorvo. *Sov. Phys. JETP*, 26:984–988, 1968. [Zh. Eksp. Teor. Fiz.53,1717(1967)].
- [54] Ziro Maki, Masami Nakagawa, and Shoichi Sakata. *Progress of Theoretical Physics*, 28(5):870–880, 11 1962.
- [55] M. Tanabashi, K. Hagiwara, K. Hikasa, et al. *Phys. Rev. D*, 98:030001, Aug 2018.
- [56] L. Wolfenstein. *Phys. Rev. D*, 17:2369–2374, May 1978.
- [57] S. P. Mikheyev and A. Yu. Smirnov. *Sov. J. Nucl. Phys.*, 42:913–917, 1985. [305(1986)].
- [58] Ivan Esteban, M. C. Gonzalez-Garcia, Alvaro Hernandez-Cabezudo, Michele Maltoni, and Thomas Schwetz. *Journal of High Energy Physics*, 2019(1):106, Jan 2019.
- [59] *NuFIT webpage*.
- [60] Animesh Chatterjee, Raj Gandhi, and Jyotsna Singh. *Journal of High Energy Physics*, 2014(6):45, Jun 2014.
- [61] N. Dash, V.M. Datar, and G. Majumder. *Astroparticle Physics*, 70:33 – 38, 2015.
- [62] Sandhya Choubey, Anushree Ghosh, and Deepak Tiwari. *Journal of Cosmol-*

- ogy and Astroparticle Physics*, 2018(05):006, 2018.
- [63] R. Santonico and R. Cardarelli. *Nuclear Instruments and Methods in Physics Research*, 187:377–380, 1981.
- [64] V.M. Datar, Satyajit Jena, S.D. Kalmani, et al. *Nucl. Instrum. Meth. A*, 602(3):744 – 748, 2009. Proceedings of the 9th International Workshop on Resistive Plate Chambers and Related Detectors.
- [65] Bheesette Satyanarayana. *Design and Characterisation Studies of Resistive Plate Chambers*. PhD thesis, Indian Institute of Technology Bombay, 2012.
- [66] Y. Fukuda, T. Hayakawa, E. Ichihara, et al. *Phys. Rev. Lett.*, 81:1562–1567, Aug 1998.
- [67] M. Honda, T. Kajita, K. Kasahara, and S. Midorikawa. *Phys. Rev. D*, 70:043008, Aug 2004.
- [68] S. Roesler, R. Engel, and J. Ranft. The monte carlo event generator dpmjet-iii. In Andreas Kling, Fernando J. C. Barão, Masayuki Nakagawa, Luis Távora, and Pedro Vaz, editors, *Advanced Monte Carlo for Radiation Physics, Particle Transport Simulation and Applications*, pages 1033–1038, Berlin, Heidelberg, 2001. Springer Berlin Heidelberg.
- [69] M. Sajjad Athar, M. Honda, T. Kajita, K. Kasahara, and S. Midorikawa. *Physics Letters B*, 718(4):1375 – 1380, 2013.
- [70] Koji Niita, Tatsuhiko Sato, Hiroshi Iwase, et al. *Radiation Measurements*, 41(9):1080 – 1090, 2006. Space Radiation Transport, Shielding, and Risk Assessment Models.
- [71] M. Honda, T. Kajita, K. Kasahara, and S. Midorikawa. *Phys. Rev. D*, 83:123001, Jun 2011.
- [72] <http://www.ngdc.noaa.gov/IAGA/vmod/igrf.html>.
- [73] J. A. Formaggio and G. P. Zeller. *Rev. Mod. Phys.*, 84:1307–1341, Sep 2012.
- [74] R. Kanishka, K.K. Meghna, V. Bhatnagar, D. Indumathi, and N. Sinha. *JINST*, 10(03):P03011–P03011, mar 2015.

- [75] S M Lakshmi, A Ghosh, M M Devi, et al. *JINST*, 9(09):T09003–T09003, sep 2014.
- [76] M. Bhuyan, V.M. Datar, S.D. Kalmani, et al. *Nucl. Instrum. Meth. A*, 661:S64 – S67, 2012. X. Workshop on Resistive Plate Chambers and Related Detectors (RPC 2010).
- [77] M. Bhuyan, V.M. Datar, S.D. Kalmani, et al. *Nucl. Instrum. Meth. A*, 661:S68 – S72, 2012. X. Workshop on Resistive Plate Chambers and Related Detectors (RPC 2010).
- [78] S. Pethuraj, V.M. Datar, G. Majumder, et al. *JCAP*, 2017(09):021–021, sep 2017.
- [79] A Aloisio et al. *Nucl. Instrum. Meth. A*, 456(1–2):113–116, 2000. Proceedings of the 5th Int. Workshop on Resistive Plate Chambers and Related Detectors.
- [80] F. Anulli et al. *Nucl. Instrum. Meth. A*, 409(1–3):542–546, 1998.
- [81] A. Abashian et al. *Nucl. Instrum. Meth. A*, 479(1):117 – 232, 2002. Detectors for Asymmetric B-factories.
- [82] G Chiodini and S Spagnolo. *Journal of Instrumentation*, 8(02):T02004, 2013.
- [83] E Cerron Zeballos et al. *Nucl. Instrum. Meth. A*, 374(1):132 – 135, 1996.
- [84] M. M. Devi, N. K. Mondal, B. Satyanarayana, and R. R. Shinde. *The European Physical Journal C*, 76(12):711, Dec 2016.
- [85] Sumanta Pal. *Development of the INO-ICAL detector and its physics potential*. PhD thesis, Homi Bhabha National Institute, 2014.
- [86] M. Bhuyan, V.B. Chandratre, S. Dasgupta, et al. *Nucl. Instrum. Meth. A*, 661, Supplement 1:S73 – S76, 2012. X. Workshop on Resistive Plate Chambers and Related Detectors (RPC 2010).
- [87] Anushree Ghosh and Sandhya Choubey. *Journal of High Energy Physics*, 2013(10):174, Oct 2013.
- [88] Kolahal Bhattacharya. *Event Reconstruction for ICAL Detector and Neutrino Mass Hierarchy Sensitivity Analysis at India-based Neutrino Observa-*

- tory (INO)*. PhD thesis, Tata Institute of Fundamental Research, 2015.
- [89] Moon Moon Devi. *Enhancing ICAL potential with hadrons, and development of multigap RPC*. PhD thesis, Homi Bhabha National Institute, 2015.
- [90] Lakshmi S Mohan. *Precision measurement of neutrino oscillation parameters at INO ICAL*. PhD thesis, Homi Bhabha National Institute, 2015.
- [91] J. Allison, K. Amako, J. Apostolakis, et al. *IEEE Transactions on Nuclear Science*, 53(1):270–278, Feb 2006.
- [92] Apache Software Foundation. Magnet, 2008.
- [93] S. P. Behera, M. S. Bhatia, V. M. Datar, and A. K. Mohanty. *IEEE Transactions on Magnetics*, 51(2):1–9, Feb 2015.
- [94] C. Andreopoulos, A. Bell, D. Bhattacharya, et al. *Nucl. Instrum. Meth. A*, 614(1):87–104, 2010.
- [95] ALI AJMI and GOBINDA MAJUMDER. *Pramana*, 88(3):55, Feb 2017.
- [96] Richard P. Mount. *Computer Physics Communications*, 45(1):299 – 310, 1987.
- [97] John Stuart Marshall. *A study of muon neutrino disappearance with the MINOS detectors and the NuMI neutrino beam*. PhD thesis, University of Cambridge, 2008.
- [98] E.J Wolin and L.L Ho. *Nucl. Instrum. Meth. A*, 329(3):493 – 500, 1993.
- [99] H Bethe, J Ashkin, and edited by E Segre. *Experimental nuclear physics*. J Wiley, New York, 1953.
- [100] Anushree Ghosh, Tarak Thakore, and Sandhya Choubey. *Journal of High Energy Physics*, 2013(4):9, Apr 2013.
- [101] Tarak Thakore, Anushree Ghosh, Sandhya Choubey, and Amol Dighe. *Journal of High Energy Physics*, 2013(5):58, May 2013.
- [102] Tarak Thakore, Moon Moon Devi, Sanjib Kumar Agarwalla, and Amol Dighe. *Journal of High Energy Physics*, 2018(8):22, Aug 2018.
- [103] Moon Moon Devi, Tarak Thakore, Sanjib Kumar Agarwalla, and Amol

- Dighe. *Journal of High Energy Physics*, 2014(10):189, Oct 2014.
- [104] A. Ajmi and S.U. Sankar. *JINST*, 10(04):P04006–P04006, apr 2015.
- [105] Ali Ajmi. *A study of muonless events and an attempt to improve the hierarchy sensitivity through neural networks at ICAL@INO*. PhD thesis, Homi Bhabha National Institute, 2016.
- [106] N. Panchal, G. Majumder, and V.M. Datar. *JINST*, 14(02):P02032, feb 2019.
- [107] Suryanarayan Mondal, V.M. Datar, Gobinda Majumder, et al. *JINST*, 14(04):P04009, apr 2019.
- [108] F. Anghinolfi, P. Jarron, F. Krummenacher, E. Usenko, and M. C. S. Williams. *IEEE Transactions on Nuclear Science*, 51(5):1974–1978, Oct 2004.
- [109] F. Anghinolfi, P. Jarron, A.N. Martemiyarov, et al. *Nucl. Instrum. Meth. A*, 533(1):183 – 187, 2004. Proceedings of the Seventh International Workshop on Resistive Plate Chambers and Related Detectors.
- [110] Puneet Kanwar Kaur, Pathaleswar, M. N. Saraf, B. Satyanarayana, and R. R. Shinde. *Springer Proc. Phys.*, 203:571–574, 2018.
- [111] V. B. Chandratre, Menka Sukhwani, Hari Prasad Kolla, et al. 60:928–929, 2015.
- [112] M. N. Saraf, U. Gokhale, A. Lokapure, et al. *Springer Proc. Phys.*, 174:565–570, 2016.
- [113] *Altera Cyclone IV Device Handbook*.
- [114] J Christiansen. HPTDC High Performance Time to Digital Converter. Technical report, CERN, Geneva, 2004. Version 2.2 for HPTDC version 1.3.
- [115] *Nios II Software Developer Handbook*.
- [116] Werner Riegler. *Nucl. Instrum. Meth. A*, 491(1):258 – 271, 2002.
- [117] Alberto Rotondi and Paolo Montagna. *Nucl. Instrum. Meth. B*, 47(3):215 – 223, 1990.

# List of Abbreviations

INO	India-based Neutrino Observatory
ICAL	Iron Calorimeter
DONuT	Direct Observation of the Nu Tau
SSM	Standard Solar Model
CNO	Carbon Nitrogen Oxygen
KGF	Kolar Gold Fields
AGN	Active Galactic Nucleus
GRB	Gamma-Ray Burst
CMB	Cosmic Microwave Background
SM	Standard Model
CC	Charged Current
NC	Neutral Current
MSW	Mikheyev-Smirnov-Wolfenstein
NH	Normal Hierarchy
IH	Inverted Hierarchy
MC	Monte Carlo
QE	Quasi-Elastic
RS	Resonant Scattering
DIS	Deep Inelastic Scattering
RPC	Resistive Plate Chamber
PHITS	Particle and Heavy-Ion Transport code System

MRPC	Multigap Resistive Plate Chamber
DAQ	Data AcQuisition
HMC	Hybrid Micro Circuits
AFE	Analog Front-End
DFE	Digital Front-End
CDR	Control and Data Router
VME	Versa Module Eurocard
TDR	Time and Trigger Router
FTM	Final Trigger Module
TDC	Time to Digital Convertor
POSIX	Portable Operating System Interface
CFD	Constant Fraction Discriminator
FC	Fully Contained
PC	Partially Contained
GHR	Ghost Hit Removal
EMI	ElectroMagnetic Interference
PS	Power Supply
LCWCS	Low Conductivity Water Cooling System
ADC	Analog to Digital Convertor
FEM	Finite Element Method
CLS	Closed-Loop gas recirculation System
RISC	Reduced Instruction Set Computer
AVR	Alf and Vegard's RISC processor
SPI	Serial Peripheral Interface
FRP	Fibre Reinforced Plastic
MFC	Mass Flow Controller
PLC	Power-Line Communication
SCADA	Supervisory Control And Data Acquisition



ASIC	Application-Specific Integrated Circuit
FPGA	Field Programmable Gate Array
HPTDC	High-Performance Time to Digital Convertor
NIOS	Network I/O System
SRB	Signal Router Board
TLB	Trigger Logic Board
TCAM	Trigger Control And Monitor
CAU	Calibration and Auxiliary Unit
TOF	Time-Of-Flight
RTC	Real-Time Clock
TCP	Transmission Control Protocol
UDP	User Datagram Protocol
LSM	Least-Squares Method
ToT	Time over Threshold

